Infrared Detectors Based on Two-Dimensional Materials and Heterostructures

by

Yuxuan Lin

B.S., Tsinghua University, Beijing, China (2012)
S.M., Massachusetts Institute of Technology (2014)

Submitted to the Department of Electrical Engineering and Computer Science
in partial fulfillment of the requirements for the degree of

Doctor of Philosophy in Electrical Engineering

at the

MASSACHUSETTS INSTITUTE OF TECHNOLOGY

September 2019

Author .....
Department of Electrical Engineering and Computer Science
August 30, 2019

Certified by .....
Tomás Palacios
Professor of Electrical Engineering and Computer Science
Thesis Supervisor

Accepted by .....
Leslie A. Kolodziejski
Professor of Electrical Engineering and Computer Science
Chair, Department Committee on Graduate Students

Infrared Detectors Based on Two-Dimensional Materials and Heterostructures

by

Yuxuan Lin

Submitted to the Department of Electrical Engineering and Computer Science
on August 30, 2019, in partial fulfillment of the
requirements for the degree of
Doctor of Philosophy in Electrical Engineering

Abstract

At the nanoscale, new forms of physical phenomena emerge that can provide remarkable opportunities for next-generation tools with unprecedented functionality and energy efficiency. Two-dimensional (2D) materials, a family of nanomaterials with atomic thickness, promise an ideal platform for nanoscience and nanotechnology research on which we are able to engineer functional structures and study their properties at the limit of the atomic scale. This thesis discusses opportunities and challenges of studying emerging light-matter interaction phenomena and developing advanced infrared detection technologies enabled by 2D materials and their heterostructures. First, we addressed some of the key challenges for reliable synthesis and characterization of 2D materials and functional nanostructures. We developed a new seeding-promoter-assisted chemical vapor deposition approach for the construction of vertical and lateral heterostructures between a variety of 2D materials over large area. This technology enables many new physics and device applications, including 1D ohmic contacts to 2D semiconductors and their integrated circuits. Another material-related challenge we addressed is the fast material characterization of 2D materials. We developed a deep learning algorithm that can perform realtime, accurate material identification on optical microscope images of 2D materials. In addition, our method is able to extract deep graphical features and provide information about structural, optical and mechanical properties of the materials.

Second, we studied three novel IR detector technologies based on 2D materials and other nanostructures that can potentially out-perform the state-of-the-art graphene thermopile, graphene-2D semiconductor photothermoelectric detector, and thermo-mechanical bolometer. For the graphene thermopile, our theoretical analysis indicates that a high-quality graphene device provides the highest thermoelectric figure of merit among existing thermoelectric materials. We further demonstrated a monolithic 3D integration of graphene and Si CMOS technologies and fabricated a mid-IR/thermal imaging camera based on graphene thermopiles. For the second IR detection technology, we studied the unique hot carrier thermalization process on a graphene-2D semiconductor lateral heterojunction device, and showed that such

a photothermoelectric photocurrent generation mechanism is advantageous in terms of picosecond response time, broadband spectral response, and room temperature operation. The third IR detection technology we demonstrated in this thesis is a thermo-mechanical bolometer, in which the IR radiation is converted into an abrupt resistance change through the special thermo-mechanical response and an artificial metal-insulator transition of engineered nanostructures. Our results show that the sensitivity of this thermo-mechanical mid-IR detector can be at least one order of magnitude better than state-of-the-art microbolometers based on VO_x.

Thesis Supervisor: Tomás Palacios
Title: Professor of Electrical Engineering and Computer Science

Acknowledgments

I would like to express my great gratitude to my thesis advisors, Professor Tomás Palacios and the late Professor Mildred Dresselhaus. Through my years of PhD study with them, I have learned from both of them how to approach problems from different perspectives. I was influenced deeply by Tomás' enthusiasm about research and I was encouraged and motivated by him many times to pursue challenging but meaningful research projects that can truly impact our society. I am also thankful for them giving me freedom to explore different great or crazy ideas. I could not have imagined having a better combination of advisors for my PhD study.

I would like to thank my close collaborator, Professor Jing Kong, who taught me not only how to become a good researcher, but more importantly, how to be a good person. Her advise about research projects and career plans was truly helpful. I would also like to thank my other thesis readers, Professor Jeffrey Lang and Professor Dirk Englund, for their support and meaningful feedback of my thesis.

I would like to thank my collaborators, Professor Xi Ling, Professor Pablo Jarillo-Herrero, Professor Farnaz Niroui, Professor Nuh Gedik, and Professor Jihao Yin for their experimental support and fruitful discussion. And many thanks to my fellow group members and colleagues, Xu Zhang, Shengxi Huang, Allen Hsu, Lili Yu, Yuhao Zhang, Ahmad Zubair, Marek Hempel, Charles Mackin, Daniel Pedra, Elaine McVay, Qiong Ma, Su-Yang Xu, Yaqing Bie, Yuan Cao, Yafang Yang, Pin-Chun Shen, Yunfan Guo, Qingqing Ji, Nannan Mao, Cong Su, Ang-Yu Lu, Albert Liao, Joaquin Rodriguez-Nieva, Yi-Hsien Lee, Cheng-Te Lin, Xi Wang, Jordan Goldstein, Cheng Peng and Xingzhi Wang for their help in variuos aspects and for their company throughout my PhD study. I am grateful that we have cultivated such a great collaborative and effective research environment.

Finally, I would like to thank my parents for their emotional and physical support. I am very fortunate to be their child. I gained tremendous energy from our barrierless communication and their understanding.

Contents

List of Figures

List of Tables

Chapter 1

Introduction

This thesis aims to address some of the key challenges in synthesis, characterization and optoelectronic device applications of two-dimensional (2D) materials, their heterostructures, and other emerging nanomaterials. Thanks to the low-dimensionality and the resulting strong quantum confinement, many novel light-matter interaction phenomena emerge that we can harness for next generation optoelectronics and sensing systems. In addition, the weak van der Waals interaction between the atomic layers gives rise to great opportunities of integrating 2D material based technology on top of conventional silicon CMOS technology. In this thesis, we prototyped and provided in-depth studies on several new infrared detector technologies based on 2D materials and their heterostructures, including graphene thermopiles, 2D lateral heterojunction photothermoelectric detectors, and thermo-mechanical bolometers. They all showed great potential for out-performing the state-of-the-art technologies. Along the way, we also developed material synthesis and characterization approaches, including a seeding promoter assisted chemical vapor deposition approach for constructing vertical and lateral heterostructures of 2D materials, and a deep-learning-enabled optical characterization approach for 2D materials.

In this chapter, we will first give a brief overview of the mainstream infrared detection technologies. Putting this in perspective, we will then introduce recent advances in 2D materials, their processing technologies, and their applications as infrared detectors. Finally, we will talk about the opportunities and challenges of 2D

materials based optoelectronics and summarize the key contributions of this thesis.

1.1 Overview of Infrared Detection Technologies

Electromagnetic radiations, although unified by J. C. Maxwell in his well-known Maxwell's Equations[28], could propagate in space and interact with matters in dramatically different ways. As a result, electromagnetic waves in different wavelength regimes have historically been named with tremendous variety (Figure 1-1). Advancing the detection technologies of each regime of the electromagnetic waves has both accompanied and facilitated the exploration of light-matter interaction phenomena in the past few hundred years. With the boosting growth of the semiconductor industry in the past decades, solid-state radiation detection technologies have been widely adopted in medicine, communications, manufacture, automobile, military, astronomy, logistics, and so on, which has truly reshaped our everyday life. Among the various radiation detection technologies, detectors in the infrared spectral ranges are of particular significance. Infrared (IR) technologies, originally connected with night vision, surveillance, and remote controlling in military applications, have been shifted gradually to applications for civilian use, including medical, industry, earth resources, and automotive applications (Figure 1-2). As shown in Figure 1-3[4], there are three spectral windows of interest for atmospheric applications: near IR (NIR) /short-wave IR (SWIR) from 0.7 to 3 μm, mid-wave IR (MWIR) from 3 to 5 μm, and long-wave IR (LWIR) /far IR (FIR) from 8 to 12 μm. A variety of materials with different detecting mechanism have been discovered and used in the detection of specific spectral ranges. For example, thermal radiations of human bodies and ordinary objects lie inside the LWIR spectral range. We can thus build LWIR cameras and use them for thermal object tracking. Such systems can be used in computer vision, gesture /motion detection, automatic vehicle, and medical diagnostics. Another example is remote sensing. With high resolution IR imagers and/or spectrograph mounted on aircrafts or satellites, it is possible to identify and localize specific chemical elements or compounds. This technology has been widely used in mineral search[29], geological

or environmental survey[30], inspection of natural hazards and disasters[31], *etc.*

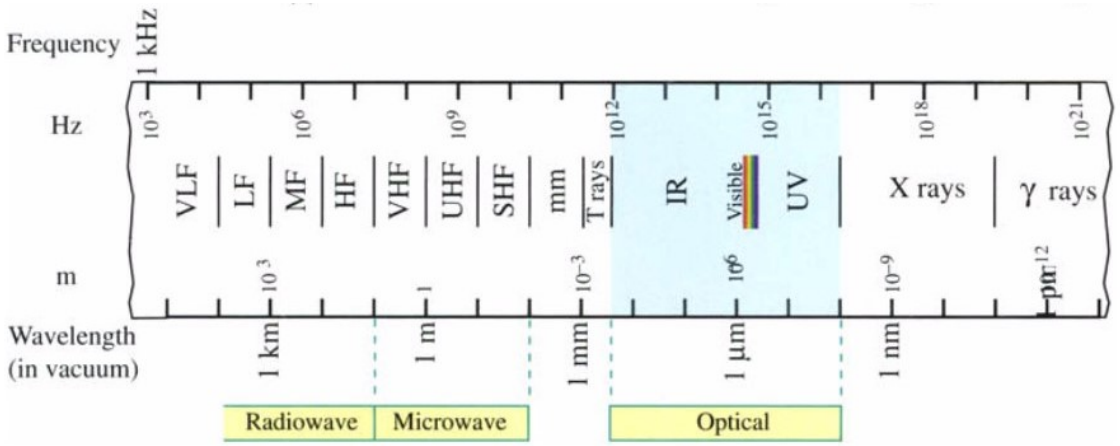

Figure 1-1: The electromagnetic spectrum as a function of wave frequency and wavelength in vacuum. [3]

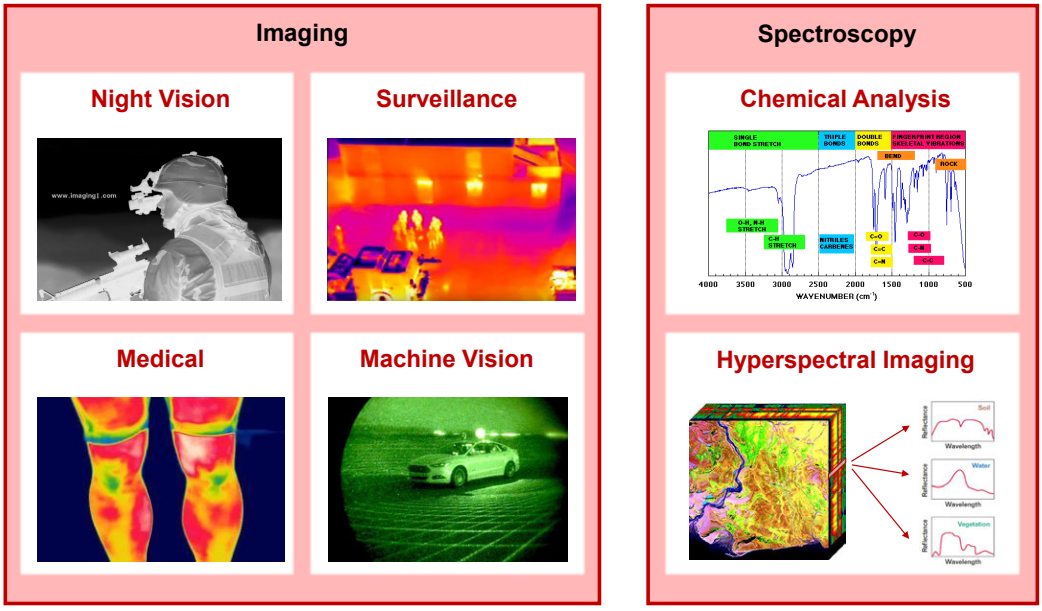

Figure 1-2: Example applications of infrared detection technologies.

1.1.1 Mechanisms of IR Detection

Depending on the path of energy conversions, IR detectors can be divided into two major classes:

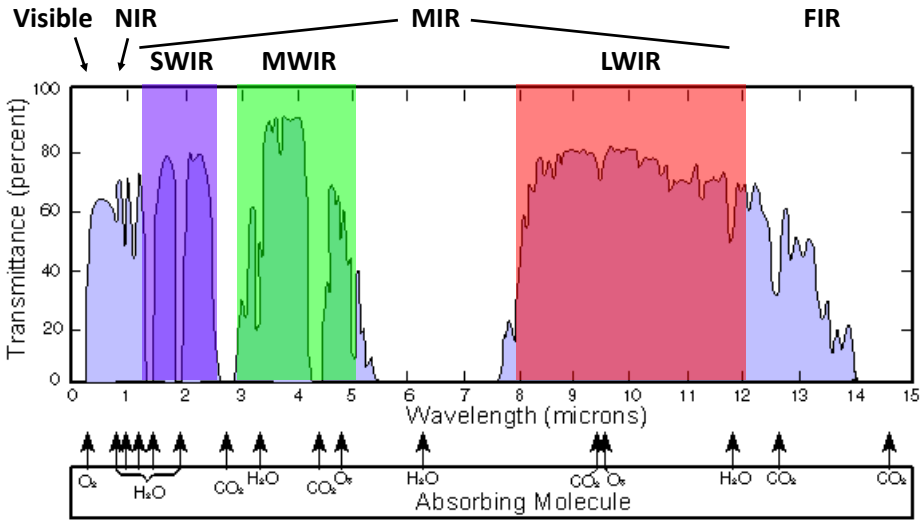

Figure 1-3: Transmission of the atmosphere for a 6000-foot horizontal path at sea level containing 17 mm of precipitate water. [4]

Photon Detector

A photon detector transfers incident photon energy directly into electrical energy. It requires the incident photons to be absorbed directly by the electronic systems of the sensing material. In other words, there must be a photo-induced transition between electronic states. Such transitions include interband transitions of direct bandgap semiconductors, mid-gap state transitions of extrinsic semiconductors, free carrier intraband transitions, superlattice inter-subband transitions, *etc.* After the direct electronic transition, the photo-excited carriers need to be separated and extracted efficiently. Photon detectors can be further classified into photovoltaic, photoconductive, photoemissive, Dember and photoelectromagnetic detectors based on the photo-carrier extraction mechanisms.

1. *Photovoltaic (PV) Detector.* When a p-n junction or a heterojunction is present, the photo-generated electrons and holes can be separated by the built-in electric field, or the discontinuity of the band edges. As a result, electrons and holes can be collected by the anode and the cathode electrodes, respectively, which

gives rise to an electromotive force. The current-voltage characteristics of a good PV detector are usually highly asymmetric, and their intersections with the axes are non-zero when light is shined onto the devices. PV detectors are active detectors, which means that they do not necessarily need external power sources, although most PV detectors may operate at a reverse bias to maximize the responsivity.

2. *Photoconductive (PC) Detector.* The incident light can also affect the conductance of a homogeneous semiconductor, through changes in carrier concentration, carrier mobility, *etc.* PC detectors are passive detectors: they need to be biased so that the photo-induced resistance change can be transduced into a measurable voltage or current change.

3. *Photoemissive (PE) Detector.* A PE detector is based on the change of the thermionic emission current because of the photo-induced majority carriers near a metal-semiconductor junction (Schottky junction). It is also an active detector. It usually requires low-temperature operation to suppress the dark current.

4. *Dember Detector.* A Dember detector is a special case of a PV detector. The built-in electric field is generated near the surfaces of a bulk homogeneous semiconductor due to the difference of the mobilities, and the resulting difference of photo-carrier diffusion lengths between electrons and holes.

5. *Photoelectromagnetic (PEM) Detector.* When a magnetic field is applied along the surface of a semiconductor, the photo-induced diffusion current into the bulk would be deflected by the Coulomb force. As a result, an electromotive force can be generated in a direction perpendicular to the magnetic field. A PEM detector is an active detector. Cooling is less critical in this technology, but an external magnetic field is required, which makes the device bulky and power-consuming.

Thermal Detector

Thermal detectors have indirect signal transducing paths. The absorbed IR radiation is first transfered into thermal energy, and then into an electrical signal through a temperature-sensitive component. Although thermal detectors are less sensitive and much slower than photon detectors, they can operate very well at room temperature, which makes them the dominant technology for portable/uncooled mid- to far-IR imaging applications. Thermal detectors can be further classified as bolometers, thermopiles, pyroelectric detectors, and optomechanical detectors.

1. *Bolometer.* A bolometer is a temperature sensitive resistor. It is also called thermistor. The electrical characteristics of a bolometer is similar to a photoconductor, but the detection mechanism is very different. The incident IR radiation heats up the bolometric material, which in turn produces a resistance change. There is no direct photon-electron interaction. Instead, the resistance change is induced by some electronic properties of materials that has a temperature dependence, such as the thermally excited carrier densities, scatterings of carriers, or even transitions of crystalline structures. Bolometers are passive detectors.

2. *Thermopile.* The electrical signal in a thermopile is transduced by a thermocouple, in which a voltage drop will be generated when any two conductive materials are connected and bridged across a temperature gradient. This effect is also called thermoelectric effect. Thermopiles are active detectors.

3. *Pyroelectric Detector.* Pyroelectric material is a class of crystalline materials that have spontaneous electric polarizations. When temperature is varied, the polarizations in the crystal will change, giving rise to a charge accumulation or extraction at the top and bottom surfaces along the polarization direction. If we sandwich a pyroelectric material between two metal electrodes to form a capacitor, a transient voltage or current because of the temperature change can be measured. As a result, pyroelectric detectors need to work with an intensity-modulated incident light.

4. *Optomechanical Detector.* Optomechanical detector is an emerging type of IR detectors. It employs a thermally induced deflection of a microcantilever. If a visible mirror is mounted at the end of the microcantilever and a visible light beam is directed to the mirror, the IR excited temperature change can be read out by measuring the deflection of the reflected visible beam.

1.1.2 Figure of Merits

In this section, we summarize the figure of merits (*FoMs*) that are used to characterize different IR detection technologies.

1. *Responsivity ($\mathcal{R}$)*

   The responsivity of an infrared detector is defined as the ratio of the average value of the output signal and the average value of the incident IR radiation power on the device. Depending on the detection mechanism, the output signal could be voltage, current, and relative resistance change. For instance, the voltage responsivity $\mathcal{R}_v$ can be expressed as

$$\mathcal{R}_v = \frac{V_s}{P_{in}} \tag{1.1}$$

   In Eq. (1.1), V_s is the photovoltage generated by the detector, and P_{in} is the power of the incident light. The unit of $\mathcal{R}_v$ is volts per watt (V/W). Note that the responsivity in most cases is strongly dependent on the wavelength (λ), operation temperature (T_{op}), input power (P_{in}) and modulation frequency (f) of the incident light, that is, $\mathcal{R}_v = \mathcal{R}_v(\lambda, T_{op}, P_{in}, f)$. Linear dynamic range ($LDR$) and response time ($\tau$) are used to characterize the power dependence and the frequency dependency of the detector.

2. *Noise Equivalent Power (NEP)*

   The noise equivalent power (NEP) is the level of incident power on the detector generating the same amount of output signal as the overall root mean square

(RMS) noise output of the detector. In another words, the *NEP* is the incident power that leads to a signal-to-noise ratio (*SNR*) of 1. The *NEP* can be expressed as

$$NEP = \frac{\sqrt{\overline{v_n^2}}}{\mathcal{R}_v} \tag{1.2}$$

where $\sqrt{\overline{v_n^2}}$ is the RMS noise equivalent voltage at the output. The unit of *NEP* is Watt (W).

3. *Specific Detectivity (D^*)*

Specific detectivity D^* is a parameter to indicate the signal-to-noise ratio that is normalized to geometry and frequency, expressed as

$$D^*(\lambda) = \frac{\sqrt{A_d \cdot \Delta f}}{NEP} \tag{1.3}$$

in which A_d is the active area of the detector, and Δf is the bandwidth, or cut-off frequency. The unit for D^* is $\mathrm{cm} \cdot \mathrm{Hz}^{1/2}\mathrm{W}^{-1}$. D^* is the figure of merits that is generally used to compare different types of IR detectors, since it normalizes the detector sensitivity with the geometry and the speed of the detector. For thermal imaging applications, the blackbody D-star is also used to characterize the detector's capacity to detect a thermal object with the black-body radiation temperature T:

$$D^*(T) = \frac{\int_0^\infty D^*(\lambda) M(\lambda, T) \mathrm{d}\lambda}{\int_0^\infty M(\lambda, T) \mathrm{d}\lambda} \tag{1.4}$$

where $M(\lambda, T)$ is the blackbody irradiance (in $\mathrm{W/cm^2}$), expressed as

$$M(\lambda, T) = \frac{2\pi hc^2}{\lambda^5} [\exp(\frac{hc}{\lambda k_B T})]^{-1} \tag{1.5}$$

where h is the Plank's constant; c is the speed of light; and k_B is the Boltzmann

constant.

4. *Linear Dynamic Range (LDR)*

   The linear dynamic range (LDR) characterizes the range of the input power where the photodetector can operate with a constant responsivity. The LDR (in dB) can be calculated by the maximum incident power ($P_{\max}$) with which the device can still work in linear regime, divided by the noise equivalent power (NEP) over the whole bandwidth, or

$$LDR = 20 \cdot \log_{10}(\frac{P_{\max}}{NEP}) \tag{1.6}$$

5. *Response Time (τ)*

   The response time (τ) measures how fast a photodetector can respond to the input signal. The response time can be extracted by finding the reciprocal of the 3-dB frequency or the first order cut-off frequency (f_c) from a frequency characteristics of the responsivity (the Bode plot of $\mathcal{R}$).

6. *Noise Equivalent Temperature Difference (NETD)*

   Noise equivalent temperature difference ($NETD$) is a FoM for an infrared imaging system. It takes into account the spectral detectivity of the detector as well as the optical loss of the imaging system. $NETD$ of an infrared detector is defined as the minimum temperature change of the target thermal object that can provide an output signal on the same level of the RMS noise level. $NETD$ is expressed as

$$NETD = \frac{\sqrt{\overline{v_n^2}}(\partial T/\partial Q)}{(\partial V_s/\partial Q)} = \sqrt{\overline{v_n^2}}\frac{\Delta T}{\Delta V_s} \tag{1.7}$$

   where Q is the spectral photon flux density (in photons/cm^{2}s) incident on a focal plane, and T is the temperature on the target thermal object.

For a single lens imaging system with $F/\#$ of the optics setting, the $NETD$ can be calculated by

$$NETD = \frac{4(F/\#)^2 \Delta f^{1/2}}{A_d} [\int_{\lambda_a}^{\lambda_b} \frac{\partial M(\lambda, T)}{\partial T} D^*(\lambda) \mathrm{d}\lambda]^{-1} \tag{1.8}$$

1.1.3 Fundamental Limits and the State-of-the-Art

This section discusses the fundamental limitations of both photon and thermal IR detectors by considering the statistical nature of carrier/temperature generation, recombination, and noise generation. We will also summarize the state-of-the-art IR detector technologies and use them as the baseline for evaluations the emerging IR detection technologies that are developed in this thesis.

Fundamental Limits of Photon Detectors[5]

Photon detectors are based on the direct photon excitation of electronic states in semiconductor materials and heterostructures. The optical absorption of a material can be characterized by the optical absorption coefficient, α (in cm^{-1}), or the penetration depth, $1/\alpha$, defined as the distance where $1/e$ of the optical power remains as compared to that at the surface of the material.

The power absorbed in the material with the thickness d can be expressed as

$$P_{abs} = P_{in}(1 - r)(1 - e^{-\alpha d}) \tag{1.9}$$

where P_{in} is the incident optical power, and r is the reflectance at the material interface.

The number of photons absorbed per incident photon is then

$$ABS = (1 - r)(1 - e^{-\alpha d}) \tag{1.10}$$

Another fundamental parameter to characterize the photo-to-electrical conversion process of a material is called internal quantum efficiency (IQE), defined as the num-

ber of photo-excited carriers generated and collected per absorbed photon. People also use the external quantum efficiency (EQE) to characterize the overall performance of the absorption and conversion efficiency, which is given by $EQE = ABS \cdot IQE$. Figure 1-4 summarizes the absorption coefficient and the IQE of various photodetection materials.

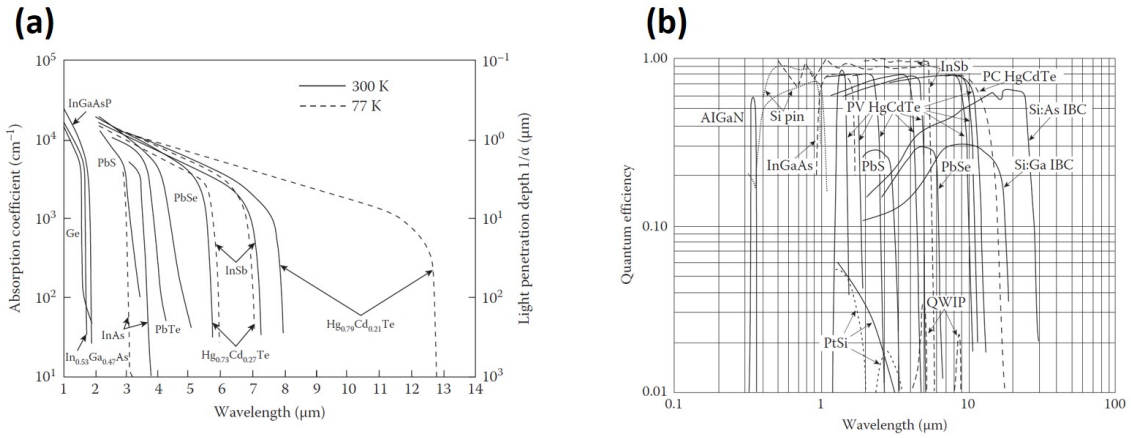

Figure 1-4: Absorption coefficients (a) and internal quantum efficiencies (b) of common photodetection materials. [5]

The current responsivity of a photon detector at a specific wavelength λ is given by

$$\mathcal{R}_i = \frac{\lambda\eta}{hc} qg \tag{1.11}$$

in which η is the quantum efficiency (EQE in a general case), and g is the photoelectric current gain.

The noise equivalent current is

$$\overline{i_n^2} = 2q^2 g_n^2 (G_{op} + G_{th} + R)\Delta f \tag{1.12}$$

where G_{op}, G_{th} and R are the optical generation rate, the thermal generation rate and the recombination rate, respectively; g_n is the gain of the noise sources in the device. In most cases, $g_n = g$.

The detectivity of a photon detector is thus given by

$$D^* = \frac{\mathcal{R}_i(A_d \cdot \Delta f)^{1/2}}{\sqrt{\overline{i_n^2}}} = \frac{\lambda\eta}{hc}\frac{g}{g_n}\sqrt{\frac{A_d}{2(G_{op}+G_{th}+R)}} \tag{1.13}$$

For an ideal situation, only the optical generation noise is present. The optical generation noise can be originated from the signal radiation generation, the background radiation generation, and the thermal self-radiation of the detector. The optical generation rate is

$$G_{op} = \Phi A_d \eta \tag{1.14}$$

where Φ is the photon flux density. As an ultimate theoretical limit of a photon detector, only background flux is considered, that is, $\Phi = \Phi_B$. The background flux can be calculated by

$$\Phi_B = \sin^2(\theta/2)\int_0^{\lambda_c} \Phi(\lambda, T_b)\mathrm{d}\lambda \tag{1.15}$$

where θ is the field of view (FOV) of the detector; λ_c is the cut-off frequency of the detector; T_b is the background temperature; and Φ is given by

$$\Phi(\lambda, T_b) = M \cdot \frac{\lambda}{hc} = \frac{2\pi c}{\lambda^4[\exp(hc/\lambda k_B T_B) - 1]} \tag{1.16}$$

The background-limited detectivity is

$$D^*_{BLIP} = \frac{\lambda}{hc}\sqrt{\frac{\eta}{2\Phi_B}} \tag{1.17}$$

In this scenario, quantum efficiency (η) is the only detector parameter for the evaluation of a detector's performance.

2π-FOV D^*_{BLIP}, or $D^*_{BLIP}(2\pi)$ is usually used as the baseline for different IR detection technologies. The conversion between 2π-FOV and realistic θ-FOV related values is given by

$$\frac{\Phi_B(\theta)}{\Phi_B(2\pi)} = \sin^2(\theta/2) \tag{1.18}$$

And

$$\frac{D^*_{BLIP}(\theta)}{D^*_{BLIP}(2\pi)} = \frac{1}{\sin^2(\theta/2)} \tag{1.19}$$

If the detector is working at the BLIP limit, one way to improve the detector sensitivity is to confine the FOV so that less background radiation is coupled to the detector.

Figure 1-5 plots Background radiation limited detectivity D^*_{BLIP} versus cutoff wavelength λ_c for and ideal photon detector ($\eta = 1$) with different background temperatures T_b, for a 2π-FOV. This is the most fundamental limit for any type of IR photon detectors.

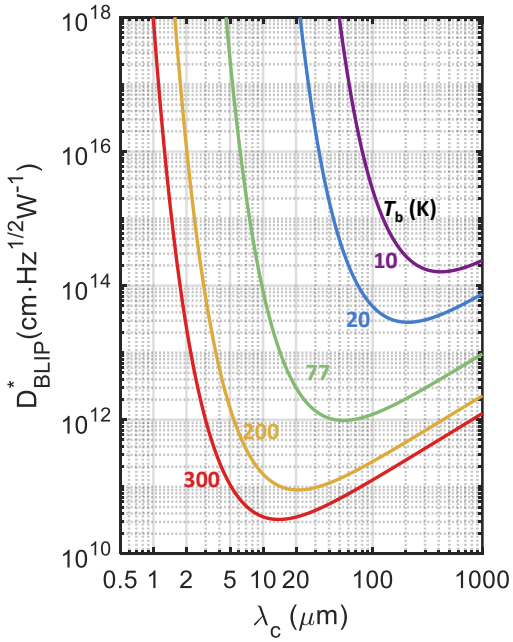

Figure 1-5: Background radiation limited detectivity D^*_{BLIP} versus cutoff wavelength λ_c for and ideal photon detector ($\eta = 1$) with different backgournd temperatures T_b, for a 2π-FOV.

Another theoretical limit is the dark current limited detectivity, expressed as

$$D^*_{DC} = \frac{\lambda\eta}{hc}\sqrt{\frac{A_d q}{2I_{dark}}} \tag{1.20}$$

For an ideal detector, the dark current is limited by the normalized thermal gen-

eration rate, G_{th}, given by

$$I_{dark} = qA_{ch}G_{th} \tag{1.21}$$

And

$$G_{th} = \frac{n_{th}}{\alpha\tau} \tag{1.22}$$

where n_{th} is the density of thermal carriers at temperature T, and τ is the carrier lifetime. In Eq. (1.21), A_{ch} is the cross-section area of the detector along the current flow. For a vertical device, $A_{ch} = A_d$.

When the device is cooled, the thermal generation rate can be reduced greatly. At some point, the thermal generation rate will be smaller than the background flux rate. Below this critical temperature, an optimized photon detector can operate with the background-limited detectivity (Eq. (1.17)).

Fundamental Limits of Thermal Detectors[5]

Reducing the heat dissipation is very critical for a thermal detector. The detector can be represented by a thermal capacitance C_{th} coupled to a heat sink at temperature T_d through a thermal conductance G_{th}. For a IR radiation influx Φ, the temperature on the detector can be obtained by solving the heat equation:

$$C_{th}\frac{\mathrm{d}T}{\mathrm{d}t} + G_{th}(T - T_d) = \epsilon\Phi \tag{1.23}$$

where t represents the time, ϵ is the emissivity (or absorbance ABS), and T_d is the temperature of the device. If the radiation influx is a sinusoidal wave,

$$\Phi = \Phi_o e^{i\omega t} \tag{1.24}$$

where Φ_o is the amplitude of the influx, and ω is the modulation frequency, the steady-state solution for the device temperature increase is

$$\Delta T = T - T_d = \frac{\epsilon \Phi_o}{G_{th} + i\omega C_{th}} \tag{1.25}$$

here we have already dropped the sinusoidal term $e^{i\omega t}$.

To make sure ΔT is maximized, we need to reduce G_{th} and C_{th}. To characterize how fast the detector can respond to the IR radiation, the thermal response time is introduced:

$$\tau_{th} = \frac{C_{th}}{G_{th}} \tag{1.26}$$

The voltage responsivity of a thermal detector is

$$\mathcal{R}_v = \frac{\Delta V}{P_{in}} = \frac{K\Delta T}{P_{in}} = \frac{K\epsilon}{G_{th}\sqrt{1+\omega^2\tau_{th}^2}} \tag{1.27}$$

Here we define the temperature coefficient of voltage K, defined as

$$K = \frac{\Delta V}{\Delta T} \tag{1.28}$$

K indicates how sensitive the sensing material is to transduce the temperature change to the electrical signal. For a thermopile, $K = \Delta S$, with ΔS the seebeck coefficient difference between the two components of the thermocouple. For a bolometer, $K = TCR \cdot R_o \cdot I_{bias}$, where $TCR = \mathrm{d}(\ln R)/dT$ is the temperature coefficient of resistance, R_o is the resistance at T_{op}, and I_{bias} is the current biased across the bolometer. For a pyroelectric detector, $K = pA_d\omega R_o$, where p is the pyroelectric coefficient.

The specific detectivity of a thermal detector is given by

$$D^* = \frac{K\epsilon}{G_{th}}\sqrt{\frac{A_d\Delta f}{(1+\omega^2\tau_{th}^2)(\overline{v_J^2}+\overline{v_{th}^2}+\overline{v_b^2}+\overline{v_{1/f}^2})}} \tag{1.29}$$

where $\overline{v_J^2}$, $\overline{v_{th}^2}$, $\overline{v_b^2}$ and $\overline{v_{1/f}^2}$ are equivalent noise voltages for Johnson noise, temperature fluctuation noise, radiative background noise, and $1/f$ noise, given by

$$\begin{cases} \overline{v_J^2} = 4k_B T_d R_o \Delta f \\ \overline{v_{th}^2} = \dfrac{4k_B T_d^2 K^2 \Delta f}{G_{th}(1+\omega^2\tau_{th}^2)} \\ \overline{v_b^2} = \dfrac{8k_B \epsilon \sigma A_d (T_d^5 + T_b^5) K^2}{G_{th}(1+\omega^2\tau_{th}^2)} \\ \overline{v_{1/f}^2} = k_{1/f} \dfrac{I^\delta}{f^\beta} \Delta f \end{cases} \tag{1.30}$$

where σ is the Stefan-Boltzmann constant; T_d and T_b are, respectively, the detector temperature and the background temperature; $k_{1/f}$ is a prefactor for the $1/f$ noise; δ and β are power factors that are very close to one.

The fundamental limits for thermal detectors include the temperature fluctuation limited detectivity and the background radiation limited detectivity, given by

$$D_{TH}^* = \sqrt{\frac{\epsilon^2 A_d}{4k_B T_d G_{th}}} \tag{1.31}$$

And

$$D_B^* = \sqrt{\frac{\epsilon}{8k_B \sigma (T_d^5 + T_b^5)}} \tag{1.32}$$

For an ideal thermal detector with $\epsilon = 1$, $T_d = T_b = 300\text{K}$, the background radiation limited detectivity is around $2 \times 10^{10} \text{cm} \cdot \text{Hz}^{1/2}\text{W}^{-1}$. Note that the background radiation limited detectivity does not improve much if we only cool down the device, but keep the background temperature constant.

State-of-the-Art of Mainstream IR Detectors

Figure 1-6[6] summarizes the specific detectivities versus wavelength of state-of-the-art detectors. The dashed black curves indicate the fundamental limits for photon and thermal detectors (Eqs. (1.17) and (1.32)). Because photon detectors are based on direct transitions of the electronic states in the semiconductor, the spectral response of photon detectors is usually limited by the energy states of the material systems, and they may need to be operated at lower temperature to reduce the thermal fluctuations

that compete with the photoelectric signals, especially when the photon energy of detection is closer to the thermal energy (26 meV at room temperature). Because of this, photon detectors for LWIR can hardly work at room temperature, and this is where uncooled thermal detectors, although with much lower detectivity, come into place. Uncooled IR detection technology is desirable especially for portable applications, mainly because cooling devices such as thermoelectric coolers, radiation coolers and cryostats are extremely bulky and power consuming.

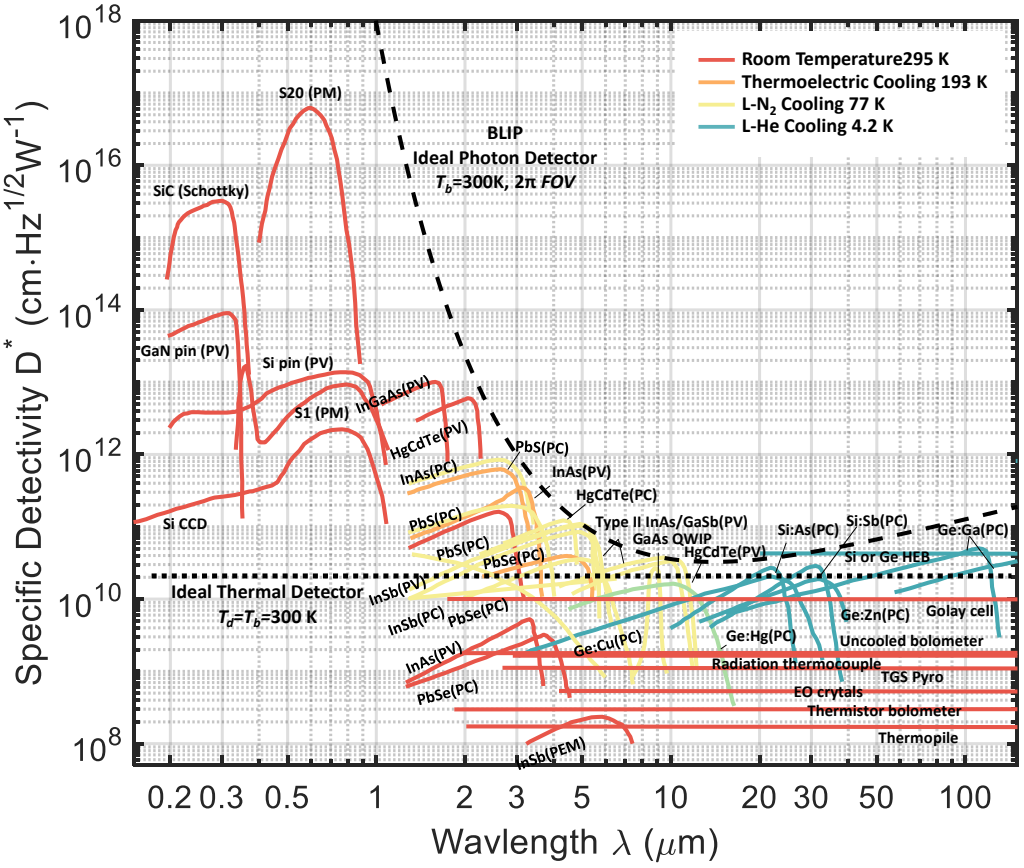

Figure 1-6: Specific detectivity versus wavelength of the state-of-the-art detector in the visible to far-IR range. The curves are colored based on the operation temperature. The black dashed curves indicate the fundamental limits for photon and thermal detectors. Abbreviations: PM: photo-multiplication; PV: photovoltaic; PC: photoconductive; PEM: photoelectromagnetic; CCD: charge-coupled device; HEB: hot-electron bolometer; QWIP: quantum well infrared photodetector; TGS Pyro: doped triglycine sulphate pyroelectric detector; EO crystals: electro-optic crystals; L-N_2: liquid nitrogen; L-He: liquid helium.[6]

Individual IR detectors need to be scaled up to a focal plane array (FPA) and integrated with readout integrated circuits (ROIC) and optical components for practical thermal imaging and spectrograph applications. As shown in Figure 1-7[6], the development of FPAs, especially the charge-coupled device (CCD) technology and CMOS image sensor technology in the visible spectral range, has been steadily advancing with a pace similar to the one in silicon CMOS micro-processors and DRAM technologies. The complexity of IR FPA has been growing as well, but they lagged behind silicon technologies by two to three generations because different materials had to be introduced to enable longer wavelengths.

Besides the growth in the number of pixels, another trend to consider is the level of integration (Figure 1-8). In early days when IR detection technology was first used, only a very limited number of pixels could be fabricated. As a result, single detector or 1D array of detector were used in a imaging/spectroscopy system, and discrete circuits components and scanning optical systems were incorporated (1st generation FPA in Figure 1-8). As the IR detection technology reached maturity, 2D FPAs became feasible, and they were integrated to ROICs either in a hybrid or in a monolithic fashion, which also simplified the optical system (2nd generation FPA in Figure 1-8). For a hybrid integration, the FPA and the ROIC are fabricated on separate chips, stacked on top of each other, and interconnected through wire-bonding or flip-bonding, whereas a monolithic integrated system involves a direct fabrication of FPA onto the as-fabricated ROIC chips. Although monolithic integration has many advantages in terms of miniaturization and reduced interconnection delay, it is usually more challenging because the fabrication process of the FPA needs to be kept at lower temperature constrained by the thermal budget of the silicon CMOS technologies for the ROIC chips. In the past decade, the 3rd generation FPA has been enabled by 3D vertical integration and complex epitaxy growth technologies. In this generation, detecting materials with different bandgaps are grown or stacked on top of each other, and FPAs with two or even more colors becomes reality. More recently, people started to think about further integrated IR imaging systems with more functionality (4th generation), such as incorporating nanophotonic structure to the detector

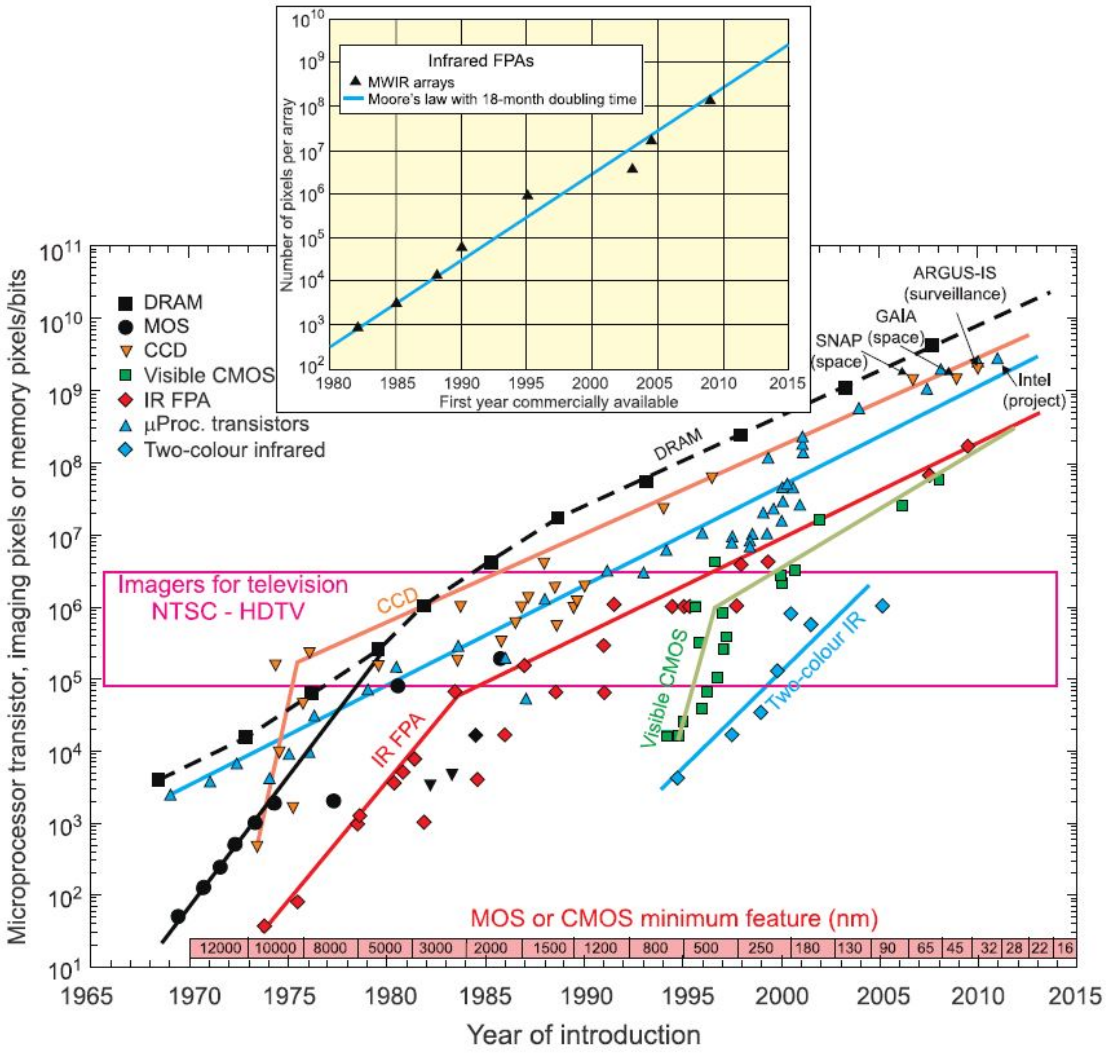

Figure 1-7: The complexity of FPAs in comparison with other semiconductor technologies. The timeline design rule of MOS/CMOS feature sizes is shown at the bottom. The inset shows the number of pixels per array for MWIR imaging systems as a function of the first commercially available year. [6]

pixels for multi-/hyper-spectral imaging or better radiation-pixel coupling, avalanche multiplication in pixels, polarization/phase/helicity/light-field sensitivity and so on.

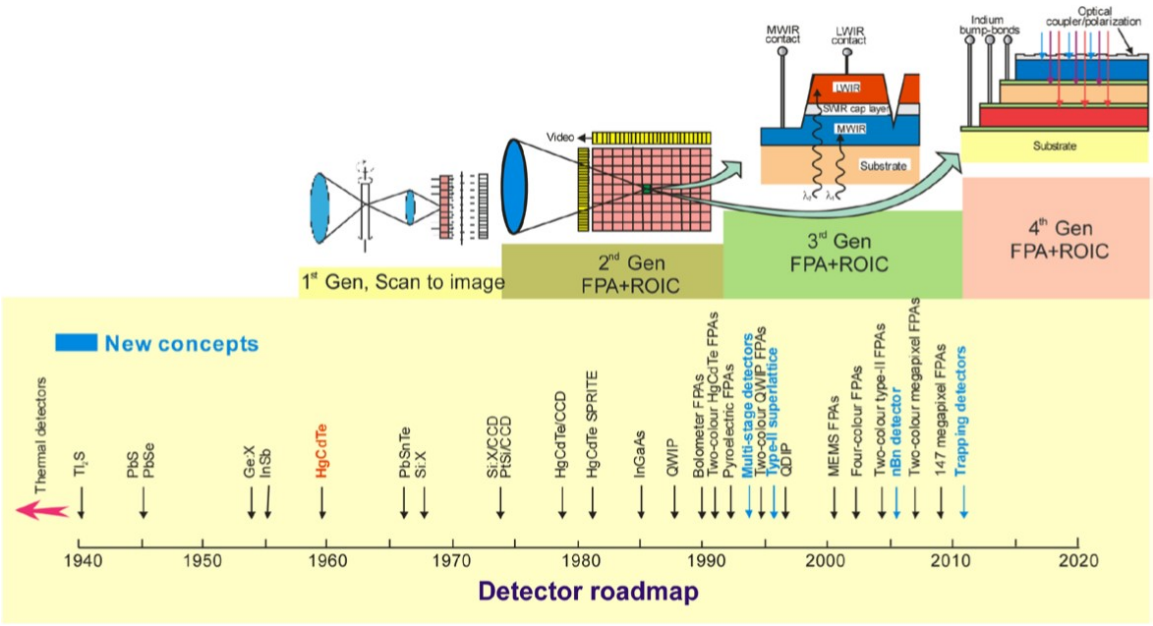

Figure 1-8: Four generations of IR detectors and imaging systems. [7]

1.2 Photodetectors Based on Two-Dimensional Materials

Two-dimensional (2D) materials are atomically thin films originally derived from layered crystals such as graphite, hexagonal boron nitride (h-BN), the family of transition metal dichalcogenides (TMDs, such as MoS_2, WSe_2, $MoTe_2$, and others), and many others [32]. Atomic planes in such crystals are weakly stacked on each other by van der Waals forces so that they can be easily isolated, leaving no dangling bonds. This is in distinct contrast to their counterpart, quasi-low-dimensional semiconductors, which are produced by thinning down conventional bulk or epitaxial crystals. The lack of dangling bonds at the interfaces and surfaces of 2D materials enables new devices with unprecedented performance. The merits of 2D materials are not limited to the absence of dangling bonds. They also show a high degree of chemical stability, as well as unique electronic and optoelectronic properties. This makes 2D materials highly suitable for a wide range of applications, from high performance transistors, to extremely sensitive photodetectors and sensors. In addition, the few-atom thickness of many of these novel devices and systems and the low temperatures required during

the device fabrication allows their seamless integration with conventional silicon electronics. It is possible to fabricate many of these devices on top of a fully fabricated silicon CMOS wafer without degrading the Si transistors underneath, bringing new functionality to the silicon chip. This integration process can be repeated numerous times to build complex 3D systems.

In this section, we will overview different types of 2D materials, their physical properties, synthesis methods, and their device applications as photodetectors.

1.2.1 Physical Properties

The bandgaps of 2D materials span from 0 electron volt (eV) in the case of monolayer graphene, all the way to around 5 eV in the case of hexagonal boron nitride, as summarized in Figure 1-9. In the following, we summarize the basic electrical and optical properties of several 2D materials that are of great interest in optoelectronic device applications.

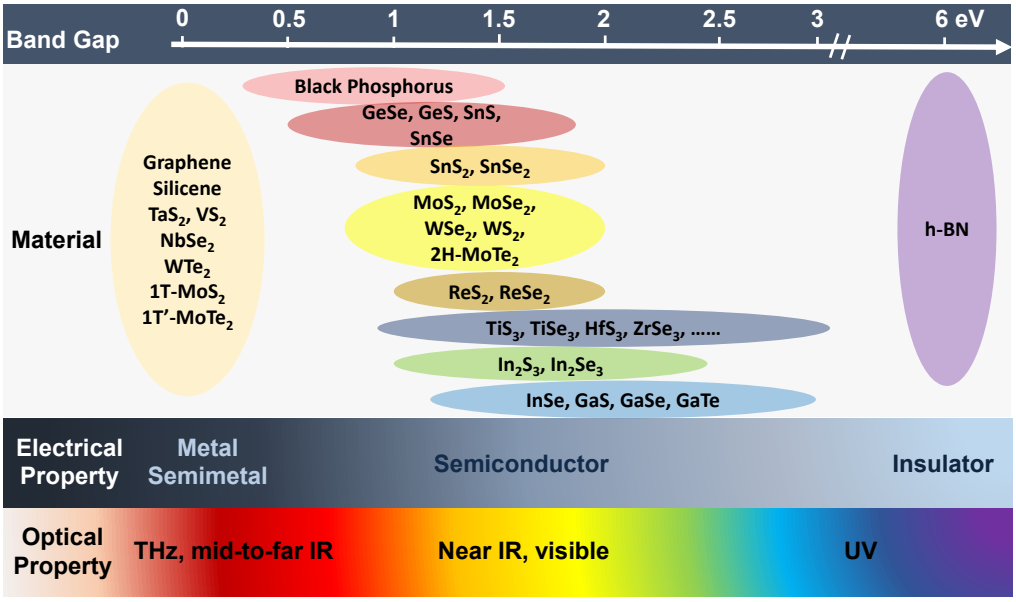

Figure 1-9: A summary of the band gaps, and the corresponding electrical and optical properties of 2D materials.[8]

Graphene

Graphene is a single layer carbon atoms constructed into a honeycomb lattice (Figure 1-10 (a)). The linear electronic dispersion relation (Figure 1-10 (b)) near the charge neutrality point (called Dirac point) in monolayer graphene gives rise to many unique transport and optical properties [9, 33]. For example, the linear electronic dispersion leads to a massless Dirac fermion transport behavior, and the electron mobility in an ideal monolayer graphene film (suspended or encapsulated with hexagonal boron nitride (hBN)) can reach up to 200,000 cm^2/Vs [34, 35, 36]. Another consequence is that the interband optical absorption of suspended monolayer graphene is $\pi\alpha \approx 2.3\%$ for a wide range of incident photon energy, determined by the fine structure constant, $\alpha = e^2/(\hbar c) \approx 1/137$. Later research revealed that the optical properties of graphene can be fully described by its optical conductivity, $\sigma(\omega)$

$$\begin{aligned}\sigma(\omega) = &\frac{2e^2T}{\pi\hbar}\frac{i}{\omega + i\tau^{-1}}\log\left[2\cosh\left(\frac{E_F}{2k_BT}\right)\right] \\ &+ \frac{e^2}{4\hbar^2}\left[\mathrm{H}\left(\omega/2\right) + \frac{4i\omega}{\pi}\int_0^\infty \frac{\mathrm{H}\left(\epsilon\right) - \mathrm{H}\left(\epsilon/2\right)}{\omega^2 - 4\epsilon^2}\mathrm{d}\epsilon\right]\end{aligned} \tag{1.33}$$

where E_F is the Fermi level, $\omega = 2\pi c/\lambda$ is the optical frequency, τ is the relaxation time, and

$$\mathrm{H}\left(\epsilon\right) = \frac{\sinh\left(\hbar\epsilon/k_BT\right)}{\cosh\left(E_F/k_BT\right) + \cosh\left(\hbar\epsilon/k_BT\right)} \tag{1.34}$$

The first term in Eq. (1.33) is due to the intraband transition, which dominates when graphene is heavily doped, whereas the second term indicates the interband transition, which only dominates when graphene is light doped, or when the Fermi level E_F is near the Dirac point. The interband transition term will drop dramatically when $\hbar\omega < |2E_F|$. This effect can be reflected from the absorption spectrum, called Pauli blocking (Figure 1-11).

The electronic structure of bi-layer or tri-layer graphene is significantly different from monolayer graphene. For instance, A-B (Bernal) stacked bi-layer graphene

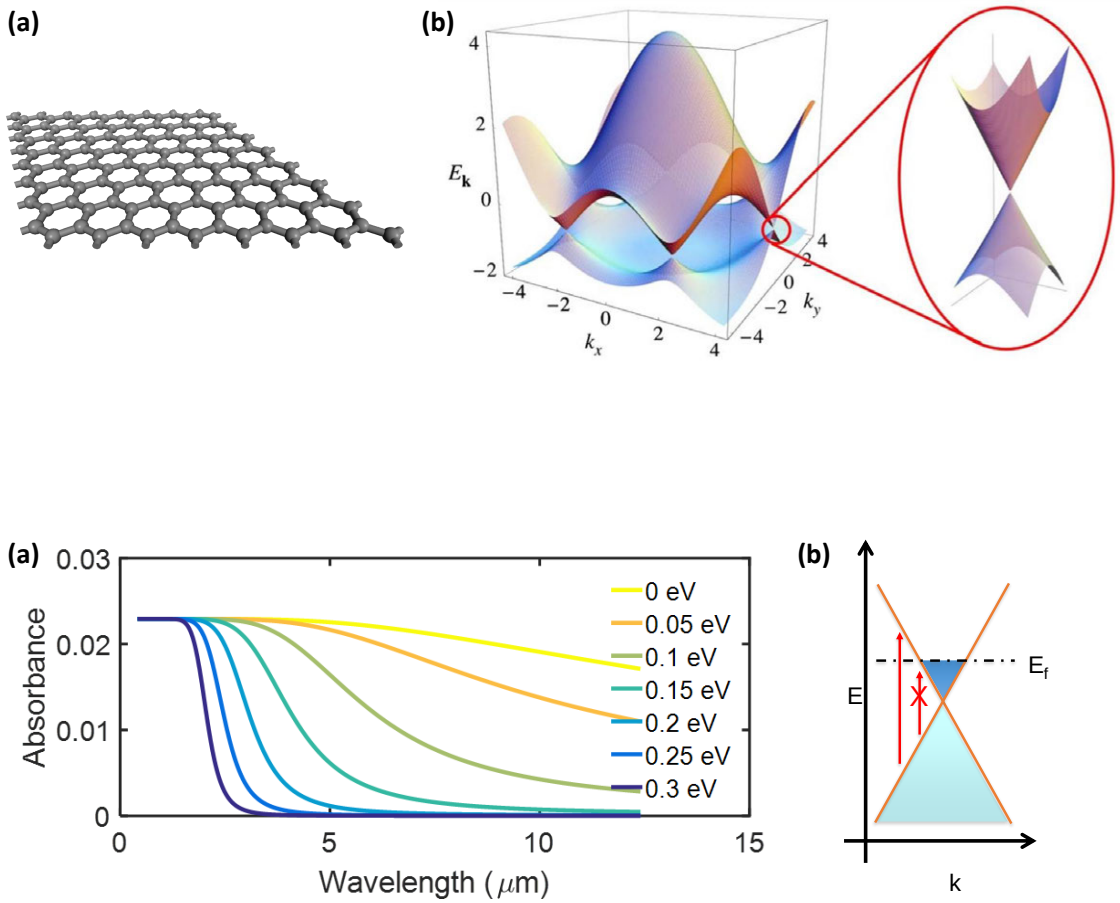

Figure 1-11: (a) Pauli blocking dominated optical absorption of monolayer graphene. (b) A schematic showing the allowed and forbidden optical transitions.

has hyperbolic dispersion for both conduction and valence bands, with their band extrema touching at a single point. However, the bandgap can be opened up by applying a transverse electric field, and thus making bi-layer graphene a narrow direct bandgap (up to 250 meV) semiconductor [37, 38]. Another way to open the bandgap of graphene is through hydrogenation [39] or fluorination [40, 41], in which the hybridization of carbon atoms in graphene changes from sp^2 to sp^3, leading to a bandgap opening up to 3 eV. The third approach to modulate the bandstructure is to further reduce the dimensionality of graphene into nanoribbons. Graphene nanoribbons can become metallic or semiconducting with various bandgaps depending on the chirality, the width, as well as the termination groups of the ribbons [42, 43, 44]. These modifications can tune the band edge absorption of graphene from THz to

ultraviolet, which could be potentially used in photodetection or optical modulation with different spectral range.

The negative permittivity due to the intraband transition in graphene, when interfacing with another dielectric, could lead to an excitation of the surface plasmon polariton (SPP), in which free electrons and holes in graphene vibrate in-plane with respect to incident light. This phenomenon could be sufficiently strong in heavily-doped graphene. Surface plasmons propagate along the graphene plane, with the wave vector k_{SP} expressed as [45, 46]

$$k_{SP} = \frac{\hbar^2 (\kappa + 1)}{4e^2 E_F} \omega \left(\omega + \frac{i}{\tau} \right) \tag{1.35}$$

where κ is the relative permittivity of the dielectric that graphene is in contact with. The coupling frequency can be enhanced efficiently by spatially confining the electromagnetic wave excitation. Two ways to achieve the spatial confinement have been proposed: (1) periodic patterning of graphene or the adjacent medium; and (2) introducing a structure with extremely high curvature near graphene, such as atomic force microscope (AFM) tip or metal nanoparticles [45, 46, 47, 48, 49].

Transition-Metal Dichalcogenides, MX_2

There are nearly 40 different compounds in the family of transition-metal dichalcogenides (TMDs) [50]. The general formula for this material family is MX_2, in which M can be Mo, W, V, Nb, Ta, Ti, Zr, Hf; and X is chosen among S, Se and Te. Each layer of TMD is three-atoms thick, with 1 transition metal layer sandwiched between 2 chalcogen layers. There are different phases of TMDs, including hexagonal (2H), octahedral (1T), distorted octahedral (1T'), rhombohedral (3R) and orthorhombic (T_d)[10]. Depending on the chemical compositions and the crystal structures, TMDs can be metallic or semiconducting. Such a diverse polymorphism and a variety of methods people have developed to induce the phase transitions make this material family very interesting from both fundamental and practical perspectives. Figure 1-12 summarizes different phases and ways to convert between different phases.

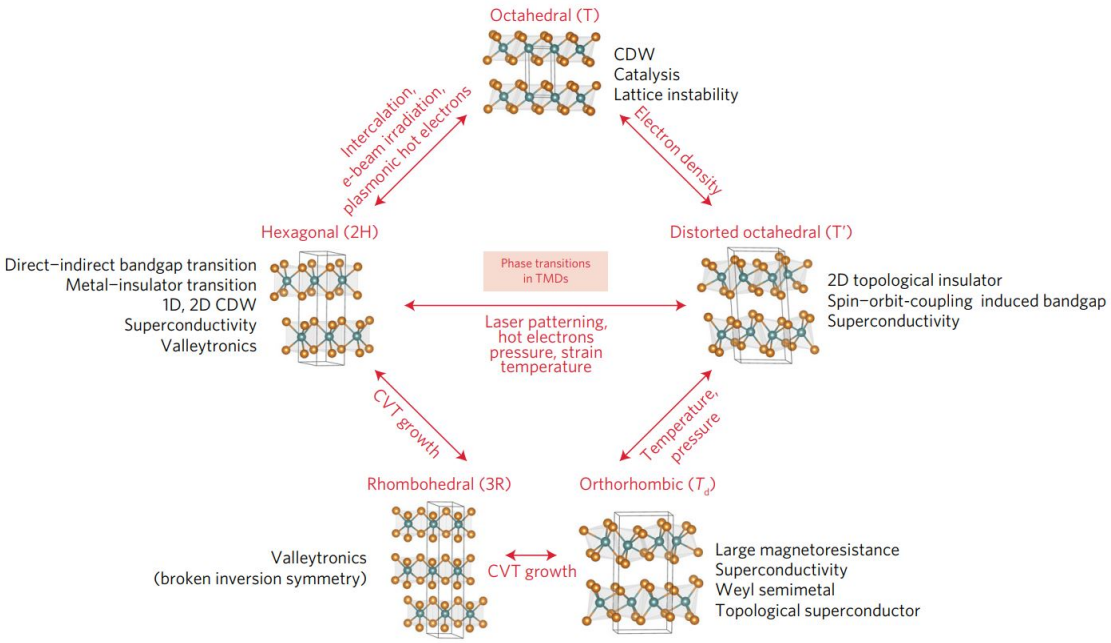

Figure 1-12: A summary of different phases, their transition methods of TMDs. [10]

Because of the reduced dimensionality and the special band structure, TMDs in 2D forms exhibit many intriguing electrical and optical properties. One interesting property is the exciton associated light-matter interaction phenomena in semiconducting TMDs, such as the layer-number-dependent band structure evolution[51, 52], the dielectric screening effect [53, 54], the exciton- or valley-dependent optical transitions [55, 56, 57, 58] and so on. The optical absorption of monolayer semiconducting TMDs is dominated by the direct interband transitions between the valence band maximum and the conduction band minimum around the K and the K' points in the Brillouin zone. For a conventional direct bandgap 3D semiconductor, such a band-edge optical absorption can be described as [59]

$$\alpha_{3D}(\hbar\omega) \propto |\hat{\mathbf{e}} \cdot \mathbf{p}_{cv}|^2 \rho_r(\hbar\omega - E_g) \tag{1.36}$$

where $\hat{\mathbf{e}} \cdot \mathbf{p}_{cv}$ is the matrix element of the optical transition; E_g is the direct bandgap; and $\rho_r(\hbar\omega - E_g)$ is the reduced density of states in 3D, expressed as

$$\rho_r(\hbar\omega - E_g) = \frac{1}{2\pi^2}\left(\frac{2m_r^*}{\hbar^2}\right)^{\frac{3}{2}}(\hbar\omega - E_g)^{\frac{1}{2}} \tag{1.37}$$

Here $m_r^* = (1/m_e^* + 1/m_h^*)^{-1}$ is the reduced effective mass.

According to Eqs. (1.36) and (1.37), the absorption edge has a square-root dependence with the photon energy. For a 2D direct bandgap semiconductor without excitonic effects, however, the absorption edge should follow a step-function [59]:

$$\alpha_{2D}(\hbar\omega) \propto |\hat{\mathbf{e}} \cdot \mathbf{p}_{cv}|^2 \rho_{2D}(\hbar\omega - E_g) \tag{1.38}$$

And

$$\rho_r(\hbar\omega - E_g) = \begin{cases} m_r^*/(\pi\hbar^2) & \text{if } \hbar\omega \geq E_g \\ 0 & \text{otherwise} \end{cases} \tag{1.39}$$

In the case of strong excitonic effects, the absorption spectrum at the band-edge is given by [59]

$$\alpha_{2D,exciton}(\hbar\omega) \propto \frac{1}{2\pi R_y a_0^2} \left[4\sum_{n=1}^{\infty} \frac{1}{\left(n-\frac{1}{2}\right)^3} \frac{\gamma}{\left[\varepsilon + \frac{1}{\left(n-\frac{1}{2}\right)^2}\right]^2 + \gamma^2} + \int_0^{\infty} \frac{\mathrm{d}\varepsilon'}{\pi} \frac{\gamma S_{2D}(\epsilon')}{(\varepsilon' - \varepsilon)^2 + \gamma^2} \right] \tag{1.40}$$

wherev $\varepsilon = (\hbar\omega - E_g)/R_y$; $R_y = m_r^* e^4/[2\hbar^2(4\pi\epsilon_s)^2]$ is the exciton Rydberg energy; $a_0 = 4\pi\epsilon_s\hbar^2/(m_r^* e^2)$ is the exciton Bohr radius; γ is the half-linewidth of the excitonic transition peaks due to scattering; and $S_{2D}(\varepsilon) = 1/[1 + \exp(-2\pi/\sqrt{\varepsilon})]$ is the 2D Sommerfeld enhancement factor.

Figure 1-13 (a) shows the step-function-like and the excitonic absorption edges for a monolayer semiconducting TMD. Several groups have proved experimentally that the monolayer TMDs such as MoS_2 and WS_2 matches the latter case [52, 56]. Meanwhile, both theoretical [60, 61, 54, 62] and experimental studies [63, 64, 65] have shown very large binding energies ($E_B = 4R_y = 0.5 - 1$ eV) and very small Bohr radius ($a_0 \approx 1$ nm) for monolayer semiconducting TMDs. In addition, higher order excitonic quasiparticles have also been observed in monolayer semiconducting TMDs, including charged excitons (or trions), bi-excitons (bound states of two exci-

tons), *etc* (Figure 1-13 (b))[11]. Because of the large quantum confinement, many of these excitonic quasiparticles even exist at room temperature. Besides, several groups have also reported defect-bound exciton photoluminescence. Such emissions can be localized to single defect level at low temperature [66]. People have harnessed these unique excitonic optical transitions for optoelectronic and photonic applications such as waveguide coupled light-emitting devices, ultra-low power lasers, optical modula-

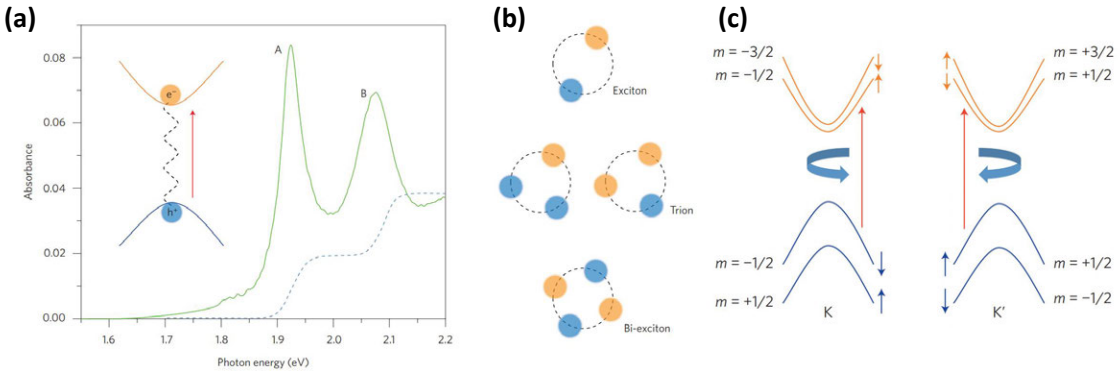

Figure 1-13: (a) Absorption spectrum of monolayer MoS_2 (green solid line). A and B are exciton resonances corresponding to transitions from the two spin-split valence bands to the conduction bands. The blue dashed line shows the absorbance without the excitonic effects. (b) A schematic showing various excitonic quasiparticles. (c) Electronic bands around the K and K' points. The spin (up and down arrows) and valley (K and K') degrees of freedom are locked together. [11]

Another unique aspect of the optical properties of semiconducting 2D TMDs is the valley-spin locking and the associated optical selection rules that are reflected in the excitonic transitions (Figure 1-13 (c))[67]. Such a strong spin-valley coupling in semiconducting TMDs have enabled the so-called "valleytronics", which may become a new approach for both classical and quantum computing in the future.

1T, 1T', Td and some of the 2H phase TMDs have metallic or semi-metallic behaviors [68]. Because of the strong electron-phonon and/or electron-electron interactions, the modulation of electron density in space can give rise to a periodic distortion of the lattice. As a result, charge-density wave (CDW) states can be induced in many of the metallic TMDs, including 1T-TaS_2, 2H-TaS_2, 2H-$NbSe_2$, 1T-$TiSe_2$,

etc[69, 70, 71, 72, 73, 74]. It has been found CDW states and the transitions among incommensurate CDW (ICCDW), nearly commensurate CDW (NCCDW), and commensurate CDW (CCDW) states can be achieved through changing the temperature, applying an electric field, and varying the crystal thicknesses. As will shown later, such CDW phase transitions can also been used for IR detection.

Black Phosphorus and Group IV Monochalcogenides

Bulk black phosphorus (bP) is a layered orthorhombic crystal. A monoalyer of bP has very low symmetry, with a puckered honeycomb structure as shown in Figure 1-14. A few years ago, bP was rediscovered as a low-bandgap semiconducting 2D materials that is complementary to graphene and semiconducting TMDs, which are semimetal and wide-bandgap semiconductors, respectively [75, 76, 77]. Since then, bP has drawn tremendous attention because of its unique low-symmetry crystal structure, the anisotropic transport and optical properties, and its widely tunable bandgap by layer numbers[77, 13]. Figure 1-15 summarizes the layer number dependent band structure evolution and the corresponding optical resonances [12]. The lowest optical absorption peaks located at near-infrared to mid-infrared ranges for thicker bP. People have demonstrated photodetectors using these optical transitions in the mid-IR with very good sensitivities as will be discussed later. In addition, experimental studies have shown that excitons are also very stable for monolayer bP, with a binding energy of 0.9 eV, which is even bigger than semiconducting monolayer TMDs [78]. More recently, people have shown that the band gap of monolayer and few-layer bP can be tuned very widely through strain engineering [79], which can enable many tunable photonic applications in the mid-IR with unprecedented performance, such as optical modulators, optomechanical devices, and tunable on-chip light sources.

Similar to bP, Black arsenic phosphorus (bAsP), arsenene, antimonene and group IV monochalcogenides are also materials with puckered or buckled lattice structures (Figure 1-16) with even more interesting low-symmetry related physical properties and potential photonic applications. For example, the bandgap of builk bAsP can be tuned continuously from 0.33 eV to 0.17 eV as we increase the As composition

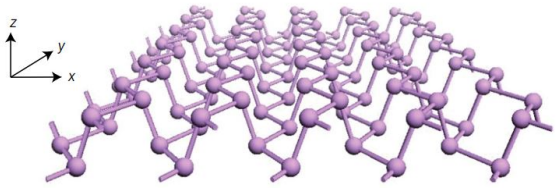

Figure 1.14: The puckered lattice structure of bP. [12]

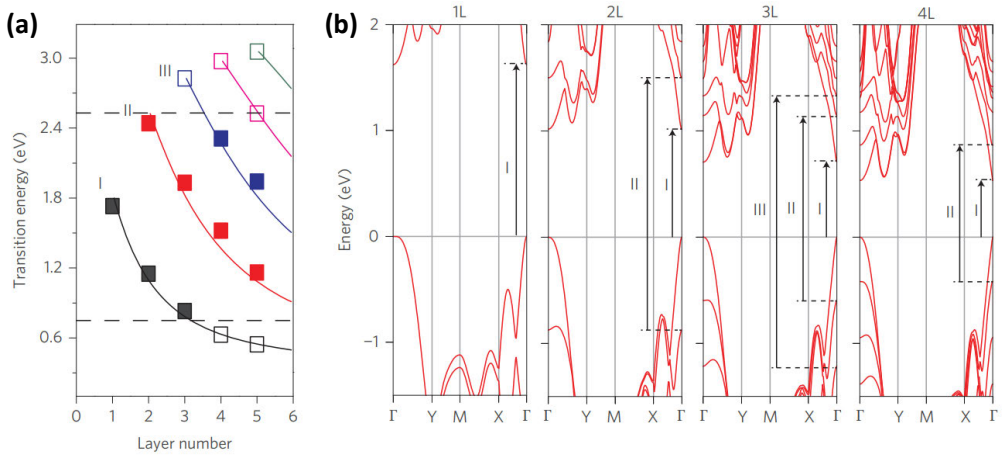

Figure 1-15: (a) Optical transition energies of bP with different layer numbers. (b) the calculated band structures of bP with different layer numbers. [12]

[13]. For group IV monocalcogenides (denoted as MX, where M=Ge or Sn, X=S, Se or Te), the inversion symmetry of the crystal structure is also broken. As a result, large in-plane piezoelectricity, pyroelectricity, or even ferroelectricity can exist in this material family [13].

Other 2D Materials

Besides the three classes of 2D materials mentioned above, there are more varieties of 2D materials and quasi-1D materials that have been or to be studied. Table 1.1 summarizes the most studied 2D materials, their crystal structures and physical properties. Besides these materials, there are more layered materials or low-symmetry materials that are likely to exist in 2D forms to be investigated, including graphene oxides, diamondene, silicene, germanene, stanene, MXenes, 2D perovskites, layered

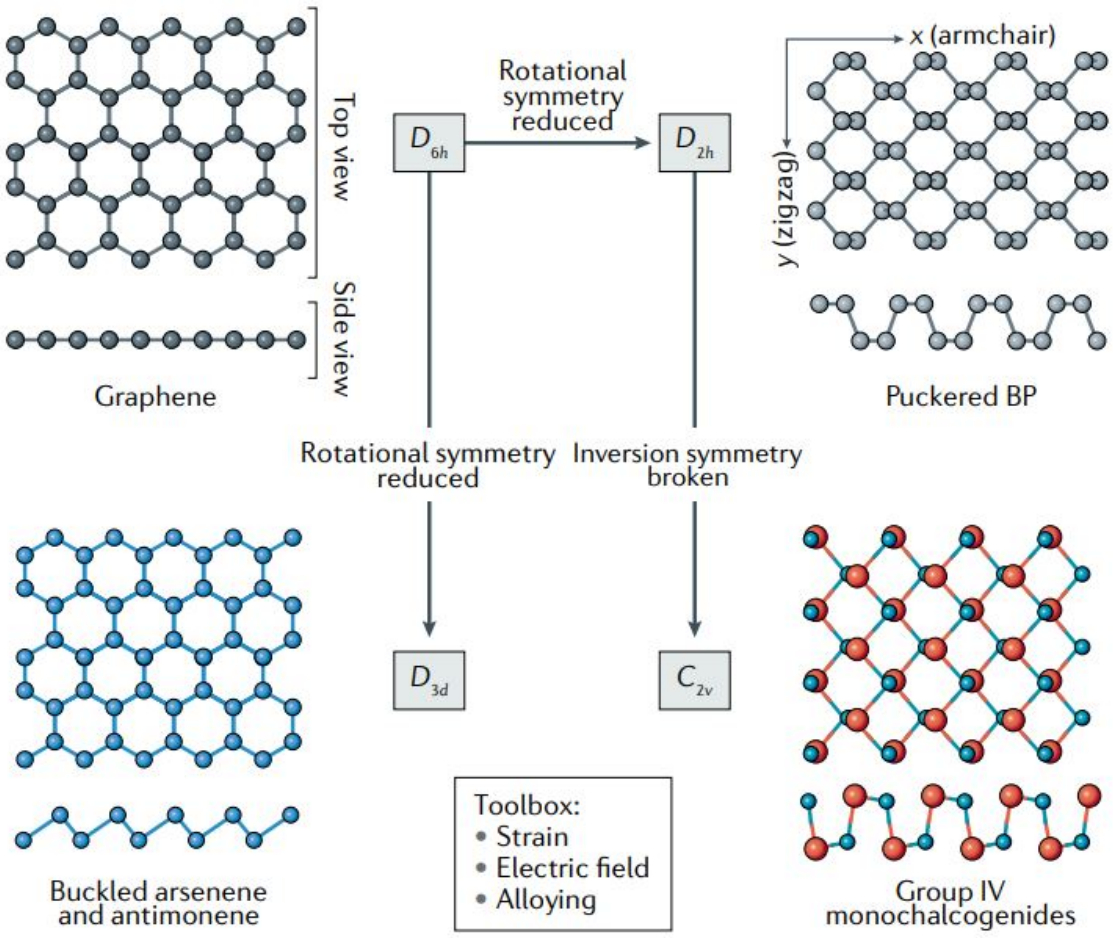

Figure 1-16: A variety of buckled or puckered lattice materials. [13]

metal oxides, layered metal double hydroxides, metal-organic frameworks (MOFs), covalent-organic frameworks (COFs) and quasi-1D crystals [80, 81, 82, 83, 84].

Table 1.1: A summary of various 2D materials.

Name	**Formula**	**Crystal System**	**Point Group**	**Physical Properties**
Graphene	–	Hex.	D_{6h}	Semimetal
hBN	–	Hex.	D_{6h}	Insulator ($E_g \sim 6$ eV)
Transition metal dichalcogenide (TMD); M=Mo,W,V,Ta,Nb, Ti,Zr,Hf; X=S,Se,Te	2H-MX_2	Hex.	D_{6h}	Mostly semiconductor
	1T-MX_2	Trig.	D_{6h}	Mostly metal
	1T'-MX_2	Mono.	C_{2h}	Metal or small bandgap semiconductor
	Td-MX_2	Orth.	C_{2v}	Metal or small bandgap semiconductor
ReS_2 or $ReSe_2$	–	Tric.	C_i	Semiconductor
bP or bAsP	–	Orth.	D_{2h}	Small bandgap semiconductor
Group IV Dicalcogenide (SnS_2, $SnSe_2$)	–	Trig.	D_{3d}	Semiconductor; high electron affinity
Group IV Monocalcogenide; M=Sn,Ge; X=S,Se,Te	β-MX	Cubic	O_h	Semiconductor; non-layered
	γ-MX	Orth.	C_{2v}	Semiconductor; inplane piezo-/pyro-/ferro-electricity; non-layered but exfoliatable
III-VI layered semiconductor; M=Ga,In;X=S,Se,Te	MX	Hex.	D_{6h}	Wide bandgap semiconductor
	β-M_2X_3	Tetra.	D_{4h}	Semiconductor; piezo-/pyro-electricity
Metal phosphorus trichalcogenide; M= Mn, Fe, Ni, Zn, *etc.*	MPS_3	Mono.	C_{2h}	Wide bandgap semiconductor /insulator; ferroelectricity
Metal trihalide ($CrCl_3$, CrI_3,$MoCl_3$,$TcCl_3$, $RuCl_3$,$RhCl_3$,$RhBr_3$, RhI_3,$IrCl_3$,$IrBr_3$, IrI_3)	–	Mono.	C_{2h}	Semiconductor; ferromagnetic

Abbreviations: Hex.=Hexagonal; Trig.=Trigonal; Tetra.=Tetragonal; Orth.=Orthorhombic; Mono.=Monolithic; Tric.=Triclinic.

1.2.2 Synthesis and Fabrication Technology

In this section, we summarize the recent advances of the key process technologies for 2D materials, including synthesis, transfer, metal contacts and doping.

Synthesis

The reliable synthesis of 2D materials is essential for both fundamental studies of their unique physical phenomena and harnessing these phenomena for practical applications. In the past decade, many strategies have been developed to produce monoalyer or few-layer 2D materials [8, 32, 68, 14]. They can be classified into two categories: top-down methods and bottom-up methods.

Top-down methods involves thinning down or separating thinner layers from bulk crystals. The easiest method is called mechanical exfoliation, or Scotch-tape method (Figure 1-17). In this method, a bulk crystal of layered materials is first placed onto a piece of tape. Then by repeatedly folding, peeling of the tape and cleaving the crystals, micrometer-sized fragments (or "flakes") of atomically thin materials can be obtained. Eventually these randomly distributed flakes are transfered onto a SiO_2/Si substrate for furthur study. This method was used for the first separation of monoalyer graphene [85, 86, 87] and are still the most predominant method nowadays for the production of high-quality 2D materials in laboratory. Although this method is very simple and works for most of 2D materials, the yield of monolayer or fewlayer 2D materials is extremely low, and the flake size is limited to 10-micrometer scale. To optimize this process, people have developed a gold mediated mechanical exfoliation method with which up to 500 μm monolayer TMD flakes can be produced [88], but it is still far from enough for scalable production.

Such a exfoliation process can also be achieved in a liquid phase, through sonication or intercalation. This method is called liquid exfoliation [32]. There are four main liquid exfoliation techniques: oxidation and dispersion, intercalation of ionic species, sonication with surfactants, and electrochemical exfoliation. These solution processes can produce large quantities of 2D nano sheets and dispersed in water or

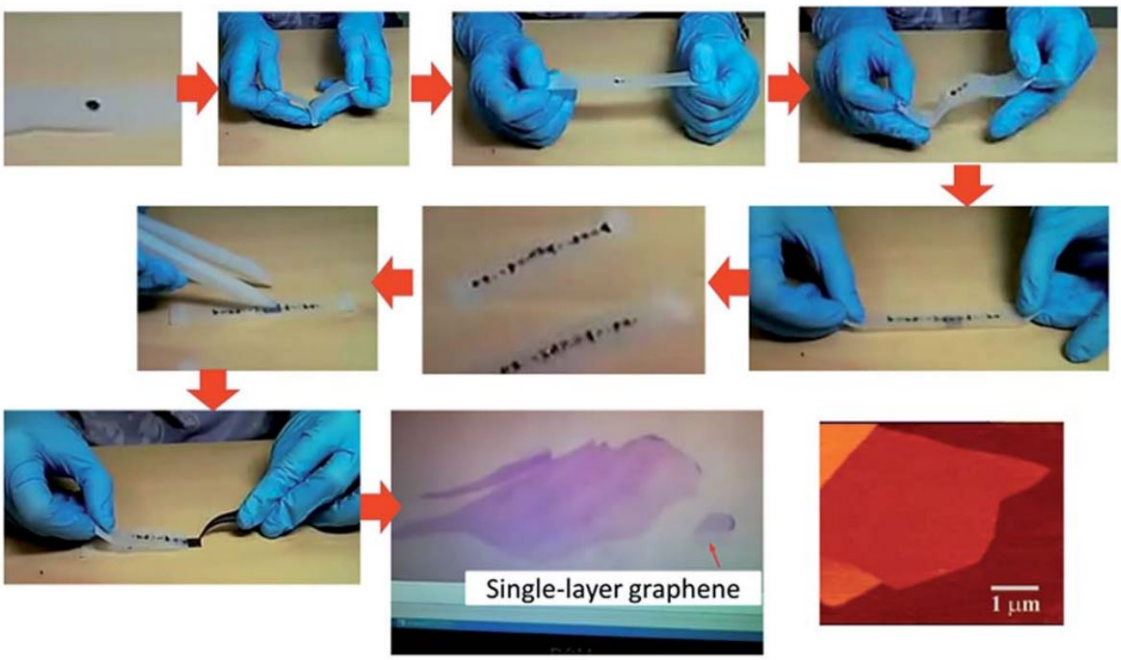

Figure 1-17: The process flow of the Scotch-tape method.[14]

organic solvents, although there are still large variations in terms of the flake sizes and thicknesses. Therefore 2D nanosheets dispersions produced by liquid exfoliation are suitable for low-cost applications, including wearable electronics, energy harvesting/storage, catalysis, *etc.*

With bottom-up methods it is possible to produce large-area and uniform 2D materials, which is very crucial for many electronic and optoelectronic applications. People have developed multiple bottom-up methods for graphene, hBN, TMDs and their heterostructures, including physical vapor deposition, chemical vapor deposition, epitaxy and liquid phase growth. Among them, CVD has several advantages such as relatively low-cost, faster growth rate, and diversity of the precursors. Figure 1-18 summarizes the recent progress of CVD technology for TMDs [8].

Transfer [8]

Because of the weak van der Waals interactions between 2D materials and the substrates, 2D materials can be easily peeled off from the growth substrate and transferred to any targeted substrate. There are two benefits. First. the easiness to

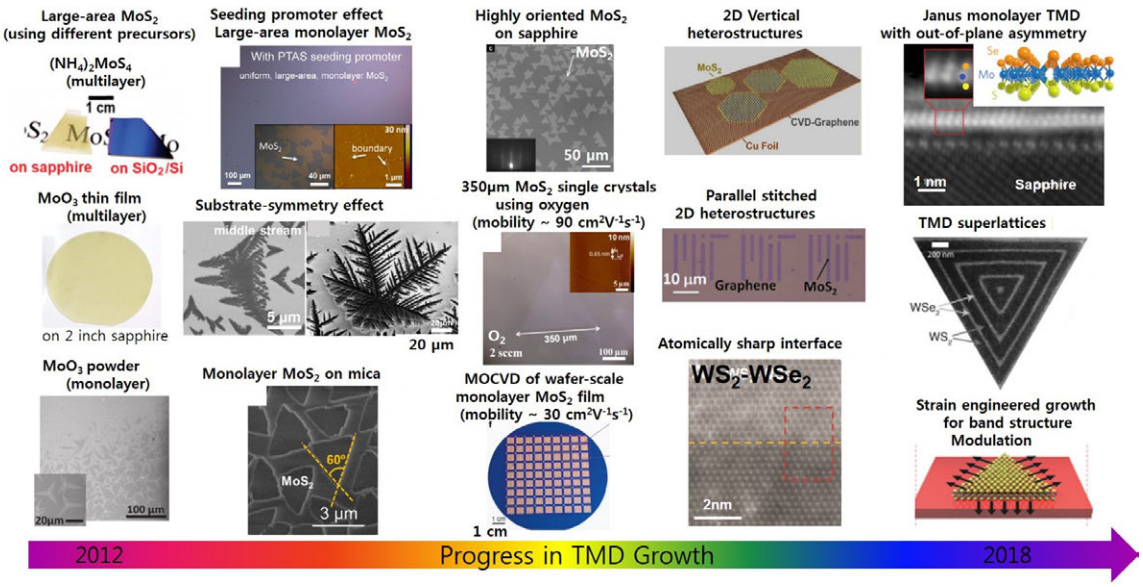

Figure 1-18: A brief overview of the recent progress of CVD technology for TMDs and their heterostructures.[8]

transfer and stacking multiple layers of 2D materials on top of each other makes it possible to form complex vertical heterostructures and superlattices. This gives us much more freedom, as compared to conventional heterogeneous epitaxial growth for 3D materials, to design the interfaces and to bring together different functionalities from different materials. Second, the transfer process decouples the high-temperature growth process from the following low-temperature fabrication process. This is a possible route to realize monolithic integration of 2D material based technologies and conventional CMOS technologies.

The basic procedure for transfer is as follows. First, a polymer supporting layer is attached to the 2D material/substrate through spin-coating or direct attachment. Then the polymer/2D material stack is separated from the original substrate, through either chemical etching of the substrate, or direct peeling off. Finally, the polymer/2D material is placed onto the target substrate and the polymer is removed. The most commonly used polymer supporting layers include poly(methyl methacrylate) (PMMA), polydimethylsiloxane (PDMS), poly(Bisphenol A carbonate) (PC), and polypropylene carbonate (PPC). Such a transfer process can also be done under an optical microscope for accurate alignment of two 2D flakes, which has enabled

many interesting fundamental studies.

To reuse expensive catalytic substrates such as Pt, Au and Ir, electrochemical delamination method has been considered as a nondestructive approach to separate graphene or h-BN from the metal growth substrates without dissolving them. The electrochemical delamination method is also called "bubble transfer". In this method, hydrogen bubbles are generated between graphene and the metal substrates to weaken the adhesion at the interface in dilute alkaline solutions, leading to the delamination of the graphene from the substrate. This method can also me reconfigured into the roll-to-roll style, which is a promising route for high throughput and large-scale production [89].

Metal Contacts and Doping [8]

A low contact resistance in a field effect transistor or any other electronic devices is crucial because the extra voltage drop through the contact resistance would degrade the overall device performance. Many attempts have been made to lower the contact resistance of 2D material based electronic devices. In order to improve the surface cleanliness, many methods have been developed and proved to reduce the contact resistance, including high-temperature post-metalization vacuum annealing [90], ultralow vacuum metal deposition [91], surface treatments using ozone or mild oxygen plasma [92], and interfacial layer insertion between 2D materials and photoresists [93]. Another way to improve the contact resistance is through edge contacts. Since the edges of 2D materials are more chemically active and easier to bond covalently with other metallic materials than the top surfaces, the electron transfer in between such connections may be much more efficient, leading to a reduction of the contact resistance. Such efforts include 1D contact to hBN/graphene/hBN stacks [94], intentional nanopore etching of graphene before the metalization [95], direct synthesis of graphene/MoS_2 in-plane junctions [2], 1T/2H MoS_2 or $MoTe_2$ phase junction formations through lithium intercalation or laser irradiation [96], *etc.* Furthermore, a proper work function matching and the interface state pinning effect need to be considered to form a good contact to 2D semiconductors especially with wider bandgaps,

such as MoS_2, WSe_2, and so on [97, 26, 98].

Controllable chemical doping is another crucial aspect of process technologies. Because of the 2D nature and the resulting high surface-to-volume ratio, many physiosorption methods are very effective to achieve decent amounts of doping. Such physiosorptive dopants could be introduced through gaseous or liquid phase treatment (NO_2, and $AuCl_3$; both are effective p-type dopants to graphene or WSe_2) [99, 100, 101] , molecular surface adsorption (2,3,5,6-tetrafluoro-7,7,8,8-tetracyanoquinodimethane, or F_4TCNQ for p-type doping, and nicotinamide adenine dinucleotide, or NADH for n-type doping) [102, 103], dipole or residual charge from surrounding dielectrics (SiO_2 and TiO_2 for p-type doping, and AlOx for n-type doping) [104, 105], etc. However, dopants introduced by physiosorptions are usually unstable, since no chemical bonding is formed. Therefore, several efforts have been made to achieve effective doping by chemical functionalization or substitution. For instance, chlorination of graphene induced through plasma treatment[106] can give rise to an efficient, non-destructive, and air-stable p-type doping. Nitrogen or boron substitutes in graphene could lead to n-type and p-type doping, respectively, which can be introduced either through extra dopant precursors during CVD synthesis, or through post-growth plasma treatment [107]. In terms of MoS_2, oxygen passivation on the naturally existing sulfur vacancies was both predicted theoretically and observed experimentally to introduce p-type doping [108, 109]; Nb and P were found to be effective p-type substitution dopants that could be introduced during synthesis or through plasma treatment [110, 111].

1.2.3 Mechanisms of Photodetection

Applying some of the unique physical phenomena that emerge on the 2D material platform could lead to ultrasensitive and/or fast-response photodetectors, which could potentially out-perform the state-of-the-art mainstream IR detection technologies. In this section, we will discuss different photodetection mechanisms that are observed in 2D materials and put more emphasis on the high-sensitivity photo-sensing structures and the special effects that are not commonly observed in conventional materials.

Photovoltaic Effect

The photovoltaic (PV) effect and photodetectors based on it with 2D materials have been studied extensively in recent years [112, 113, 114]. The PV effect is very similar in 2D materials to that in bulk semiconductors. There are still some fundamental differences and practical advantages of PV effect in 2D materials. First, because of the strong quantum confinement and the resulting excitonic optical properties, carriers in 2D semiconductors can interact more strongly with light and with each other. One benefit is that the optical absorption coefficients of 2D semiconductors are sufficiently larger than their 3D counterparts (Figure 1-19), so it is possible to make ultrathin PV devices with high efficiency. Second, the low dimensionality also makes it possible to design and construct vertical or lateral homo-/hetero-junctions with much more freedom. Vertical heterojunctions can be implemented through the polymer assisted alignment transfer method as discussed in section 1.2.2, whereas lateral homo- or hetero-junctions can be achieved either by synthesis methods (chapter 2) or split electrostatic gating. For example, people have demonstrated monolayer WSe_2 and $MoTe_2$ lateral p-n junction PV devices that can be readily integrated to silicon photonics [115, 116]. With careful band alignment engineering, people also implemented high performance PV photodetectors or even avalanche photodiodes with 2D/2D or 2D/3D vertical heterostructures [117, 118, 119]. Third, some of the low-symmetry 2D or quasi-1D crystals may give rise to unconventional PV effects, such as the bulk photovoltaic effect observed in WS_2 nanotubes and TaAs [120, 121].

Photogating Effect

Photogating effect is a special type of extrinsic photoconductive effect [122, 123]. Photogating effect exists in a defective low-dimensional semiconductor or an artificially designed heterostructures. One type of photocarriers (either electrons or holes) can be trapped by the defect or interface states, leading to a prolonged relaxation lifetime of these trapped carriers. As a result, the trapped carriers can accumulate over time and play a role of electrostatic gating to the free carriers in the semiconduc-

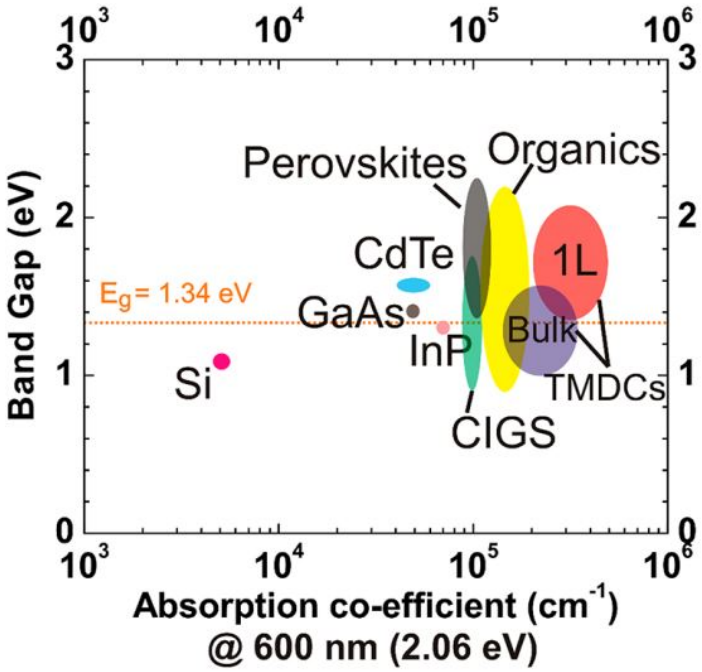

Figure 1-19: Optical bandgaps versus absorption coefficients at 600 nm for different materials.[15]

tor channel. Because of the charge accumulation, photogating effect is a simple yet extremely sensitive mechanism, with the current gain of up to 10^8 for structures like graphene/quantum dots hybrid phototransistors [124]. The drawback of this sensing mechanism is that the same charge accumulation effect also leads to a very slow response of the photodetector (from milliseconds to thousands of seconds).

Thermoelectric and Photothermoelectric Effect

As will be discussed in more detail in chapter 4, graphene and some of the other 2D semiconductors are good candidates as the thermoelectric sensing component in a thermopile. In addition, because of the strong electron-electron interaction and the weak electron-phonon interaction, hot-carrier-assisted transport is very prominent in graphene. This special photoresponse in graphene is called photothermoelectric effect, which will be covered in chapter 5.

Bolometric and Pyroresistive Effect

Because of the ultrasmall thermal mass, many of the 2D materials have been proposed to be good bolometric materials. Several novel bolometric effects have also been found to be very efficient for IR detection in graphene and other 2D materials. For graphene, because the cooling of electrons by acoustic phonons is very inefficient, and cooling by optical phonons only happens at high temperature, electrons of graphene are thermally isolated from the environment very well, which would give rise to a very efficient bolometric sensitivity (TCR) [122]. Two signal transducing mechanisms in graphene have been studied, including the temperature-dependent mobility degradation [125, 126], and the temperature dependent noise [127]. Sharp temperature induced phase transitions are another sensitive signal transducing mechanism. To this end, the CDW transitions near room temperature for some of the metallic TMDs have shown great potential for efficient bolometric detectors [128, 129].

The low-dimensionality of 2D materials also gives rise to efficient electrostatic gating of 2D semimetals and 2D semiconductors. Besides the photogating effect, people also demonstrated thermal detectors that incorporate pyroelectric dielectrics to a graphene transistor [130, 131]. This is called pyroresistive effect.

Thermo-Mechanical Effect

The thermo-mechanical effect is based on the special mechanical properties and the thermo-mechanical response of 2D materials and nanostructures based on them. This topic will be covered in chapter 6.

1.2.4 Opportunities and Challenges

Because of the diversity of 2D materials and many unique light-matter interaction phenomena in such a quantum-confined system, infrared detectors made with 2D materials have shown promising performance that can potentially be better than the state of the art (Figure 1-6). Figure 1-20 summarizes the D^*-λ relation of high-performance detectors made with 2D materials in the visible to long IR range. In

Figure 1-20, we also outlined the design space of the three IR detector technologies studied in this thesis. Each of them have their unique advantages as will be discussed in chapter 4, chapter 5 and chapter 6.

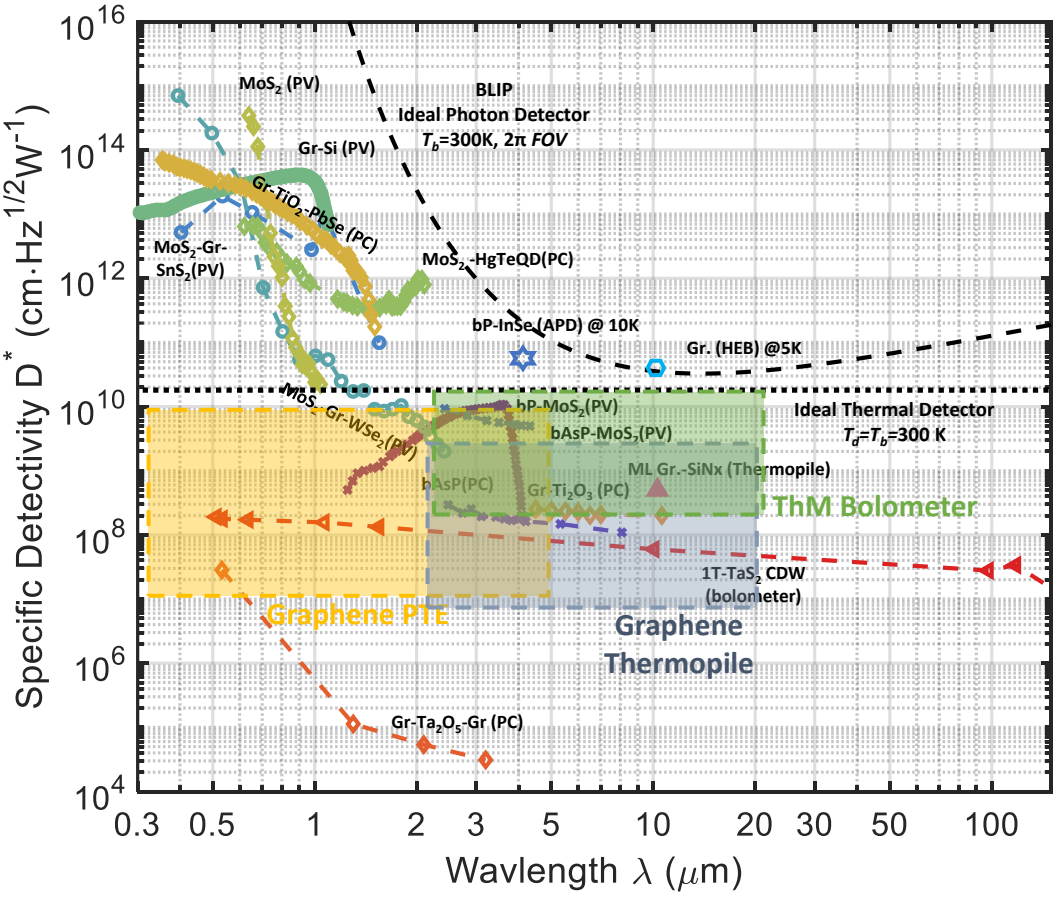

Figure 1-20: D^* versus λ of 2D material based detectors.TODO: citation

Another practical benefit of 2D material based IR detectors is their compatibility with CMOS process and the feasibility of a higher level of integration.The easiness to transfer 2D materials onto arbitrary substrate and its low-temperature fabrication process make it feasible to monolithically integrate 2D material based IR detectors with CMOS integrated circuits. This gives rise to great opportunities for next generation IR FPAs with much smaller form factors and better performance. Furthermore, we can even integrate more functionalities such as multiple color detectors, optical filters and so on made with 2D materials onto such IR FPAs without much additional

complexity to realize the goal of 4th generation imaging system (Figure 1-8). This topic about 2D-CMOS integration will be covered briefly in chapter 4.

Finally, it is worth mentioning that several challenges still exist in order to push the 2D material based IR detector technologies into practical application. The first challenge is from the material end. Although tremendous advance has been made in synthesizing 2D materials in large scale with high uniformity and good material quality, most of them are still in the early stage of laboratory exploration. It is time to develop production lines that can meet industrial standard. Besides, there are still some material issues that are still unsolved, including reliable and scalable 2D material transfer, bottom-up assembly of complex 2D heterostructures (chapter 2), and fast characterization of these materials (chapter 3). The second challenge comes from the device fabrication process, including making good metal contacts to 2D semiconductors, reliable passivation and packaging, and minimizing the material degradation during the fabrication process. Thirdly, we also need to collaborate with circuit designers and system engineers to develop new strategies to improve the yield as well as the complexity of emerging 2D material based technologies, and push them into system-level application.

1.3 Thesis Outline

The aim of this thesis is to address some material challenges of 2D materials and to demonstrate and benchmark emerging IR detector technologies based on 2D materials and their heterostructures.

In chapter 2, we developed a general methodology for the scalable synthesis of 2D material heterostructures. We first introduced the seeding promoter assisted chemical vapor deposition of monolayer transition metal dichalcogenides. Based on this method, we demonstrated the scalable synthesis of 2D material vertical and lateral heterostructures. Finally, we studied the transport property of graphene-MoS_2 lateral heterostructures and demonstrated their application in integrated circuits.

In chapter 3, we addressed another material challenge regarding the fast optical

characterization of 2D materials. We developed a deep learning algorithm to process the optical microscopic imaging data of various exfoliated 2D materials, and showed that such an algorithm can be used for identify the material and thickness, in real time, in un-labeled microscopic images. We also showed that the algorithm is able to "understand" the microscopic images and provide probabilistic prediction about physical properties of the 2D materials.

In chapter 4, we performed a theoretical analysis on graphene thermopile. Based on our model, we discussed about how to further optimize the materials and the device structures, and benchmarked this technology. Finally, we integrated graphene thermopile FPAs with a silicon CMOS ROIC in a monolithic fashion and demonstrated an integrated mid-IR image sensor for real-time thermal imaging application.

In chapter 5, we studied the photothermoelectric effect in a graphene-2D semiconductor lateral heterojunction. Both experimental and theoretical studies were made to understand the asymmetric thermalization pathways of photo-induced hot carriers in the junction. We also showed that the photothermoelectric effect can potentially be used to make IR detectors with wider spectral range, much faster response, and up to room-temperature operation.

In chapter 6, we proposed and implemented a new sensing scheme, called thermo-mechanical bolometer, that transduces infrared radiation into an abrupt electrical resistance change through the special thermo-mechanical response and the sharp artificial metal-insulator transition of engineered nanostructures based on graphene, polymer and self-assembled monolayers. Our studies indicated that this new sensing technology can be at least one order of magnitude more sensitive than the state of the art.

Finally, in chapter 7, we summarize the key achievement of this thesis and propose several future directions that are worth further studying.

Chapter 2

Synthesis and Electronic Application of Two-Dimensional Material Heterostructures

As the fundamental limit of Moore's law is approaching, the global semiconductor industry is intensively looking for applications beyond CMOS electronics [17]. The atomically thin and ultra-flexible nature of two-dimensional (2D) materials (such as graphene, hexagonal boron nitride (hBN) and TMDs) offer a competitive solution not only to push the forefront of semiconductor technology further, towards or perhaps beyond the Moore's law, but also to potentially realize a vision of ubiquitous electronics and optoelectronics in the near future.[132, 133] Hybrid structures between 2D materials are essential building blocks with multi-functionality and broader capacity for nanoscale modern electronics and optoelectronics [134, 135, 35, 136, 137, 138, 139]. Although 2D heterostructures can be achieved by pick-up-and-transfer method[134, 135, 35, 137, 138], chemical vapor deposition (CVD) allows the direct growth of lattice aligned TMDs layers for both vertical heterojuctions with clean interfaces and seamlessly 1D lateral heterostructures with atomically sharp interfaces.

We developed the seeding promoter assisted chemical vapor deposition for large-scale synthesis of monoalyer transition metal dichalcogenides. Such method was then generalized for constructing a variety of vertical and lateral heterostructures depend-

ing on the choise of the seeding promoter molecules and their wettability to the substrates. We further proved that the proposed synthesis methodology is general for constructing vertical or lateral heterostructures between a 2D and a TMD material regardless of the lattice mismatch between the two materials, with large-scale production capability. This also enables both multifunctional electronic/optoelectronic devices and their large-scale integration.

2.1 Seeding Promoter Assisted Synthesis of Transition Metal Dichalcogenides[1]

The experimental setup and a typical growth condition for chemical vapor deposition (CVD) of TMDs are shown in Figure 2-1 (a) and (b). Briefly, 0.018 g of MoO_3 (molybdenum oxide) powder in a ceramic crucible was placed in the center of the furnace. Also 0.016 g of sulfur powder was placed in a crucible 15 cm away from the center of a quartz tube. The substrate was placed face-down on the crucible of the MoO_3 powder. A seeding promoter substrate coated with aromatic molecules is placed next to the growth substrate. 5 sccm Ar was used as a carrying gas to carry both the sulfur vapor and the seeding promoters to the growth substrate. The growth temperature was controlled at 650 °C. A uniform, large-area and monolayer MoS_2 film can be grown throughout most of the growth substrate if using perylene-3,4,9,10-tetracarboxylic acid tetrapotassium salt (PTAS) as the seeding promoter (the optical microscopic (OM) image is shown in Figure 2-1 (c)), where as isolated triangular domains are grown on the edges of the substrate (left inset of Figure 2-1). The atomic force microscopy (AFM) image shown in the right inset of Figure 2-1 confirms that the obtained MoS_2 film is atomically smooth. As comparison, only MoS_2 particles are obtained for a growth process without any seeding promoter (Figure 2-1 (d)).

According to our experimental results, we believe that the presence of PTAS on the growth substrate can facilitate the nucleation as well as the lateral growth of

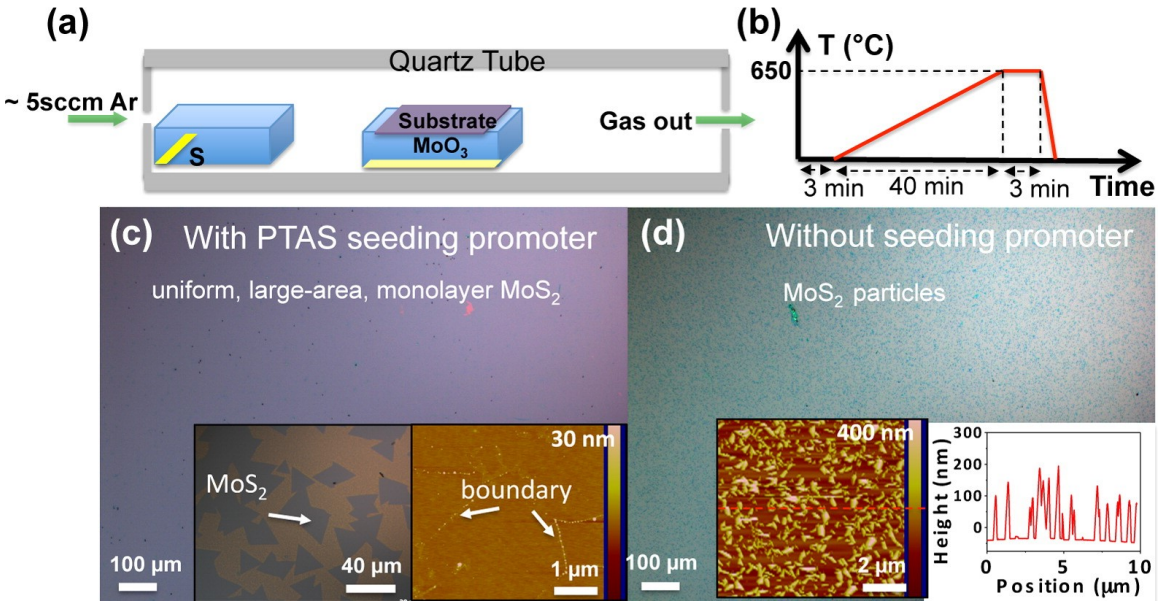

Figure 2-1: Seeding promoter assisted chemical vapor deposition. (a) Schematic of the experimental setup. (b) A typical temperature control process for the synthesis. (c) An optical microscopic image of a continous monoalyer MoS_2 film when grown with the PTAS seeding promoter. Left inset: an optical microscopic image of isolated triangular domains of monolayer MoS_2. Right inset: the AFM iamge of the continous film. (d) An optical microscopic image, the corresponding AFM image, and the height profile extracted from the AFM image of MoS_2 particles grown without any seeding promoter.[1]

the MoS_2 crystals. The density (or concentration) of the seeding promoters exhibits a significant effect on the MoS_2 nucleation density. A high seed density usually results in a high nucleation density on the growth substrate, where MoS_2 flakes can merge to form a continuous film. The presence of seeding promoters possibly increases the surface adhesive force of MoS2 and lowers the free energy barrier of the nucleation. These two factors together facilitate the large-area layered growth of MoS_2 and decrease the required growth temperature. We found that many aromatic molecules can work as well as PTAS as the seeding promoter. Besides PTAS, twelve types of aromatic molecules were found to be effective seeding promoters, including copper(II) 1,2,3,4,8,9,10,11,15,16,17,18,22,23,24,25-hexadecafluoro-29H,31H-phthalocyanine ($F_{16}CuPc$), 3,4,9,10-perylene-tetracarboxylicacid-dianhydride (PTCDA), copper phthalocyanine (CuPc), dibenzo[f,f']-4,4',7,7'-tetraphenyl-diindeno [1,2,3-cd:1',2',3'-lm]perylene (DBP), 4'-nitrobenzene-diazoaminoazobenzene (NAA), N,N'-bis(3-methylphenyl)-

N,N'-diphenyl-9,9-spirobifluorene-2,7-diamine (spiro-TDP), tris(4-carbazoyl-9-ylphenyl) amine (TCTA), bathocuproine (BCP), 1,3,5-tris(N-phenylbenzimiazole-2-yl)benzene (TPBi), 2,2',7,7'-tetra(N-phenyl-1-naphthyl-amine)-9,9'-spirobifluorene (spiro-2-NPB), and iridium, tris(2-phenylpyidine) ($Ir(ppy)_3$). The OM images of monolayer MoS_2 crystals grown with the help of these aromatic molecules are shown in Figure 2-2.

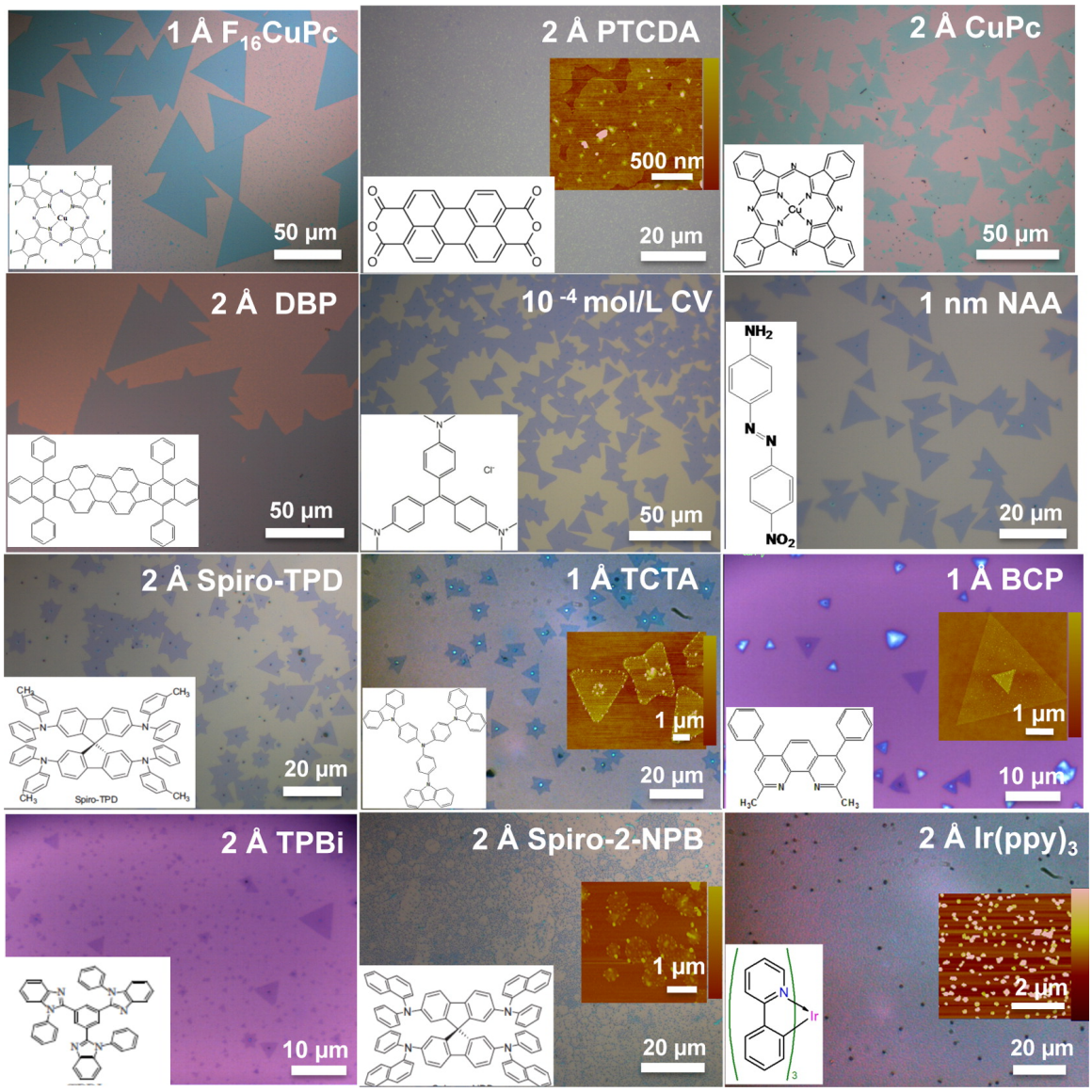

Figure 2-2: OM images of monolayer MoS_2 crystals grown with a variety of seeding promoters. The insets are the molecular structures and the AFM images.[1]

Recent studies have shown that the proposed seeding promoter assisted CVD method is effective for the growth of other TMDs, including $MoSe_2$, WS_2 and WSe_2

[140, 141, 142]. In addition, by carefully choosing the seeding promoters and matching their wetting properties to the growth substrate, it is also possible to realize spatially confined growth[143], and construction of vertical and lateral heterostructures, as will be shown in the next section.

2.2 Synthesis of Vertical and Lateral Heterostructures[1, 2]

Depending on the wettability between the seeding molecule and the growth substrate, we can confine the positioning of the seeding molecules and as a result achieve spatially confined synthesis of TMDs. On one hand, PTAS as a seeding promoter works exceedingly well for promoting MoS_2 growth on hydrophilic substrates, since it is a salt and is typically applied with an aqueous solution. On the other hand, we could deposit $F_{16}CuPc$ seeding promoter via thermal evaporation on hydrophobic substrates. These two types of molecules are complementary to each other. We can thus construct a variety of vertical and lateral structures at will.

2.2.1 Vertical Heterostructure

To construct vertical heterostructures, because 2D materials are mostly hydrophobic, we choose $F_{16}CuPc$ as the seeding promoter. To demonstrate this, we tested on exfoliated graphene, hBN samples as well on electron-beam evaporated gold substrates. We shows typical optical images of MoS_2 grown directly on a 100 nm $Au/SiO_2/Si$ substrate and on exfoliated $hBN/SiO_2/Si$ and exfoliated $graphene/SiO_2/Si$ substrates by evaporating 2 Å $F_{16}CuPc$ on each of the substrates as a seeding promoter (Figure 2-3 (a)–(c)). The resulting whole surface of the substrate in this case is covered by a continuous MoS_2 monolayer. This result was not achieved by using PTAS as seeding promoter since PTAS solution is hard to deposit on these kinds of substrates uniformly. The PL and Raman spectra were collected on the area with Au, hBN, and graphene (graphite) (Figure 2-3 (d) and (e)). The PL signal and the E_{2g} and A_{1g}

Raman modes indicate MoS_2 is obtained on the Au, hBN, and graphene (graphite) substrates, even though the contrast differences in the optical images are not strong enough to see if there is MoS_2 on the surface of hBN or graphite. It should be noted that, if there was no $F_{16}CuPc$ seeding promoter on these substrates, crystalline MoS_2 were obtained on the substrates (Figure 2-4). Since there are some specific interaction effects on such hybrid structures, some interesting phenomena were observed, such as the enhancement of the PL intensity on Au and the quenching of the PL intensity on the hBN and graphene (graphite) substrates, and the shift of the PL and Raman peak frequencies.

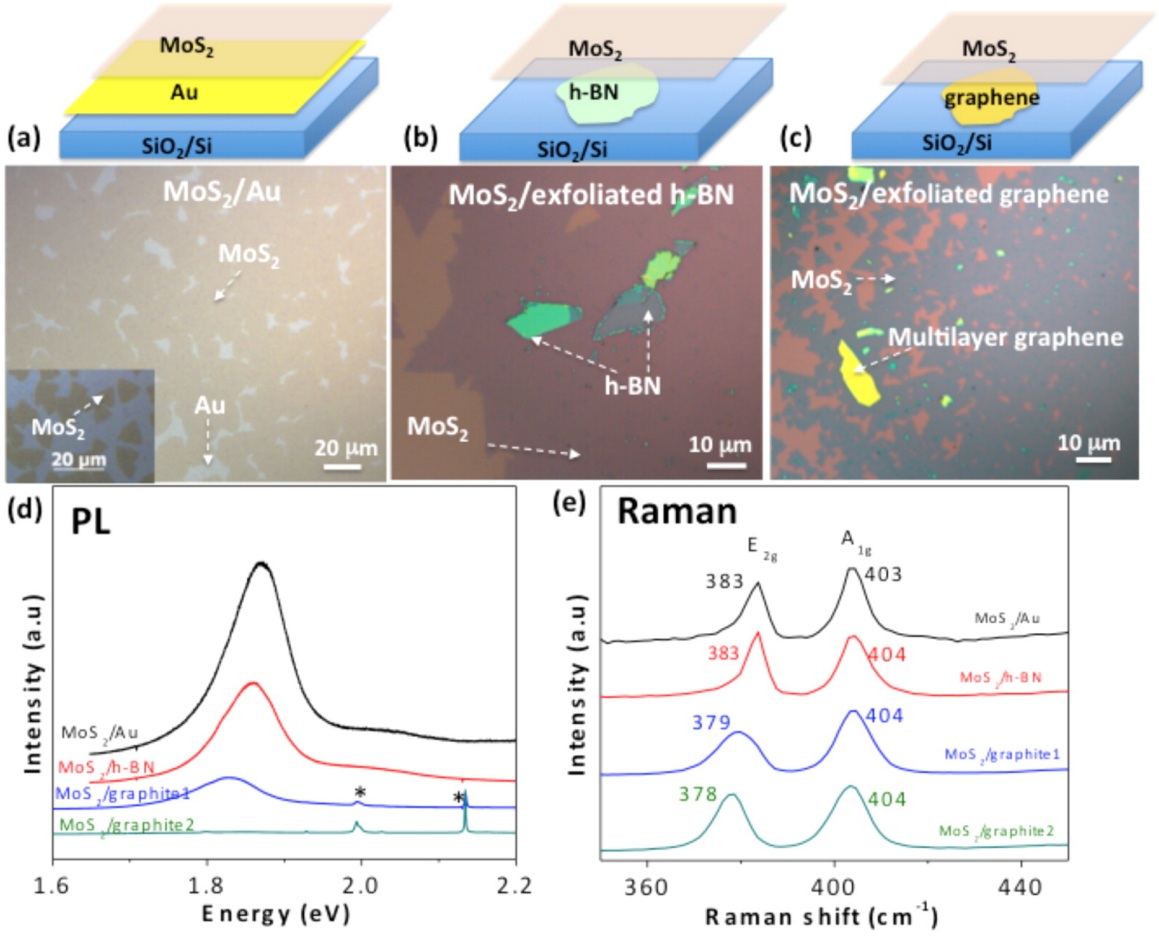

Figure 2-3: Vertical heterostructure. (a-c) Typical OM images of vertical structures grown by using $F_{16}CuPc$ as the seeding promoter. (a) MoS_2; (b) MoS_2/hBN; (c) MoS_2/graphene. (d) PL and (e) Raman spectra of MoS_2 on Au, h-BN and graphene.[1]

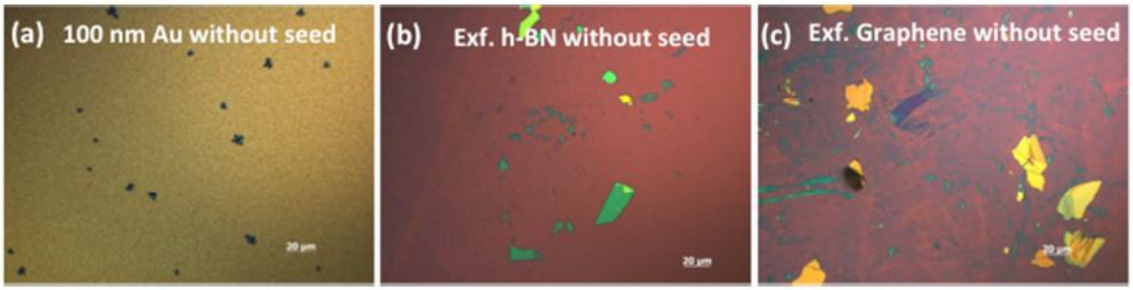

Figure 2-4: OM images after MoS_2 growth without any seeding promoters on (a) Au, (b) hBN, and (c) graphene/graphite.[1]

2.2.2 Lateral Heterostructure

To construct lateral heterostructure, we choose PTAS as the seeding promoter. Figure 2-5 (a) illustrates the growth procedure of the parallel stitched heterostructure between a TMD and another 2D material through the selective "sowing" of PTAS molecules on the growth substrate.The first 2D material is transferred onto a SiO_2/Si substrate (growth substrate) and can be patterned by lithography and etching. During the growth, PTAS molecules are carried by the carrier gas (Ar) and "sowed" selectively onto the blank parts of the hydrophilic SiO_2 substrate. This promotes the growth of the second 2D material (TMD) within the SiO_2 region with abundant seed molecules, whereas there is very limited TMD growth in the first 2D material region, due to the negligible amount of seed molecules. Consequently, the growth of the second 2D material only occurs in the SiO_2 regions, allowing the formation of parallel stitched heterostructures along the edges of the first 2D material.

Figure 2-5 (b) to (j) show the growth results of the lateral heterostructures of graphene-MoS_2, WS_2-MoS_2 and hBN-MoS_2 as the prototypes of metal-semiconductor (M-S), semiconductor-semiconductor (S-S), and insulator-semiconductor (I-S) heterostructures, respectively. Optical microscopy, atomic force microscopy (AFM) (insets in Figure 2-5 (c), (e), and (g)) and spectroscopy characterizations (Figure 2-5 (h) to (j)) were carried out. These studies reveal that high quality MoS_2 is grown on the exposed SiO_2 regions, not on top of the first 2D materials, but are well connected with them at the edges. The photoluminescence (PL) and Raman spectra are collected on and outside the first 2D materials, as shown in Figure 2-5 (h) to (j). The intense PL

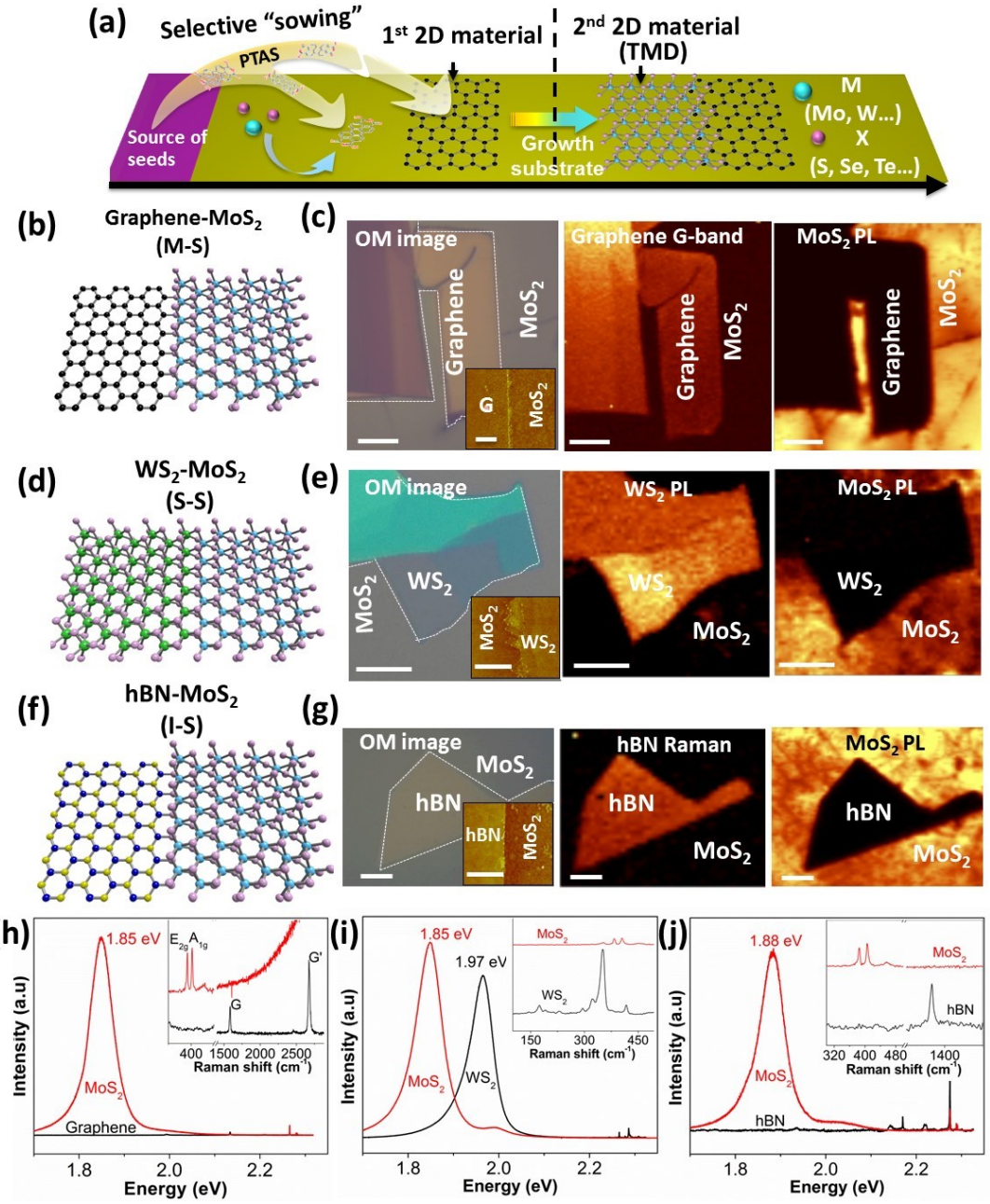

Figure 2-5: Diverse parallel stitched heterostructures between MoS_2 and various 2D materials. (a) Schematic illustration of the CVD setup and the process for the synthesis of the parallel stitched 2D-TMD heterostructure. (b,d,f) Schematic illustration of the parallel stitched heterostructures of graphene-MoS_2 (b), WS_2-MoS_2 (d), and hBN-MoS_2 (f). (c,e,g), Typical optical images, spectroscopy intensity mapping images on the structures corresponding to (b), (d), and (f). The boundaries between MoS_2 and the pre-existing 2D materials are marked by the white dashed line. The scale bars are 5 μm. Insets in the optical images are the AFM images on the heterojunction (the scale bars are 500 nm). (h,i,j), Typical PL spectra and Raman spectra (insets) collected on MoS_2 and the pre-existing 2D materials areas of the parallel stitched heterostructures (h), WS_2-MoS_2 (i), and hBN-MoS_2 (j).[2]

signal around 1.85 eV, and the E_{2g} and A_{1g} Raman modes ($\Delta\omega = 21\,cm^{-1}$) obtained in the MoS_2 region (red traces in Figure 2-5 (h) to (j)) indicates the high quality of the monolayer MoS_2 [1]. While on top of the first 2D materials (black traces in Ffigreffig:lateral (h) to (j)), only the Raman modes from them (monolayer graphene: G-band at 1582 cm^{-1} and G'-band at 2676 cm^{-1}; WS_2: 174, 295, 322, 350 and 417 cm^{-1}; hBN: 1368 cm^{-1}) were observed. The intensity mappings of the Raman (or PL) signals from the first 2D materials and the PL from MoS_2 further indicate that high-quality monolayer MoS_2 was only grown outside the first 2D materials (Figure 2-5 (c), (e), and (g)). We consequently conclude that sharp and well-stitched boundaries were formed at the edges of the first 2D materials, with no breaks or tears.

Since there is a large lattice mismatch (25%) between graphene and MoS_2, the epitaxial growth between graphene and MoS_2 is, in principle, more difficult than that between graphene and hBN, or between two different TMDs. High resolution transmission electron microscopy (HRTEM) was therefore carried out on the graphene-MoS_2 parallel stitched heterostructures for structural characterization (Figure 2-6 (a) and (b)). Selected-area TEM diffractograms indicate that the dark area between the dashed lines in Figure 2-6 (b) consists of graphene and MoS_2, while only MoS_2 (left side) or graphene (right side) can be observed outside the interface region. This indicates that MoS_2 overlaps with graphene at the boundary between them. The width of most of the overlapping region is 2 nm -30 nm (Figure 2-6 (b) and Figure 2-7). Figure 2-6 (b) shows a heterojunction with an overlap region of only 2.5 nm wide. The atomic structures are clearly seen on the MoS_2, graphene, and overlapping regions (Figure 2-6 (b)).Figure 2-6 (c) to (e) show the diffractograms through fast Fourier transform (FFT) in each of these three regions. The red circle marks the diffraction pattern from the MoS_2 lattice structure with a spacing of 2.7 Åcorresponding to the (100) planes. The orange circle marks the 2.1 Åspacing from (110) planes of graphene lattice structure. The FFT diffraction pattern of the overlapping region indicates that there is a 5° rotation angle between the MoS_2 and graphene lattices. Comparing Figure 2-6 (d) with Figure 2-6 (c) and (e), the corresponding MoS_2 and graphene lattice spacing individually remain at 2.7 Åand 2.1 Å, respectively, in the

overlapping region, indicating that there is no lattice distortion at their interface. As the lattice mismatch between MoS_2 and graphene is relatively large, the unchanged lattice constants for both of them at the interface indicate that MoS_2 and graphene are connected with each other probably through van de Waals interaction. Similar analysis was done on more samples, which shows that the rotation angles between the two materials are all within a small range of 0-10° (Figure 2-7).

A closer look reveals more atomic defects in the overlapping region (Figure 2-6 (f)) than that in the regions away from the interface. There are mainly two kinds of defects in the MoS_2 lattice: Mo-Mo bond defects and -S- bridge defects.[20,21] The -S- bridge defect looks like an 8-member ring in the lattice, while the Mo-Mo bond defect corresponds to a 4+8-member ring. Both defects have been observed at MoS_2 grain boundaries.[21] In the overlapping regions of the lateral structures, however, the MoS_2 defects are mainly 8-member ring defects, as marked in the Figure 2-6 (f), suggesting that the absence of seed molecules on graphene is related to a lack of sulfur for MoS_2 growth. Possibly, the increased density of defects at the interface results in the inhibition of MoS_2 growth further into the graphene region.

2.3 Device Application: Integrated Circuits Based on Graphene-MoS_2 Lateral Heterojunctions

One unique advantage of thel lateral synthesis method is that it enables large scale integration. Here, we demonstrate the construction of many graphene-MoS_2 lateral heterostructures with arbitrary patterns. Figure 2-8 shows the typical optical images and spectroscopy characterization of a graphene-MoS_2 lateral heterostructure array (Figure 2-8 (a) to (c)), “MIT” logo (Figure 2-8 (d) to (f)) and MIT mascot "Tim the beaver" (Figure 2-8 (g) to (i)). It is observed that the mapping images of the G-band Raman intensity from graphene (Figure 2-8 (b), (e) and (h)) and PL intensity from MoS_2 (Figure 2-8 (d), (f) and (i)) are highly correlated with each other, and match well with the corresponding optical image (Figure 2-8 (a), (d), and (g)). The AFM

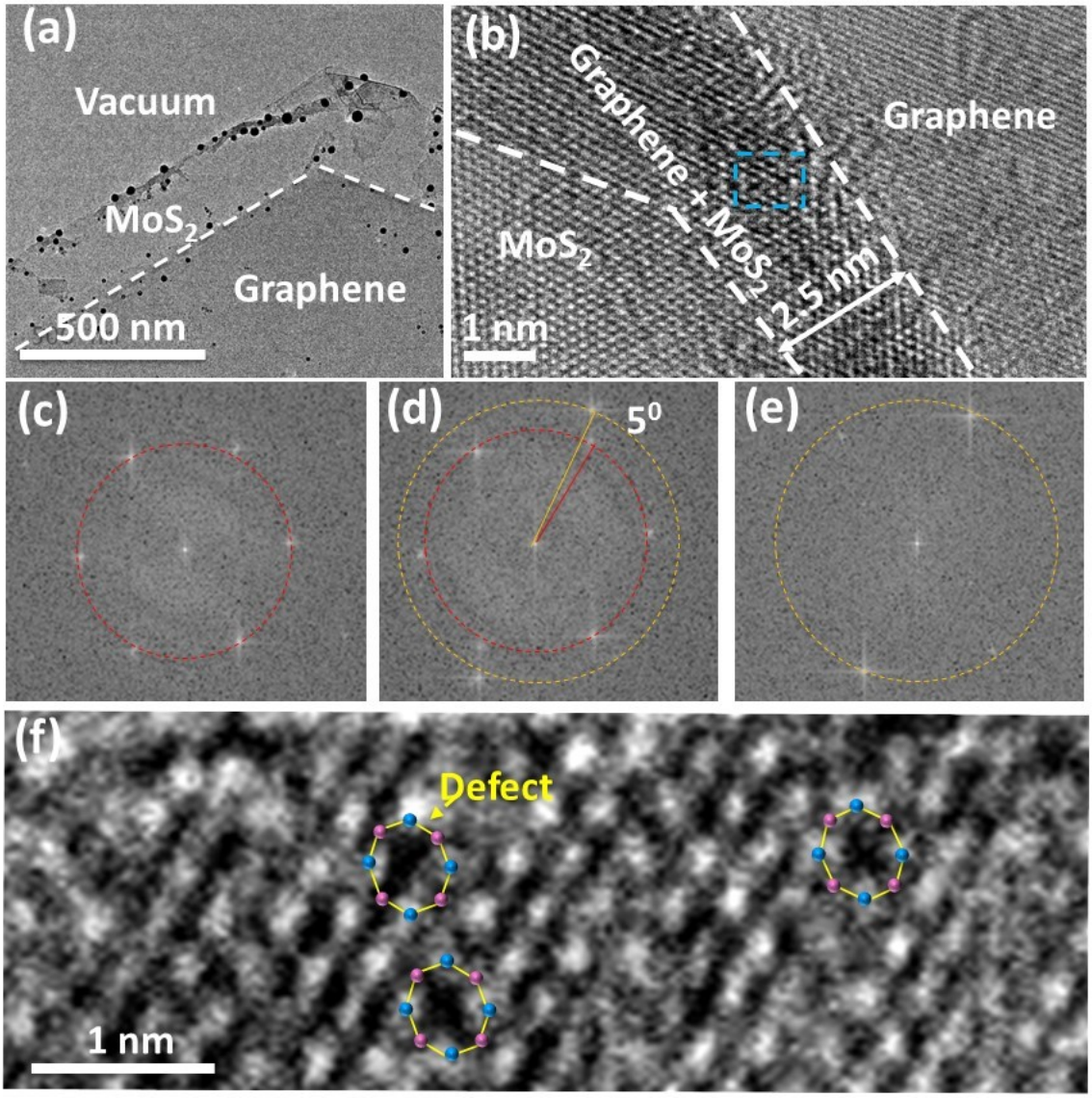

Figure 2-6: TEM characterizations of the graphene-MoS_2 lateral heterojunction. (a) Low magnification bright field TEM (BF-TEM) image showing the graphene-MoS_2 interface. (b) HRTEM image showing the atom arrangement at the graphene-MoS_2 heterojunction with the size of the overlapping region of 2.5 nm. (c-e) Diffractograms corresponding to the MoS_2 region (c), graphene-MoS_2 overlapping region (d) and graphene region (e), respectively. The red and orange circles mark the diffraction patterns from MoS_2 and graphene, respectively. (f) Magnified HRTEM image of the graphene-MoS_2 overlapping area marked by blue in (b) showing the 8-member rings defects.[2]

image in the inset in Figure 2-8 (a) indicates that the periodic heterostructures are well connected with very narrow overlaps at the interfaces. These morphological and

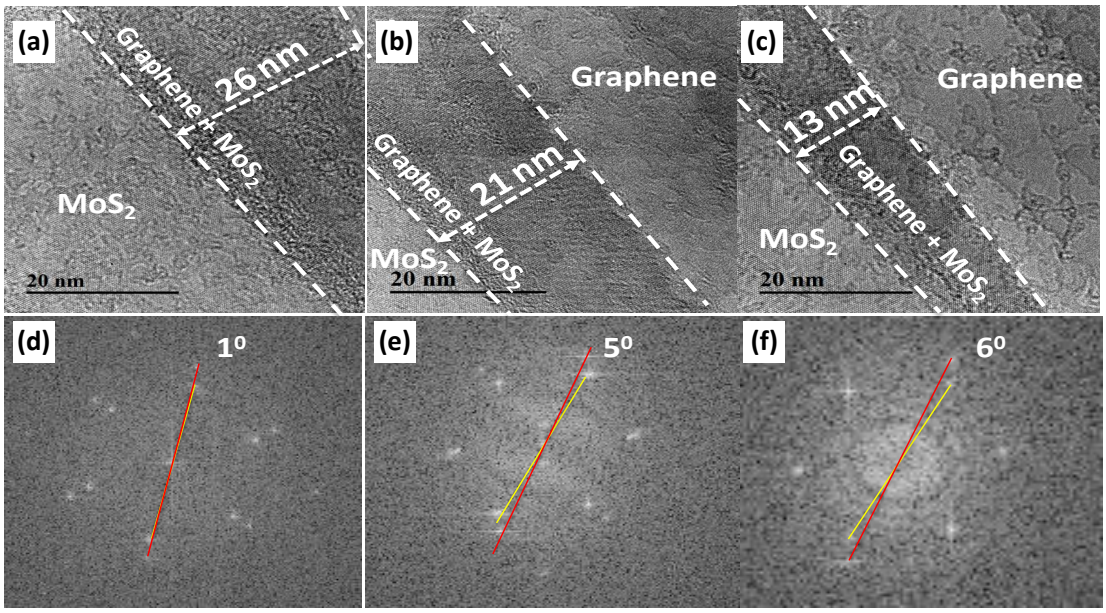

Figure 2-7: High magnification BF-TEM images of the Graphene-MoS_2 heterostructures with different sizes for their overlapping regions. (a) 26 nm; (b) 21 nm; (c) 13 nm. (d,e,f) are the corresponding diffractograms (FFT) in the overlapping areas, showing their twist angles between the two overlapped lattices.[2]

spectroscopic measurement results give further evidence that the MoS_2 and graphene are separated in space and stitched together at the edges. Using this method, one can design graphene-MoS_2 heterojunctions at will. As shown by the MoS_2 filled "MIT" logo (Figure 2-8 (d) to (f)) and MoS_2 filled MIT mascot "Tim the beaver" (Figure 2-8 (g) to (i)), the spatial resolution of the MoS_2 patterns in the images can be as low as 1 μm (limited by the spatial resolution of the spectrometer). The geometrical flexibility, good controllability and large-scale fabrication capability offers great opportunity for 2D hybrid multifunctional applications.

Transport measurements across graphene-MoS_2 lateral heterojunctions indicate that a weak tunneling barrier forms at the junction. Figure 2-9 (a) shows an optical image of the device. As shown in Figure 2-9 (b), both the reverse-bias current (when $V_J < 0$) and the forward-bias current (when $V_J > 0$) increase superlinearly with the junction voltage. This behavior is an indication that a tunneling barrier is present [144, 145, 16].

To extract the barrier height, we performed the temperature dependent transport

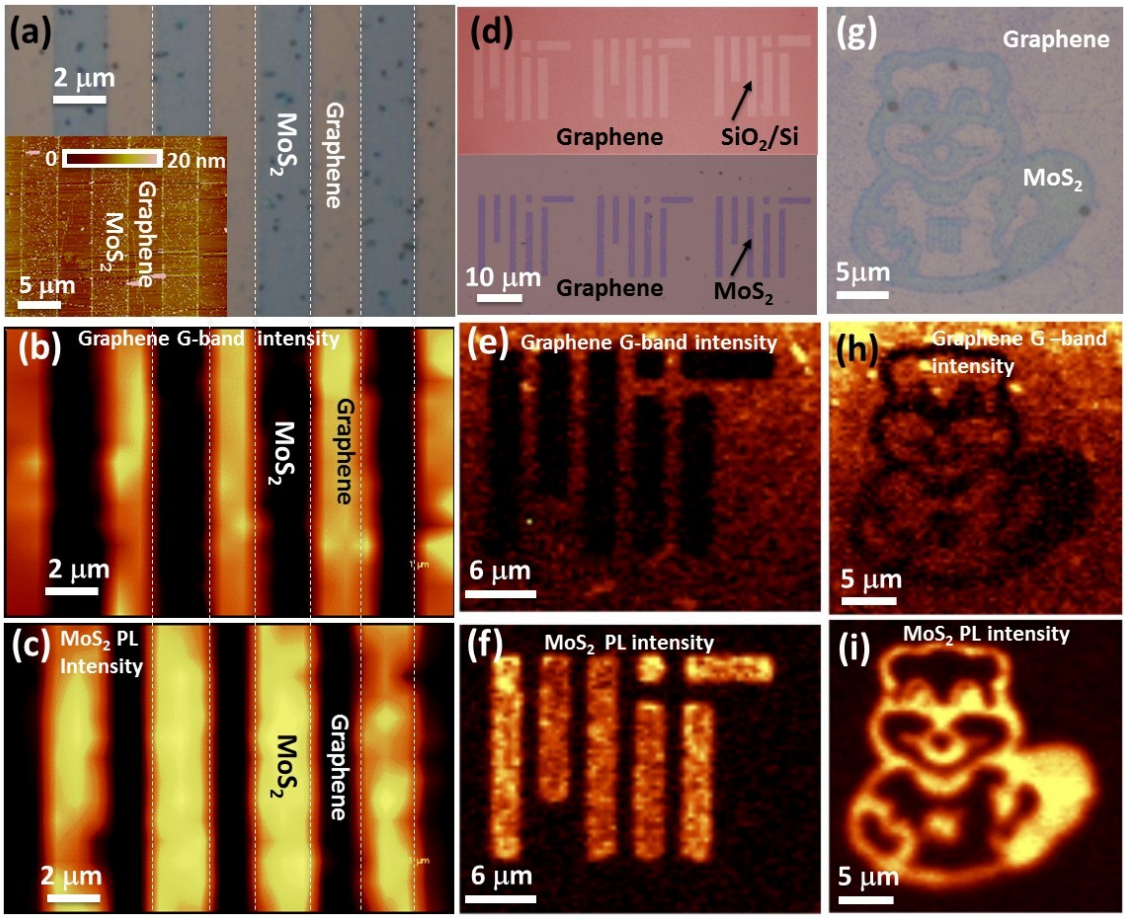

Figure 2-8: Demonstration of the parallel stitched graphene-MoS_2 heterojunction in a large scale with arbitrary patterns. (a-c), Typical optical images of the graphene-MoS_2 periodic array (a), the corresponding mapping image of G-band intensity of graphene (b) and PL intensity of MoS_2 (c). Inset in (a) shows the typical AFM image of graphene-MoS_2 periodic array. d), Optical images before (top) and after (bottom) MoS_2 grown on a pattered graphene pattern with "MIT" logo. (e-f), Mapping images of the G-band intensity of graphene (e) and PL intensity of MoS2 (f) obtained on the MoS_2 filled "MIT" logo. (g-i), Optical image of a MoS_2 filled MIT mascot "Tim the beaver" on graphene pattern (g), the corresponding mapping images of G-band intensity of graphene (h) and PL intensity of MoS2 (i).[2]

measurement. Figure 2-10 (a) shows an Arrhenius plot of the junction current in the lateral graphene-MoS_2 heterostructure with a small bias ($V_J = -0.2$ V). At high temperature ($T > 100$ K), the junction current decreases exponentially with $1/T$; however, at low temperature ($T < 100$ K), a very weak temperature dependence was observed. The high-temperature regime is dominated by the combined thermionic-tunneling mechanism, and the low-temperature regime is dominated by the tunneling

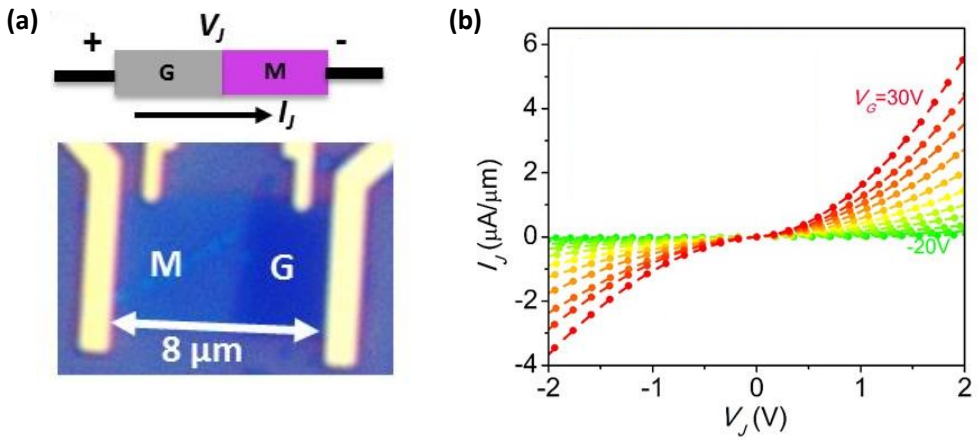

Figure 2-9: (a)Schematic and microscopic image of the 4-probe graphene-MoS_2 heterojunction device on top of a 300 nm SiO_2 as the back gate dielectric. (b) Output characteristics of the graphene-MoS_2 heterojunction with different gate bias from -20V to 30V with 5V intervals.[2]

mechanism.

In the high-temperature region, the reverse-bias current can be expressed by: [144, 16]

$$|I_R| = A^* T^{\frac{3}{2}} P \exp\left(\frac{q\Phi_B}{k_B T}\right) \tag{2.1}$$

where A^* is the effective Richardson's constant, k_B is the Boltzmann constant, q is the electron charge, P is the tunneling probability, and Φ_B is the Schottky barrier height. This equation can be rewritten as

$$\ln\left(\frac{|I_R|}{T^{\frac{3}{2}}}\right) = \ln(A^* P) - \frac{q\Phi_B}{k_B T} \tag{2.2}$$

The Schottky barrier height can be extracted from the slope of the linear fit between $\ln(|I_R|/T^{\frac{3}{2}})$ and T^{-1}, as shown in Figure 2-10 (b).

Figure 2-11 shows the extracted barrier height (Φ_B) at the junction as a function of the gate voltage. The barrier height is around 70 meV at zero gate and less than 20 meV at high positive gate voltage ($V_G > 30$ V), which is similar to that for the graphene-MoS_2 vertically stacked heterostructure [16]. The junction resistance ($R_J = V_J/I_J$) is around 0.3 k$\Omega \cdot$mm when MoS_2 is turned on ($V_G = 30$ V). Re-

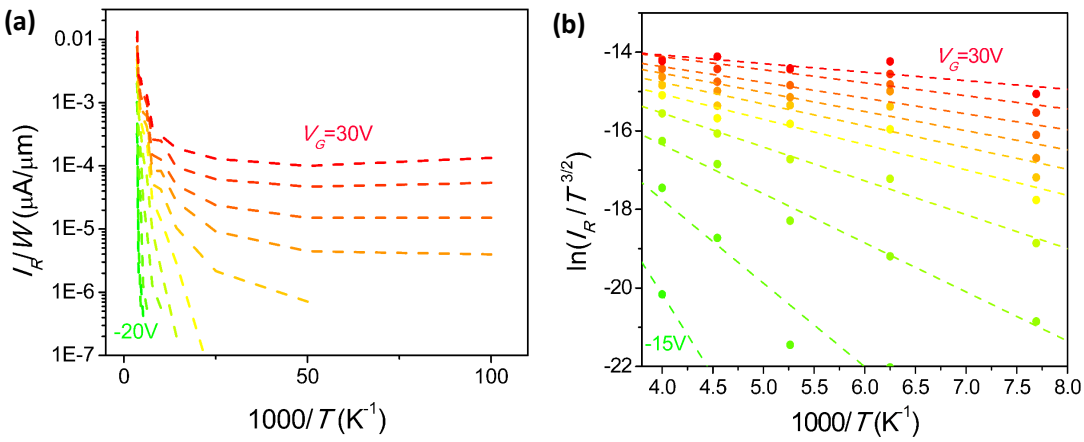

Figure 2-10: Temperature-dependent transport measurement of the graphene-MoS_2 lateral heterojunction. a, The reverse-bias current density (I_R/W) at $V_J = -0.2$ V as a function of the reciprocal temperature ($1000/T$) with different gate voltages (V_G) ranging from -20 V to 30 V. b, The $\ln(I_R/T^{3/2})$ versus $1000/T$ plot at high temperature ($T > 100$ K). The dots are experimental data, and the dashed lines are fitted lines according to Eq. (2.2).[2]

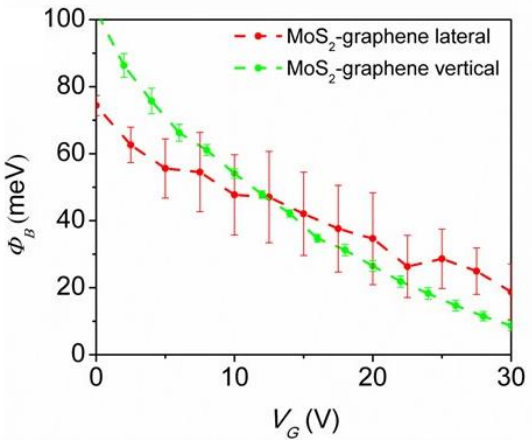

Figure 2-11: The barrier height at the lateral (red) and vertical (green, ref. [16]) graphene-MoS_2 heterojunctions as a function of the gate voltage. [2]

cent works have shown that graphene-MoS_2 vertically stacked heterostructures, when used as contacts to MoS_2 channels, can lead to a much lower contact resistance than conventional metal contacts [16, 26, 27], as summarized in Table 2.1. However, the vertically stacked structures would suffer from various problems when the MoS_2 transistors are scaled down to nanometer scale, such as (i) difficulty in alignment with a high spatial resolution, (ii) the lack of a selective etching technique, and (iii) the

large parasitic impedances. In contrast, the parallel stitched junctions grown with the method presented here can serve as a self-aligned lateral Ohmic contact to the MoS_2 channel. Such contact has been referred to as 1D contact [94], and has been shown to be able to address these problems very well without degrading contact quality. Implementing these 1D contacts has been a tremendous challenging task previously [94], but can be simply realized with our selective "sowing" method here.

Table 2.1: Schottky barrier heights for different metal contacts to MoS_2 transistors [16, 26, 27].

Contact	Φ_B
graphene-MoS_2 (lateral or vertical)	20 meV
Sc-MoS_2	30 meV
Ti-MoS_2	50 meV
Au-MoS_2	130 meV
Ni-MoS_2	150 meV
Pt-MoS_2	200-400 meV

Using graphene-MoS_2 lateral heterostructures as the source/drain contacts of top-gated MoS_2 transistors, we fabricated arrays of the basic building blocks of integrated circuits (shown in Figure 2-12(a)).Figure 2-12 (b) shows the microscopic image and the transistor-level schematic of a diode-connected MoS_2 transistor, indicating good rectifying behavior, with an on-off current ratio on the order of 10^6, obtained according to the I-V characteristics in Figure 2-12 (c). Based on the direct-coupled transistor logic (DCTL) technology [16], which has been widely used in high-speed logic circuits with low power consumption, we successfully fabricated inverter (Figure 2-12 (d) to (f)) and NAND gates (Figure 2-12 (g) and (h)), which are a complete set of logic circuits and can, in principle, realize any 2-level combinational logics. Figure 2-12 (d) plots the typical voltage transfer characteristics of an inverter, with the power supply voltage (V_{dd}) ranging from 3 V to 6 V, with a full logic swing and a symmetric and

abrupt on-off transition. The voltage gain, given by $A_v = \mathrm{d}V_{out}/\mathrm{d}V_{in}$, as shown in the inset of Figure Figure 2-12 (d), has a sharp peak at the medium voltage level ($V_{dd}/2$), with a value up to 7. This, together with the well-matched input-output range, guarantees the normal operation when multiple stages of logic gates are cascaded. Figure 2-12 (f) and (h) show the transient responses of an inverter and a NAND gate, respectively, in which the output voltage of the inverter is always the opposite of the input voltage, and the output voltage of the NAND gate is "low" only when both its inputs are "high".

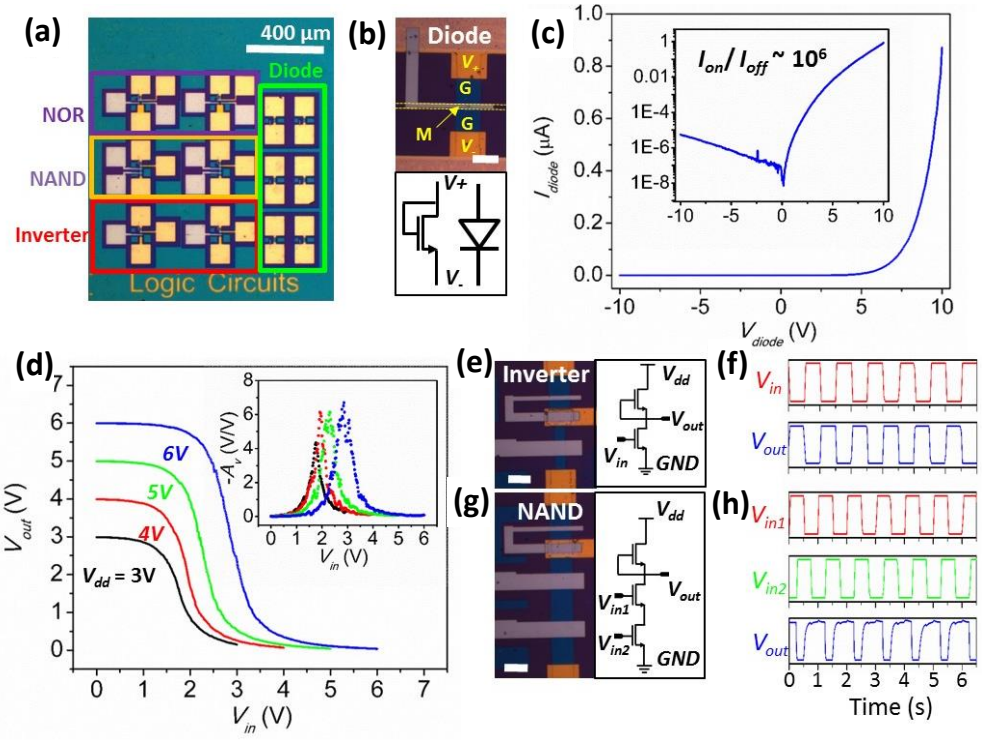

Figure 2-12: (a), Microscopic image of the test chip of the logic circuit arrays based on the parallel stitched graphene-MoS_2 heterojunctions. (b,e,g), Microscopic images and transistor-level schematics of the diode-connected transistor (b), the inverter (e) and the NAND gate (g). Scale bar: 10 μm. (d), I-V characteristic of the diode-connected transistor. Inset: I-V characteristic of the diode in a log scale. The on-off ratio is around 10^6. (d), The voltage transfer characteristic of the inverter, with the power supply voltage (V_{dd}) from 3 V to 6 V. Inset: the corresponding voltage gain ($A_v = \mathrm{d}V_{out}/\mathrm{d}V_{in}$) of the inverter. (f,h), transient response of the inverter (f) and the NAND gate (h) with $V_{dd} = 5$ V.[2]

2.4 Summary

In summary, as conventional lithography/selective etching is incapable for use in the large scale integration of 2D materials to achieve various junctions for future electronics and optoelectronics, in this work a universal methodology is proposed to address such challenges. By introducing the selective "sowing" of the molecules as seeds at different positions on a growth substrate during the synthesis of monolayer TMD materials, vertical and lateral heterojunctions of TMD with other 2D materials can be constructed. The method of heterojunction formation is effective, simple, and powerful, not only offering solutions for large-scale 2D materials integration but also enabling development of versatile parallel stitched in-plane junctions which are unique in structure and properties, thus offering tremendous potential, as demonstrated through the example of large-scale manufacturing of lateral graphene–MoS_2 heterostructures and the investigation of their potential applications.

Chapter 3

Deep Learning Enabled Fast Optical Characterization of Two-Dimensional Materials

Characterizations of nanomaterial morphologies with advanced microscopy and/or spectroscopy tools have been indispensable in nanoscience and nanotechnology research [146], as rich information about the chemical compositions, crystallography, physical and chemical properties, as well as the synthesis process can be extracted from the morphology analysis. The tremendous advance of microscopy and spectroscopy technologies in recent years has enabled us to visualize the morphologies with much improved resolutions and new domains of physical properties [147, 148, 149, 150]. However, current predominant methods for interpreting the imaging or spectroscopy data heavily rely on the "intuition" of experienced researchers. As a result, only qualitative analysis can be made on the most prominent and independent features, which is only a small portion of the information contained in morphological data. The difficulty comes from the high-dimensionality and intricacy of the morphological data and the highly non-linear and codependent relations between the morphologies and the physical properties of interest. Therefore, a systematical or statistical approach to analyzing the morphological data is of vital importance to accelerate scientific discoveries in the nanomaterial research. Machine learning,

especially recently developed neural network (NN) based semantic image analysis algorithms, can potentially address this challenge very well. With the rapid development of deep learning, current semantic segmentation methods based on convolutional neural networks (CNNs) can analyze more complicated scenes than traditional methods, for applications such as autonomous vehicles and medical image diagnostics [151, 152, 153, 154]. These methods also fit the needs for processing microscopy or spectroscopy data.

As a case study, here we demonstrate a deep learning method to process and "understand" the microscopic images of exfoliated two-dimensional (2D) materials. An encoder-decoder semantic segmentation network called "SegNet" [154] is modified and applied for pixel-wise identification of optical microscopic images of 2D materials, and we demonstrate that this architecture can solve the problem quickly by extracting deep graphical features from optical microscopic images. Once properly trained, the same network can be used for the real-time identification of images taken with different microscopes, under different configurations or user preferences. In addition, a detailed analysis on the feature maps of all the layers of the network reveals that the trained network is able to capture deep graphical features, based on which we propose that the network can be used for advanced applications such as prediction of material properties. Finally, we demonstrate that the deep learning algorithm can be generalized for solving different optical identification problems by applying a transfer learning technique to the pretrained network with minimal effort of additional training.

3.1 Limitation of Conventional Optical Identification Methods

Up to now, hundreds of 2D materials have been isolated and studied, offering a wide range of optical and electronics properties, including metals, semiconductors, insulators, magnets, and superconductors. As briefly introduced in subsection 1.2.2 The

most widely used approach to obtain high-quality 2D crystals in laboratories is mechanical exfoliation, followed by 2D crystal "hunting" under an optical microscope (OM) (Figure 3-1). This task is time-consuming and difficult especially for inexperienced researchers. Very recently, there has been growing interest in automating such a process [155]. An automatic optical identification and/or characterization system requires an algorithm that performs reliably for different materials and with different user requirements, is easily adaptable to different optical setups, and is fast enough for real-time processing. However, existing optical identification methods are completely based on optical contrast of the 2D crystals [156, 157, 158, 159, 160, 161]. Optical constrast method is based on the optical interference effect of the air/2D material/SiO_2/Si multilayer structures. The film thickness or the layer number is obtained by finding the color different between the 2D flake and the blank substrate, and comparing this difference to a standard database, or fit it to a mathematical model. This method is often specific to types of 2D crystals, conditions and configurations of the microscopes being used, image qualities, *etc.* In reality, however, there are randomness introduced by different microscope setups, user preferences, and sub-

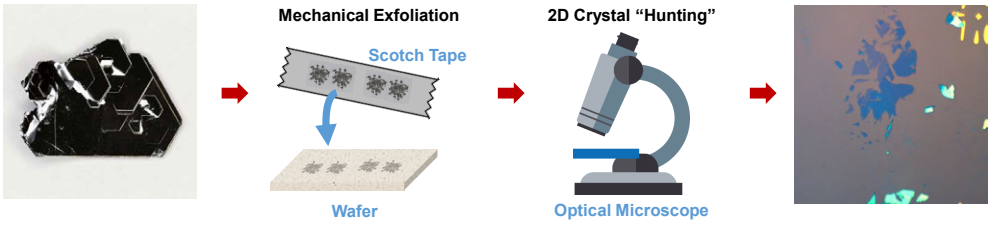

Figure 3-1: The flake "hunting" procedure. From left to right are: a photograph of a graphite crystal; a schematic of the mechanical exfoliation process; flake "hunting" under an optical microscope; the resulting graphene flakes on a SiO_2/Si substrate.

In addition, optical contrast based methods would fail completely for harder problems in which the classes to be differentiated are not separable in the color space, such as identifying the materials in unlabeled optical images. Figure 3-3 shows typical OM

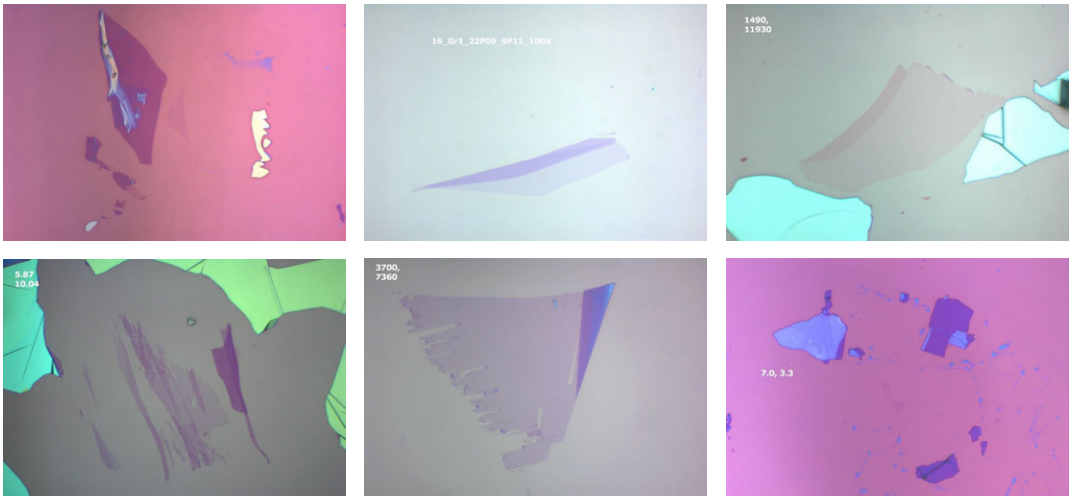

Figure 3-2: Examples of optical microscopic images of exfoliated graphene.

images and their distributions in RGB color space of four 2D materials. It is observed that the color distributions for these four materials overlap with one another to the extend that any algorithm merely based on this color information would fail completely to differentiate them.

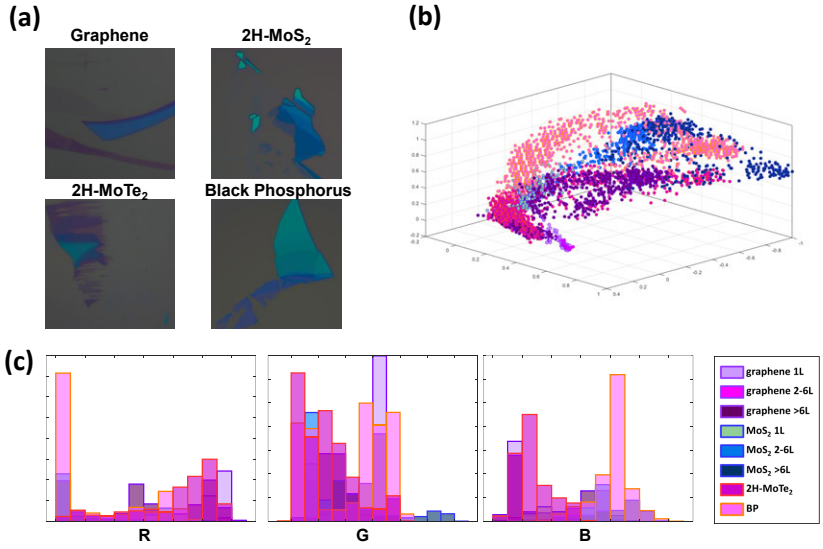

Figure 3-3: Optical contrast analysis of 4 different 2D materials, including graphene, MoS_2, 2H-$MoTe_2$, and black phosphorus. (a) typical OM images. (b) RGB distribution of the images in (a). (c) Distribution of the R, G, and B values.

3.2 Deep Learning Based Optical Identification Method

OM images contain rich, often unused information other than optical contrast. These deep graphical features can be extracted through deep learning, especially semantic segmentation methods based on convolutional neural networks (CNNs) [151, 152, 153, 154]. In the following, we demonstrate an encoder-decoder semantic segmentation network called "SegNet" [154] for pixel-wise identification of OM images of 2D materials. Our results indicate that this architecture can identify, in real time, various 2D materials in OM images regardless of variations in optical setups. Additionally, we find that the algorithm finds correlations between the OM images and physical properties of the 2D materials and can thereby be used to anticipate the properties of new, as-yet uncharacterized 2D crystals.

3.2.1 Constructing, Training and Testing of the Deep Learning Algorithm

Network Structure

Figure 3-4 illustrates the flow chart of our deep learning based optical identification method. Figure 3-4 (a) and (c) show 13 different 2D materials used for training, their crystal structures, photos of their bulk (three dimensional) source crystals 24 and representative OM images of exfoliated 2D crystallites (or “flakes”) on top of 285 nm or 90 nm SiO_2/Si substrates. The SegNet shown in Figure 3-4 (d) consists of a series of downsampling layers (encoder) and a corresponding set of up sampling layers (decoder) followed by a pixel-wise classifier. As an end-to-end network, the SegNet can predict labels of 2D materials at the pixel level, and the size of the output label map is exactly the same as the input optical microscope image. This can help us directly identify the material identities and the thicknesses of individual 2D material flakes. We select a well-known network structure VGG16 [162] as the basis of the encoder network in the SegNet. Table 3.1 summarizes the VGG16 network structure. The encoder contains a stack of convolutional layers which have 3 by 3 receptive field and

pixel stride 1, followed by a batch normalization and a nonlinear activation (ReLU) layer. Then a max-pooling layer with a 2 by 2 window and stride 2 is applied for the image downsampling. The decoder net and the encoder net are symmetric. The only difference between them is that in decoder we use an upsampling layer to replace max-pooling layer. The indices in upsampling layers are grabbed directly from the indices of the corresponding max-pooling layers. In this way, the locations of the poolings are memorized and recovered in the upsampling layers, which improves the spatial accuracy of the network. Finally, a soft-max classifier is added at the end of the network for pixel-wise classifications. The output label maps have the same dimension as the input OM images.

Table 3.1: Detailed information of the SegNet based on the VGG16 network.

	Encoder	**Decoder**
	Input	Output
	224×224 RGB image	Softmax
Depth=1	Conv 3×3×64	Conv 3×3×64
	Conv 3×3×64	Conv 3×3×64
	Maxpooling 2×2	Upsampling 2×2
Depth=2	Conv 3×3×128	Conv 3×3×128
	Conv 3×3×128	Conv 3×3×128
	Maxpooling 2×2	Upsampling 2×2
Depth=3	Conv 3×3×256	Conv 3×3×256
	Conv 3×3×256	Conv 3×3×256
	Maxpooling 2×2	Upsampling 2×2
Depth=4	Conv 3×3×512	Conv 3×3×512
	Conv 3×3×512	Conv 3×3×512
	Maxpooling 2×2	Upsampling 2×2
Depth=5	Conv 3×3×512	Conv 3×3×512
	Conv 3×3×512	Conv 3×3×512
	Maxpooling 2×2	Upsampling 2×2

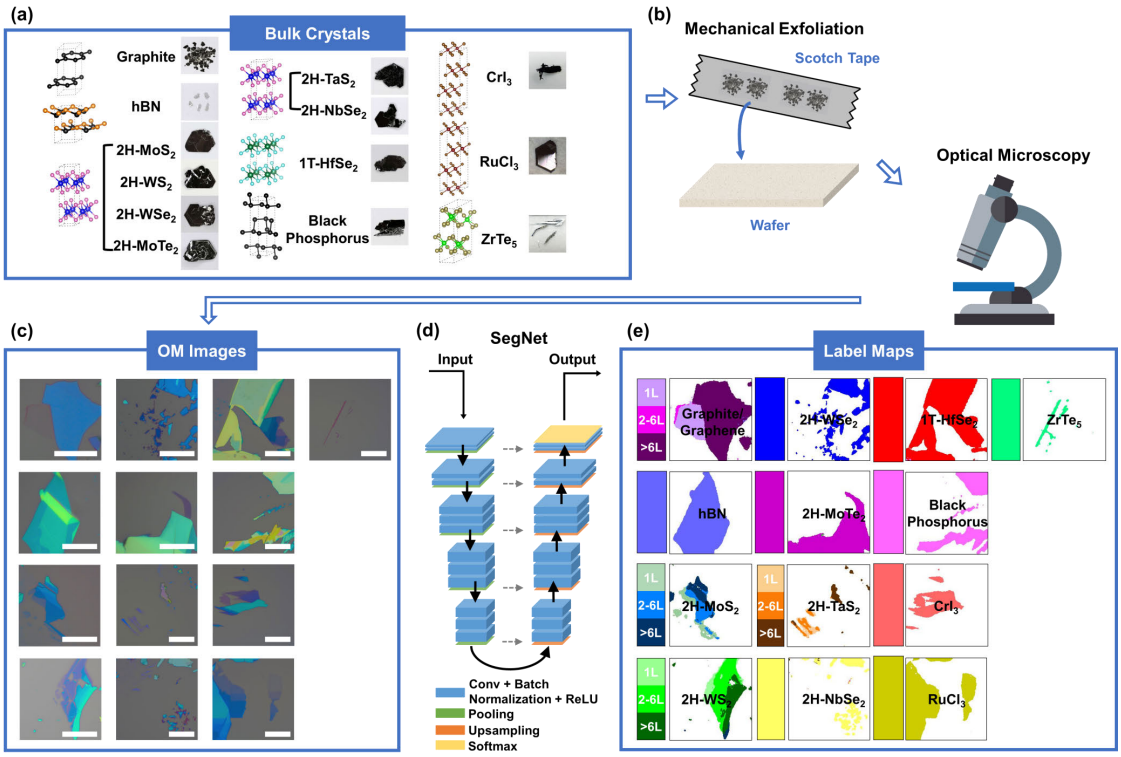

Figure 3-4: The flow chart of the proposed deep learning based optical identification method. We select 13 typical 2D materials (crystal structure and photographs 24 of the bulk crystals are shown in panel (a)). After mechanical exfoliation, the 2D flakes are randomly distributed on SiO_2/Si substrates. We then use optical microscopes to take the images (b). Panel (c) shows representative optical microscopic (OM) images of the 13 materials. When inputting these images to the trained SegNet (as shown in (d)), the label maps (e) will be predicted that segment individual 2D flakes and provide the labels (materials identities and thicknesses) of them. The SegNet is composed of a series of convolutional layers, batch normalization layers, ReLu layers (in blue), pooling (downsampling) layers (in green), upsampling layers (in orange), as well as a soft-max layer (in yellow) as the output layer. Scale bars in (c), 20 μm.

Data Generation

To make the training data representative of the typical variability of OM images, the training and test data were sampled from a collection of OM images generated by at least 30 users from 8 research groups with 6 different optical microscopes over a span of 10 years. These optical images have considerable variations in brightness, contrast, white balance, and non-uniformity of the light field (Figure 3-2) because of the variations between different setups and user preferences. Note that the previously

reported optical-contrast-based optical identification methods require the images to be taken in the same optical setup and with very similar hardware and software configurations [156, 157, 158, 159, 160, 161].

The data generation procedure is illustrated in Figure 3-5. There are 3 steps to generate the pixel-wise labeled dataset for the training of the SegNet: labeling, color normalization, and data augmentation.

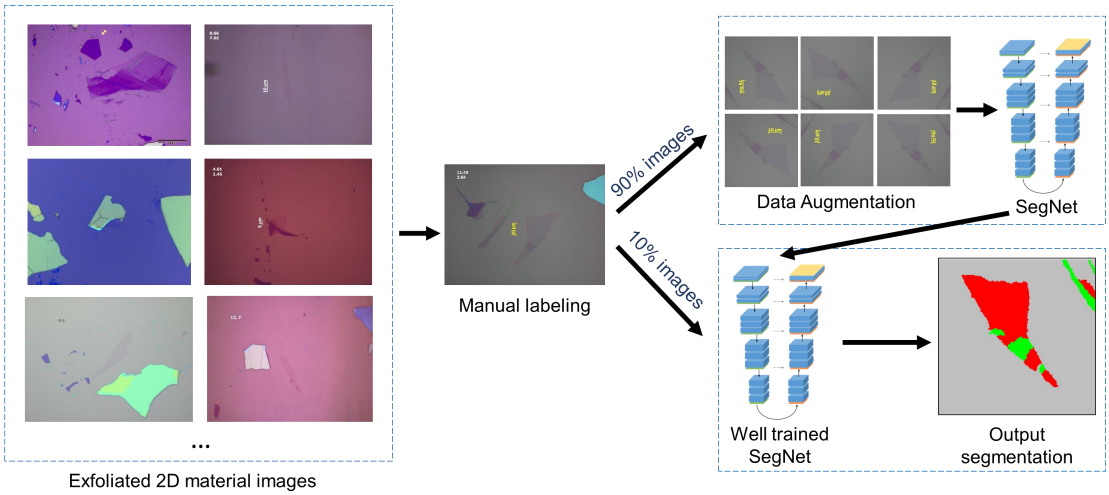

Figure 3-5: Schematic of the data generation procedure.

To generate pixel-wise labeled OM images for the training and testing, we used a semi-automatic graph-cut method implemented by MATLAB. Graph-cut is a traditional semantic segmentation method based on graph theory [163]. Although the initial segmentation performance of this method is poor, we can promote the performance by adding human assistance. By drawing loosely the foreground regions and the background regions, the algorithm can find the boundary of the segment of interest with good accuracy. Figure 3-6 demonstrate the labeling procedure under human-assisted graph-cut method.

We select thirteen 2D materials as experiment samples. They are graphene/graphite, hexagonal boron nitride (hBN), 2H-MoS_2, 2H-WS_2, 2H-WSe_2, 2H-$MoTe_2$, 2H-TaS_2, 2H-$NbSe_2$, 1T-$HfSe_2$, black phosphorous (bP), CrI_3, $RuCl_3$ and $ZrTe_5$. 100 images for each of Graphene/Graphite, 2H-MoS_2, 2H-WS_2 and 2H-TaS_2 were labeled with three classes ("monolayer", "fewlayer (2-6L)" and "multilayer (>6L)") to demonstrate

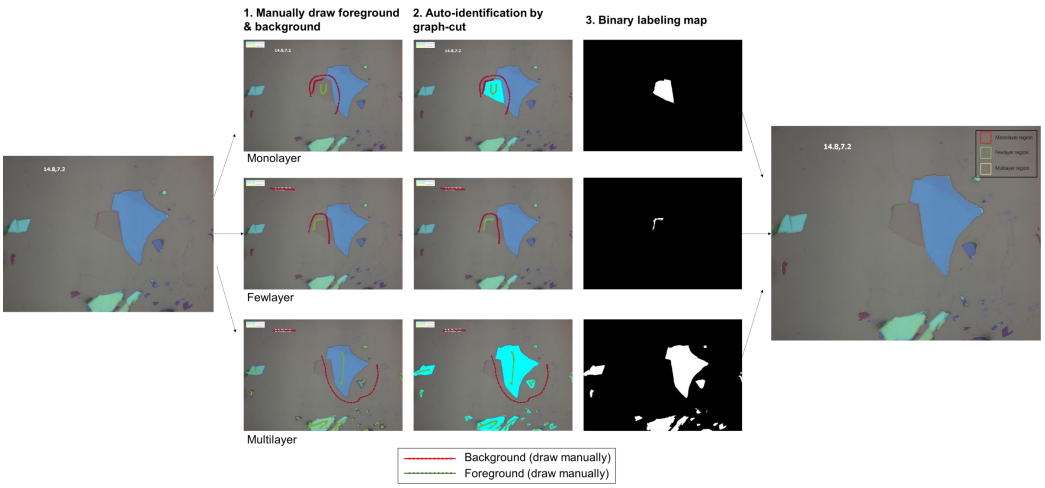

Figure 3-6: Schematic of the semi-automatic labeling procedure.

the thickness identification capabilities, and 50 images for each of the other 9 materials were labeled with only single classes. The total number of classes (including background) is 22, and the total number of labeled OM images is 850.

To partially reduce the color-related variations of the OM images because of different setups and user preferences, a color normalization was performed on all the images. We first converted the RGB images into the Lab color space, and the following transformation was applied to all the pixels: $L \leftarrow 30L/L_{ref}$, $a \leftarrow a - a_{ref}$, and $b \leftarrow b - b_{ref}$, where L_{ref}, a_{ref} and b_{ref} are the Lab values of the background obtained by finding the median L, a and b of each image. The resulting Lab images were then converted back to RGB images.

After labeling and color normalization, we selected 90% of the labeled images as the training dataset, and 10% as the test dataset. The original images were first resized and chopped into 224 by 224 pixel images, then a data augmentation strategy is applied to provide more training examples to the network and thus to improve the accuracy of the network. Each chopped image was flipped (horizontal and vertical) and rotated (by 0°, 90°, 180° and 270°) to generate 6 augmented images. Finally, we obtained 22, 950 images in the training dataset and 2, 550 images in the test dataset.

Training and Testing

The training and testing of the SegNet were implemented in MATLAB R2018b with the help of the Deep Learning Toolbox, the Parallel Computing Toolbox, the Computer Vision Toolbox and the Image Processing Toolbox. The training and testing were performed using a desktop computer equipped with a CPU (Intel(R) Core (TM) i7-8700K @ 3.70GHz, 32.0GB RAM) and a GPU (NVIDIA GeForce GTX 1080 Ti, 11 GB GDDR5X). The stochastic gradient descent with momentum (SGDM) method [164] was used to find the weights in the convolutional filters of the SegNet during the training process. To compensate for the imbalanced numbers of pixels for different classes (for example, the "background" labels take more than 85% of areas in most images), class weightings based on inverse frequencies were used in the soft-max classifier.

3.2.2 Performance Analysis

We first show that the trained SegNet can be used to segment the OM images among 13 different exfoliated 2D materials and find the material identity and thickness of each flake with good accuracy. Examples of the OM images and the corresponding label maps predicted by the trained SegNet can be found in Figure 3-4 (c) and (e). Figure 3-7 shows additional results of the test OM images, the ground-truth label maps (labeled semi-automatically by humans), as well as the predicted label maps. The trained SegNet is able to outline individual flakes from the background and distinguish both the material identities and thicknesses of the thirteen 2D materials with high success rate. As shown in Table 3.2, the pixel-by-pixel global accuracy reaches 96.11%; the mean class accuracy is 77.98%; and the mean intersection over union (IoU, defined as the intersection of the ground truth and the predicted region of a specific label over the union of them) is 53.47% for the training dataset.

Table 3.2: Overall classification performance of the SegNet.

Global Accuracy (by Pixel)	**Mean Accuracy** (by Class)	**Mean IoU** (by Pixel)	**Training Time**	**Frame Per Second (FPS) in Test**	
				Use CPU	Use GPU
0.9611	0.7798	0.5347	8 hr 40 min	2.6	20.2

Note: The experiment environment is: CPU: Intel(R) Core(TM) i7-8700K CPU @ 3.70GHz, 32.0GB RAM; GPU: NVIDIA GeForce GTX 1080 Ti, 11 GB GDDR5X.

The class prediction accuracies can also be shown through the confusion matrix. The confusion matrices were obtained by using the OM images in the test dataset as the input of the trained SegNet and comparing the corresponding output label maps with the ground truth label maps. Figure 3-8 presents the pixel-level (Figure 3-8 (a-e)) and the flake-level (Figure 3-8 (f-j)) confusion matrices of the test dataset. The diagonal elements are the success rate of each class, and the off-diagonal elements are the rate of misclassified pixels or flakes in the test OM images. For example, the element on i-th row and j-th column corresponds to the fraction of the i-th class that are labeled as the j-th class by the SegNet. We also present two types of confusion matrices: the pixel-level confusion matrices (Figure 3-8 (a)-(e)) and the flake-level confusion matrices (Figure 3-8 (f)-(j)). For the pixel-level confusion matrices, the matrix elements are the ratio counted pixel by pixel, whereas the flake-level confusion matrices take the majority label of all the pixels in each segmentation, or "flake", as the label of the flake and calculated the fraction based on the flake labels. Note that the flake labels ignored any segmentations with fewer than 100 pixels, because they are either fractures on the edges of the actual 2D crystal flakes, or some non-uniform regions on the background. The classification accuracies of material identities (Figure 3-8 (a) and (f)) are well above 70% and the classification accuracies of thicknesses (Figure 3-8 (b-e) and (g-j)) are mostly above 60%.

Note that the calculated performance metrics of the SegNet are likely an underestimate: after the SegNet's analysis, we discovered a number of OM images in which

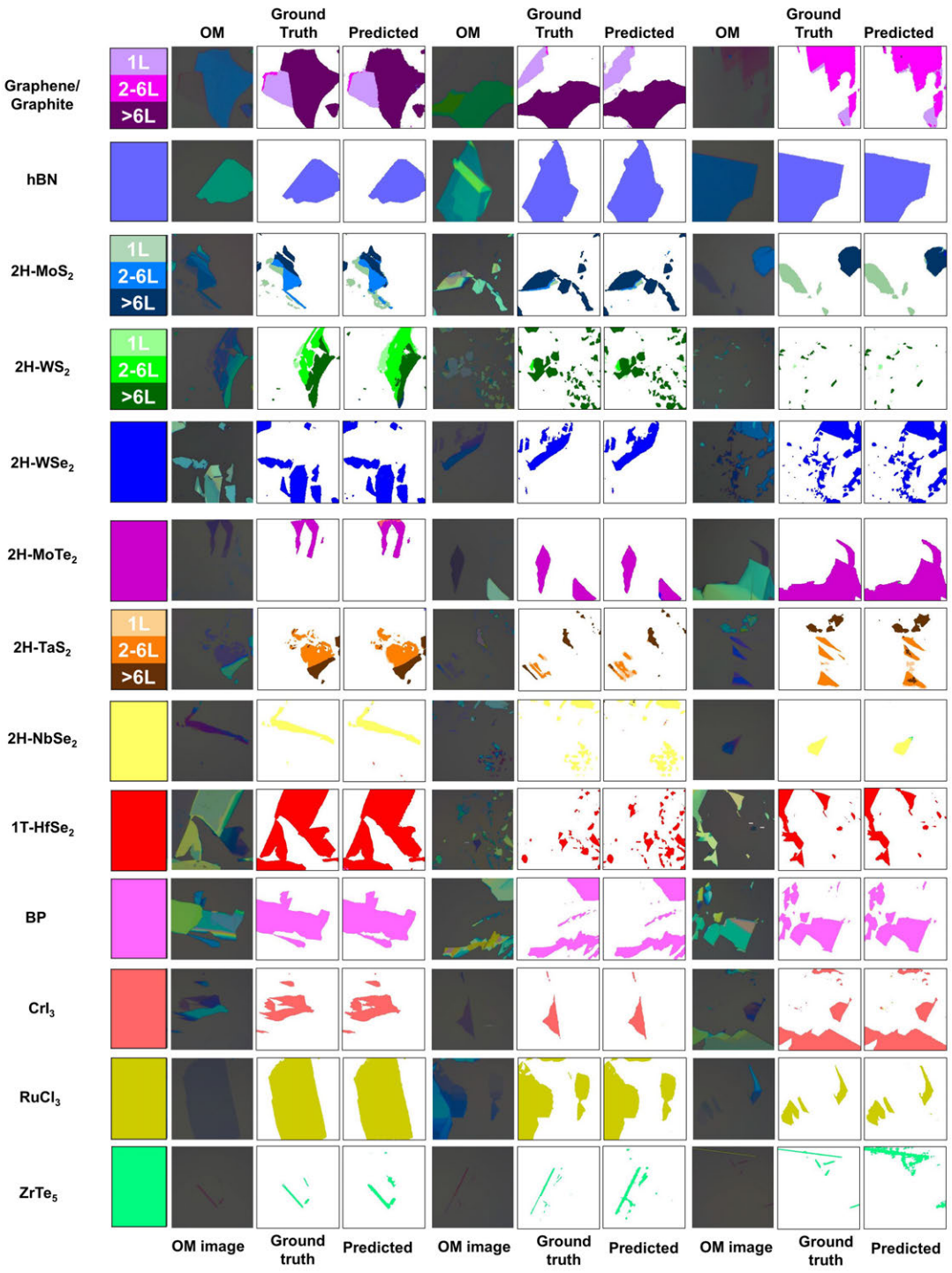

Figure 3-7: Additional results predicted by the SegNet.

the ground-truth was initially mislabeled, but predicted correctly by the SegNet (Figure 3-9). This scenario is considered as a classification mistake in the above metrics. On the other hand, it is observed that many of the mistakes made by network are due

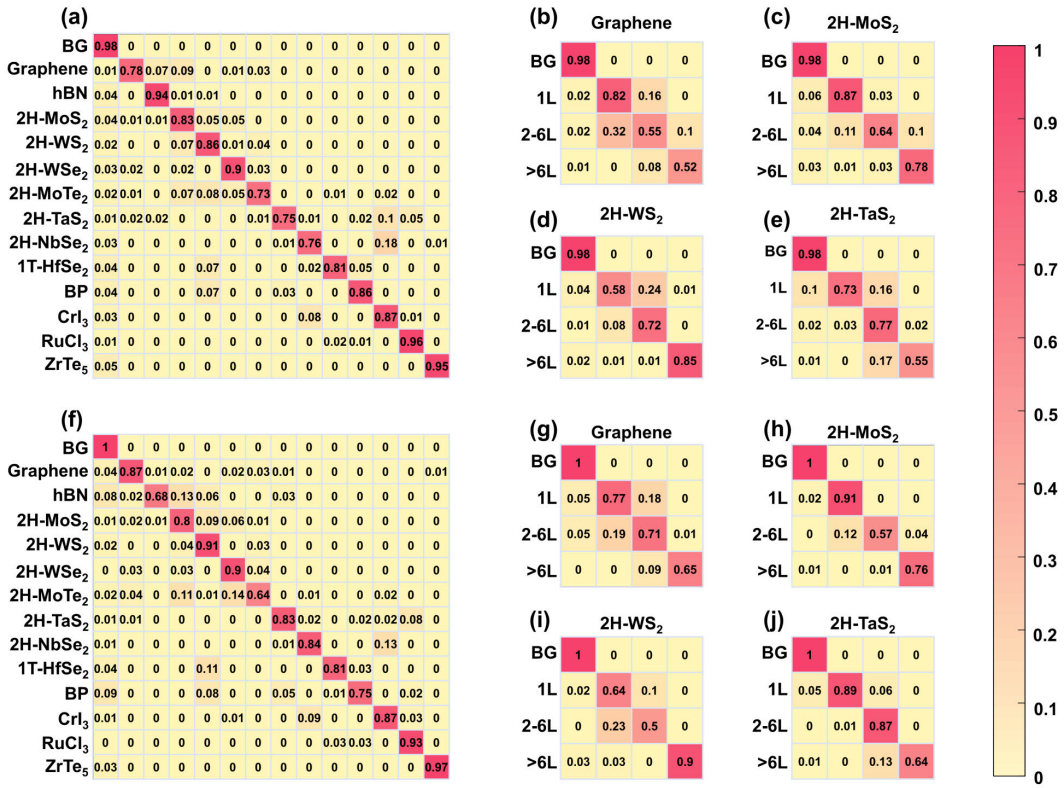

Figure 3-8: Confusion matrices calculated from the test results. (a)-(e) are pixel-level confusion matrices, and (f)-(j) are flake-level confusion matrices. (a) and (f) are for material identities. (b)-(e) and (g)-(j) are for thicknesses. In each confusion matrix, the diagonal terms are the success rate of the predicted classes, and the non-diagonal terms are the rate of misclassified pixels.

to the similarities between different materials. For example, misclassification rates among 2H-MoS_2, 2H-WS_2, 2H-WSe_2 and 2H-$MoTe_2$ are as high as 8%, which is likely a consequence of their similar crystal structures and optical properties. Another type of common mistake is that metal markers, tape adhesive residue and text labels in the OM images were misidentified as a 2D material (Figure 3-9). These non-2D material features were labeled as "background" together with the blank substrate in the ground-truth, but they have high color contrast and other structures relative to the substrate, thereby confusing the network. In a future version of the network, this may be solved by introducing specific labels for these non-2D material features. Another common mistake is inaccuracy in the profiles of the flakes. This usually happens when the profiles are very complex, or if the flakes are highly fragmentary (Figure

3-9). These mistakes are mainly due to the downsampling of the encoder layers in the SegNet, which inevitably drops the high frequency spatial features of the images.

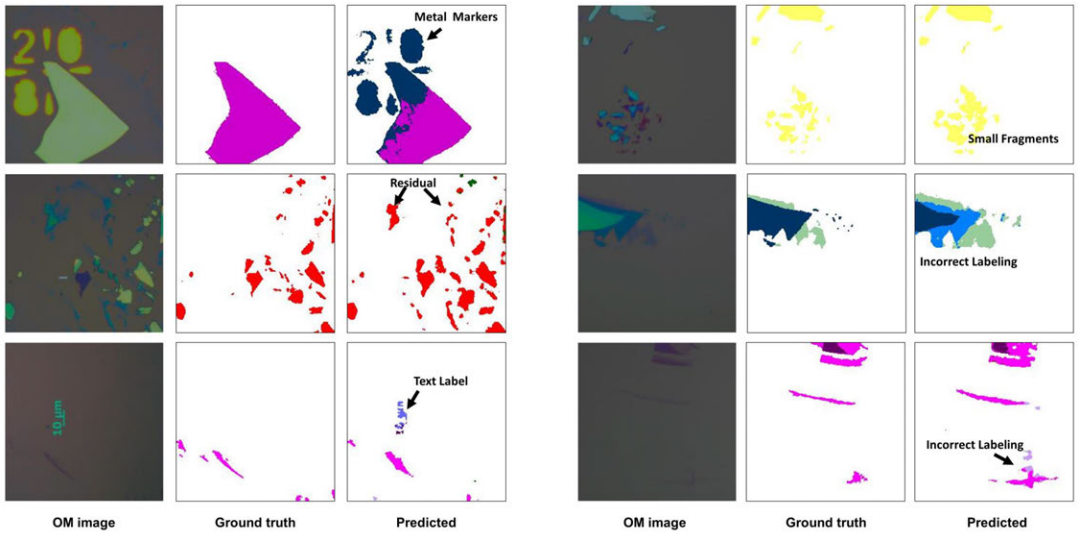

Figure 3-9: Examples of misclassified images.

We also investigated the network with various numbers of depth (number of pooling layers, as indicated in Figure 3-4 (d)) and tested their performance on the same data set. In this experiment, we fix the number of convolutional kernels in each convolutional layer and the number convolutional layers in each depth to be 64 and 2, respectively, rather than varying them gradually as the layer becomes deeper, as in the case of the VGG16 structure. Table 3.3 shows the metrics for the networks with various depth. As we can see, Depth=5 network results in the best global accuracy, mean accuracy and mean IoU among all depth of networks. In Figure 3-10, we present the training loss and the training accuracy under different depths of networks during the training process. The networks with their depths from 1 to 6 can all reach 80% accuracy quickly within the first several epochs. This corresponds to the successful differentiation between the background and the foreground (2D material flakes). After that, the Depth=4 and Depth=5 network continue to reduce the loss and improve the training accuracy, while other networks only show limited training progress.Figure 3-11 and Figure 3-12 are examples of the label maps predicted by

networks with different depths. We can clearly see that the Depth=5 network results in the best prediction accuracy, while the other networks could outline the flakes from the background, but fail to differentiate different classes (thicknesses and types of 2D materials).

Table 3.3: Classification performance of SegNet under different depth (each depth has 2 conv layer, the dimension of convolutional kernel is 64).

	Global Accuracy (by Pixel)	**Mean Accuracy** (by Class)	**Mean IoU** (by Pixel)	**Training Time**	**Frame Per Second (FPS) in Test**	
					Use CPU	Use GPU
Depth=1	0.8925	0.4291	0.2067	260 min	6.3	32.0
Depth=2	0.9016	0.4751	0.2322	307 min	5.1	32.0
Depth=3	0.9164	0.5558	0.2757	322 min	4.8	31.0
Depth=4	0.9232	0.6225	0.3363	329 min	4.8	30.0
Depth=5	0.9414	0.7063	0.4219	336 min	4.6	29.8
Depth=6	0.9145	0.5875	0.3152	346 min	4.7	29.6

Note: The experiment environment is: CPU: Intel(R) Core(TM) i7-8700K CPU @ 3.70GHz, 32.0GB RAM; GPU: NVIDIA GeForce GTX 1080 Ti, 11 GB GDDR5X.

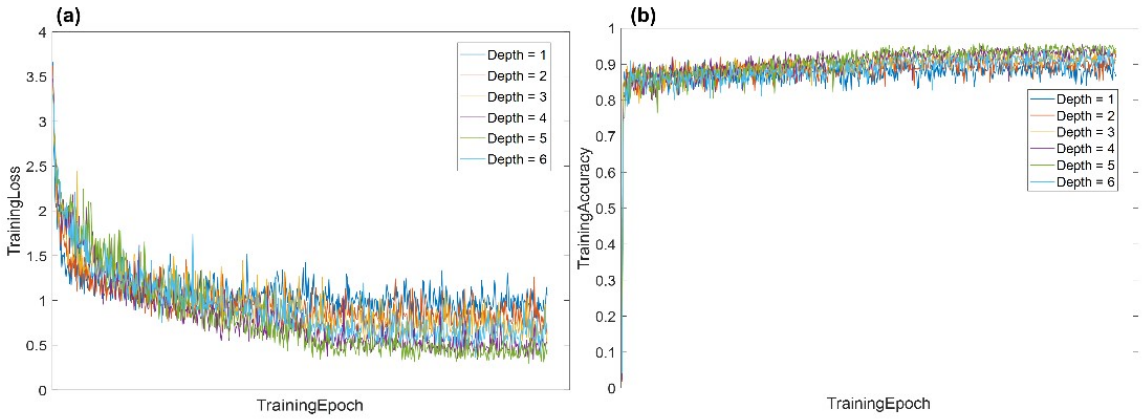

Figure 3-10: (a) Training loss and (b) training accuracy as a function of the training epoch for SegNets with different depths.

We believe that the proposed deep learning algorithm is well suited to real-time

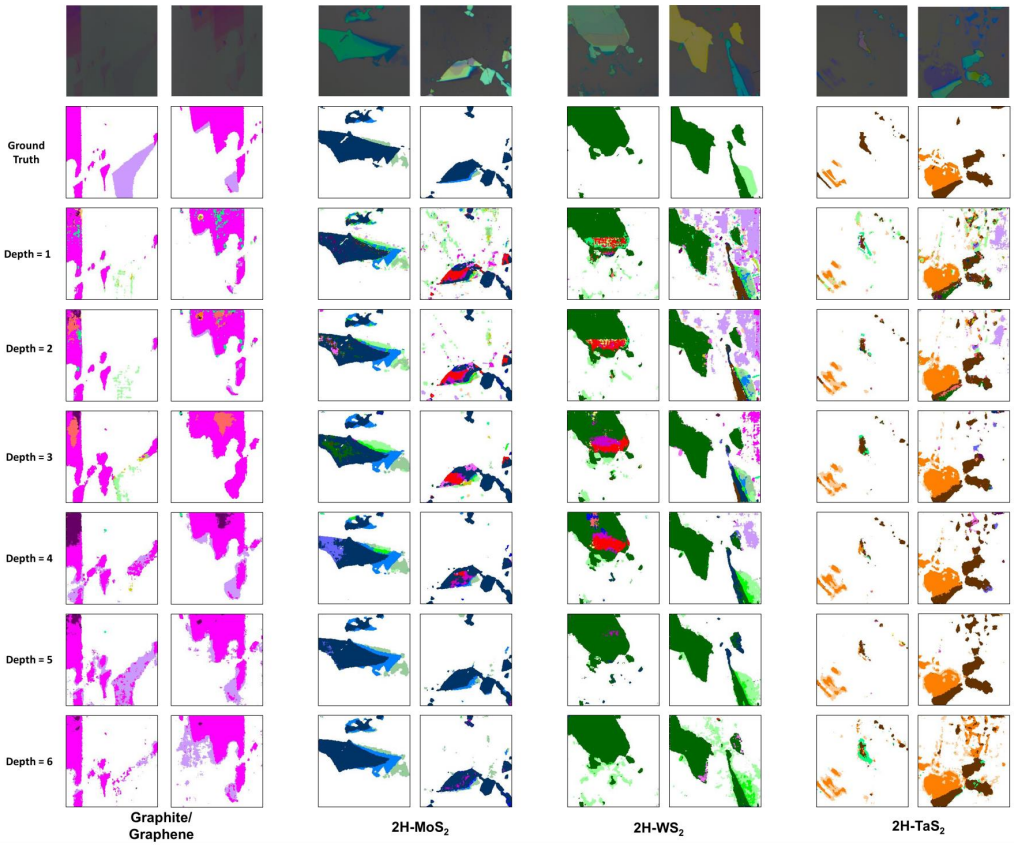

Figure 3-11: Example training results for networks with different depths.

processing according to the metrics given in Table 3.2. With our computing environment, the training process for the VGG16 SegNet requires 9 hours with a GPU, whereas the testing speed can be as high as 3 frames per second (fps) using a CPU, and 20 fps using a GPU for the 224-by-224-pixel test images. This means the SegNet, once properly trained, can be easily adapted to standard desktop computers and integrated with optical microscopes with automatic scanning stages for fast or even real-time identification.

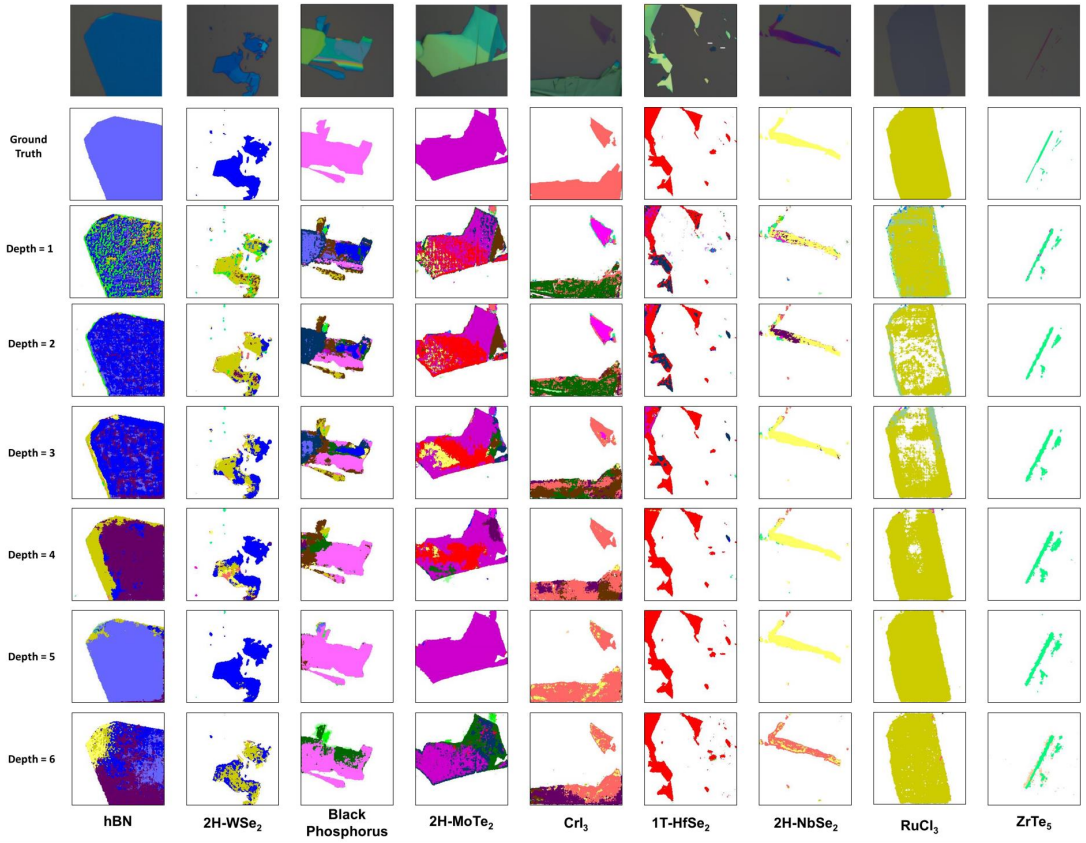

Figure 3-12: Example training results for networks with different depths (continued).

3.3 Deep Graphical Feature Extraction and Material Property Prediction

3.3.1 Understanding the Deep Learning Algorithm

To understand how the SegNet extracts features from 2D material OM images, we analyzed the output feature maps of all the layers in the trained network for the OM images in the test dataset as the inputs. As a demonstration, we used a typical image of graphite/graphene (shown in Figure 3-13 (a)) as the input. The corresponding convolutional feature maps of all the layers in the encoder, decoder, and output sections of the SegNet are summarized in Figure 3-13 (b)-(d). Taking the convolutional feature maps in the encoder as an example (Figure 3-13 (b)), we can clearly see that Depth=1 feature maps are highly correlated to color and contrast information. In

this shallow layer, the background and monolayer region of graphene are not easily separable because of the weak contrast between the two classes, whereas multilayer graphene region is already quite distinguishable. In Depth=2 feature maps, more boundary characteristics are detected, and the edges of graphene monolayer regions start to stand out in some of the feature maps. With the increase of the depth, the size of each feature map becomes smaller because of the pooling layers in the network, and the receptive field of each convolutional kernel (the area in the input image each neuron in the current layer can respond to) becomes relatively larger, which leads to a higher level abstraction of the global graphical features. For instance, Figure 3-13 (e) displays the most prominent feature map (channel #153) of the Depth=5 encoder layer with the largest activation value. It is observed that this feature map is highly correlated to the monolayer graphene region. By feeding the network with more test images as summarized in Figure 3-22, we further confirmed that channel #153 is sensitive to pink/ light purple flakes with smooth edges and regular shapes.

After further analysis on the 512 channels of the Depth=5 encoder layer with more test images randomly chosen from our database, we concluded that the trained SegNet is able to capture deep and subtle graphical features that were overlooked by previously reported optical contrast based approaches [156, 157, 158, 159, 160, 161]. Many of the deep graphical features reflect in part the physical properties of the 2D materials. To illustrate this, we select 14 easily interpreted channels and discuss their associated graphical features and the related physical properties as summarized in Figure 3-14, Table 3.4, as well as Figure 3-15 to Figure 3-28. We divide the graphical features captured by these channels into four broad categories: (1) contrast or color, (2) edge or gradient, (3) shape, and (4) flake "size". Figure 3-14 shows the heat maps of several channels that belong to each category. In particular, channels #153, #389 and #457 under the "contrast/color" category (Figure 3-14 (b)) are sensitive to flakes with purple/pink, yellow/green/gray and dark purple/dark blue colors, respectively; channels #13 and #465 under the "edge" category (Figure 3-14 (c)) reveal bottom and right edges, respectively; channels #153, #206 and #490 under the "shape" category (Figure 3-14 (e)) are indicators of shapes with edges at 60/120 degree angles, acute

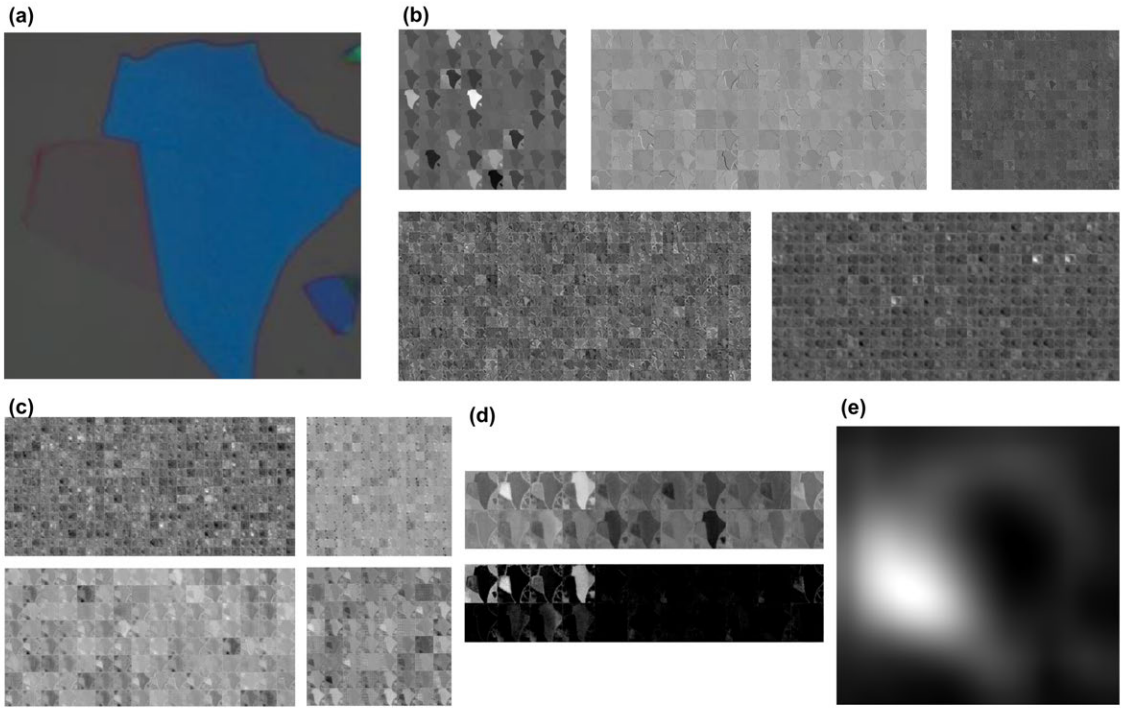

Figure 3-13: Feature maps in the trained SegNet. (a) the input OM image. (b) Depth=1 to 5 encoder layers. (c) Depth = 5 to 2 decoder layers. (d) The last decoder layers (conv. and ReLU layer). (e) Channel # 153 feature map of the Depth=5 encoder layer.

angles shapes and slender shapes; and channels #76 and #138 under the "flake size" category (Figure 3-14 (f)) capture small or fragmentary flakes. Table 3.4 and Figure 3-15 to Figure 3-28 provide more details about the typical images, their corresponding heat maps as well as the extracted graphical features of the 14 channels. Note that some channels can only respond to images that meet a combinational criterion under multiple categories, whereas some channels can be sensitive to several different scenarios. For example, channel #13 only shows high intensities in the heat map around the bottom edges of purple or pink flakes (Figure 3-16), and channel #470 can be used to identify both non-uniform, thick flakes and uniform, thin, pale-purple flakes (Figure 3-27).

Table 3.4: A summary of selected channels and their interpretations in the Depth=5 encoder layer of the trained SegNet.

Ch.#	**Case**	**Contrast/Color**	**Edge**	**Shape**	**Flake Size**
#8	–	Purple/pink/dark blue			
#13	–	Purple/pink	Bottom edges		
#69	Case 1				Fragmentary
	Case 2			Acute angle	
	Case 3	Non-uniform			
#76	Case 1				Fragmentary
	Case 2			Slender	
#103	Case 1	Purple/pink			Small
	Case 2			Slender	
#129	Case 1	Purple/pink	All edges		
	Case 2	Purple/pink		Slender	
#138	–				Small/ Fragmentary
#153	–	Purple/pink	Straight/ smooth edges	60°/120° angles	
#206	–	Purple/blue		Acute Angle	
#389	–	Yellow/green/ gray			
#457	–	Dark purple/ dark blue			
#465	–		Right edges		
#470	Case 1	Non-uniform			
	Case 2	Pale purple			
#490	–			Slender	

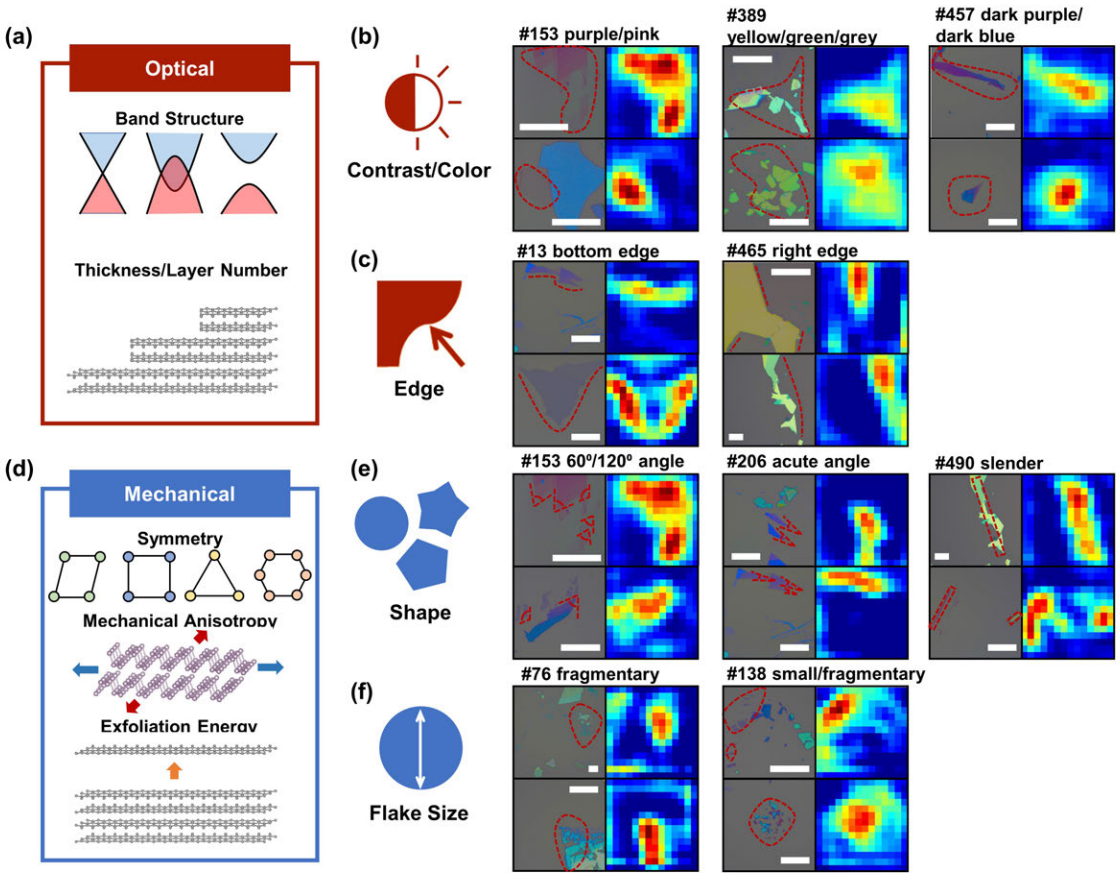

Figure 3-14: Deep graphical features captured by the SegNet. (a) schematics of the physical properties such as the band structure and the thickness that determine the optical responses of the 2D flakes. (b) Contrast/color and (c) edge and typical feature maps in the Depth=5 layer of the SegNet that are associated with the optical responses. (d) schematics of the physical properties such as the crystal symmetry, the mechanical anisotropy and the exfoliation energy that determine the mechanical responses of the 2D flakes. (e) flake shape and (f) flake size and typical feature maps in the Depth=5 layer of the SegNet that are correlated to the mechanical properties of the materials. The high-activation regions in the feature maps are also indicated by red dashed curves in the corresponding OM images. Scale bars: 20 μm.

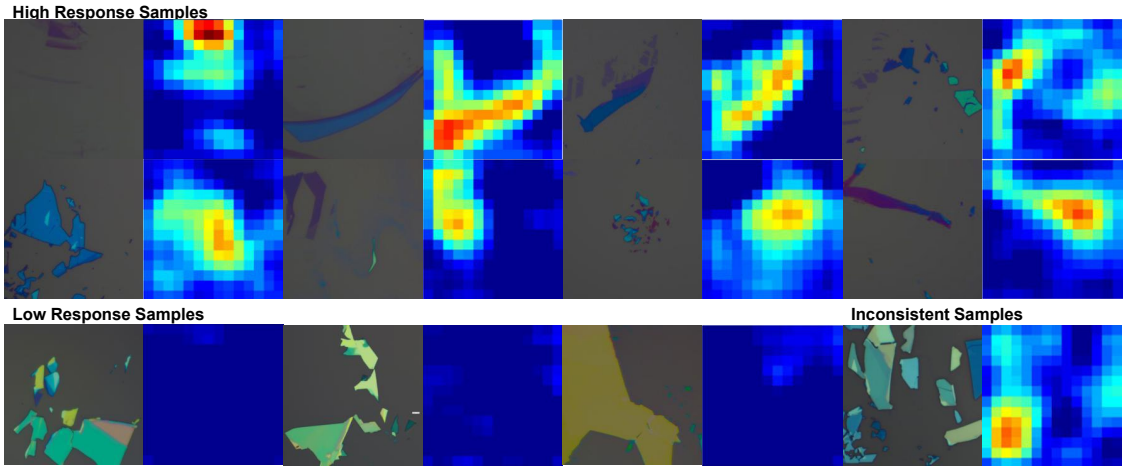

Figure 3-15: Represented optical images and their corresponding feature maps of Channel #8 of the Depth=5 encoder layer.

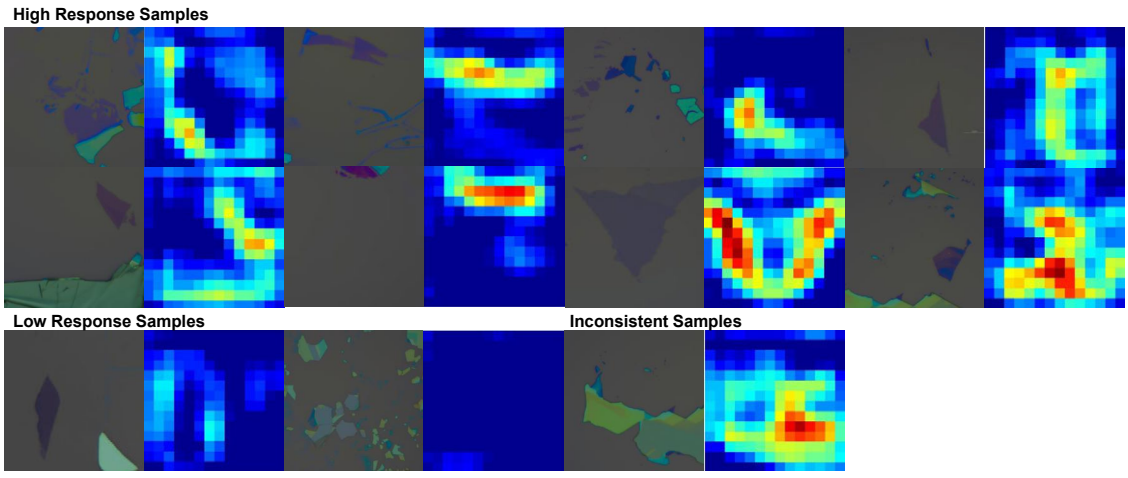

Figure 3-16: Represented optical images and their corresponding feature maps of Channel #13 of the Depth=5 encoder layer.

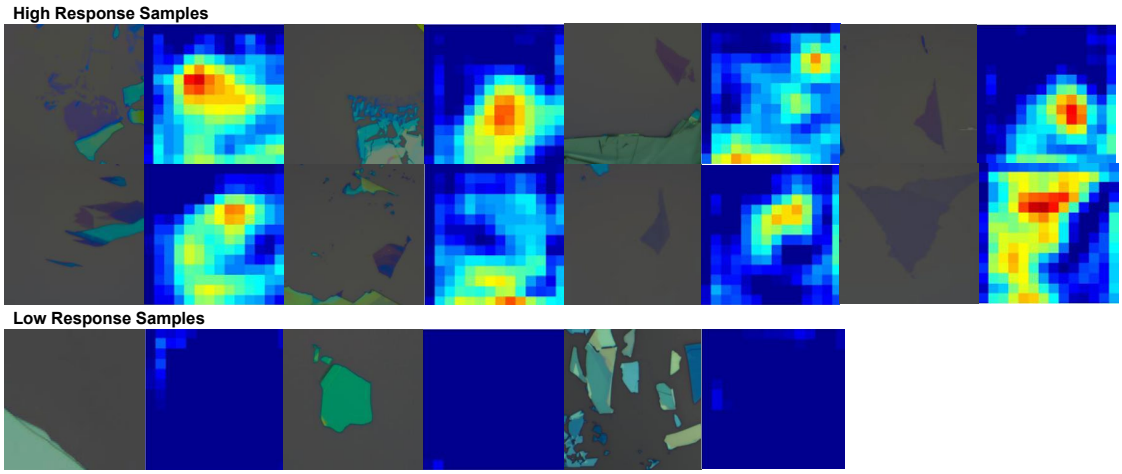

Figure 3-17: Represented optical images and their corresponding feature maps of Channel #69 of the Depth=5 encoder layer.

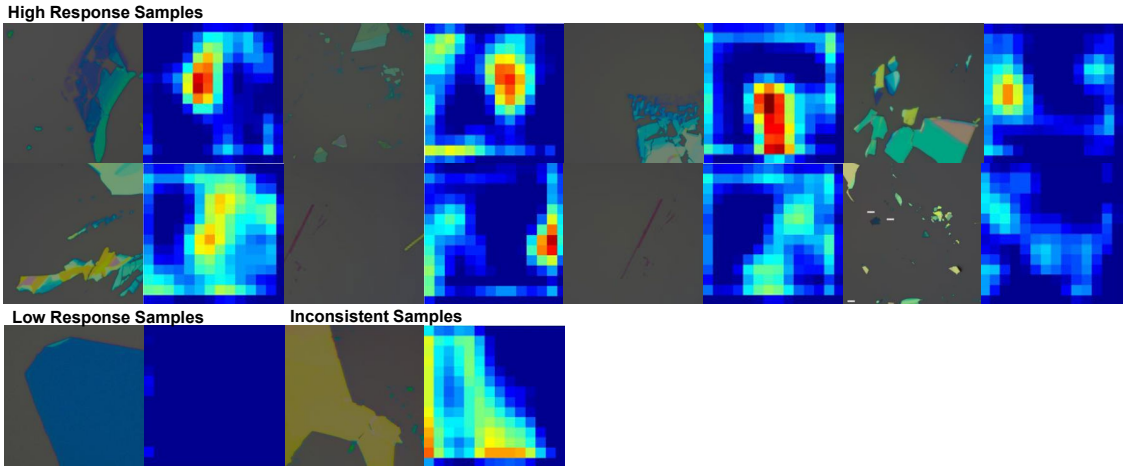

Figure 3-18: Represented optical images and their corresponding feature maps of Channel #76 of the Depth=5 encoder layer.

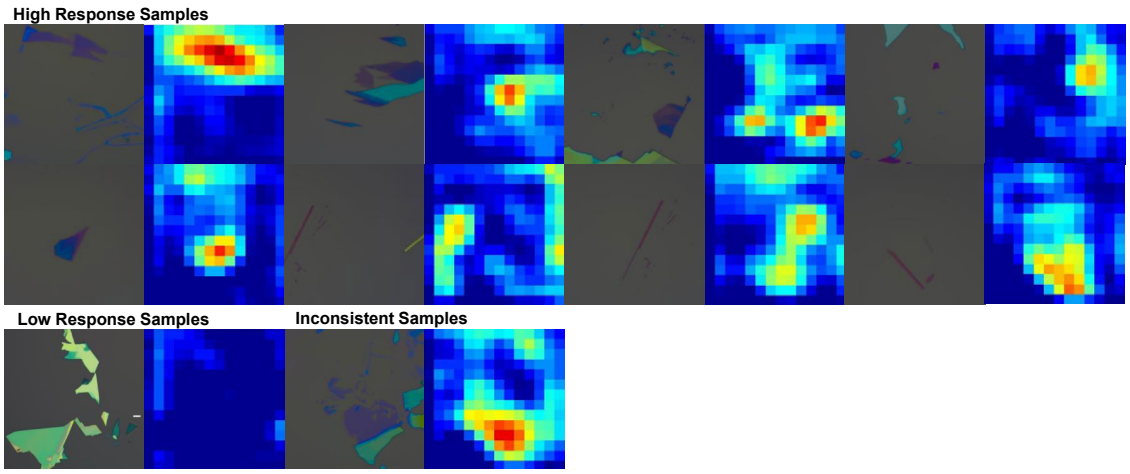

Figure 3-19: Represented optical images and their corresponding feature maps of Channel #103 of the Depth=5 encoder layer.

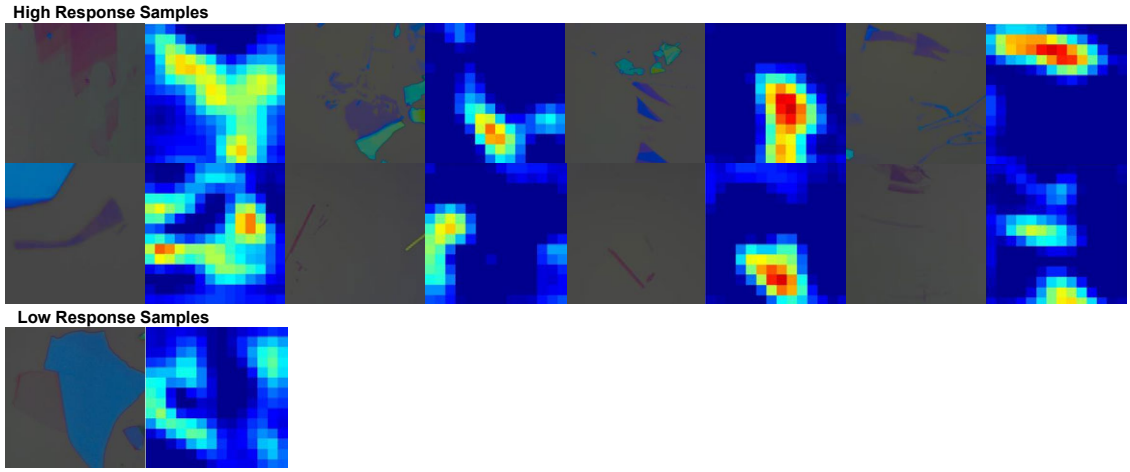

Figure 3-20: Represented optical images and their corresponding feature maps of Channel #129 of the Depth=5 encoder layer.

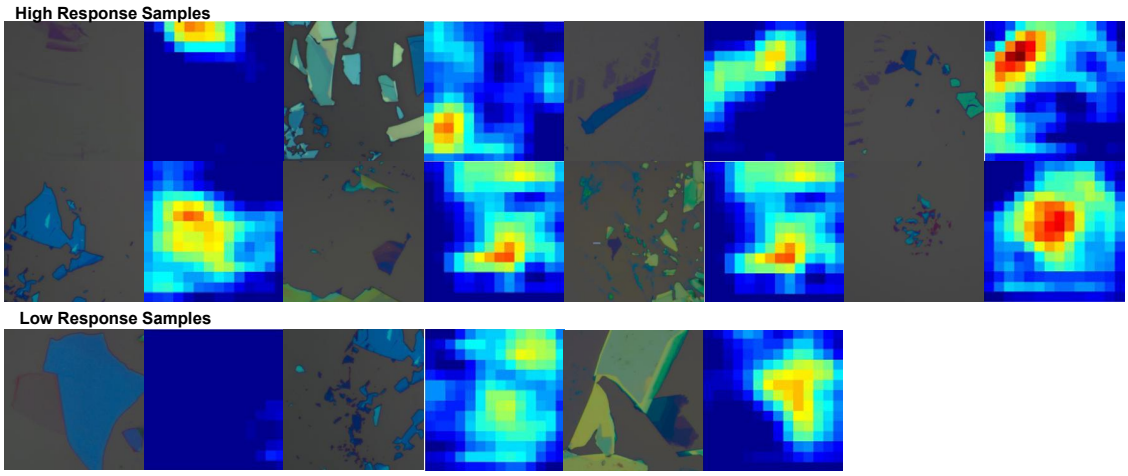

Figure 3-21: Represented optical images and their corresponding feature maps of Channel #138 of the Depth=5 encoder layer.

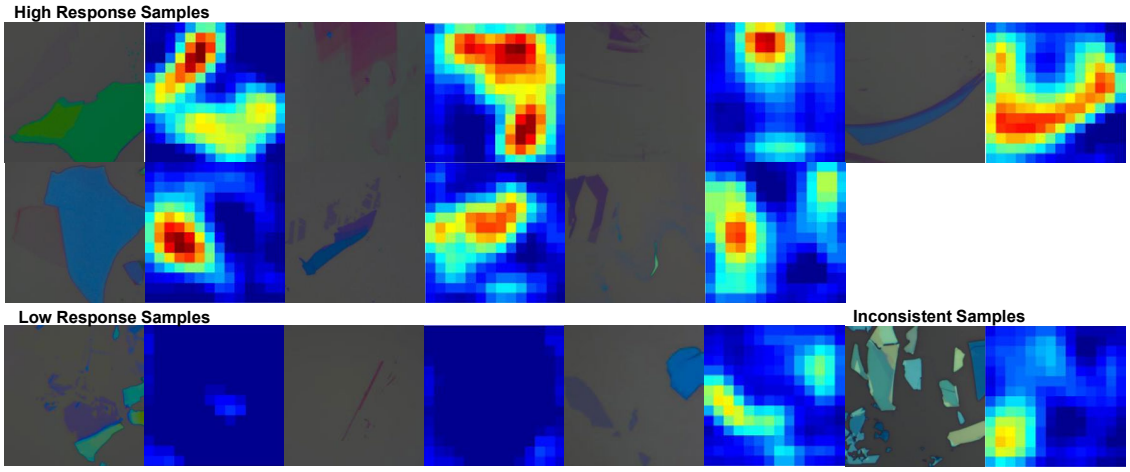

Figure 3-22: Represented optical images and their corresponding feature maps of Channel #153 of the Depth=5 encoder layer.

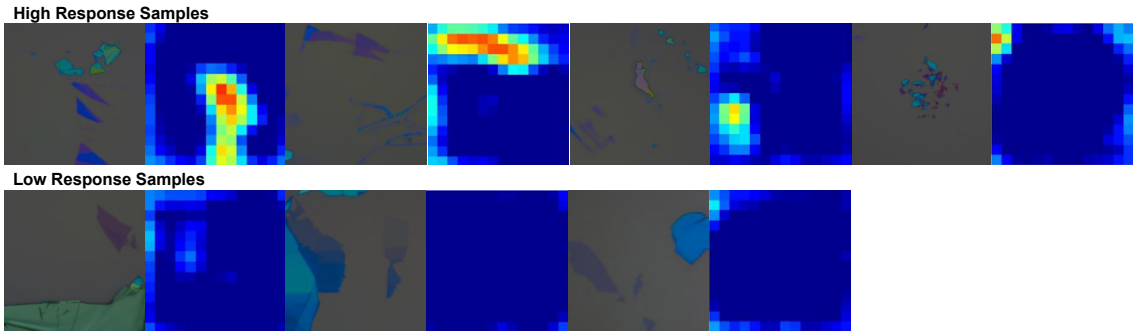

Figure 3-23: Represented optical images and their corresponding feature maps of Channel #206 of the Depth=5 encoder layer.

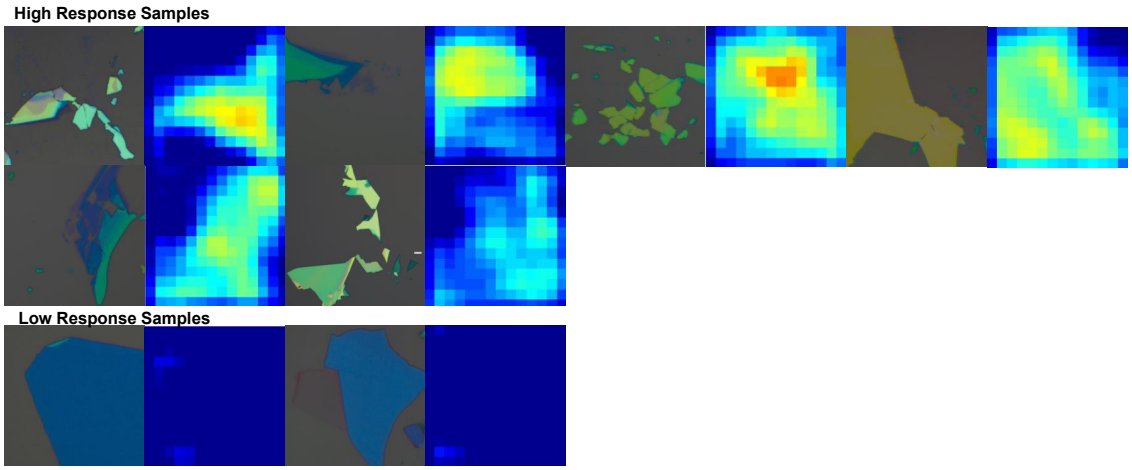

Figure 3-24: Represented optical images and their corresponding feature maps of Channel #389 of the Depth=5 encoder layer.

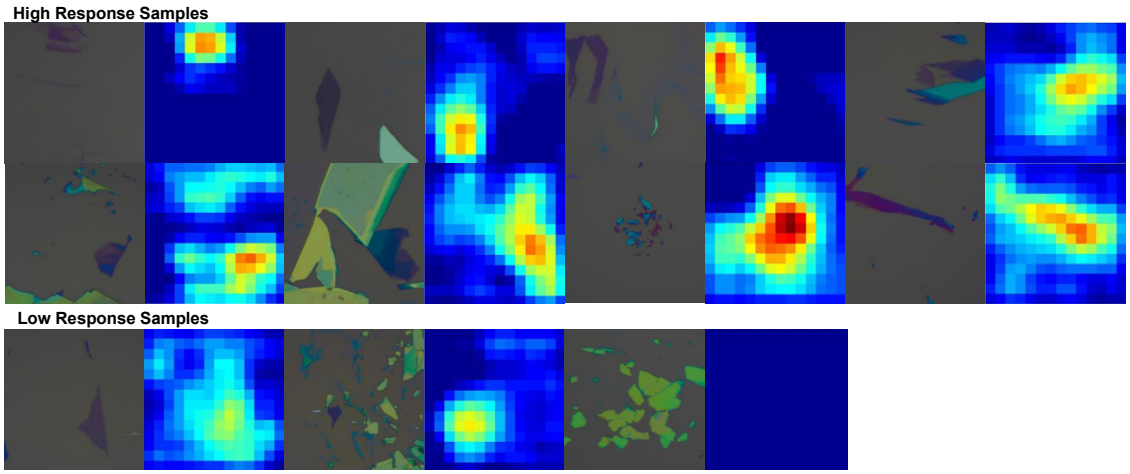

Figure 3-25: Represented optical images and their corresponding feature maps of Channel #457 of the Depth=5 encoder layer.

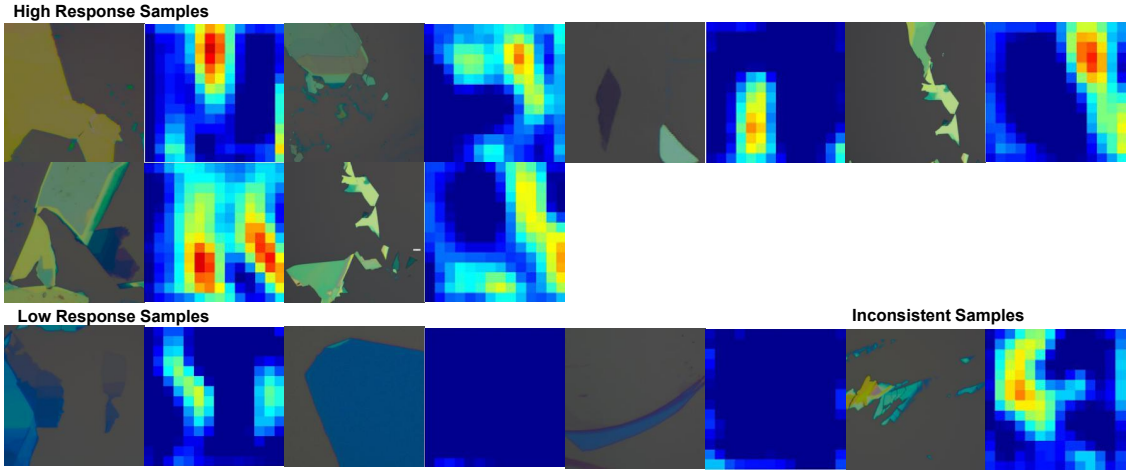

Figure 3-26: Represented optical images and their corresponding feature maps of Channel #465 of the Depth=5 encoder layer.

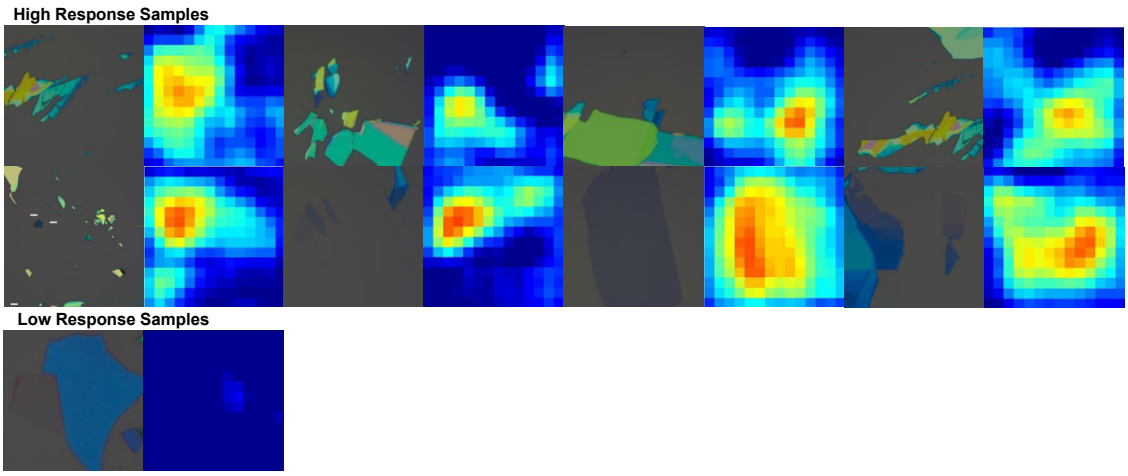

Figure 3-27: Represented optical images and their corresponding feature maps of Channel #470 of the Depth=5 encoder layer.

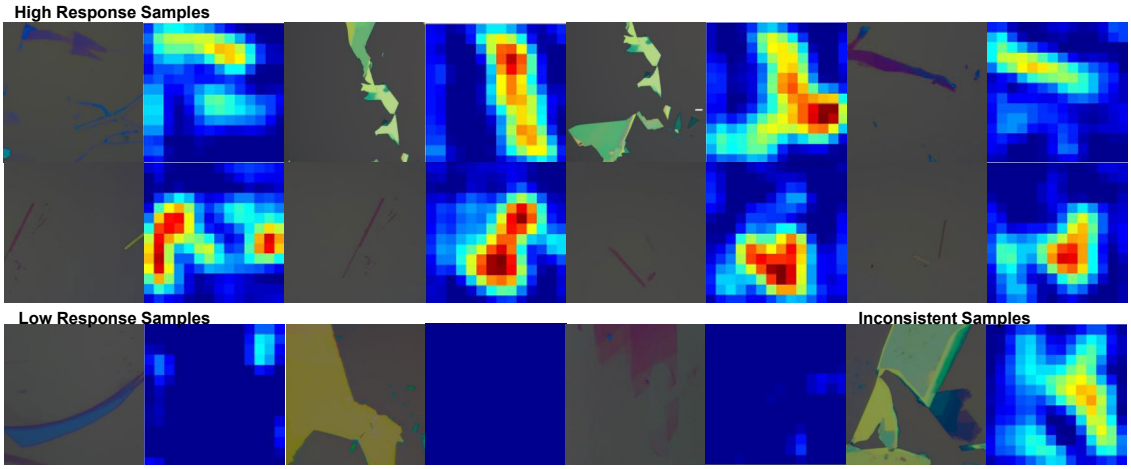

Figure 3-28: Represented optical images and their corresponding feature maps of Channel #490 of the Depth=5 encoder layer.

3.3.2 Prediction of Material Properties

The above feature map analysis has provided a better understanding about how deep graphical features can be extracted by the SegNet for more accurate and generic optical identification of exfoliated 2D materials. However, the algorithm is not limited to this particular task, and we found that it can be used for more advanced optical characterization tasks such as the prediction of material properties. The graphical features captured by the network are correlated to the optical and mechanical proper-

ties of the material. As shown schematically in Figure 3-14 (a), the contrast/color and the edge features are determined by the optical response of the material, which reflect the electronic band structures and the thicknesses of the flakes. In addition, because the samples were made through mechanical exfoliation, the typical distribution of shapes and sizes of the flakes depends heavily on the mechanical properties of the materials, such as the crystal symmetry, mechanical anisotropy and the exfoliation energy (Figure 3-14 (d)). We can thus use the trained network with the knowledge of the 13 materials to predict properties of unstudied materials.

To demonstrate the SegNet's capability of predicting physical properties of unknown 2D materials, we also fed the trained SegNet with additional OM images of new 2D materials that were not used in the training dataset, and calculated the "extended" confusion matrix as shown in Figure 3-29. The new materials include 2H-$MoSe_2$, 1T'-$MoTe_2$, Td-WTe_2, ReS_2, SnS_2, $SnSe_2$, GeSe, SnSe, GaS, $CrCl_3$, $CrBr_3$, $MnPS_3$, $FePS_3$, TiS_3, ZrS_3, Bi_4I_4 and Ta_2Se_8I. The row vectors in the extended confusion matrix can be used to characterize how similar the physical properties of one material are to the 13 known materials. As we can see, different vector components in the similarity vectors (or columns of the extended confusion matrix) have distinct values for each of the untrained materials, from which we can immediately summarize some qualitative patterns. For example, GaS, CrI_3, $CrBr_3$ and $MnPS_3$ in the untrained material group shows high similarity to hBN in the trained material group, which matches the fact that these materials are wide-bandgap semiconductors or insulators with the band gaps higher than 2.5 eV and are mostly transparent in the infrared, red and green spectral ranges. As another example, 1T'-$MoTe_2$ and Td-WTe_2 in the untrained material group are predicted to be similar to 1T-$HfSe_2$ in the trained material group, which is in accordance with the similar crystal structure of these materials.

For a more quantitative analysis, we can construct physical property predictors based on the extended confusion matrix. One simple way is to project the "similarity" vectors in a set of base vectors that are correlated to the physical property of interest. We can define each base vector as the average of the vectors of the known materials

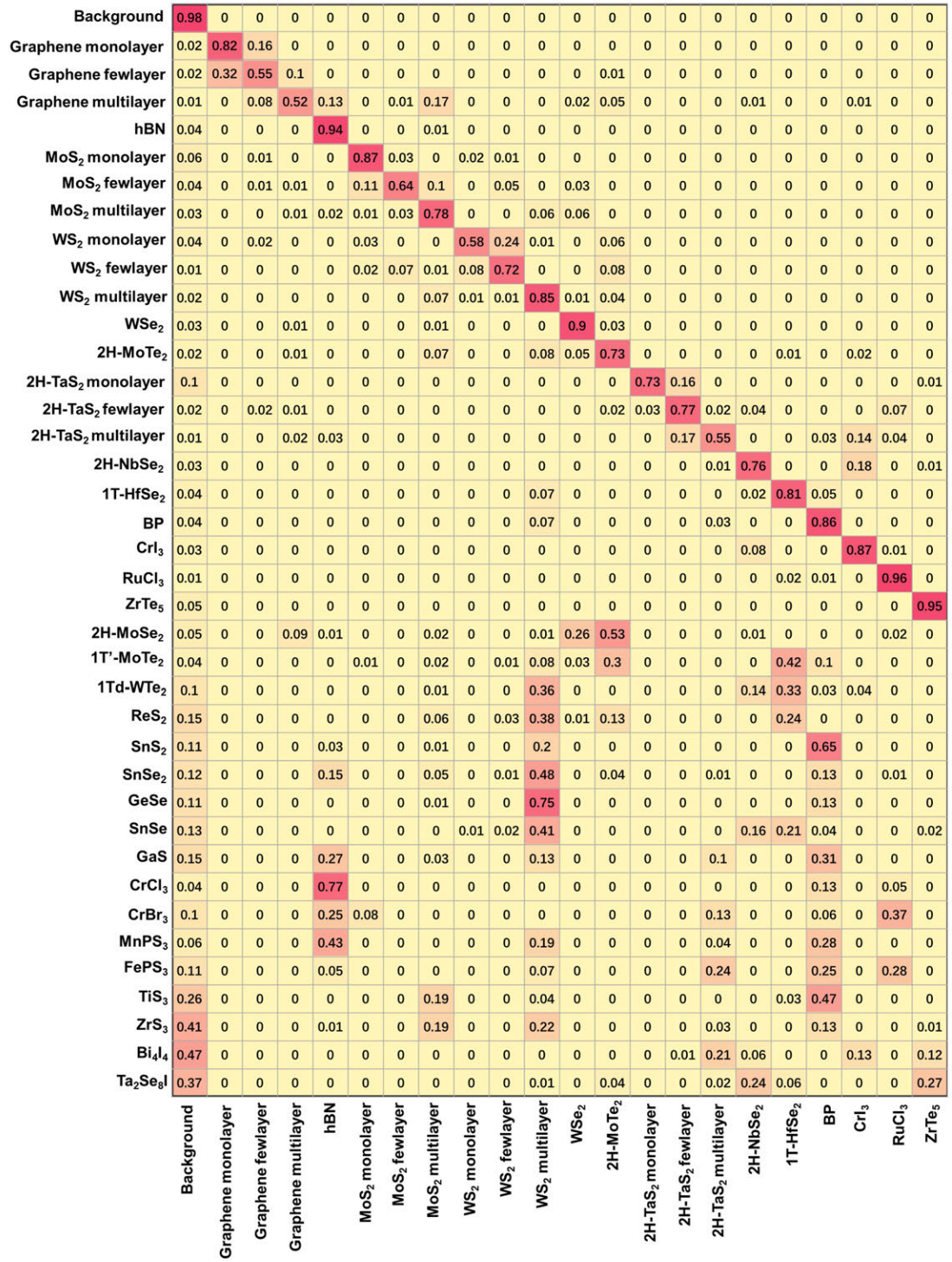

Figure 3-29: Extended confusion matrix.

that have the same value or range of the physical property of interest, expressed as

$$\mathbf{v}_k = \frac{1}{\|\mathbf{M}_k\|} \sum_{x \in \mathbf{M}_k} \mathbf{v}_x \tag{3.1}$$

where $\mathbf{v}_k$ is the base vector of the k-th class in the material property predictor; $\mathbf{v}_x$ is the base vector of the material x in the training set; $\mathbf{M}_k$ is the subset of materials in the training set that have matched criteria of the physical properties in the k-th class in the predictor; and $\|\mathbf{M}_k\|$ is the number of materials in the $\mathbf{M}_k$ subset.

We selected two different predictors that are associated with the band gaps and the crystal structures of the material. For the band gap predictor, the base vector subsets are $\mathbf{M}_1$={Graphene/Graphite, 2H-TaS_2, 2H-$NbSe_2$, $ZrTe_5$, bP, 2H-$MoTe_2$, 1T-$HfSe_2$, $RuCl_3$, CrI_3}, $\mathbf{M}_2$={2H-MoS_2, 2H-WSe_2, 2H-WS_2}, $\mathbf{M}_3$={hBN}; for the crystal structure predictor, the base vector subsets are $\mathbf{M}_1$={Graphene/Graphite, hBN, 2H-MoS_2, 2H-WSe_2, 2H-WS_2, 2H-$MoTe_2$, 2H-TaS_2, 2H-$NbSe_2$}, $\mathbf{M}_2$={1T-$HfSe_2$}, $\mathbf{M}_3$={bP}, $\mathbf{M}_4$={ $RuCl_3$, CrI_3}, $\mathbf{M}_5$={$ZrTe_5$}. A summary of physical properties of the 2D materials being used in this study can be found in Table 3.5 and Table 3.6.

Table 3.5: A summary of the physical properties of the 2D materials (bulk) used in the training set of this study.

Material	**Crystal System**	**Point Group**	**Space Group**	**Bandgap (Optical)**	**Exfoliation Energy**
graphite	Hexagonal	D_{6h}	P6/mmm	0 eV	70.36 meV
hBN	Hexagonal	D_{6h}	$P6_3/mmm$	~6 eV	71.34 meV
2H-MoS_2	Hexagonal	D_{6h}	$P6_3/mmm$	1.8 eV	76.99 meV
2H-WS_2	Hexagonal	D_{6h}	$P6_3/mmm$	2.1 eV	76.27 meV
2H-WSe_2	Hexagonal	D_{6h}	$P6_3/mmm$	1.7 eV	79.63 meV
2H-$MoTe_2$	Hexagonal	D_{6h}	$P6_3/mmm$	1.1 eV	90.98 meV
2H-TaS_2	Hexagonal	D_{6h}	$P6_3/mmm$	0 eV	87.15 meV
2H-$NbSe_2$	Hexagonal	D_{6h}	$P6_3/mmm$	0 eV	98.28 meV
1T-$HfSe_2$	Trigonal	D_{3d}	$P\bar{3}m1$	1.1 eV	92.05 meV
bP	Orthorhombic	D_{2h}	Cmce	0.35 eV	111.62 meV
CrI_3	Monoclinic	C_{2h}	C2/m	1.2 eV	–
$RuCl_3$	Monoclinic	C_{2h}	C2/m	0.3 eV	–
$ZrTe_5$	Orthorhombic	D_{2h}	Cmcm	0 eV	90.00 meV

Note: The values for the optical bandgap the direct bandgap, or the lowest peak energy in the optical absorption spectra. Data source: Refs [165, 166, 167, 168, 169, 170, 171, 172, 173, 174, 175, 176, 177, 178, 179, 180, 181].

Table 3.6: A summary of the physical properties of the 2D materials (bulk) used in the prediction set of this study.

Material	**Crystal System**	**Point Group**	**Space Group**	**Bandgap (Optical)**	**Exfoliation Energy**
2H-$MoSe_2$	Hexagonal	D_{6h}	$P6_3/mmm$	1.5 eV	80.24 meV
1T'-$MoTe_2$	Monoclinic	C_{2h}	$P2_1/m$	0 eV	86.87 meV
Td-WTe_2	Orthorhombic	C_{2v}	$Pmn2_1$	0 eV	–
GeSe	Orthorhombic	D_{2h}	Pnma	2.1 eV	–
SnSe	Orthorhombic	D_{2h}	Pnma	1.3 eV	152.65 meV
$CrBr_3$	Monoclinic	C_{2h}	C2/m	3.2 eV	–
$CrCl_3$	Monoclinic	C_{2h}	C2/m	3.1 eV	69.52 meV
Bi_4I_4	Monoclinic	C_{2h}	C2/m	0.04 eV	77.69 meV
Ta_2Se_8I	Tetragonal	D_4	I422	0 eV	–
GaS	Hexagonal	D_{6h}	$P6_3/mmc$	2.5 eV	56.22 meV
ReS_2	Triclinic	C_i	$P\bar{1}$	1.4 eV	71.00 meV
SnS_2	Trigonal	D_{3d}	$P\bar{3}m1$	2.4 eV	83.28 meV
$SnSe_2$	Trigonal	D_{3d}	$P\bar{3}m1$	1.6 eV	93.47 meV
$MnPS_3$	Monoclinic	C_{2h}	C2/m	2.8 meV	–
$FePS_3$	Monoclinic	C_{2h}	C2/m	1.5 meV	–
TiS_3	Monoclinic	C_{2h}	$P2_1/m$	1.1 eV	54.49 meV
ZrS_3	Monoclinic	C_{2h}	$P2_1/m$	2.5 eV	55.49 meV

Note: The values for the optical bandgap the direct bandgap, or the lowest peak energy in the optical absorption spectra. Data source: Refs [165, 166, 167, 168, 169, 170, 171, 172, 173, 174, 175, 176, 177, 178, 179, 180, 181].

The projected values of each material based on these two predictors are plotted into a histogram and summarized in Figure 3-30 and Figure 3-31, respectively. Clear correlations between the projected values and the true physical parameters (band gap in Figure 3-30, and crystal structure in Figure 3-31) are found. We can thus use the projected values as an indication of the probability of the physical property of interest

of an unknown material belonging to each classes (represented by each base vector of the corresponding predictor). Note that there are also misclassified instances, which we believe can be improved by expanding the training data set in terms of both the number of images and the number of materials. This method can potentially be used for systematic studies of other factors such as the effect of different mechanical exfoliation techniques, bulk crystal qualities, and so on.

3.4 Transfer Learning

Finally, we demonstrate that the trained SegNet can be adapted for different applications through transfer learning. The basic idea is to use the trained SegNet as the initialization for the new training problem rather than a random initialization. With this approach, we are able to train the SegNet for new optical identification/characterization problems with minimal extra computation time and data for the training. Here we use OM images of graphene synthesized by chemical vapor deposition (CVD) as a demonstration. We only labeled 5 OM images of CVD grown graphene, and generate 600 images (224 by 224 pixels) by data augmentation. We divided the graphene region into five classes based on its layer number (from monolayer to 5-layers). We varied the size of the training dataset from 30 to 360, and sampled randomly from the 600 images. For the transfer learning, the initial weights in the network before the training are taken from the pretrained SegNet (trained with the 13 exfoliated 2D materials) as compared to the conventional random initialization strategy. Figure 3-32 (a) shows the test images, the ground truth label maps as well as the corresponding prediction results after the training with the transfer learning approach. As we can see, the prediction results match the ground truths very well. To compare the pre-training transfer learning approach with the conventional approach with random initialization, we plot the global test accuracy of networks trained with both approaches as a function of the number of OM images in the training data set as shown in Figure 3-32 (b). Representative test images and their predictions can be found in Figure 3-33. With the pre-training approach, we were able to achieve 65%

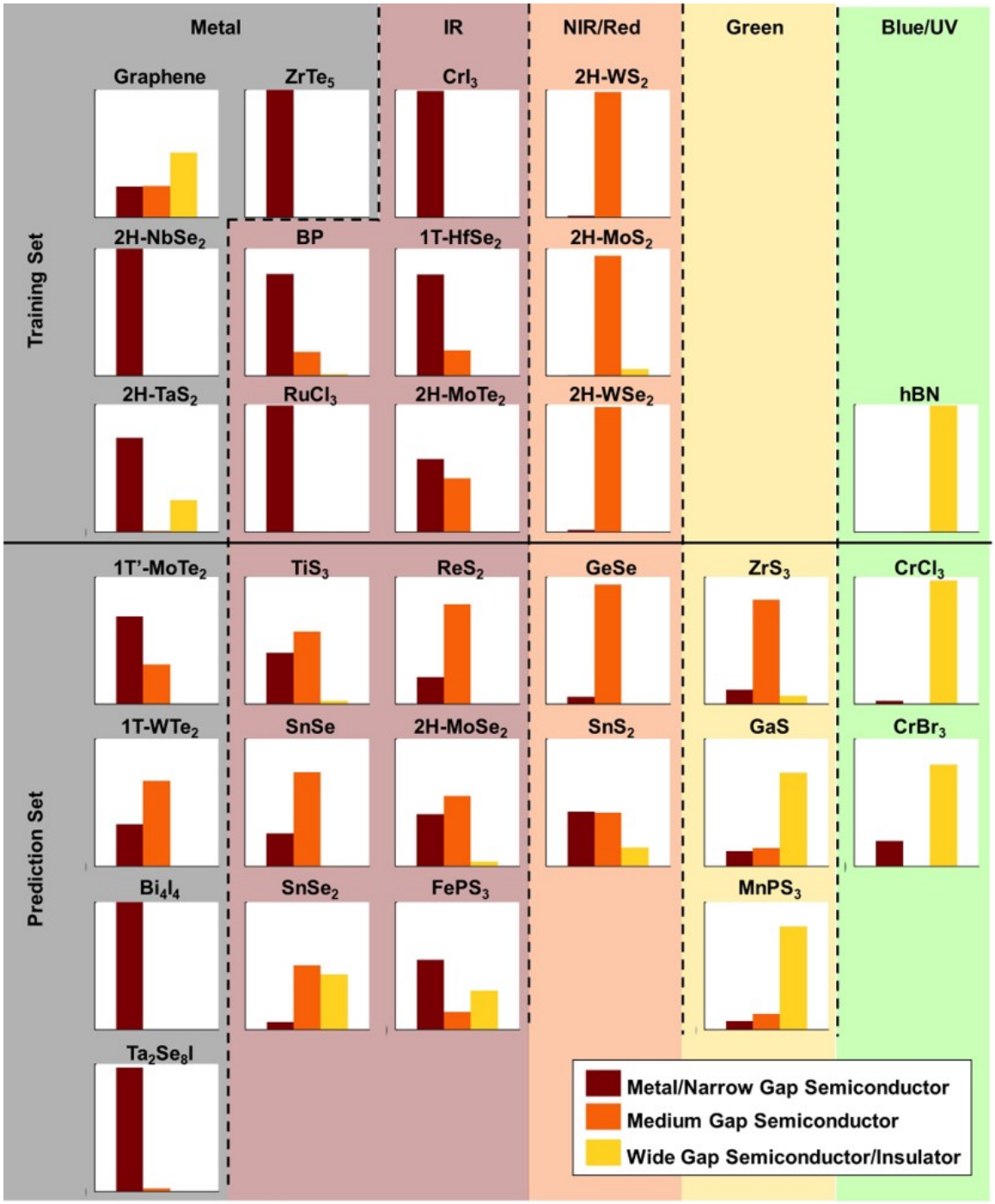

Figure 3-30: Prediction of optical bandgaps based on the similarity vectors produced by the SegNet. The histograms are the projected values of the materials in the training set (top half) and in the prediction set (bottom half, unused when training the SegNet) that predict the bandgap of the materials.

global accuracy with only 30 training images, whereas at least 60 images are required for the conventional random initialization approach to reach comparable accuracy.

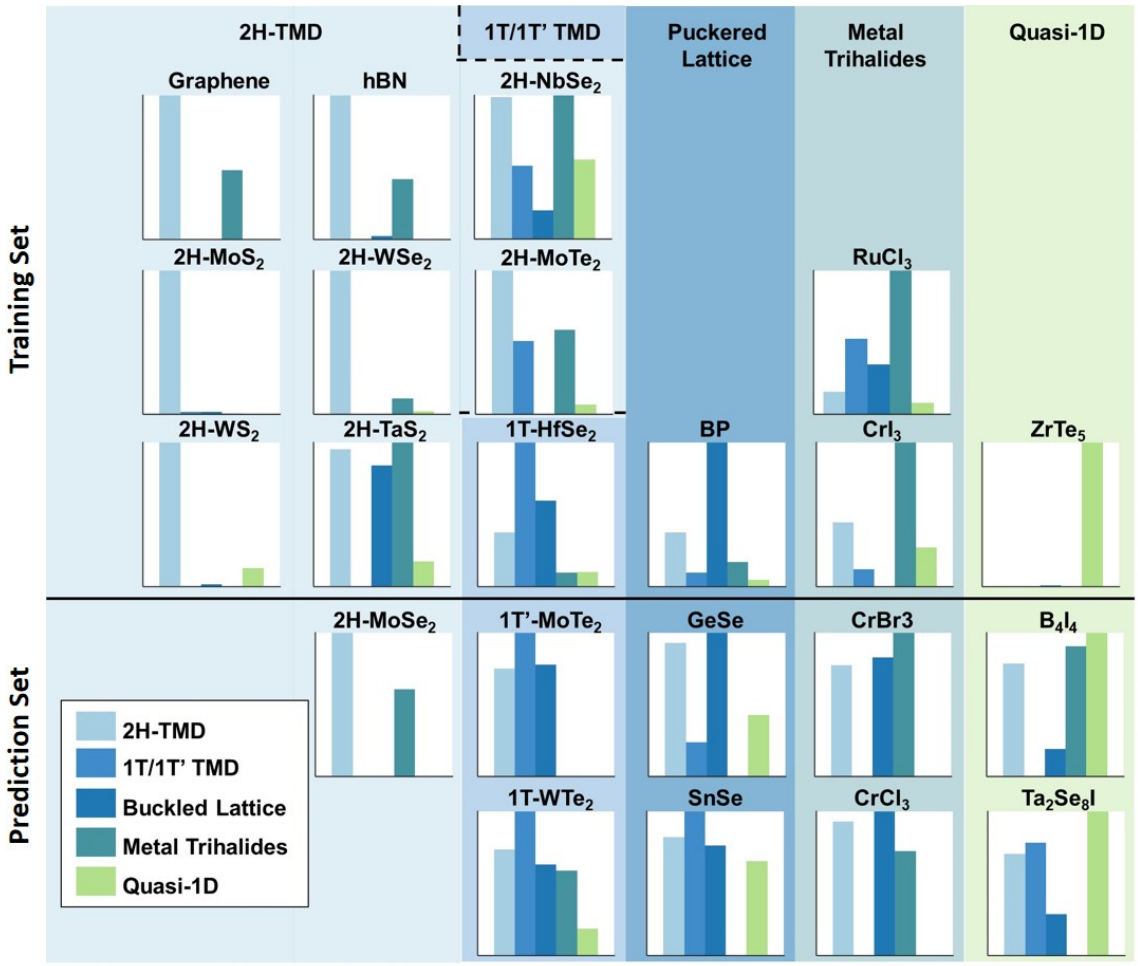

Figure 3-31: Prediction of crystal structures based on the similarity vectors produced by the SegNet. The histograms are the projected values of the materials in the training set (top half) and in the prediction set (bottom half, unused when training the SegNet) that predict the crystal structures of the materials.

3.5 Summary

In summary, we developed for the first time a deep learning algorithm for the optical characterization of 2D materials and the extraction of deep graphical features from optical microscopic images that can be used for anticipating material properties. We set up a encoder-decoder semantic segmentation neural network ("SegNet") for identification and characterization of exfoliated 2D materials from optical microscopic images. After training, the neural network can achieve rapid characterization of material identities, their thicknesses and physical properties with >95% global accuracy,

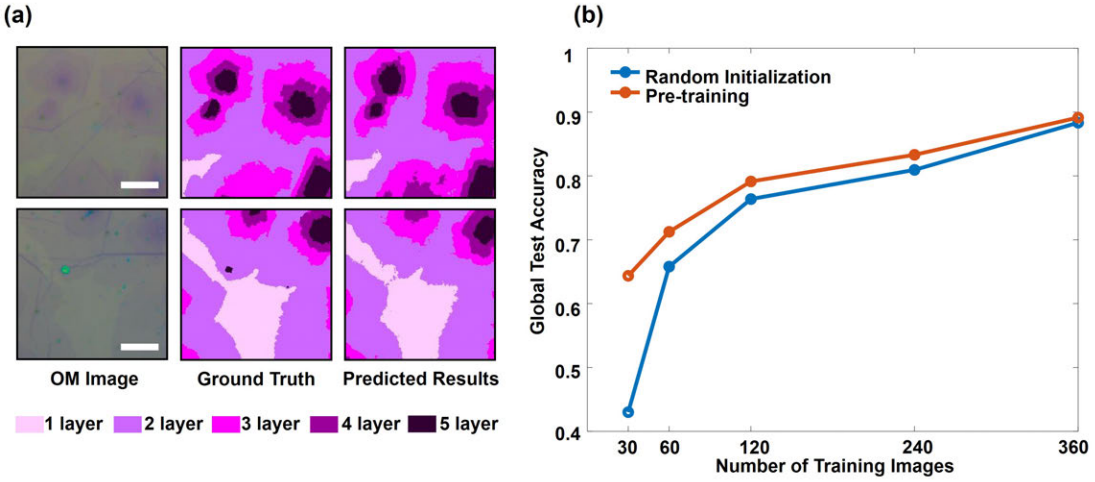

Figure 3-32: Transfer learning for CVD graphene. (a) Typical training results with 360 images in the training dataset. The left column are OM images, the middle column are the ground truth label maps, and the right column are the label maps predicted by the re-trained SegNet. Scale bars: 20 μm. (b) Global test accuracy as a function of the number of images in the training dataset for the pre-training method (red) and the random initialization method (blue).

with a frame rate of 20 fps. A fully automated system utilizing this algorithm can be used to free up tremendous amount of time for researchers. We would like to emphasize that the capability of predicting structural, optical, and mechanical properties of nanomaterials from optical microscopic images in our approach was not possible previously. A systematic analysis was made to understand how the network captures deep graphical features such as color, contrast, edges, shapes and flakes sizes from the optical images. We also demonstrate that the trained network can be adapted for different optical characterization applications with minimal additional training through a transfer learning technique. The proposed methodology can potentially be extended for identification and understanding other morphological or spectroscopic data of diverse nanomaterials.

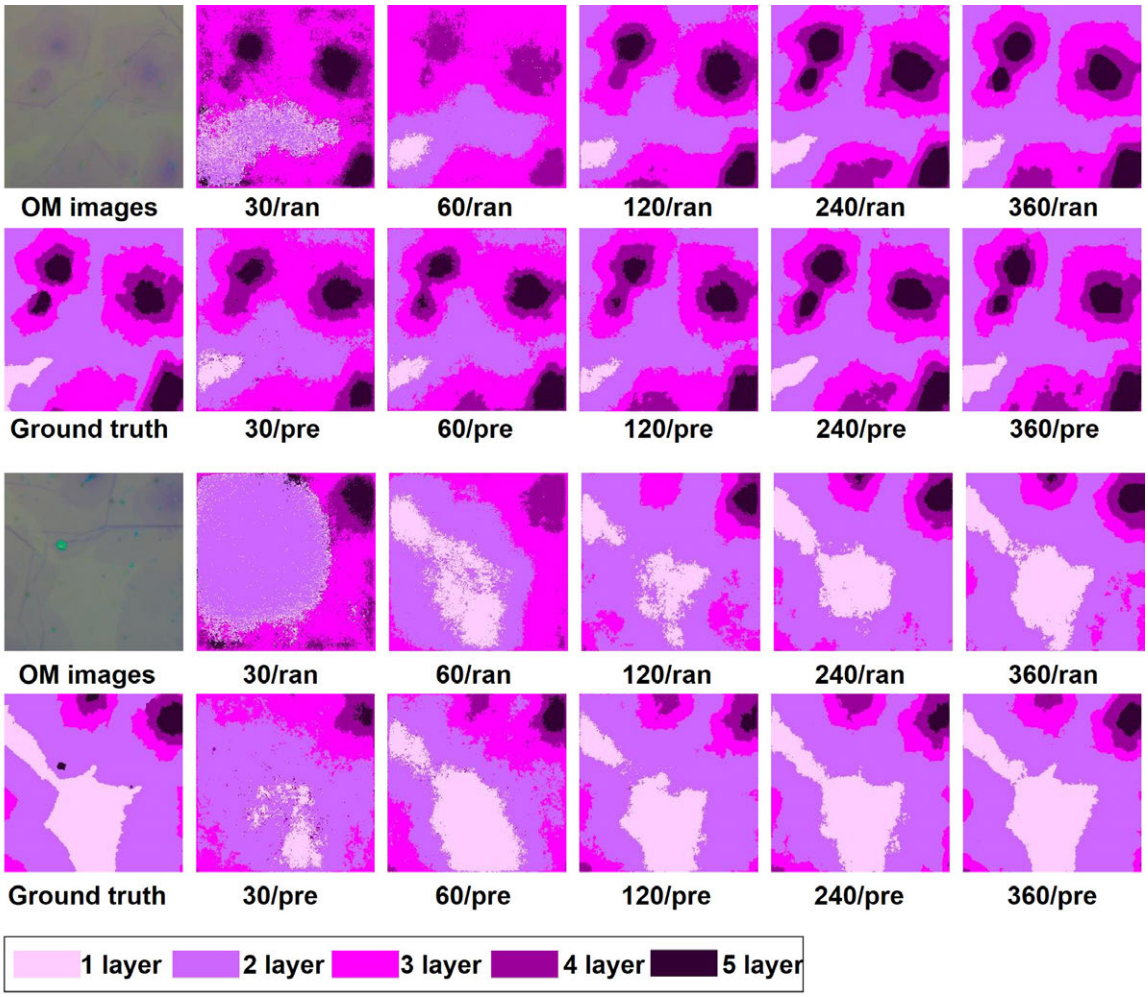

Figure 3-33: Additional transfer learning results for CVD graphene. The number of training images are varied from 30 to 360 for both the pretraining method (pre) and the random initialization (ran).

Chapter 4

Graphene Thermopile

4.1 Principle of Operation

In the visible to near infrared range, the photoresponse of a graphene p-n junction has been proven to be dominated by the hot-electron photothermoelectric (PTE) effect (see chapter 5). In the mid-infrared range, however, the absorption edge is limited to around 5 μm by Pauli blocking for regularly doped graphene (Figure 1-11). Early work has studied the mid-infrared photoresponse of an electrostatically doped graphene p-n junction on a supported dielectric substrate [182, 183]. They concluded that the photoresponse of the graphene p-n junction is dominated by the heating of the substrate and the resulting thermoelectric effect in graphene. The thermoelectric voltage can be expressed as

$$V_{TE} = \Delta S \cdot \Delta T \tag{4.1}$$

where ΔS is the difference of the Seebeck coefficients between the p-type and n-type graphene; ΔT is the temperature increase because of the IR induced heating of the substrate.

As shown in Figure 4-1 (a), a thermopile is composed of an infrared absorber that is suspended from the substrate, a series of thermal arms that connect the absorber and the surrounding, with interleaved p- and n- type graphene channels on top. The

structure is schematically reshaped in Figure 4-1 (b) with geometrical parameters shown below. The graphene channels are parallel in terms of temperature gradient, but connected in series electrically. When IR radiation is present, the IR absorber (dielectric multilayer thin film) is heated up, which can be then probed electrically by the graphene p-n junctions due to the thermoelectric effect. According to Eqs. (1.25) to (1.29), the specific detectivity (D^*), considering the Johnson noise, can be expressed as

$$\begin{aligned} D^* &= \frac{N_j \Delta S \Delta T}{P_{in}\sqrt{\overline{v_J^2}}} \\ &= \left(\frac{ABS}{t}\right) \cdot \left(\frac{\Delta S}{\sqrt{\rho_{2D}}}\right) \cdot \left(\frac{1}{\kappa_{th}}\right) \cdot \left(\frac{L^{1/2} D_{abs}}{N_j^{1/2} W^{1/2}}\right) \sqrt{\frac{1}{32 k_B T}} \end{aligned} \tag{4.2}$$

Here the first term ABS/t is absorbance per thickness, indicating the capability if IR absorption of the absorber; the second term $\Delta S/\sqrt{\rho_{2D}}$ is determined by the electrical or thermoelectric properties of the sensing material, with ρ_{2D} denoting the 2D resistivity or sheet resistance of graphene; the third term $1/\kappa th$ indicates the quality of the thermal isolation, with κ_{th} denoting the thermal conductivity of the thermal arms; the fourth term $(L^{1/2} D_{abs})/(N_j^{1/2} W^{1/2})$ is determined by the geometrical parameters in the parallel direction, where N_j is the total number of graphene p-n junctions.

The response time of such a device is

$$\tau = \frac{C_{th}}{G_{th}} = \frac{1}{2}\left(\frac{c_V}{\kappa_{th}}\right)\left(\frac{L D_{abs}^2}{N_j W}\right) \tag{4.3}$$

where c_V is the volume specific heat capacity.

4.2 Optimization of Graphene Thermopile

The detectivity of supported graphene thermopile with Al_2O_3 as the substrate/IR absorber (1st generation, Figure 4-2 (a)) [182] is only $10^2\,\mathrm{cmHz^{1/2}s^{-1}}$. We have aimed previously to optimize the device structure, and achieved the detectivity of

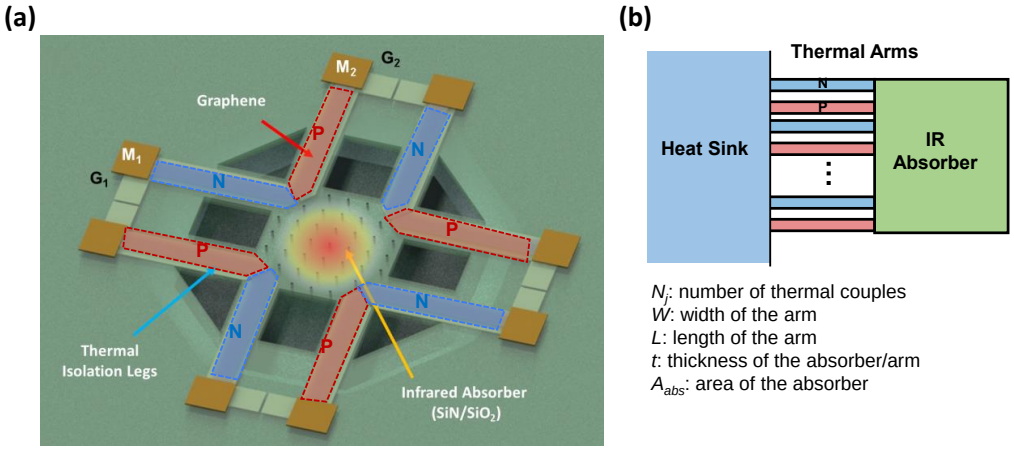

Figure 4-1: Schematics of the graphene thermopile. (a) 3D diagram. (b) simplified diagram for the electrical and thermal connections.

10^5 cmHz$^{1/2}$s^{-1} (2nd generation, Figure 4-2 (b)) [184]. This three orders of magnitude increase was attributed to two structural improvement. Firstly, a combination of SiO_2 and Si_3N_4 films with optimized thickness instead of a single dielectric layer as the IR absorber was used as shown in Figure 4-2 (b). Because SiO_2 and Si_3N_4 have strong resonant absorption at 9 μm and 11.5 μm, respectively, a 100 nm SiO_2/500 nm Si_3N_4/100 nm SiO_2 sandwiched structure could achieve $> 40\%$ absorption in the 8-12 μm spectral range, as compared to less than 1% absorption by 60 nm Al_2O_3 in the previous work. Secondly, the deposition $SiO_2/Si_3N_4/SiO_2$ sandwich structure was done with plasma enhanced chemical vapor deposition (PECVD) with optimized high-frequency to low-frequency ratio of plasma in order to make the thin film stress free, which was then suspended by undercutting the silicon underneath with XeF_2 isotropic etching. When measured in vacuum (less than 10^{-2} torr), both thermal conduction and convection in the vertical direction were efficiently attenuated. As a result, the temperature generated by the IR irradiance at the absorber with respect to the ambient can be sufficiently higher, leading to a much improved detectivity of the device.

In order to further optimize this device, we need to come up with a universal figure of merit and decouple geometrical parameters from the material related parameters.

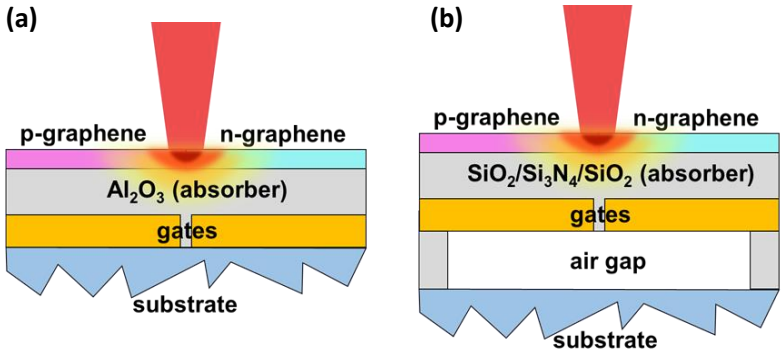

Figure 4-2: Schematics for the two generations of graphene thermopile. (a) 1st generation, where graphene is supported by the Al_2O_3 substrate. (b) 2nd generation, where graphene is put on top of a suspended 100 nm SiO_2/500 nm Si_3N_4/100 nm SiO_2 sandwiched structure.

According to Eqs.(4.2) and (4.3), we notice that $(D^*)^2/\tau$ is independent of lateral geometries:

$$\frac{(D^*)^2}{\tau} = \left(\frac{ABS}{t}\right) \cdot \left(\frac{\Delta S^2}{\rho_{2D}}\right) \cdot \left(\frac{1}{16 k_B T}\right) \tag{4.4}$$

The first three factors in Eq. (4.4) are absorbance per thickness (ABS/t), thermoelectric figure of merit ($FOM = \Delta S^2/\rho_{2D}$), and the thermal dissipation factor ($1/(\kappa_{th} c_V)$).

According to Eq. (4.4), the thermoelectric FOM plays a significant role in thermopile IR detectors. In order to benchmark graphene based thermoelectric detectors with respect to the other material systems, we plot the Seebeck coefficient S and the FOM, respectively, as a function of resistivity ρ in Figure 4-3 and Figure 4-4. Note that the FOM of the today's standard CVD graphene on SiO_2, with the average mobility of 2,000 $cm^2V^{-1}s^{-1}$, can already potentially out-perform the performance of any thermopiles made with metals and most of TE materials. The use of higher quality graphene and properly passivating the dangling bonds on the substrate with hBN could make the FOM two orders of magnitude higher than that of all the other material systems. We also noticed that the FOM of TMDs in two-dimensional (2D) form also increases dramatically as compared to their 3D counterparts, which also

shows great potential for thermal detection and other thermoelectric applications.

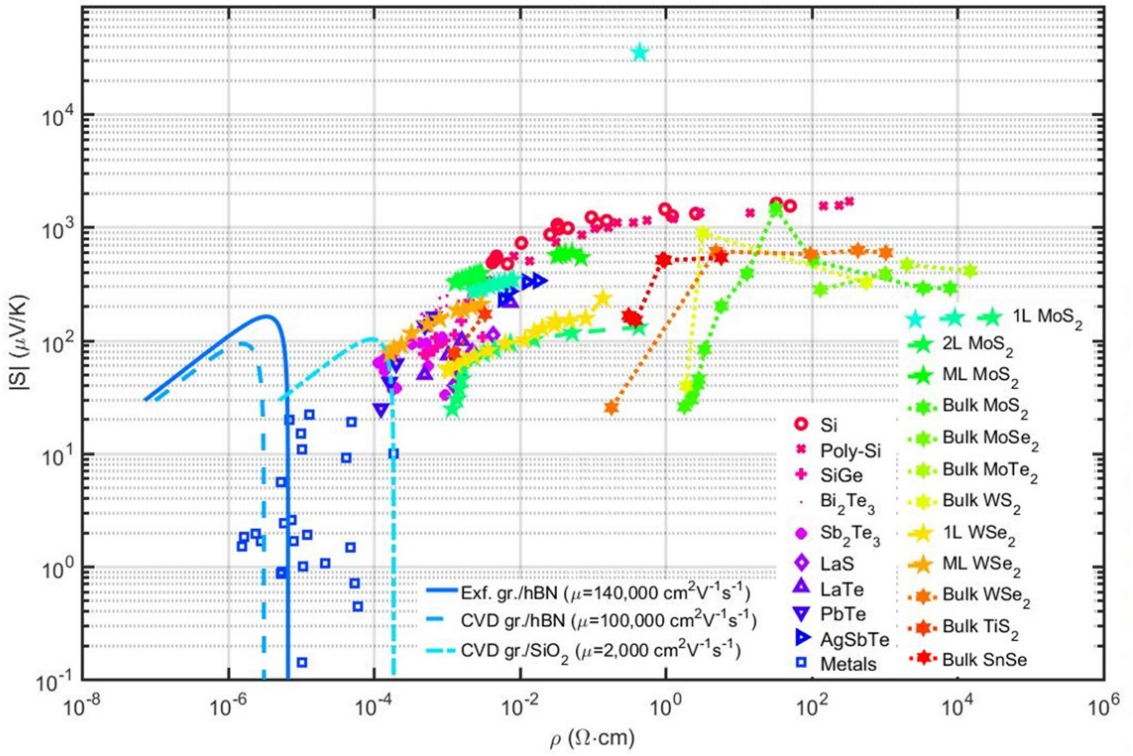

Figure 4-3: Seeback coefficient S versus resistivity ρ for various thermoelectric sensing materials [17].

The optical absorption per thickness (ABS/t) can also be improved through properly engineering of the material and the structure of the IR absorber. For a simple single-component thin film, this parameter increases as we make the film thinner. Figure 4-5 (a) shows ABS/t versus wavelength for Si_3N_4 films with different thicknesses. The optical absorption per thickness will approach the absorption coefficient, α as the thickness goes to zero. To overcome this limit, we can enhance the light field near the IR absorber through nano-photonic structures. The most simple way is to add a backplane mirror underneath the IR absorber to form an optical cavity. For instance, if we put a silver mirror underneath the freestanding silicon nitride film and set the distance to be 2.5 μm, such as cavity would be in resonance when the wavelength of the incident light is at around 10 μm, leading to a much enhanced ABS/t (Figure 4-5 (b)). People have also demonstrated metal-based metamaterial perfect absorbers in the mid-infrared range [185, 186, 187], which could also be applied in this application.

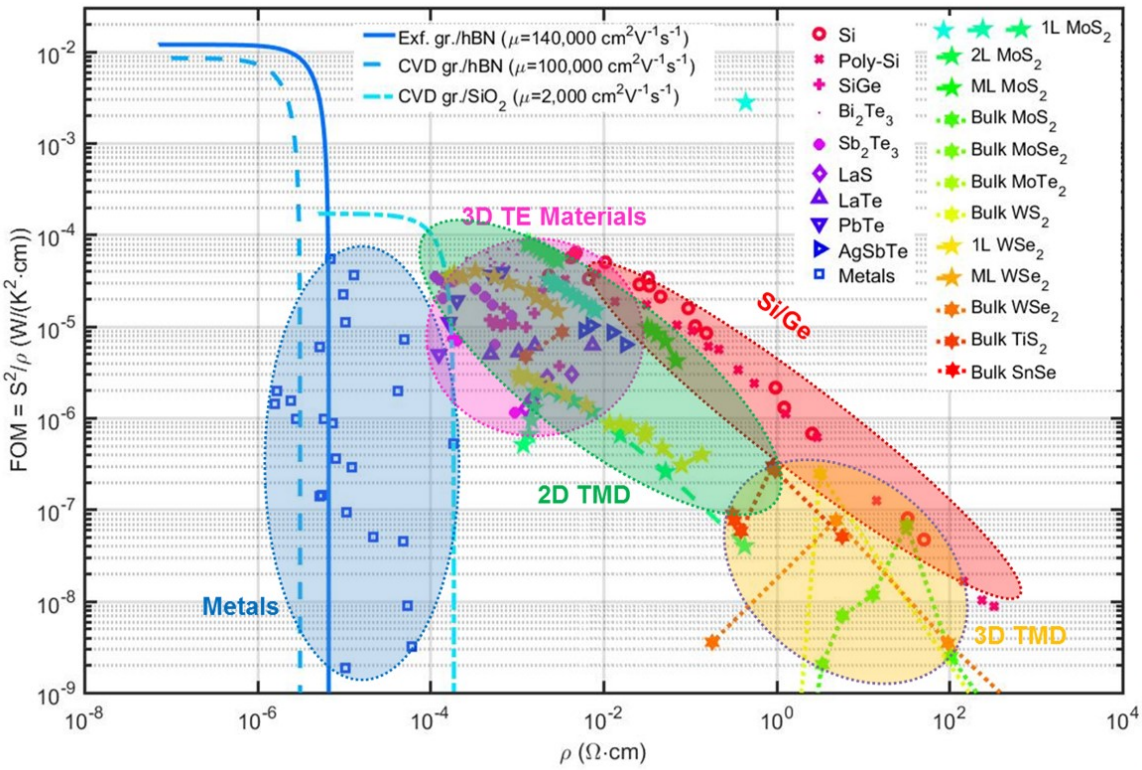

Figure 4-4: Thermoelectric figure of merit *FOM* versus resistivity ρ for various thermoelectric sensing materials [17].

Interestingly, the surface plasmon palariton (SPP) in graphene [45, 46] and phonon palariton (PP) in hBN [188, 189] have been studied recently. With appropriate engineering of the light field to enhance the light-matter interaction, absorption based on these mechanisms could be in strong resonance with negligible loss. Boosting by the SPP in graphene or PP in hBN, it is possible to fabricate nanometer-thick IR absorber with near-unity absorbance at resonance.

We also compared the specific detectivity (D^*) and the response time (τ) of graphene thermopiles with different type of state-of-the-arts thermal detector technologies, including bolometers (VO_x, CMOS-MEMS, etc.) [190, 191, 192, 193, 194, 195, 196, 197, 198, 199, 200], thermopiles (poly-Si, Al, thermoelectric materials, etc.) [201, 202] and pyroelectric devices [203], as shown in Figure 4-6. Here we exploit the dimensionless relation from Eq. (4.4) to represent each technology node of graphene thermopiles. Although our current graphene thermopile technology is still not as

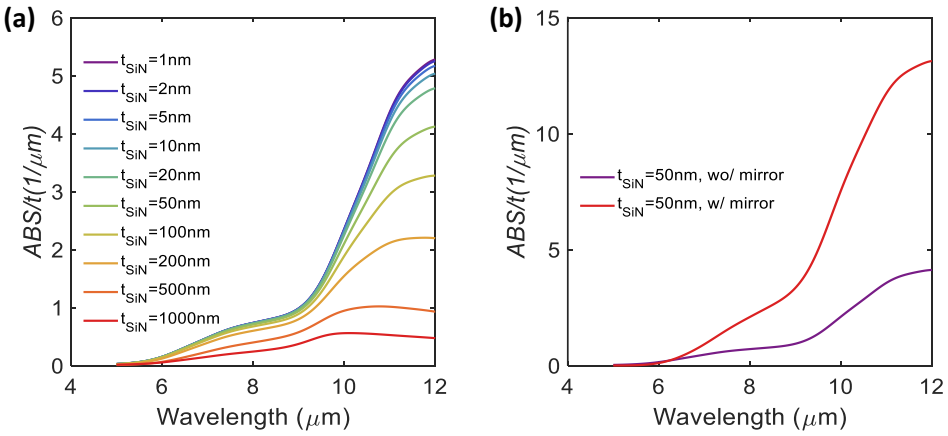

Figure 4-5: (a) ABS/t versus wavelength for freestanding silicon nitride films with different thicknesses.(b) ABS/t versus wavelength for freestanding silicon nitride films without and with a backplane mirror.

good as the state-of-the-art thermal detectors, the performance is predicted to be competitive, or even better than the cutting-edge technologies, if we further optimize our devices. For example, a 100-fold improvement in the thermoelectric FOM could be achieve if we encapsulate large area, high-quality CVD graphene with hexagonal boron nitride, which would increase the mobility and Seebeck coefficient to 100,000 $cm^2V^{-1}s^{-1}$ and 200 μV/K, respectively. Furthermore, the absorber can be thinned down to 10 nm with good mechanical stability, and 100% perfect absorption can still be achieved through nano-photonic structure. With these material and structural improvement, we predict the 3rd generation thermopile could have better performance than the best bolometer so far in the literature, and still being able to operate at room temperature.

4.3 Graphene-CMOS Integration for Thermal Imaging Applications

As discussed in chapter 1, monolithic integration is highly desirable for miniaturized integrated microsystems with multifunctionality; yet it is extremely challenging with

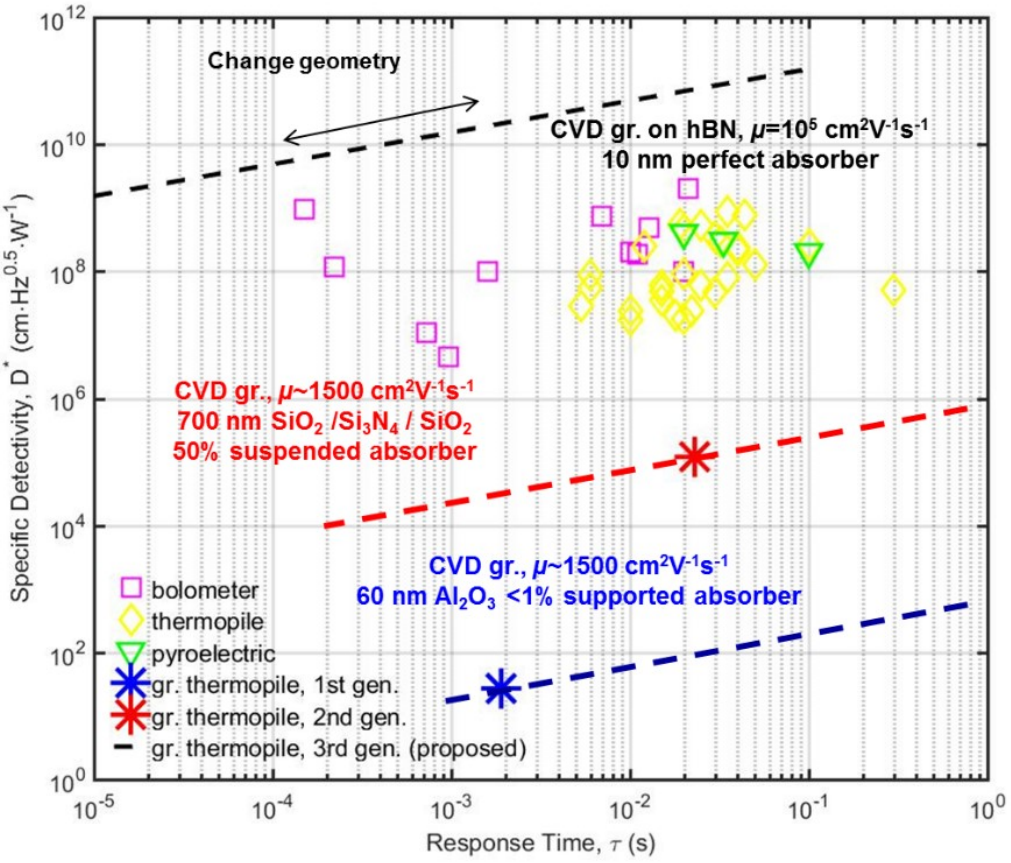

Figure 4-6: Specific detectivity (D^*) versus response time (τ) for different technology nodes of graphene thermopiles in comparison with mainstream uncooled thermal IR detectors. [17]

conventional 3D technologies. 2D material based devices can solve this very well, because the transfer process decoupled the high temperature growth of 2D crystals from the low temperature device fabrication process. As a result, we can easily transfer high quality 2D materials on top of a fabricated silicon CMOS chip and fabricate 2D materials based sensing arrays on top without breaking the thermal budget of the CMOS chip.

To demonstrate this 2D-CMOS monolithic integration capability, we developed a back-end-of-line (BOEL) low temperature process to fabrication a graphene thermopile focal plane array (FPA) directly on top of a Si CMOS readout integrated circuit (ROIC) chip. The BEOL of graphene thermopile FPAs fabricated directly

on CMOS ROIC chips is schematically shown in Figure 4-7 (a). After receiving the CMOS ROIC chip from an industrial foundry, we first etched away the passivation oxide (PASS) through CF_2/H_2 reactive ion etching (RIE). Then a photolithography, an electron-beam evaporation, followed by a lift-off process was done to defined the metal plugs and the gates. After depositing the Al_2O_3 gate dielectric layer through atomic layer deposition (ALD), a continuous monolayer graphene film synthesized by CVD was transfered and patterned into the p-n junction channels. Finally, the dielectric on top of the metal plugs are etched through an the metal contacts to the graphene channels were deposited. The optical images of the completed graphene thermopile-CMOS image sensor are shown in Figure 4-7 (b) and (c).

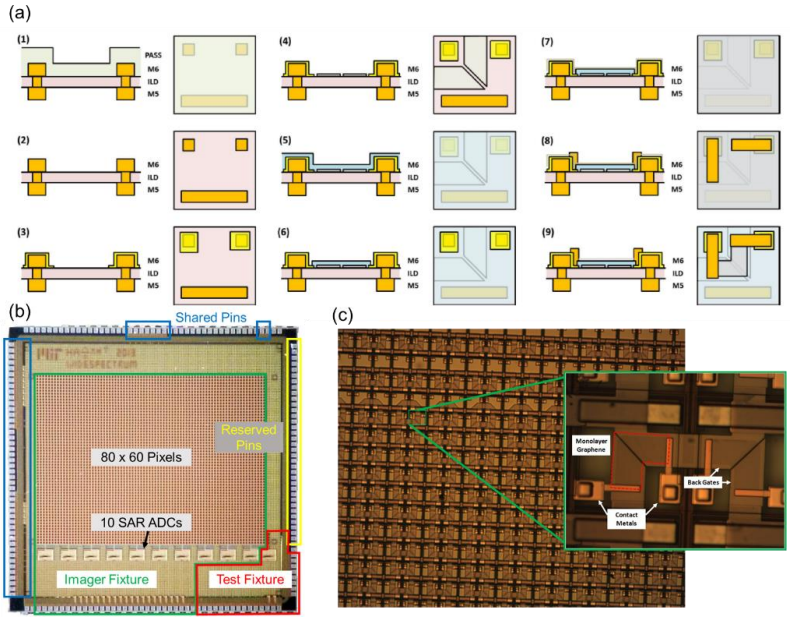

Figure 4-7: Graphene thermopile/CMOS monolithic integration. (a) Back-end-of-line process of the graphene thermopile FPA fabricated directly onto a CMOS ROIC chip. PASS=passivation, ILD=interlayer dielectric, M6=Metal 6 (Cu), M5=Metal 5 (Cu), blue=PECVD SiO_2, grey line is graphene. The left and right images are the side and top view of the pixel area, respectively. (b) Photograph of the CMOS ROIC chip. (c) Microscopic images of the completed Graphene thermopile FPA/CMOS ROIC chip. [17]

Chapter 5

Photothermoelectric Detector Based on Graphene-2D Semiconductor Lateral Heterojunction

5.1 Principle of Operation

Because of the linear electronic dispersion relation (Figure 1-10), the relaxation of photo-excited carriers is very different from conventional semiconductors. The time scales of different photo-carrier relaxation processes in graphene is summarized in Figure 5-1. Consider a sheet of graphene illuminated at time zero. Within tens of femtoseconds, because of the relatively strong electron-electron scattering, the photo-excited electrons will first scattered by surrounding electrons and share their energy with the electron reservoir. This gives rise to a wider energy distribution of free electrons in graphene, or an increased electron temperature (Figure 5-2). These optically heated electrons are called "hot electrons". As time goes on, the hot electrons will start to interact with the lattice through the relatively week electron-phonon scattering, and eventually reach thermal equilibrium with the lattice. Therefore, as a general case, the electron temperature is higher than the lattice temperature in graphene, or $T^{\mathrm{el}} > T^{\mathrm{L}}$.

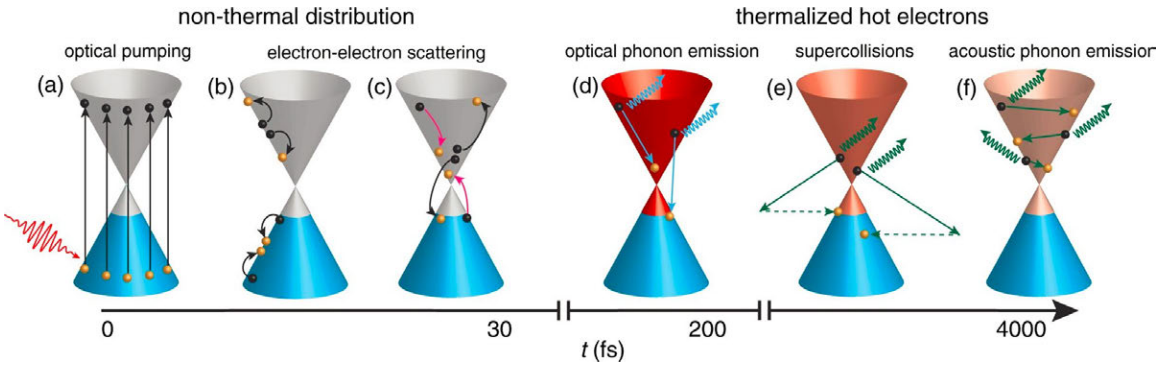

Figure 5-1: A summary of the time scales of various photo-carrier relaxation processes

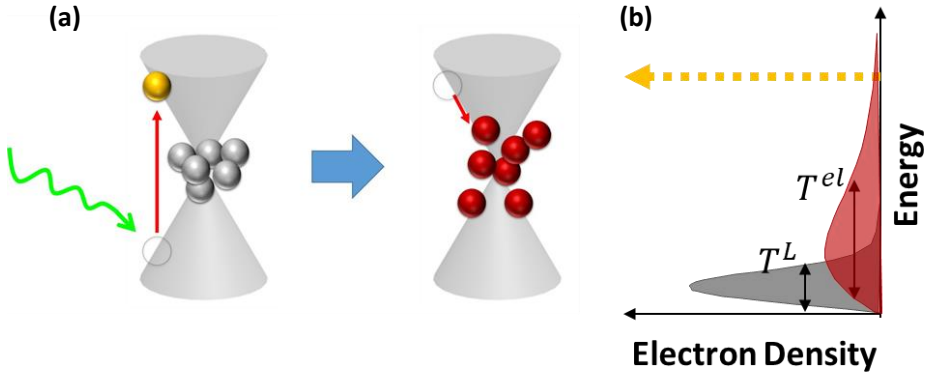

Figure 5-2: Hot electrons in graphene. (a) Illustration of the formation of the hot electrons in graphene. (b) Energy distributions of hot (red) and cold (grey) electrons.

Such an increased electronic temperature can be probed in a graphene p-n junction through the thermoelectric effect (chapter 4). This hot-carrier related thermoelectric effect in graphene is called photothermoelectric (PTE) effect. The photovoltage is given by

$$V_{\mathrm{PTE}} = \Delta S \cdot \Delta T_j^{\mathrm{el}} \tag{5.1}$$

where ΔS is the Seebeck coefficient different between the p- and n-type regions of graphene; and $\Delta T_j^{\mathrm{el}} = T_j^{\mathrm{el}} - T^{\mathrm{L}}$ is the electron temperature increase at the junction with respect to the lattice, or the environment.

According to the Mott relation [204], graphene's Seebeck coefficient S is tunable

through its Fermi-level E_F, which can be expressed as

$$S = -\frac{2\pi k_B^2 T}{3e} \frac{E_F}{\Delta^2 + E_F^2} \tag{5.2}$$

where Δ is the electrical conductivity broadening near the Dirac point of graphene.

For an electrostatically gated graphene p-n junction, the Seeback coefficients can be tuned continuously with the gate voltages (Figure 5-3 (c)). The resulting PTE voltage or current should follow the same trend. As a comparison, for a conventional photovoltaic effect, the photovoltage or photocurrent would undergo a monotonic relation with the gate voltage Figure 5-3 (b) and (d). This will lead to the six-lobe signature as we sweep the gate voltages as we sweep the graphene p-n junction independently, as shown in Figure 5-3 (a). And people have used this to prove the PTE effect is the dominated photocurrent generation mechanism in graphene p-n junctions, especially in the visible to near infrared spectral range[204, 19, 205].

5.2 Photothermoelectric Effect in Graphene-2D Semiconductor Lateral Heterojunction

In this chapter, we aim to study the photocurrent response at graphene-2D semiconductor lateral heterojunctions. As just mentioned, because of the ultrafast electron-electron scatterings (on the order of 10 fs) and relatively slow electron-phonon scatterings (on the order of ps) as shown in Figure 5-1, the photo-induced carriers are thermalized by the electronic system and dissipate the heat very slowly to the lattice. In a conventional semiconductor with parabolic electronic dispersion, on the other hand, the photo-induced electrons and holes are either separated and collected directly by a built-in electric field (the photovoltaic or PV effect), or scatter strongly with phonons and impurities and transfer their kinetic energy to heat or lattice vibrations. If the Dirac semimetallic graphene and the parabolic 2D semiconductor are put in close proximity with each other within the 2D plane, the vast asymmetry of the energy transfer pathways on the two sides gives rise to very interesting

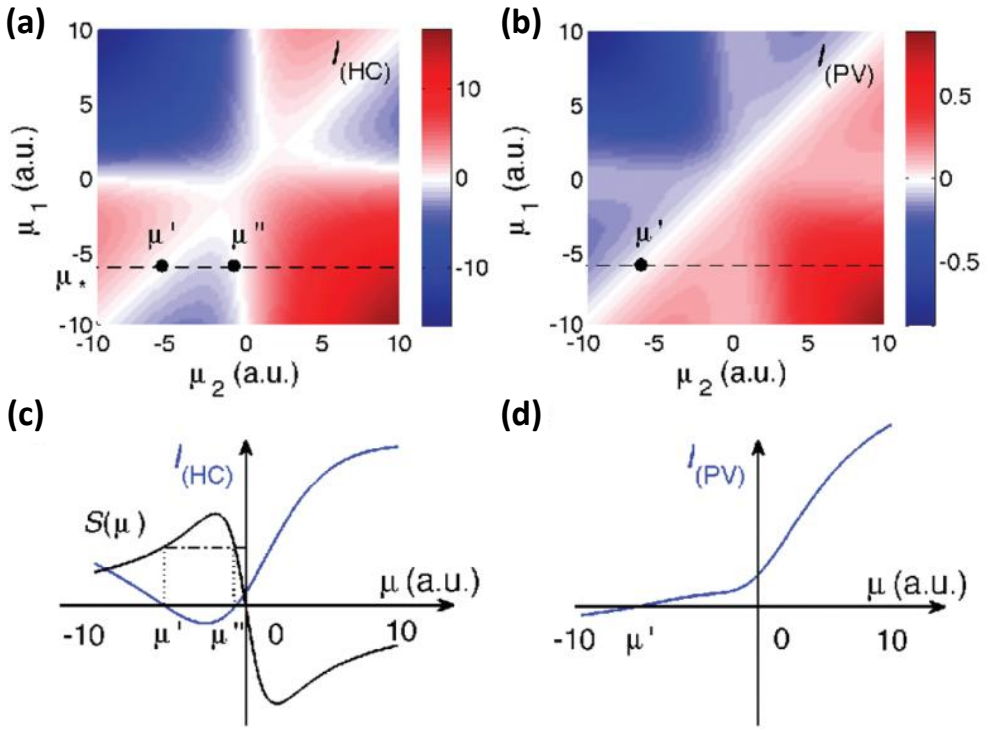

Figure 5-3: Photocurrent map as a function of chemical potential μ, or Fermi level E_F for a electrostatically gated graphene p-n junction. (a) and (c) are the 2D mapping and the 1D sweep of PTE effect, whereas (b) and (d) are the 2D mapping and the 1D sweep of the PV effect. [19]

features that can be addressed spatially through localized light excitation. In this work, we demonstrate such asymmetric hot-electron thermalization on a synthetic graphene-MoS_2 lateral heterojunction.

5.2.1 Device Structure and Transport Property

The graphene-MoS_2 lateral heterostructures were obtained through the seeding promoter assisted chemical vapor deposition (CVD) (chapter 2). Atomic force microscopic (AFM) images, high-resolution transmission electron microscopic (HR-TEM) images, as well as Raman and photoluminescence mappings (Figure 2-5 and Figure 2-7) at the graphene-MoS_2 interfaces confirm that the two materials overlap only a few tens of nanometers at the interface. Note that such a nanometer-scale overlap

does not significantly affect the photoresponse at the interfaces, because the optical excitations cannot resolve any structural features that are below the wavelengths, and both the depletion width (on the order of 100 nm)(39) in a PV effect or the cooling length (on the order of 100 nm to 1 μm)[204, 19, 205] in a PTE effect are sufficiently larger than the size of the overlaps.

Figure 5-4 (a) shows a schematic of the lateral graphene-MoS_2 heterojunction device. Figure 5-4 (b) shows the optical microscopic image of the graphene-MoS_2 lateral heterojunction device. Multiple long and short electrodes (30 nm Ni/20nm Au by electron-beam evaporation) were fabricated near the graphene-MoS_2 interface in order to perform transport and photocurrent measurement on both the lateral junction and each homogeneous material. All the devices were fabricated on top of a

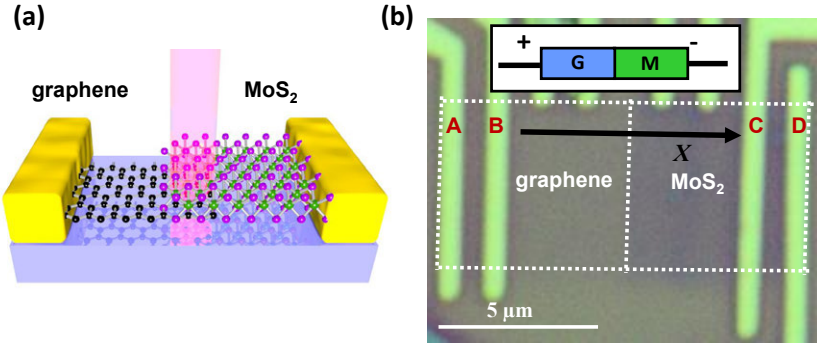

Figure 5-4: Graphene-MoS_2 lateral heterojunction photodetector. (a) Schematic of the device. (b) A microscopic image of the as-fabricated device. The inset diagram indicates the cathode and the anode of the device for the electrical and photocurrent measurements; The axis indicates the direction of the x-axis for the X-V_g mappings and the simulation results. [20]

We first performed transport measurements to the device. Figure 5-5 (a) plots the transfer characteristics for devices fabricated on the graphene layer, the MoS_2 layer and across the interface (channel current, I_{ch}, versus back-gate voltage, V_g). The charge neutrality point of graphene is around 3 V, whereas the threshold voltage of MoS_2 is very negative (around -17 V). The weak non-linearity of the output characteristics (channel current, I_{ch}, versus channel voltage, V_{ch}, with various V_g) as shown

in Figure 5-5 (b) indicates that the Schottky barrier height at the graphene-MoS_2

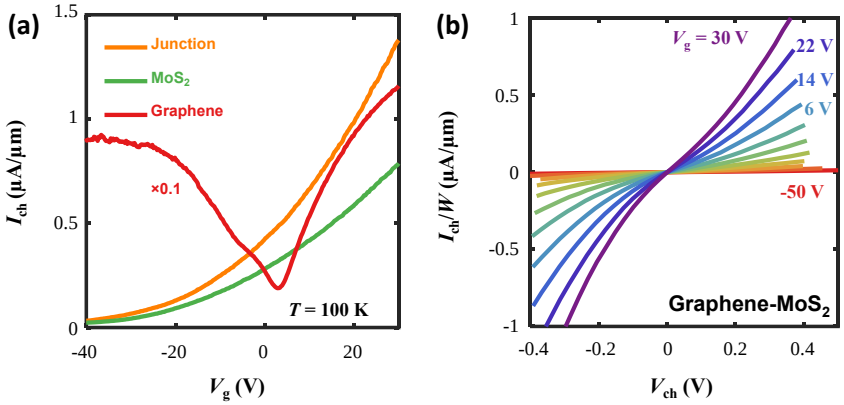

Figure 5-5: Transport measurement results of the graphene-MoS_2 lateral heterojunction device. (a) transfer characteristics. (b) output characteristics. [20]

5.2.2 Scanning Photocurrent Microscopy (SPCM)

We used a confocal laser scanning microscopy setup to carry out the measurement about the spatial distributions of the photocurrent response throughout the device. This technique is called scanning photocurrent microscopy (SPCM). The chips were wire-bonded onto a chip carrier and mounted in a Janis ST-500 helium optical cryostat equipped with electrical connections, a well-defined microscopic optical path and a temperature controlling system. The device was kept under high vacuum ($< 10^{-5}$ Torr) throughout the measurements. Sourcemeters (Agilent B2902a), current preamplifiers (Ithaco DL1211) and data acquisition cards (NI PXI module) were used for the electrical sourcing and probing. Both the transport and the photocurrent measurements were performed at 100 K if not mentioned explicitly in the text. For the scanning photocurrent measurements, a broadband supercontinuum fibre laser (Fianium) was combined with a monochromator to generate the monochromatic laser beam with desired wavelength (tunable from 400 to 1600 nm). A two axis piezo-controlled scanning mirror was coupled to a microscope objective through two confocal lenses to perform the spatial scanning with the laser beam spot of around 1 μm on the device.

The photocurrent and the reflected light intensity were recorded simultaneously to form the scanning photocurrent images and the reflectance images. All the photocurrent results were measured under the short-circuit condition, in which zero voltage bias was applied across the device. The photovoltage corresponds to the open-circuit voltage, in which the current flowing across the junction is set to zero. The absolute location of the photo-induced signal was found by comparing the photocurrent map to the reflection image. The incident laser power was measured at the output of the microscope objective using a calibrated photodetector.

The SPCM mapping results for different laser excitation wavelengths are shown in Figure 5-6. It is observed that the strongest photocurrent response is localized at the graphene-MoS_2 junction.

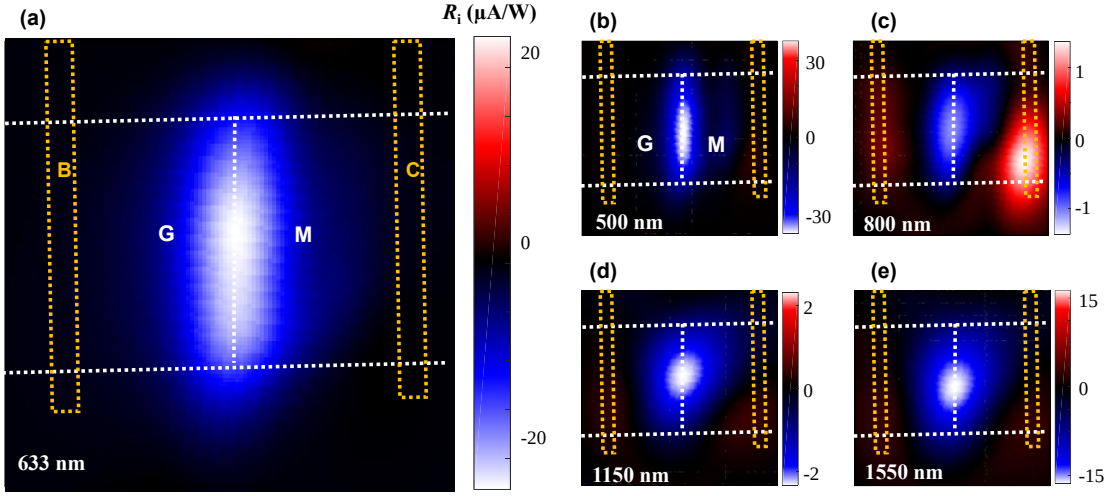

Figure 5-6: Scanning photocurrent microscopy mappings of the graphene-MoS_2 lateral heterojunction device with different laser excitation wavelengths. (a) 633 nm. (b) 500 nm. (c) 800 nm. (d) 1150 nm. (e) 1550 nm. [20]

5.2.3 Photothermoelectric Effect Dominated Photoresponse

We first excluded that the measured photoresponse at the graphene-MoS_2 lateral heterojunction is from photovoltaic, photoconductive or bolometric effects, for two

reasons. First, we showed that the graphene-MoS_2 lateral heterojunction has a smaller Schottky barrier height than conventional metal contacts to MoS_2 (Figure 2-11 and Table 2.1), but the photocurrent response at the graphene-MoS_2 lateral heterojunction is larger than that at the MoS_2-metal Schottky junction (Figure 5-6). This is in contradiction to the photovoltaic effect. Second, the I-V curves with the 633 nm light

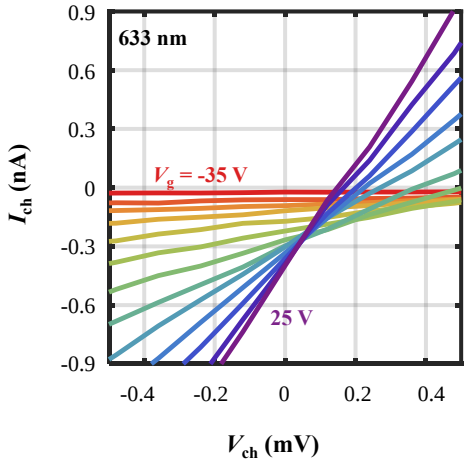

Figure 5-7: I-V characteristics with 633 nm light illumination and various gate voltages. Note that the I-V curves do not intersect with the origin, which means there is an electromotive force generated. [20]

Now let us consider the PTE effect. As discussed in section 5.1, the Seebeck coefficient of graphene follows a non-monotonic relation with respect to the Fermi level, or gate voltage. Given that the Seebeck coefficient of MoS_2 changes very slowly and monotonically with the gate voltage when MoS_2 is heavily doped, the photovoltage induced by the PTE effect should follow approximately the non-monotonic trend of the Seebeck coefficient of graphene with gate voltage (Figure 5-3). Meanwhile, the photovoltage induced by the PV effect should change monotonically with the gate voltage, simply because the change of the barrier height at the junction is positively correlated to the difference between the Fermi level shifts of graphene and MoS_2, which could only change monotonically with a global gate voltage.

Gate-dependent SPCM measurements were carried out to confirm that the PTE

effect is dominant in the graphene-MoS_2 lateral heterojunction. Figure 5-8 (a) shows the photocurrent mapping for an 850 nm laser beam sweeping along the linecut across the junction shown in Figure 5-4 as the x-axis while the gate voltage varies for each laser position sweep as the y-axis. In addition to the main photocurrent peak at the graphene/MoS_2 interface, two extra peaks were also observed at the graphene-metal and the MoS_2-metal junction. While the photocurrent at the MoS_2-metal junction increases monotonically with the gate voltage, the photocurrent at the graphene-metal junction follows a "S"-shape curve with the gate voltage (Figure 5-9). It is also observed that the photocurrent at the graphene-MoS_2 junction undergoes a very non-monotonic change with respect to the gate voltage around the charge neutrality point of graphene. This can be seen more clearly in Figure 5-8 (b) as we stack the gate-dependent photocurrent line profiles on top of each other. The peak photocurrent and the corresponding photovoltage as a function of the gate voltage for four different excitation wavelengths are plotted in the first and second columns of Figure 5-8 (c), where the photovoltages are obtained by multiplying the photocurrent value by the resistance of the junction. With shorter excitation wavelengths (550 nm and 650 nm) or photon energies above the band gap of MoS_2, both the photocurrent and the photovoltage changes monotonically with the gate voltage, whereas a "S"-shaped relation was observed with longer excitation wavelengths (750 nm and 850 nm) or photon energies below the band gap of MoS_2. Given that such an "S"-shaped photovoltage trend matches well with the trend of the Seebeck coefficient change of graphene as a function of the gate voltage (Figure 5-3), we concluded that the photoresponse mainly originates from the PTE effect, especially at longer wavelengths.

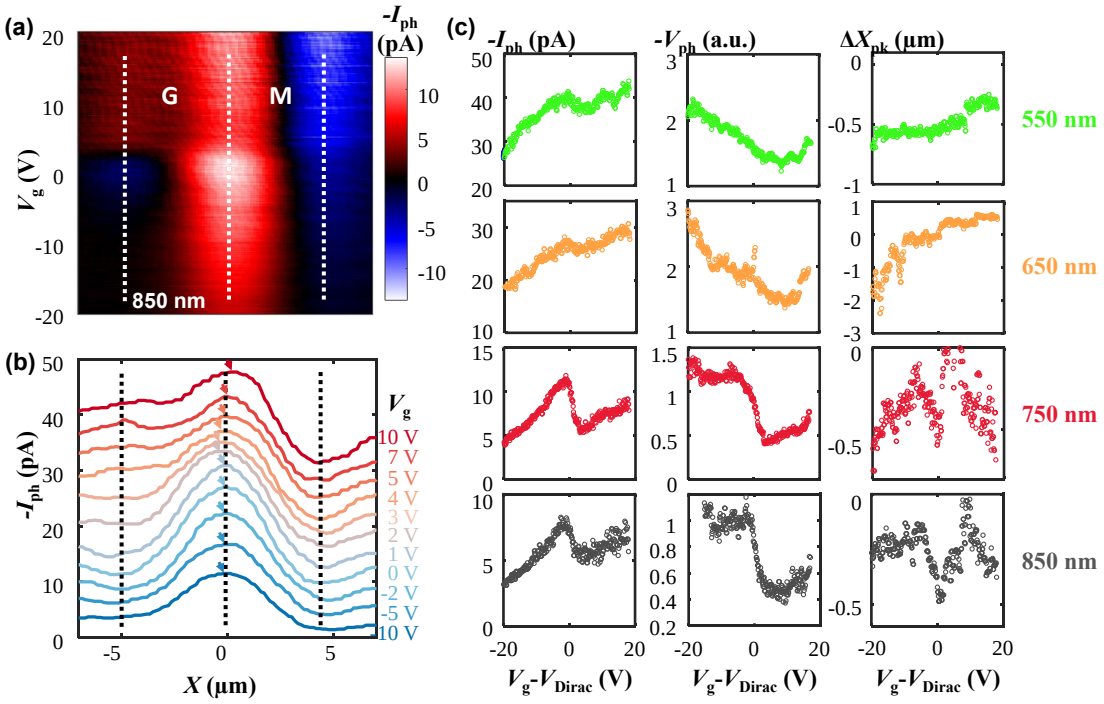

Figure 5-8: Gate-dependent SPCM measurements of the device. (a) Gate voltage (V_g) - linecut (X) mapping of the photocurrent (I_{ph}) under an 850 nm laser excitation. The three dotted line indicate (from left to right) the junctions of metal-graphene, graphene-MoS_2, and MoS_2-metal. The magnitude of I_{ph} was flipped to make the photoresponse at the graphene-MoS_2 junction positive. (b) Stacked linecuts along the x-axis of I_{ph} with different V_g. The arrows indicate the peak positions. (c) peak photocurrent I_{ph} (left column), peak photovoltage V_{ph} (middle column), and peak offsets ΔX_{pk} (right column) as a function of the gate voltage with respect to the charge-neutrality point of graphene (V_{Dirac}), extracted from the V_g-X mappings with laser excitations of 550 nm (first row), 650 nm (second row), 750 nm (third row) and 850 nm (fourth row). V_{ph} is estimated by $I_{\text{ph}}\Delta R_{\text{dark}} = I_{\text{ph}}\Delta V_{\text{offset}}/I_{\text{dark}}$, in which the dark resistance R_{dark} is inversely proportional to the dark current I_{dark} averaged throughout the points whenever the laser spot is off the device in the V_g-X mappings, assuming that a constant voltage offset V_{offset} is supplied by the measurement setup. [20]

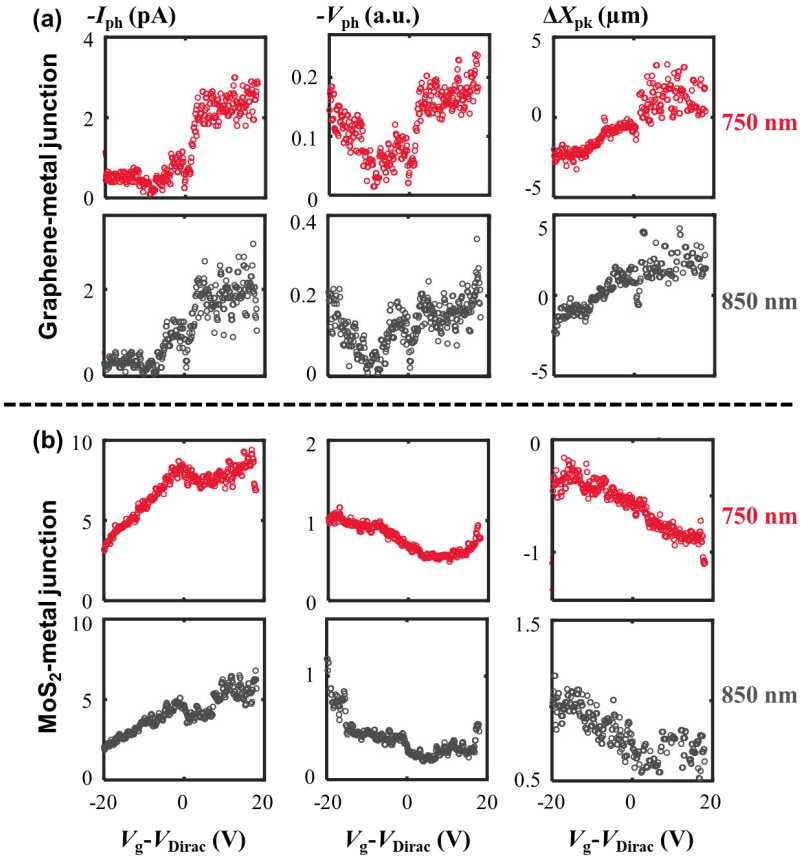

Figure 5-9: Gate-dependent photocurrent (I_{ph}), photovoltage (V_{ph}) and the peak position shift (ΔX_{pk}) on graphene-metal (a) and MoS_2-metal (b) junctions. [20]

5.3 Understanding the Asymmetric Hot Carrier Thermalizatoin Pathways

5.3.1 Experiment Observation

The lateral geometry and the asymmetry of the graphene-MoS_2 junction also make it possible to access different positions around the junction with light excitation. As a result, the spatial patterns due to the vast discrepancy of the thermalization pathways towards the two sides can be revealed. As shown in Figure 5-8 (b) and the third column of Figure 5-8 (c), the photocurrent peak position was observed to undergo an unusual shift towards the graphene side by up to 500 nm as the graphene reaches its charge neutrality. This effect could be observed clearly at longer excitation

wavelengths (750 nm and 850 nm). Note that no obvious shifts around graphene's charge neutrality voltage were observed on the graphene-metal or the MoS_2-metal junction (Figure 5-9). Given that the incident light power is relatively low, the Seebeck coefficients would not be affected by the laser position to the first order approximation. As a result, the photocurrent profile should follow the profile of the electron temperature change at the lateral junction as we move the laser beam position across the junction.

5.3.2 Theoretical Analysis

To understand such a unusual photocurrent peak position shift and the electron temperature distribution, we need to discuss about the photo-carrier relaxation processes along the two sides of the graphene-MoS_2 lateral heterojunction The photo-excited carriers are first thermalized through either electron-electron scattering or electron-phonon scattering, leading to a broader energy distributions of electrons. On the graphene side, because of the linear electronic dispersion and its low dimensionality, the electron-electron scatterings are substantially stronger than the electron-phonon scatterings (including scattering with optical phonons, acoustic phonons, and disorder-assisted supercollisions) [208, 209, 210, 205, 211]. Consequently, electrons in graphene would not reach thermal equilibrium with the lattice before being collected (the left panel of Figure 5-10), given that the cooling length of hot electrons in graphene is typically hundreds of nanometers to micrometers [204, 19, 205]. On the MoS_2 side, however, the electronic dispersion at the band edge is parabolic, in which the electrons and lattices are always in thermal equilibrium because of the much stronger electron-phonon scatterings (the right panel of Figure 5-10). Such an asymmetric behavior of heat dissipations on the two sides of the graphene-MoS_2 junction could lead to very asymmetric temperature distributions and unusual photocurrent profiles.

In the following, we set up a numerical model for the hot electron temperature distributions.

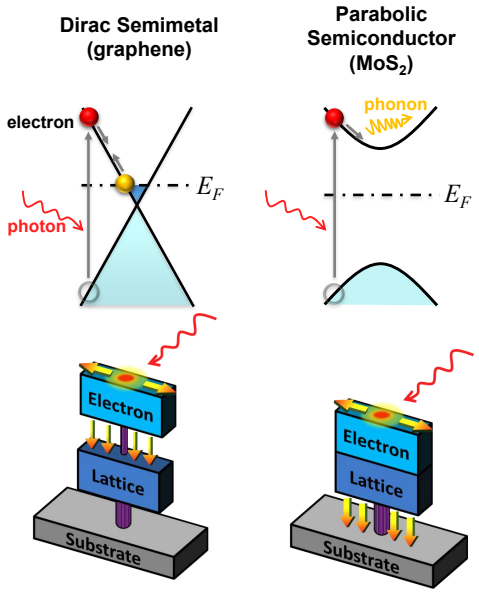

Figure 5-10: Schematics of the dominating hot-electron cooling processes (upper) and the spatial hot-electron thermalization pathways (lower) of the Dirac semimetallic graphene (left) and the parabolic semiconducting MoS_2 (right). In the lower panels, the arrows indicate possible heat transfer paths, and the diameters of the purple cylinders connecting the electron, the lattice and the substrates indicate the strength of thermal couplings. [20]

Heat Equation

The photo-induced distribution of electron temperature is governed by the heat transfer equation [204, 19, 205]:

$$\kappa^{\mathrm{el}}\nabla^2 T^{\mathrm{el}} - g^{\mathrm{el-L}}\left(T^{\mathrm{el}} - T^{\mathrm{L}}\right) + p_{\mathrm{in}} = 0 \tag{5.3}$$

$$\kappa^{\mathrm{L}}\nabla^2 T^{\mathrm{L}} - g^{\mathrm{sub}}\left(T^{\mathrm{L}} - T_0\right) + g^{\mathrm{el-L}}\left(T^{\mathrm{el}} - T^{\mathrm{L}}\right) = 0 \tag{5.4}$$

where κ^{el} and κ^{L} are the 2D thermal conductivity of electron and lattice, respectively; $g^{\mathrm{el-L}}$ and g^{sub} are the electron-lattice heat loss rate and the heat loss into the substrate; T^{L} is the lattice temperature; T_0 is the temperature of the environment; and p_{in} is the input power density which is provided, in our case, by the incident laser

beam..

The electron-lattice heat loss can be expressed as

$$g^{\mathrm{el-L}} = \gamma C^{\mathrm{el}} \tag{5.5}$$

with γ and C^{el} denoting the electron-lattice cooling rate and the electron heat capacity, respectively.

In the case of MoS_2 with a parabolic electronic dispersion, γ is sufficiently large, leading to an efficient electorn-lattice heat transfer. This guarantees that the electrons are always in thermal equilibrium with the lattice, that is, $T^{\mathrm{el}} \equiv T^{\mathrm{L}} \equiv T$. The heat equations can therefore be simplified to

$$\kappa^{\mathrm{tot}} \nabla^2 T^{\mathrm{el}} - g^{\mathrm{sub}} \left(T^{\mathrm{el}} - T_0 \right) + p_{\mathrm{in}} = 0 \tag{5.6}$$

in which $\kappa^{\mathrm{tot}} = \kappa^{\mathrm{el}} + \kappa^{\mathrm{L}}$ is the total thermal conductivity.

In the case of graphene with a linear electronic dispersion, however, both γ and C^{el} are very small, meaning that the vertical heat dissipation is mainly limited by the electron-lattice cooling. Considering the vertical thermal conductance of electron-lattice and lattice-substrate are in series, the temperature increase of lattice at a given location should be much smaller than the temperature increase of electron at the same location. Therefore, we can assume that $T^{\mathrm{L}} \equiv T_0$ throughout the device. The heat equations can thus be simplified to

$$\kappa^{\mathrm{el}} \nabla^2 T^{\mathrm{el}} - g^{\mathrm{tot}} \left(T^{\mathrm{el}} - T_0 \right) + p_{\mathrm{in}} = 0 \tag{5.7}$$

with $g^{\mathrm{tot}} = [(g^{\mathrm{el-L}})^{-1} + (g^{\mathrm{sub}})^{-1}]^{-1} \approx g^{\mathrm{el-L}}$.

We can define the cooling length to characterize the length the hot electrons can travel before reaching thermal equilibrium with the lattice:

$$\xi = \sqrt{\frac{\kappa}{g}} \tag{5.8}$$

The heat equations were solved numerically through the finite difference method

with the use of *Matlab*.

Parameters of Graphene

The 2D electrical conductivity of graphene can be expressed as [19]

$$\sigma = \sigma_{\min}\left(1 + \frac{E_F^2}{\Delta^2}\right) \tag{5.9}$$

where $\sigma_{\min}$ and Δ denote respectively the minimum conductivity and the broadening of the conductivity. These two terms are related to the impurity scatterings as well as the homogeneity of the graphene film. According to the transfer characteristic of the graphene side of our device (red curve in Figure 5-5 (a)), we can extract the values of these two parameters: $\sigma_{\min} \approx 190.86\ \mu$S or $5(e^2/h)$, and $\Delta \approx 54.9$ meV. The experimental data and the fitted curve are plotted in Figure 5-11. The Fermi level E_F can be obtained from

$$E_F = \hbar v_F \left[\frac{4\pi}{g_s g_v}\frac{C_{\text{ox}}}{e}(V_g - V_{\text{Dirac}})\right]^{\frac{1}{2}} \tag{5.10}$$

where $C_{\text{ox}} = 1.21\times10^{-8}$ F/cm^2 is the capacitance of the gate dielectric (285 nm SiO_2); $g_s = g_v = 2$ are the degeneracy factors; and $v_F = 10^8$ cm/s is the Fermi velocity of graphene.

The electron heat capacity C^{el}, and the electron thermal conductivity κ^{el} of graphene are given by [19, 205]

$$C^{\text{el}} = \frac{\pi^2 k_B^2 T}{e} D(E_F) \tag{5.11}$$

$$\kappa^{\text{el}} = \frac{\pi^2 k_B^2 T}{3e^2}\sigma \tag{5.12}$$

with $D(E_F)$ denoting the 2D density of states.

To determine the electron-lattice cooling rate, two electron-lattice cooling mechanisms are considered, that is, the acoustic phonon cooling (scaled by T) and the supercollision cooling (scaled by $1/T$). The cooling rate γ is then given by [205, 209]

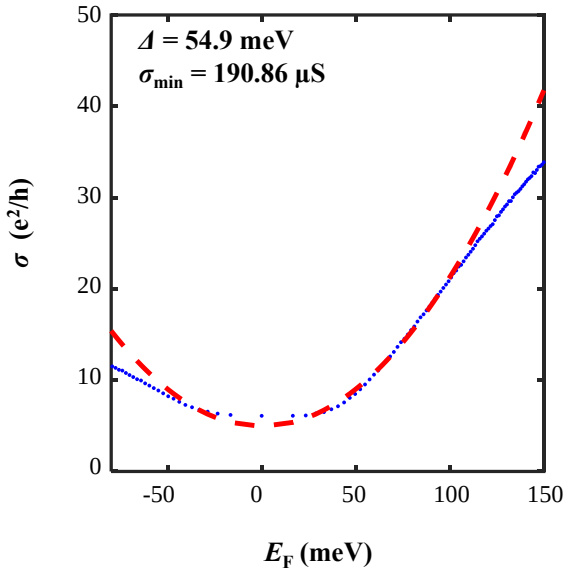

Figure 5-11: Extraction of graphene properties. The blue dots and the red dashed curve are measured and fitted conductivity according to Eq. (5.9). [20]

$$\gamma = b\left(T + \frac{T_*^2}{T}\right) \tag{5.13}$$

The prefactor b and the cross-over temperature T_* are given by

$$b = 0.55\frac{g^2 D(E_F)k_B}{\hbar k_F l} \tag{5.14}$$

$$T_* = (0.43k_F l)^{\frac{1}{2}} T_{\mathrm{GB}} \tag{5.15}$$

in which g is the electron-phonon coupling strength; $k_F l$ is the unitless mean free path; and $T_{\mathrm{GB}} = s\hbar k_F/k_B$ is the Bloch-Grüneisen temperature.

The mean free path is related to the electrical conductivity, σ:

$$k_F l = \frac{\sigma}{2(e^2/h)} \tag{5.16}$$

The cooling length is therefore given by

$$\xi = \sqrt{\frac{\kappa^{\mathrm{el}}}{\gamma C^{\mathrm{el}}}} \propto \left[T\left(1 + \frac{0.43 s^2 \hbar^2 (k_F l) k_F^2}{(k_B T)^2}\right)\right]^{-\frac{1}{2}} \frac{(k_F l)}{k_F} \tag{5.17}$$

Note that $\sigma_{\min}$ and Δ are the only two free parameters, which can be determined by experiment. Figure 5-12 and Figure 5-13 plot the calculated cooling rate γ, the electron thermal conductivity κ^{el}, the electron-lattice vertical loss $g^{\mathrm{el-L}} = \gamma C^{\mathrm{el}}$ and the electron-lattice cooling length ξ of graphene with various values of $\sigma_{\min}$ and Δ.

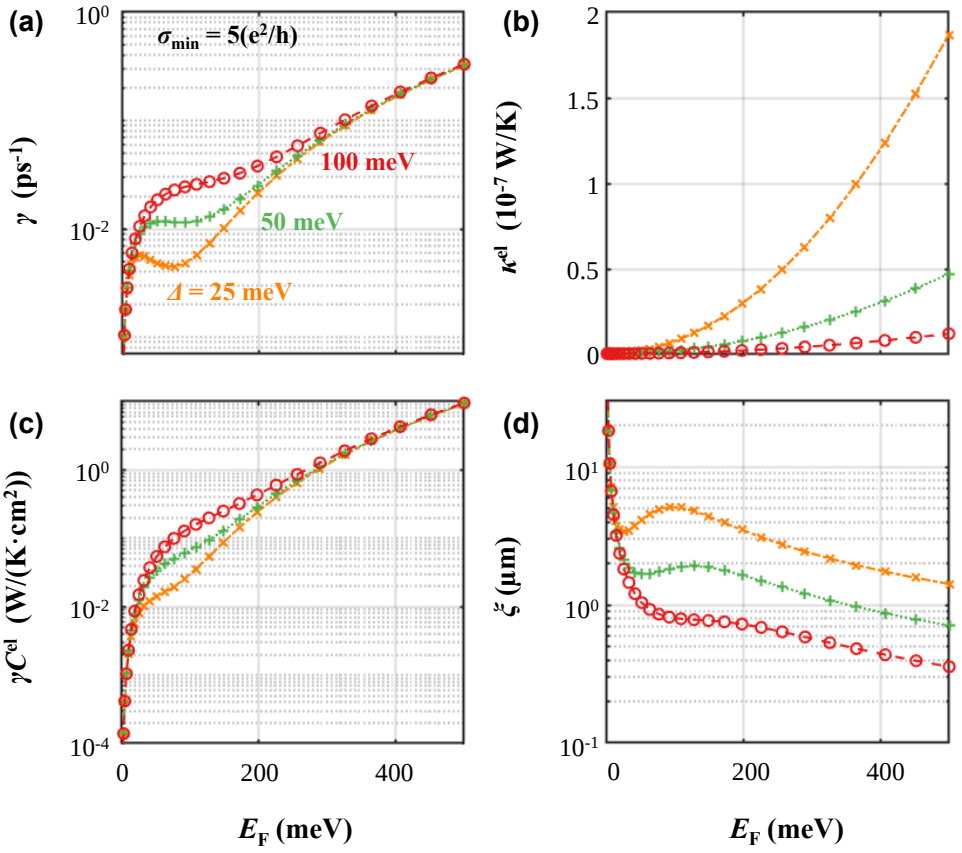

Figure 5-12: Calculated cooling rate γ (a), electron thermal conductivity κ^{el} (b), vertical loss $g^{\mathrm{el-L}} = \gamma C^{\mathrm{el}}$ (c), and cooling length ξ (d) of graphene with $\sigma_{\min} = 5(e^2/h)$, and $\Delta = 25$, 50 and 100 meV, respectively. [20]

Other Parameters

The thermal contact resistance at the metal contacts can be calculated by [212]

$$R_{\mathrm{thm}} = \frac{L_{\mathrm{Hm}}}{k_m t_m (W + 2L_{\mathrm{Hm}})} \tag{5.18}$$

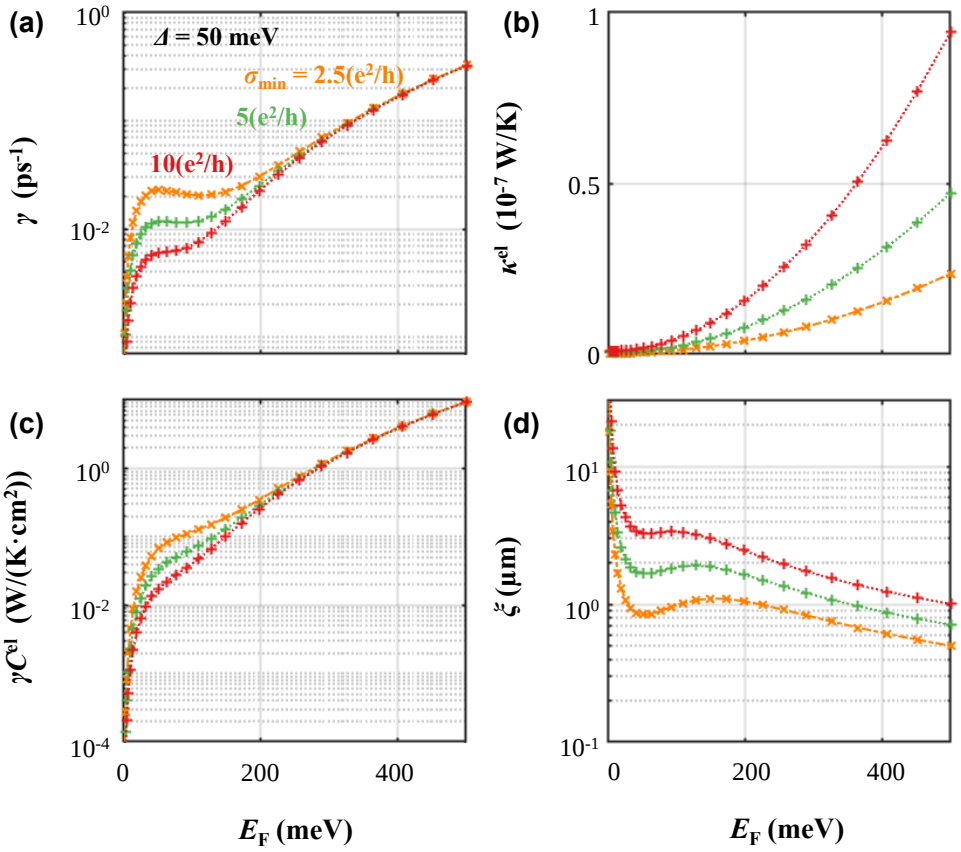

Figure 5-13: Calculated cooling rate γ (a), electron thermal conductivity $\kappa^{\rm el}$ (b), vertical loss $g^{\rm el-L} = \gamma C^{\rm el}$ (c), and cooling length ξ (d) of graphene with $\Delta = 100$ meV, and $\sigma_{\rm min}$ =2.5, 5, and 10 (e^2/h), respectively. [20]

where k_m=90 W/m/K is the 3D thermal conductivity, and t_m is the thickness (50 nm), respectively, of the contact metal; $L_{\rm Hm}$ is the healing length, given by $L_{\rm Hm} = [(k_m/k_{\rm ox})t_m t_{\rm ox}]^{1/2}$, which is calculated to be around 1 μm. The thermal conductivity and thickness of the oxde are $\kappa_{\rm ox}$=1.3 W/m/K and $t_{\rm ox}$= 285 nm.

The vertical heat loss into the substrate is given by [212]

$$g^{\rm sub} = R_{\rm Cox} + \frac{t_{\rm ox}}{k_{\rm ox}} + \frac{t_{\rm Si}}{k_{\rm Si}} \tag{5.19}$$

where $R_{\rm Cox} = 4 \times 10^{-8}$ Km^2/W is the thermal contact resistance between the 2D materials and the substrate; $k_{\rm Si}$=100 W/m/K and $t_{\rm Si}$=500 mum are the thermal conductivity and the thickness of the silicon wafer. The value of $g^{\rm sub}$ is then calculated to be 1.9×10^5 W/m^2/K.

The 2D thermal conductivity of MoS_2 is calculated by $\kappa_{MoS_2} = k_{MoS_2} t_{MoS_2}$, with k_{MoS_2}=35 W/m/K [213], and t_{MoS_2}=0.65 nm.

Simulation Results

From the above analysis, we can estimate that the typical values of the g and κ ratios are g^{el-L}/g^{sub}=10^{-5}–10^{-1}, and $\kappa^{el}_{gr}/\kappa^{tot}_{MoS_2}$=0.01-1.5, which gives rise to much stronger heat dissipations towards the MoS_2 side than towards the graphene side. Figure 5-14 (a) to (d) and Figure 5-15 show the simulated 2D temperature distributions and 1D linecuts across the junction of the device as the laser is shined at the graphene, at the graphene-MoS_2 junction, and at MoS_2. It is clearly observed that the peak electron temperature becomes much higher when the laser is shined on the graphene side, which matches the aforementioned discussion about the asymmetric heat dissipation pathways. This also explains why the junction temperature ΔT_j^{el} may reach its maximum when the center of the laser spot is away from the geometric junction, toward the graphene direction (Figure 5-14 (f)). The distance between the peak position of ΔT_j^{el} and the geometrical junction can be characterized by the cooling length ξ of hot electrons, given by Eq. (5.17). ξ becomes much bigger as the Fermi level (E_F) of graphene moves towards the charge neutrality point, as shown in Figure 5-12 and Figure 5-13. The simulated electron temperature profiles at the junction as the laser spot moves across the junction when graphene is at (lightly doped case, see the upper panel of Figure 5-14 (e)) and away from (heavily doped case, see the lower panel of Figure 5-14 (e)) the charge neutrality are plotted in Figure 5-14 (f), from which it is observed that the peak of the ΔT_j^{el} profile shifts around 400 nm farther away from the geometrical junction in the lightly doped graphene case than that in the heavily doped graphene case. The trend of the cooling length, the simulated ΔT_j^{el} peak offset with various E_F of graphene, together with the peak photocurrent offsets with 750 nm and 850 nm light excitations are plotted in Figure 5-14 (g), which are in accordance with one another.

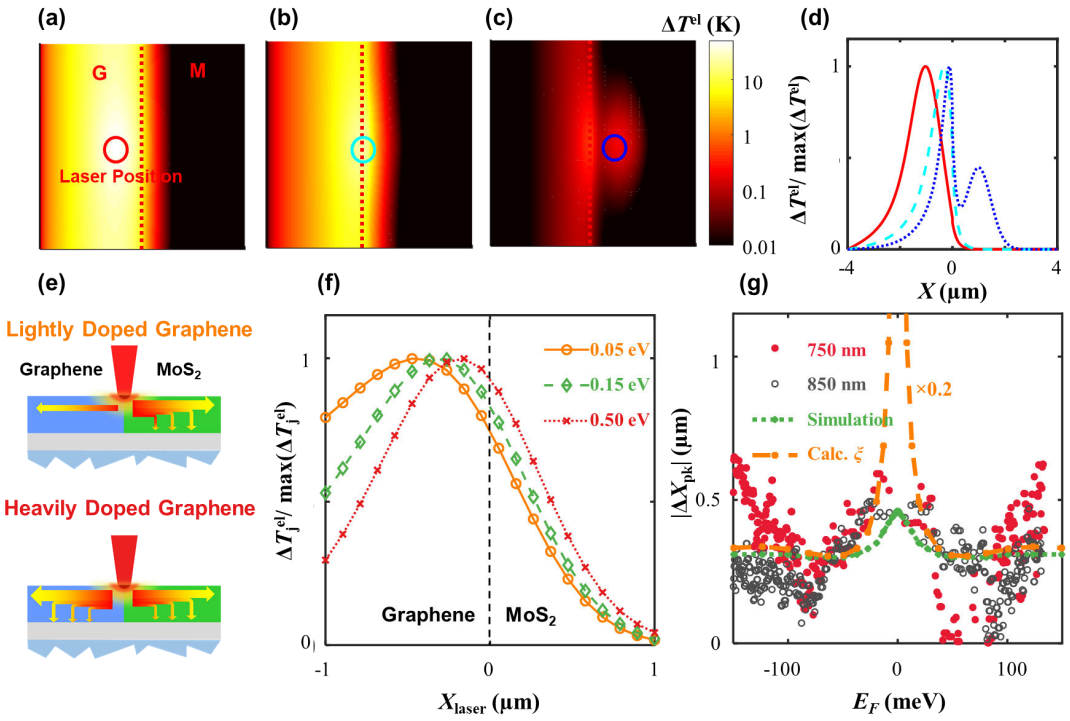

Figure 5-14: Theoretical analysis of the thermalization pathways. (a-c) Simulated distributions of electron temperature increase (ΔT^{el}) as the laser spot is on the graphene side (a), on the junction (b), and on the MoS_2 side (c). The circles indicate the center positions of the incident laser. (d) Linecuts of ΔT^{el} along the X-axis normalized to the maximum ΔT^{el} as in (a-c). (e) Schematics of the heat dissipations of photo-induced hot electrons when graphene is lightly doped (with the graphene Fermi level E_F=0.05 eV, upper panel) and heavily doped (E_F=0.5 eV, lower panel). (f) Normalized electron temperature at the graphene-MoS_2 junction with different E_F. The dashed line indicates the geometric junction. (g) Measured magnitudes of peak position offsets ($|\Delta X_{\mathrm{pk}}|$) with 750 nm (filed circles) and 850 nm (open circles) laser excitations, as well as the simulated $|\Delta X_{\mathrm{pk}}|$ and calculated electron-lattice cooling length on the graphene side (ξ), as a function of E_F.[20]

5.4 Benchmarking the Photothermoelectric Effect

Finally, we demonstrate the broad spectral range of photoresponses of such a graphene-semiconductor lateral heterojunction promised by the PTE effect. Strong photoresponse localized at the graphene-MoS_2 lateral junction were observed from SPCM mappings with a variety of wavelengths ranging from visible to short-wave infrared (SWIR) range (Figure 5-6). In Figure 5-16, the spectral photoresponsivity of three different devices is also exhibited. The response at shorter wavelengths (below 700

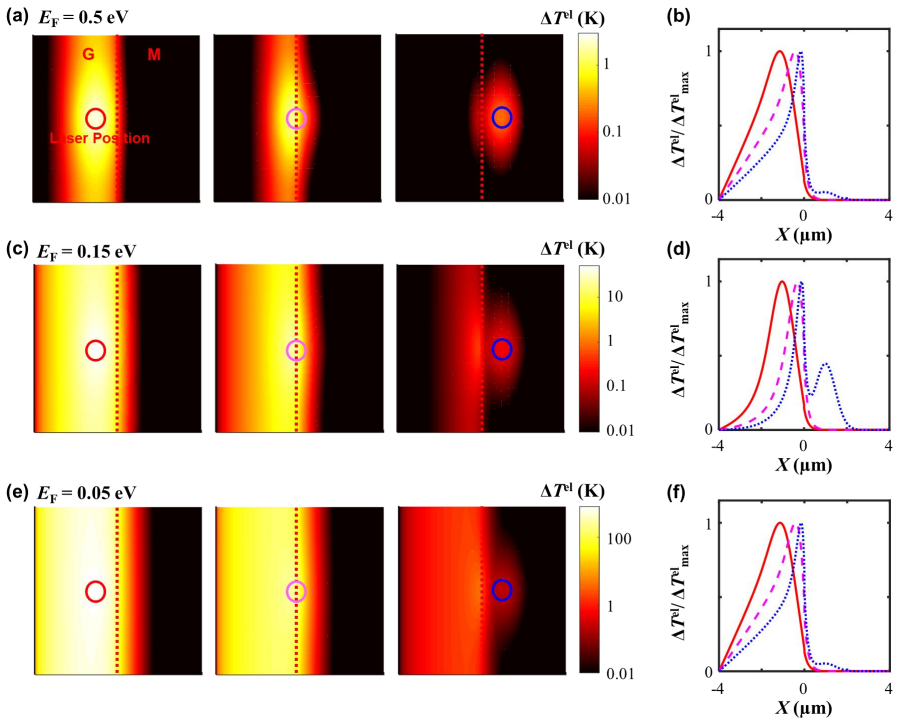

Figure 5-15: Simulated electron temperature distributions with different Fermi level of graphene.[20]

nm) follows the absorbance of MoS_2, whereas the response at longer wavelengths (above 700 nm) matches better with the absorbance of graphene on a 285 nm SiO_2/Si substrate. This, combined with the different gate-dependent photocurrents, photovoltages, and photocurrent peak positions at shorter wavelengths (550 nm and 650 nm) and longer wavelengths (750 nm and 850 nm), clearly indicates that the photoresponse with the excitation photon energies above and below the MoS_2 bandgap are dominated by the photovoltaic or photoconductive effect in MoS_2, and the PTE effect in graphene, respectively. Note that the photoresponsivity reaches its minimum at around 900 nm which corresponds to the valley of the interference fringes of the substrate. No sign of cut-off was observed in the spectral range (from 500 nm up to 1600 nm) of our measurements. Theoretically the spectral response of such a structure should be extended to at least 5 μm, limited by the Pauli blocking of graphene.

In addition, the photocurrent scaled linearly with the incident power among all the wavelengths as shown in Figure 5-17 (a). Temperature dependent measurements reveal a relatively weak non-monotonic relationship between the photoresponsivity

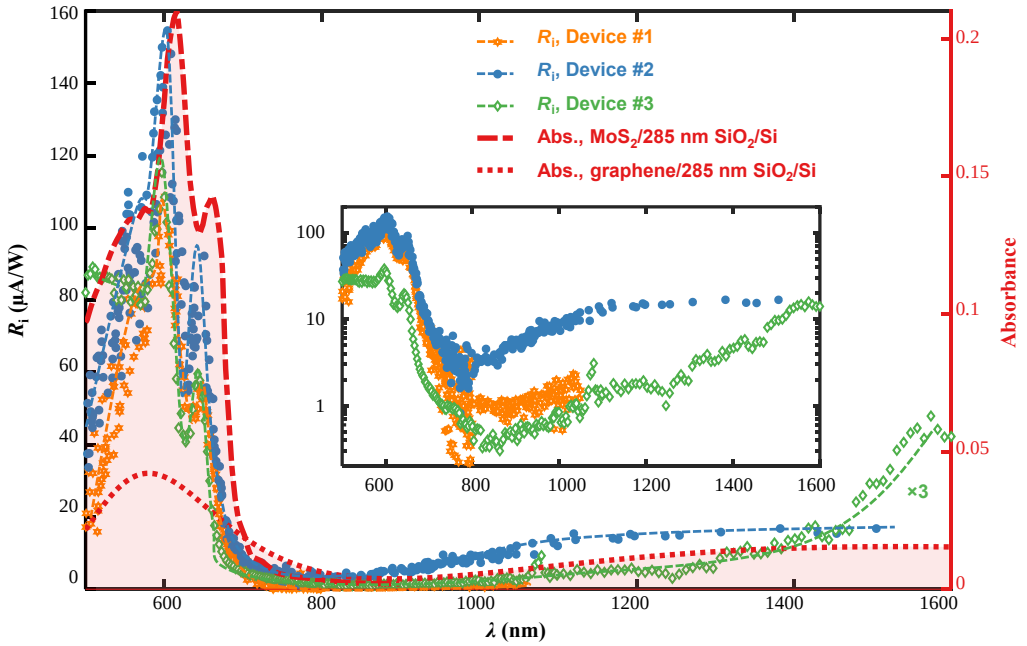

Figure 5-16: Spectral photocurrent response of the devices. Left axis: photocurrent responsivity ($\mathcal{R}_i$) as a function of the wavelength of incident light (λ) of three different devices. Right axis: Calculated absorbance of MoS_2 (red dashed) and graphene (red dotted) on a 285 nm SiO_2/Si substrate based on the complex refractive indices from Refs. [21, 22]. The inset plots the spectral responsivity in log-scale.[20]

and the temperature (Figure 5-17 (b)), which can be explained by the competition between two hot-carrier cooling mechanisms, that is, acoustic-phonon cooling (dominate at low temperature) and disorder-assisted supercollision cooling (dominate at high temperature) [205, 209]. Gate dependent SPCM measurements at different temperatures (Figure 5-18) reveals that the photocurrent peak position shifts reaches maximum at intermediate temperature (50-100 K), in accordance with such competing hot-carrier cooling mechanisms as well. According to the ultrafast photocurrent autocorrelation measurement, the intrinsic time constant of the photogeneration process was extracted to be 14 ps. These observations suggest that the graphene-2D semiconductor lateral heterojunction can be potentially used as a broadband (visible to mid-infrared), ultrafast (10 ps), and room-temperature photodetector.

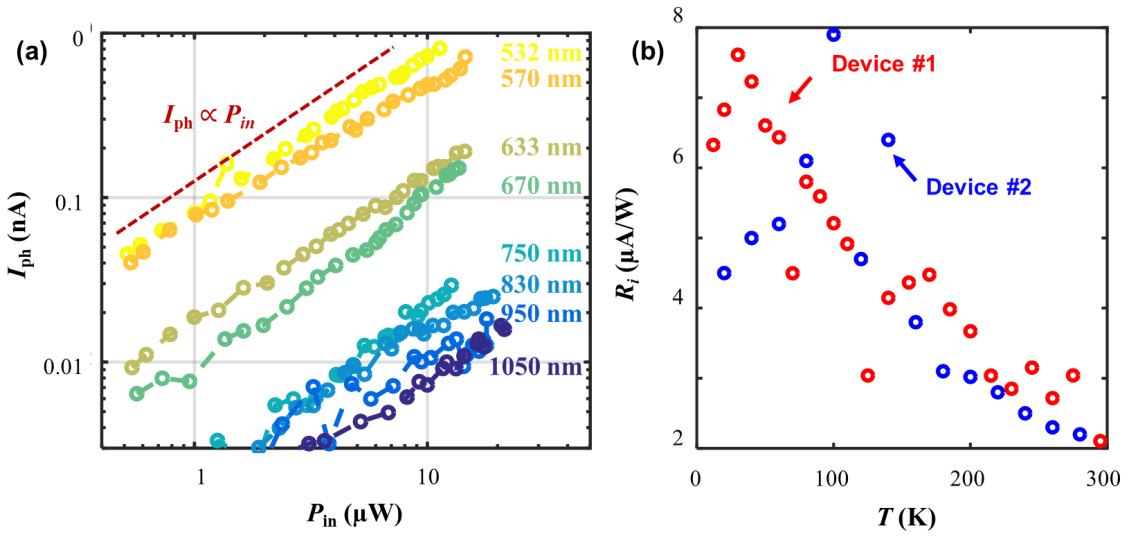

Figure 5-17: (a) photocurrent as a function of the incident power with different wavelengths. The dashed line indicates the slope of a linear power dependence. (b) Temperature dependent photoresponsivity of the devices with a 750 nm laser excitation.[20]

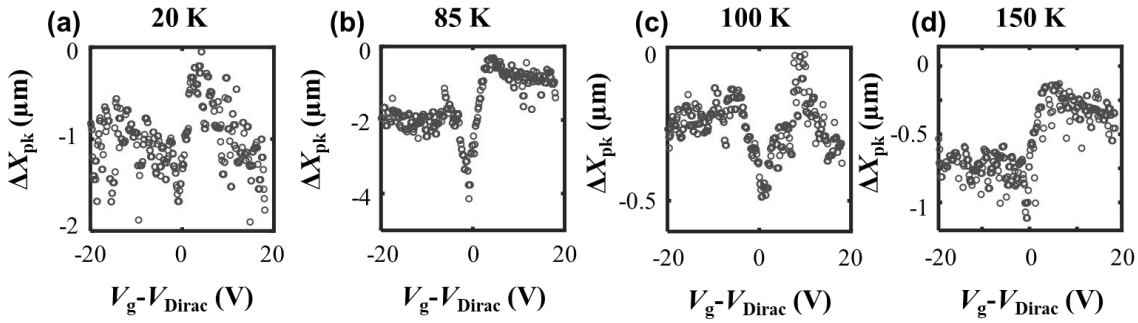

Figure 5-18: Photocurrent peak position shift extracted from the V_g-X mappings with 850 nm laser excitation and at various temperatures. (a) T=20 K; (b) T=85K; (c) T=100 K; (d) T=150 K.[20]

5.5 Summary

In summary, we have studied the photoresponse on an asymmetric lateral heterojunction between Dirac semimetal graphene and parabolic semiconductor MoS_2, and have attributed the broadband photoresponse to the PTE effect. A theoretical model was

built to describe the asymmetric thermalization pathways of the photo-generated hot carriers, which has successfully explained the spatial feature from experiments. Our study provides a new perspective to study light-matter interactions in low-dimensional systems and paves the way to novel optoelectronic applications with 2D heterostructures. With a rational design of such an in-plane asymmetry, one could possibly study many new phenomena that were either forbidden or requiring more advanced instrumentation in a homogeneous film, including exciton diffusion, dichroic spin-valley photocurrent in 2D semiconductors, and electron-electron scattering, surface plasmon polaritons in graphene.

Chapter 6

Thermo-Mechanical Bolometer

6.1 Principle of Operation

Traditional bolometers typically employ the inherent electronic properties of materials that have a temperature dependence, such as the thermally excited carrier densities, scatterings of carriers, or even transitions of crystalline structures. Here we propose a new scheme that transduces EM-radiation-induced heating into a change of resistance through mechanical deformation of the sensing component. We call it thermo-mechanical (ThM) bolometer.Our proposed device is composed of: (1) a EM wave absorber that efficiently absorbs the incident EM radiation and generates, either globally or locally, a change in temperature; (2) a thermo-mechanical transducer that converts the temperature difference into a deformation or mechanical movement; and (3) a strain sensor that senses such deformation or mechanical movement and eventually results in a resistance change of the device, which is then probed by an electronic circuit. Since these three components could be optimized relatively independently, we could achieve an ultrahigh temperature coefficient of resistance (TCR).

Figure 6-1 schematically depicts the components as well as the signal transducing path of a ThM bolometer. Firstly, the incident EM wave needs to be absorbed and converted into a change in temperature. This involves a co-optimization of the electromagnetic wave propagation and the heat transfer process of such an absorber. In the mid-IR range, incident light could be absorbed through optical phonon resonance

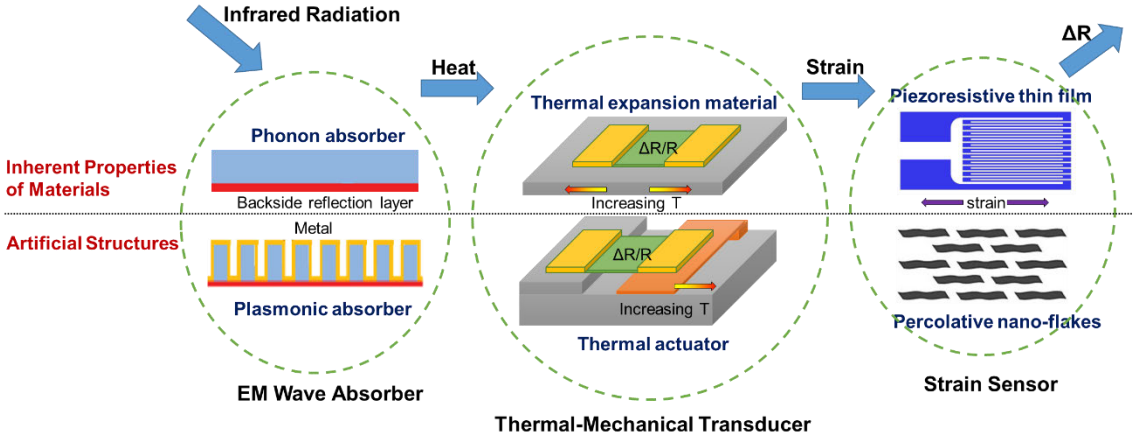

Figure 6-1: A general energy transition diagram of the proposed thermo-mechanical bolometer.

of solids, or excitation of vibrational mode of molecules, such as silicon dioxide, silicon nitride, aluminum oxide, and polymers. Another option is to artificially fabricate a periodic array of metal "nano-antennas" (refer to the "slot antenna"), and use the plasmonic resonances in the antenna array to modulate the local EM field, which could give rise to very efficient and tunable IR absorption. Regarding the optimization of the heat transfer process, both the heat capacity and the thermal conductance need to be reduced to maximize the temperature difference for a given amount of incident EM energy. To achieve this goal, the absorber may need to be thin and suspended on the substrate. Two variables are used to characterize the IR absorber: (1) the absorbance (A), defined as the percentage of the light intensity that is being absorbed, and (2) the thermal resistance (R_{th}), defined as the temperature elevation of the structure per absorbed EM power.

Secondly, the change in temperature will be converted to a mechanical deformation through a thermo-mechanical transducer. This could be realized easily by using the natural thermal expansion properties of materials, that is, the change in shape, area, and volume of matter in response to a change in temperature. The linear coefficient

of thermal expansion, α, is defined as

$$\alpha = \frac{1}{X}\frac{\mathrm{d}X}{\mathrm{d}T} \tag{6.1}$$

where X denotes the length of the film, and T represents the temperature.

Thirdly, a strain-sensitive material or structure is introduced to detect the strain generated by the thermo-mechanical transducer and convert it into electrical signal. We could either employ the inherent piezoresistive effect of materials, where the resistance changes due to the modifications of geometry or electronic structure of the materials with respect to the applied strain, or leverage the special electro-mechanical response of engineered nanostructures, which leads to a strain-dependent resistivity. A figure of merit to benchmark this component is gauge factor (GF), expressed as

$$GF = \frac{(\mathrm{d}R/R)}{\mathrm{d}X/X} \tag{6.2}$$

with R denoting the resistance.

The overall sensitivity of the ThM bolometer can be then calculated by

$$TCR = \frac{1}{R}\frac{\mathrm{d}R}{\mathrm{d}T} = \alpha \cdot GF \tag{6.3}$$

In the following, we first discuss about two different nanostructures for the strain sensor components, and then integrate these sensitive strain sensors with thermal actuators for ThM bolometers with high sensitivity.

6.2 Strain Sensors Based on Engineered Nanostructures

An essential and challenging step to "invent" any sensitive sensor is to find a material that has some signal transducing mechanism with a very sharp transition. Among them, phase transition materials (for example, metal-insulator transition, superconductor transition, *etc.*) are very promising candidates. Although these phase tran-

sitions can give rise to an extremely sharp change of resistance, and ultrasensitive bolometric sensing mechanisms, these phenomena are rarely observed in natural materials especially for those with transition temperatures at around room temperature. With rational design of nanostructures that harness some of the unique physical phenomena at nanoscale, we can possibly construct artificial metal-insulator transitions at room temperature and use them as high-sensitivity sensors. We worked on two different nanostructures whose resistance can be changed abruptly by applying strain on them. They can be used as good strain sensors, and later we implement ThM bolometers based on them.

6.2.1 Graphene Nanoflake Network

One good candidate for sensitive strain sensor is the graphene nanoflake network, or percolative graphene film. It is a resistance network composed of a number of randomly distributed graphene flakes. The basic mechanism of its strain-responsive resistance can be explained with the help of Figure 6-2 (a) and (b). The resistance of such a film is mainly from the electron hopping of the nano-gap of the overlapping regions between adjacent flakes. If a strain is applied, the overlap between adjacent flakes is decreased, leading to a larger hopping resistance throughout the percolative graphene film.

In this thesis, the graphene nano-flake dispersion was prepared through electrochemical exfoliation [214] in a sulfuric acid electrolyte, followed by the exchange of the solvent to a mixture of butanol and ethanol. The dispersion was then sonicated and diluted to obtain the desired average flake sizes and flake concentrations. The graphene nanoflake network was self-assembled through a Marangoni process at the water/alcohol interface [215].

To measure the gauge factor of the film, millimeter-sized stretchable devices were fabricated. First, a 1 mm thick polydimethylsiloxane (PDMS) film was bonded through O_2 plasma to two parallel glass bars that will be used to mount the strain sensor stably to the measurement setup. After that the Ti/Au electrodes were deposited on the two ends of the PDMS film through shadow mask and electron-beam

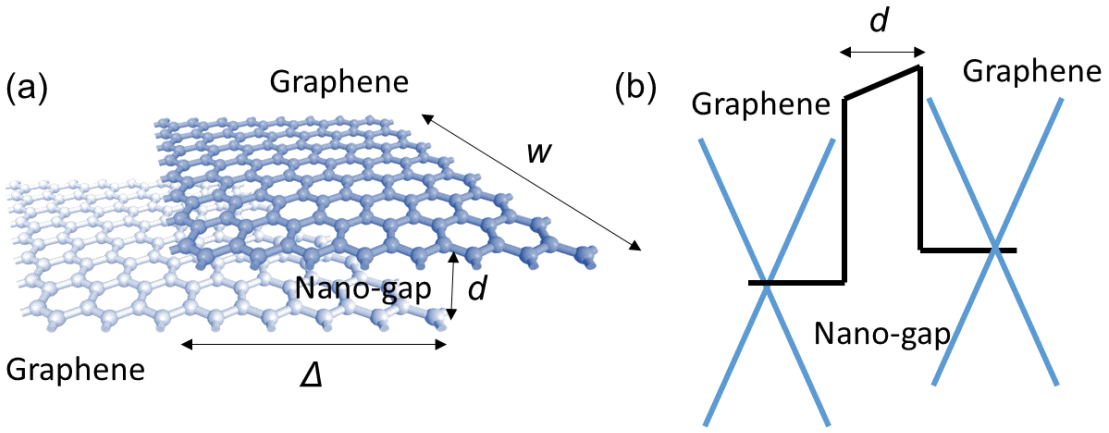

Figure 6-2: (a) Schematic and (b) band diagram of two adjacent graphene flakes with a nanometer-size gap in the overlap region.

evaporation. To define the dimension of the self-assembled graphene film, stripes of Kapton tape were used to cover the perimeter of the PDMS film as the mask for the graphene film. Then the self-assembled graphene nanoflake network film was transfered on top of the Kapton-tape-covered PDMS film. After transfer, the Kapton tape stripes were peeled off from the PDMS film, leaving only the center part of the graphene film. Figure 6-3 illustrates a schematic of the strain sensor device.

The *GF* of the assembled films are measured to be 10-300 depending on the parameters of the dispersion. Figure 6-4 plots a typical resistance-strain curve of the self-assembled graphene nanoflake network. When the strain is below 0.025, the resistance change very slowly with the strain, whereas there is an abrupt resistance change when the strain becomes bigger. The *GF* is extracted to be 10 and 300, respectively, in these two strain ranges. We found that reducing the overlapped area between neighboring flakes is very critical for enhancing the *GF* of the film. The Marangoni self-assembly guarantees that the neighboring flakes are merely touching each other, with minimal area of overlaps. Typical optical microscopic and scanning electron microscopic (SEM) images of the self-assembled films are shown in Figure

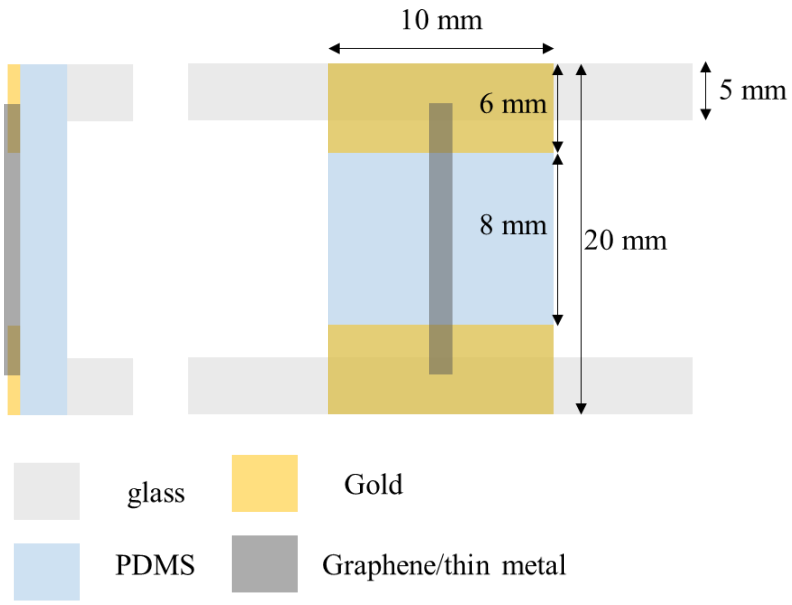

Figure 6-3: A schematic of the millimeter-sized strain sensor.

6-5. The overlapping width is below 100 nm. Such a small overlap was found widely on the self-assembled graphene film. As a comparison, the graphene nanoflake network film produced by the spray-coating method with much larger overlaps only gives an average *GF* of around 10 [216]. From our experiment, we also found that the *GF* is also related to the average thickness and lateral size of the graphene flakes, which can be tuned by changing the bulk graphite source for the electrochemical exfoliation process, and changing the sonication time during the dispersion process, respectively. The average flake size can be characterized by the optical transmittance of the self-assembled graphene film. Table 6.1 summarizes the *GF* for the graphene films produced with different recipes.

Table 6.1: The geometrical parameters and the *GF* for graphene films produced by different recipes.

Recipe	**Flake Size**	**Transmittance**	*GF*
Spray-coating	1-5 μm	Low	$<$10
Self-assembly; graphite foil	1-5 μm	78%	20-30
Self-assembly; graphite in a wrap	5-20 μm	92%	100-300
Self-assembly; graphite in a wrap; 3 hr. sonication	0.3-2 μm	90%	30-50

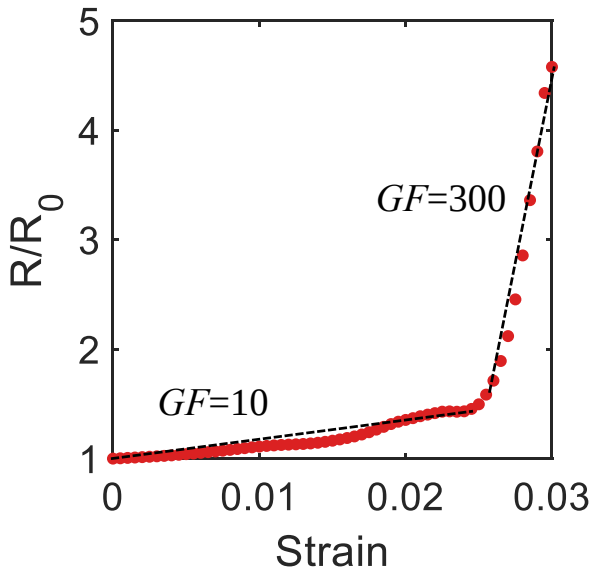

Figure 6-4: Relative resistance R/R_0 versus strain for a typical graphene nanoflake network strain sensor.

Another interesting observation is that the *GF* is strongly dependent on the number of flakes in the graphene nanoflake network film. The number of flakes can be indicated by the film size/flake size ratio. For a macroscopic film (millimeter size) with the film size/flake size ratio of 10^3, there are thousands of conduction paths in the graphene resistance network. Because of the variations in the flake sizes and overlapping areas of these conduction paths, the conductance change of each path will change differently as we stretch the film. This will lead to an averaged overall

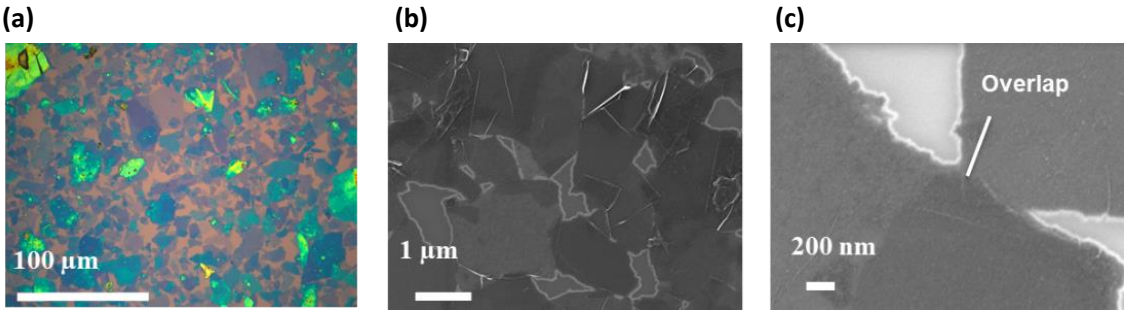

Figure 6-5: Morphologies of the self-assembled graphene nanoflake network film. (a) optical microscopic image. (b) SEM image. (c) SEM image with higher magnification to show the overlapped region.

conductance change of the resistance network and a smaller GF. For a microscopic film (tens of micrometer size) with the film size/flake size ratio of only 1-10, there are very few, if not only one, conduction paths. As a result, a much more abrupt resistance change with respect to the strain can be measured. This effect is illustrated in Figure 6-6, and the measurement results are summarized in Table 6.2.

Table 6.2: The size effect of the graphene nanoflake network strain sensor

Film Size	**Film Size/Flake Size**	GF
5 mm (macroscopic)	10^3	100-300
10 μm (microscopic)	1-10	~50,000

6.2.2 Metallic Nanogap with Self-Assembled Monolayer

Another approach to artificially engineering conductivity in a very accurate fashion is through mechanically tunable tunneling. A tunneling nano-gap can be defined by two metal segments connected by a self-assembled monolayer as schematically shown in Figure 6-7. If the gap distance is smaller than 5 nm, there can be a tunneling current flowing through such a gap. As we stretch the film, the gap distance can be

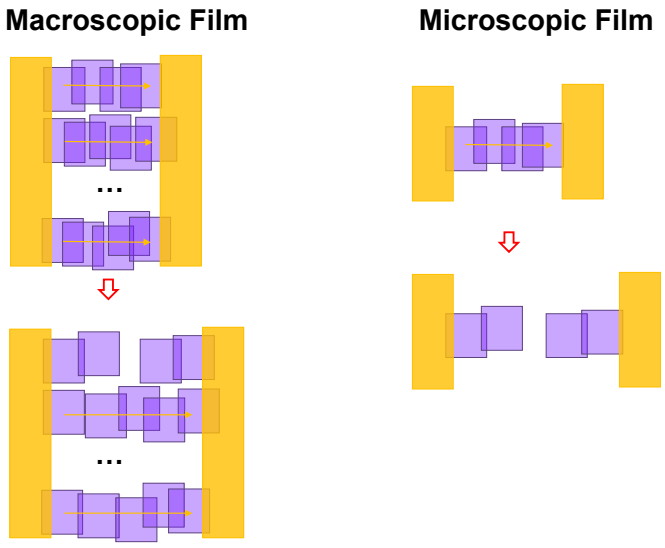

Figure 6-6: An illustration of the size effect of the graphene nanoflake network film.

changed dramatically, giving rise to a abrupt change of the tunneling resistance.

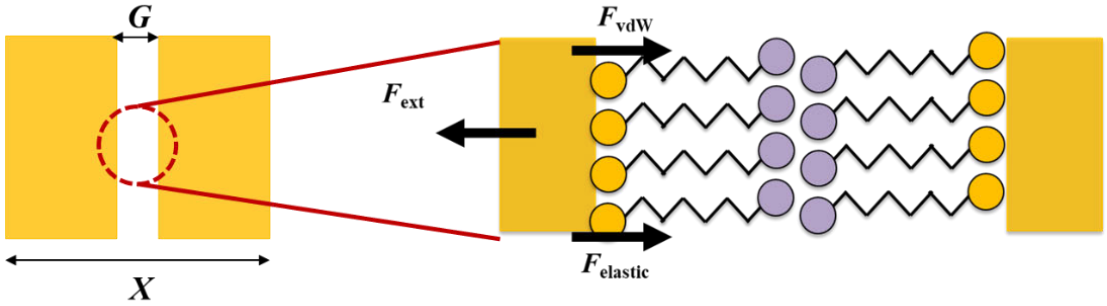

Figure 6-7: A schematic of a tunneling nano-gap defined by a self-assembled monolayer (SAM).

Theoretical Analysis

The tunneling current at low bias is dominated by direct tunneling, which can be estimated by the Simmons model [217, 218, 219, 220]:

$$I = \left(\frac{eA}{4\pi^2\hbar G^2}\right)\left\{\left(\Phi - \frac{eV}{2}\right)\exp\left[-\frac{2(2m)^{1/2}}{\hbar}\alpha\left(\Phi - \frac{eV}{2}\right)G\right]\right. \\ \left. - \left(\Phi + \frac{eV}{2}\right)\exp\left[-\frac{2(2m)^{1/2}}{\hbar}\alpha\left(\Phi + \frac{eV}{2}\right)G\right]\right\} \tag{6.4}$$

where A is the area of the metal junction; m and e are the electron mass and electron charge; G is the gap distance; V is the applied voltage, Φ is the energy barrier height; and α is an adjustable parameter that accounts for the effects of the barrier shape and the electron effective mass.

If assuming the total length of the metal film is X, and at the low-bias limit ($\frac{eV}{2} << \Phi$), the gauge factor (GF) can be expressed as

$$GF = \frac{\mathrm{d}R/R}{\mathrm{d}X/X} = -\frac{\mathrm{d}\log(I)}{\mathrm{d}G}\cdot\frac{\mathrm{d}G}{\mathrm{d}X}\cdot X \\ \approx \left(\frac{2}{G} + \frac{2(2m)^{1/2}}{\hbar}\alpha\Phi^{1/2}\right)\cdot\frac{K_{\mathrm{metal}}}{K_{\mathrm{gap}} + K_{\mathrm{metal}}}\cdot X \tag{6.5}$$

where K_{gap} and K_{metal} are the effective spring constants of the metal and the SAM (gap) sections. As a simple estimation, assuming $\Phi \approx 4$ eV, $\alpha = 1$, and $K_{\mathrm{metal}} >> K_{\mathrm{gap}}$, for a $G = 3$ nm gap in a $X = 5$ μm metal film, the gauge factor is $GF \approx 21.14\mathrm{nm}^{-1}\cdot 1\cdot 5\mu\mathrm{m}$ =105,700. This is an extremely sensitive mechanism.

The SAM plays two roles in this structure. First, the gap distance can be defined by the SAM thickness, which is determined by the length of the molecular chains. Second, the existence of SAM can avoid the two metal segments from being too close to each other, which can cause the stiction problem. If no SAM is present, the nano-gap is determined by the external force (applied by the polymer base) and the van der Waals (vdW) force between the metal surfaces. Because the vdW force is inverse proportional to the cube of the gap distance G, such a system is mechanically unstable. If a SAM layer is added to the nano-gap, the attraction force can then be determined by an elastic force which is almost independent of the gap distance. Therefore, the gap distance can be tuned stably and smoothly by the external force.

Experimental Results

Metal nanogaps were fabricated through a prestretching method. Very thin (<10 nm) and continuous Pt film was first deposited onto the PDMS film through electron-beam evaporation. The device structure is similar to the graphene nanoflake network device, as shown in Figure 6-3. To guarantee the uniformity of the thin Pt film, very slow deposition rate (0.1-0.2 Å/s) was used for the metal deposition. Before the actual measurement, the Pt/PDMS film was slowly pre-stretched to a large strain (>0.05) to generate aligned cracks perpendicular to the direction of stretching. Then a small strain was applied to measure the strain sensor characteristics. Figure 6-8 shows the optical microscopic image and the SEM image of the cracked Pt film generated by the

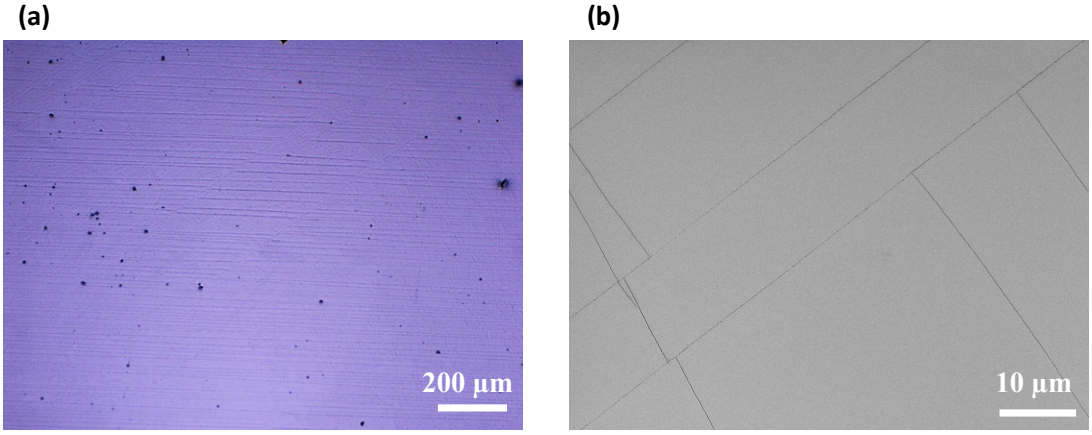

Figure 6-8: (a) Optical microscopic image and (b) SEM image of the Pt metal cracks generated by the prestretching method.

Figure 6-9 plot the strain sensor characteristics of the cracked Pt films with different thicknesses. The gauge factors were extracted to be 100-1000 for all the devices. This is much lower than the theoretical prediction given by Eq. (6.5), which may be caused by the roughness of the gaps and the non-uniform distributions of the cracks throughout the film. Another trend is that the thinner Pt film results in higher initial resistance but wider dynamic range of the strain sensors. This is because of the reduction of the conductance and the stiffness of the film as the thickness becomes smaller.

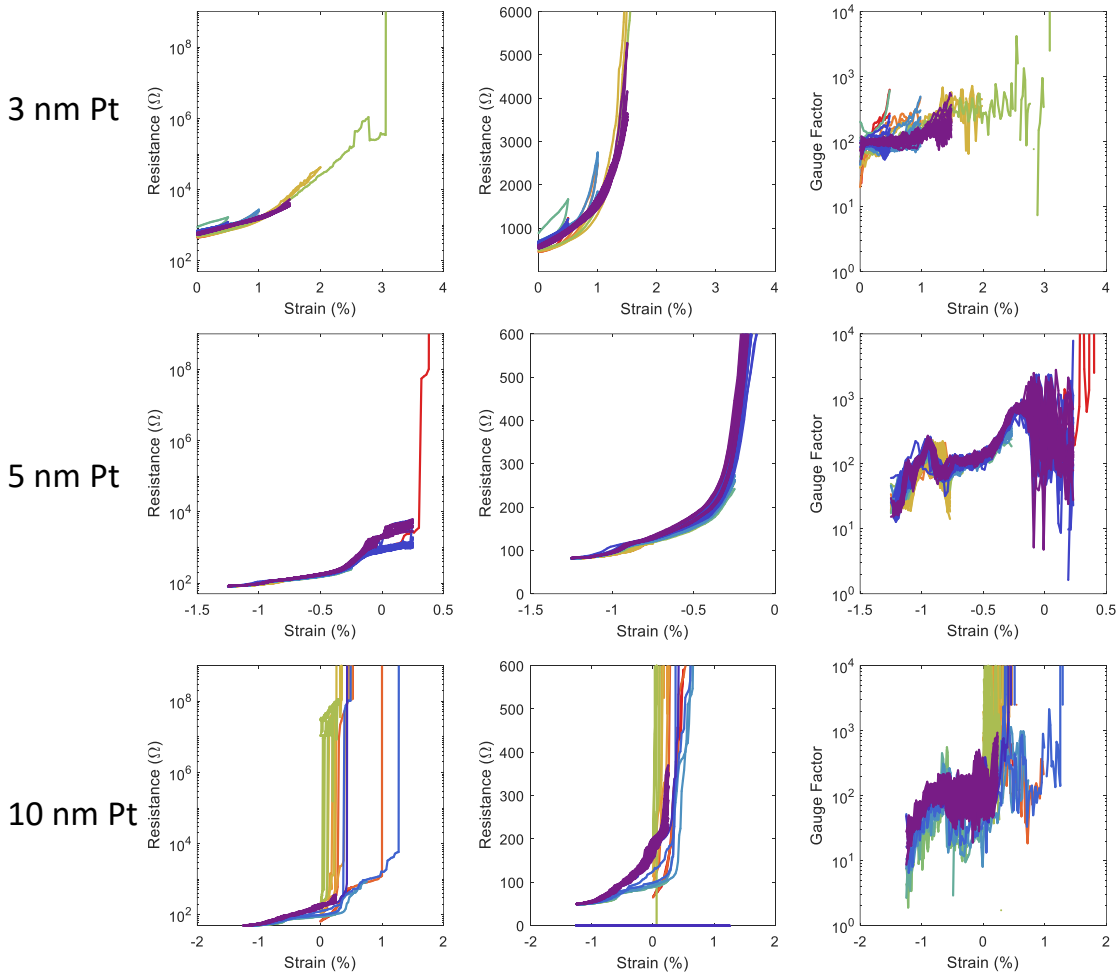

Figure 6-9: Strain sensor characteristics of cracked Pt films with different Pt thickness.

It is also interesting to note that after a certain threshold, there is an abrupt increase of the resistance, which could lead to a much higher GF. However, the resistance-strain characteristics in this regime become very inconsistent. This is due to the stiction problem as discussed earlier.

To solve this problem, we can introduce a SAM layer into the nanogaps. We chose 1H,1H,2H,2H-perfluorooctyl-1-thiol as the SAM molecule. The SAM layer can be grown either in a liquid phase in which the thiol molecules are disolved in ethanol, or in a gaseous phase in which the thiol molecules are vaporized in a vacuum chamber. Figure 6-10 plots the strain sensor characteristics of a 10 nm cracked Pt film before

and after the SAM growth. The device with the SAM layer shows an improved dynamic range (from 0.003 to 0.045 in strain) and six orders of magnitude consistent resistance change.

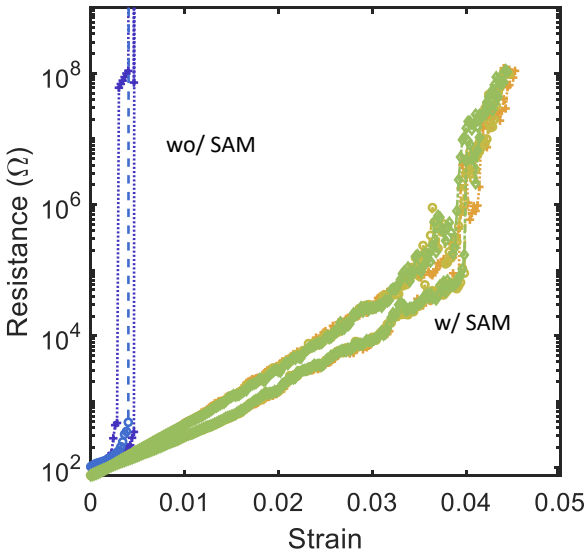

Figure 6-10: The resistance-strain characteristics of a 10-nm cracked Pt film with and without the SAM layer.

Finally, we benchmark the two strain sensor technologies that we developed and compared the measured *GF* with other technologies as shown in Figure 6-11. The microscopic graphene nanoflake network films displays one order of magnitude higher sensitivity than other technologies, and the metal nanogap based strain sensors also have a *GF* up to 1000, which is among the best strain sensor technologies.

6.3 Graphene-Polymer Thermo-Mechanical Bolometer

6.3.1 Device Structure and Fabrication Process

We can integrate the graphene nanoflake network strain sensor with a polymer based thermal actuator to implement the ThM bolometer. Two geometries are considered in

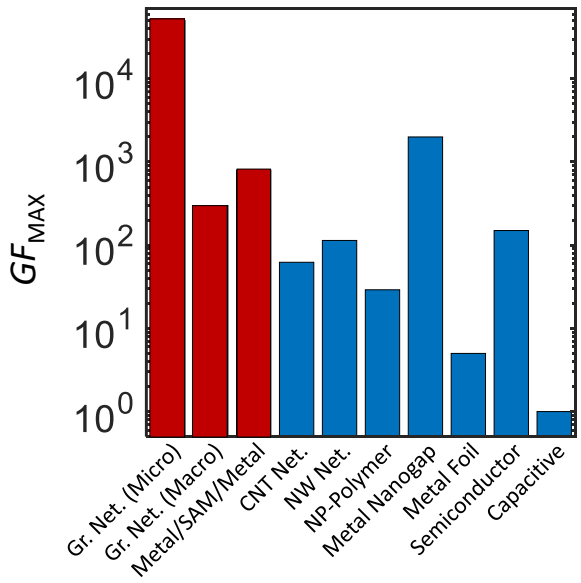

Figure 6-11: A summary of the measured *GF* of the graphene nanoflake network and the metal/SAM/metal nanogap strain sensors in comparison with existing strain sensor technologies [23, 24].

the implementation of the proposed devices (Figure 6-12). In the vertical structure, the percolative graphene channel and the polymer base are stacked directly on top of each other, whereas in the lateral structure, the graphene channel and the polymer base are placed on the same plane, and connected through a "T" shaped rigid frame. In the vertical structure, because of the mismatch of the thermal expansion coefficients and the elastic modulus between the two layers, both the lateral expansion and the vertical bending need to be taken into account. In the lateral structure, however, the symmetric mechanical architecture makes the lateral expansion dominate the thermal deformation. In addition, the "T" shaped rigid frame transfers the larger displacement induced by the longer polymer bases to the shorter graphene channel, which equivalently amplifies the strain of the graphene channel. Figure 6-12 (c) and (d) shows the microscopic images of the as-fabricated vertical and lateral thermo-mechanical bolometers.

The fabrication process flow of the device is shown in Figure 6-13. A 300 nm SiO_2/Si wafer is used as the substrate. Firstly, a photolithography and a reactive

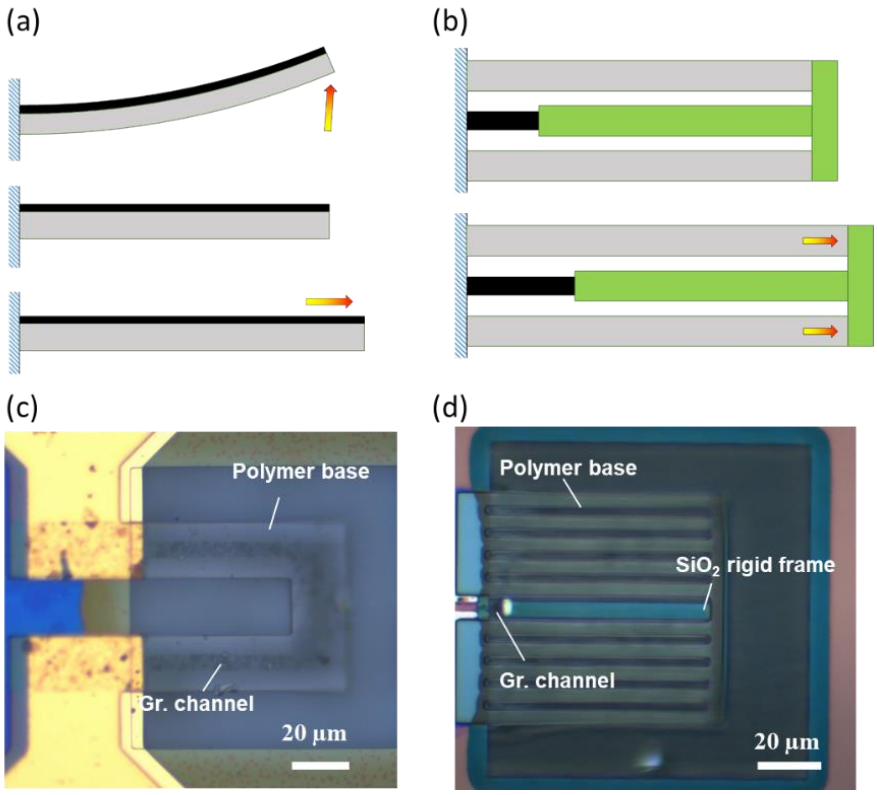

Figure 6-12: Schematics of the vertical (a, side view) and lateral (b, top view) and the corresponding microscopic images (c and d) of the graphene-polymer thermos-mechanical bolometers.

ion etching (RIE) step with CF_4 and O_2 as the reactive gas are employed to open windows on the SiO_2 layer. Secondly, gold electrodes are defined by photolithography, and deposited through e-beam evaporation followed by a lift-off process. Thirdly, the substrate is treated with diluted potassium hydroxide solution and the percolative graphene film is transferred onto it. If the graphene layer has a different pattern than the polymer base layer, photolithography and RIE with O_2 and He are carried on to define the graphene channel. Fourthly, the polymer (PDMS in hexane, or SPR700) is spin-coated onto the substrate followed by baking at required temperature to cure the film. Fifthly, another photolithography is made to define the patterns of the polymer base, and a RIE with CF_4 and O_2 is done to etch the unwanted PDMS film if PDMS is used. Finally, XeF_2 etching is employed to undercut the underlining silicon to suspend the thermo-mechanical bolometer. Although this process is currently designed for a

silicon-based platform, it is also possible to replace the supporting film with glass, plastics, or any other low-cost/flexible substrate.

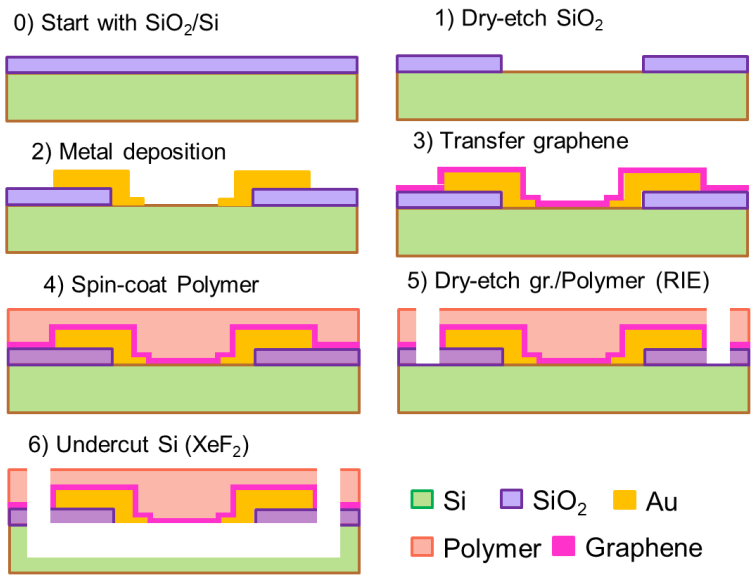

Figure 6-13: Process flow of the graphene/polymer thermo-mechanical bolometer.

6.3.2 Theoretical Analysis

In this section, we performed a theoretical analysis of the thermo-mechanical response in the vertical and lateral thermal actuators as described in subsection 6.3.1.

Vertical Thermal Actuator

The structure and dimensions are schematically shown in Figure 6-14. The length of the bilayer beam is L, and the widths and thicknesses of the two layers are w_1, t_1, and w_2, t_2, respectively. The Young's modulus and the thermal expansion coefficients of the two layers are E_1, α_1, and E_2, α_2, respectively. We define the y-axis to be in the vertical direction with the origin at the interface of the two layers.

The axial strain of each layer can be expressed by

$$\varepsilon_{xxi} = \frac{\sigma_{xxi}}{E_i} + \alpha_i \Delta T = \varepsilon_0 + \frac{y}{\rho_0}, i = 1, 2 \tag{6.6}$$

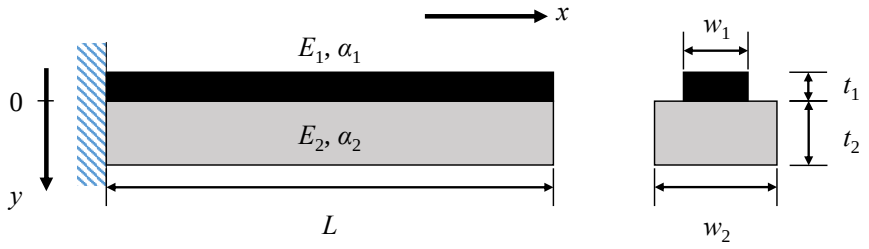

Figure 6-14: Schematic of the vertical thermal actuator.

where ΔT is the temperature change; σ_{xxi} is the axial stress; ε_0 and ρ_0 are the strain and radius of curvature at $y = 0$.

If no external force is applied on the beam,

$$\int_{-t_1}^{0} \sigma_{xx1} w_1 \mathrm{d}y + \int_{0}^{t_2} \sigma_{xx2} w_2 \mathrm{d}y = 0 \tag{6.7}$$

$$\int_{-t_1}^{0} \sigma_{xx1} w_1 y \mathrm{d}y + \int_{0}^{t_2} \sigma_{xx2} w_2 y \mathrm{d}y = 0 \tag{6.8}$$

We can solve for Eqs. (6.6) to (6.8) to obtain

$$\begin{aligned} \varepsilon_0 =& \frac{\Delta T}{D} \left[4 \left(\alpha_1 E_1 w_1 t_1 + \alpha_2 E_2 w_2 t_2 \right) \left(E_1 w_1 t_1^3 + E_2 w_2 t_2^3 \right) \right. \\ & \left. - 3 \left(\alpha_2 E_2 w_2 t_2^2 - \alpha_1 E_1 w_1 t_1^2 \right) \left(E_2 w_2 t_2^2 - E_1 w_1 t_1^2 \right) \right] \end{aligned} \tag{6.9}$$

$$\begin{aligned} \frac{1}{\rho_0} =& \frac{6\Delta T}{D} \left[\left(\alpha_2 E_2 w_2 t_2^2 - \alpha_1 E_1 w_1 t_1^2 \right) \left(E_1 w_1 t_1 + E_2 w_2 t_2 \right) \right. \\ & \left. - \left(\alpha_1 E_1 w_1 t_1 + \alpha_2 E_2 w_2 t_2 \right) \left(E_2 w_2 t_2^2 - E_1 w_1 t_1^2 \right) \right] \end{aligned} \tag{6.10}$$

where

$$D = \left(E_2 w_2 t_2^2 - E_1 w_1 t_1^2 \right)^2 + 4 E_1 E_2 w_1 w_2 t_1 t_2 \left(t_1 + t_2 \right)^2 \tag{6.11}$$

In our case, the thickness of the graphene layer (1st layer) is much smaller than

the thickness of the polymer layer (2nd layer), whereas the Young's modulus of the graphene layer is much bigger than that of the polymer layer. We can thus simplify the above expressions by assuming $t_1 << t_2$, and $E_1 w_1 t_1 \approx E_2 w_2 t_2$. Therefore, we can obtain the strain ε_{xx1} in the 1st layer ($y = -t_1/2$) and the bending radius ρ_1 to be

$$\varepsilon_{xx1} = \varepsilon_0 - \frac{t_1}{2\rho_0} \approx \frac{4K_1\alpha_1 + K_2\alpha_2}{4K_1 + K2}\Delta T \tag{6.12}$$

$$\frac{1}{\rho_1} \approx \frac{1}{\rho_0} \approx \frac{6K_1}{4K_1 + K_2}\frac{\alpha_2 - \alpha_1}{t_2}\Delta T \tag{6.13}$$

where $K_i = E_i w_i t_i$, $(i = 1, 2)$.

To make the lateral stretching of the polymer layer the dominating deformation, we need to guarantee that $K_2 >> K_1$.

Lateral Thermal Actuator

For the lateral device, the structure in the vertical direction is symmetric, so the vertical deformation can be neglected. Then the thermo-mechanical response of this structure can be simply considered as two sets of elastic beams (graphene and polymer) stretching against each other. The device structure and dimension is illustrated in Figure 6-15. The lengths, widths, thicknesses, and numbers of the graphene (no. 1) and the polymer (no. 2) beams are denoted as L_i, w_i, t_i, and N_i $(i = 1, 2)$, respectively. Assuming the mechanical deformation of the rigid SiO_2 frame (green) can be neglected, we have

$$\varepsilon_{xxi} = \frac{\sigma_{xxi}}{E_i} + \alpha_i \Delta T = \varepsilon_0 + \frac{y}{\rho_0}, i = 1, 2 \tag{6.14}$$

$$\sigma_{xx1} w_1 t_1 N_1 + \sigma_{xx2} w_2 t_2 N_2 = 0 \tag{6.15}$$

$$\varepsilon_1 L_1 = \varepsilon_2 L_2 \tag{6.16}$$

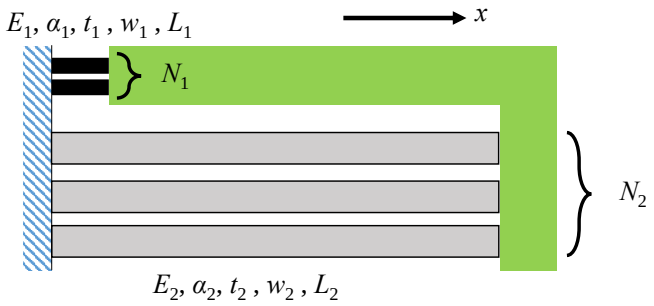

Figure 6-15: Schematic of the lateral thermal actuator.

Solving Eqs. (6.14) to (6.16), we can obtain

$$\varepsilon_1 = \frac{k_1\alpha_1 + k_2\alpha_2\,(L_2/L_1)}{k_1 + k_2}\Delta T \tag{6.17}$$

where $k_i = N_i E_i w_i t_i / L_i = N_i K_i / L_i$ is the overall spring constant of the two sets of beams.

When the spring set of the polymer is much stronger, or $k_1 << k_2$, Eq. (6.17) can be simplified as

$$\varepsilon_1 \approx \left(\frac{L_2}{L_1}\right)\alpha_2 \Delta T \tag{6.18}$$

As a result, the thermal expansion induced in the polymer layer can be transduced to the graphene layer with an amplification factor (L_2/L_1).

Comparison of Vertical and Lateral Geometries

According to Eqs. (6.12), (6.13) and (6.18), we draw the following observations: (1) Only the lateral deformation contributes to the sensitivity of the device. Therefore, we need to select the material properties and design the geometry very well to prevent the vertical structure from bending vertically, instead of stretching laterally. (2) The lateral geometry is symmetric in the vertical direction, so there is not vertical bending motion. (3) There is a mechanical amplification factor of the lateral structure that is decided simply by the ratio of the lengths of the polymer layer and graphene layer. We can thus further amplify the thermo-mechanical resistance change by increasing

this geometrical factor. Overall, the lateral thermal actuator is advantageous in terms of both the design complexity and the sensitivity over the vertical thermal actuator, although the lateral device is more challenge to fabricate, given that the graphene sensing layer needs to be suspended by itself. In the following, we implemented both designs and showed that the experimental results matches with our theoretical analysis very well.

6.3.3 Experimental Results

Material Selection

According to the theoretical analysis, we can see that the polymer beam should be stiff enough to dominate the thermo-mechanical response for both the vertical and the lateral geometries. Two key material parameters are the thermal expansion coefficient α and the Young's modulus E. Figure 6-16 summarizes α versus E for different materials. The groups of elastomer and polymer are among the materials with higher thermal expansion coefficients ($\alpha \sim 10^{-4}$ K^{-1}). Although elastomers may have even larger thermal expansion coefficient, their Young's modulus are two to three orders of magnitude lower than the polymer group. We selected PDMS in the elastomer group, and a photoresist (SPR 700, a type of phenolic basin) in the polymer group, and fabricated the vertical thermal actuators. The microscopic images of the as-fabricated devices are shown in Figure 6-17. It is observed that there is a severe initial vertical bending for the PDMS/graphene device, whereas the photoresist/graphene structure is completely flat. This initial morphology indicate that the PDMS film may be too soft to dominate the mechanical deformation of the actuator. Therefore, we selected the SPR700 as the polymer part of the final devices.

Temperature Dependent I-V Characteristics

To measure the temperature dependence of the I-V characteristics of the ThM bolometers, the as-fabricated chip was wire-bonded to a chip carrier, and mounted inside a cryostat with electrical feedthroughs. The devices were kept in vacuum ($< 10^{-4}$ Torr)

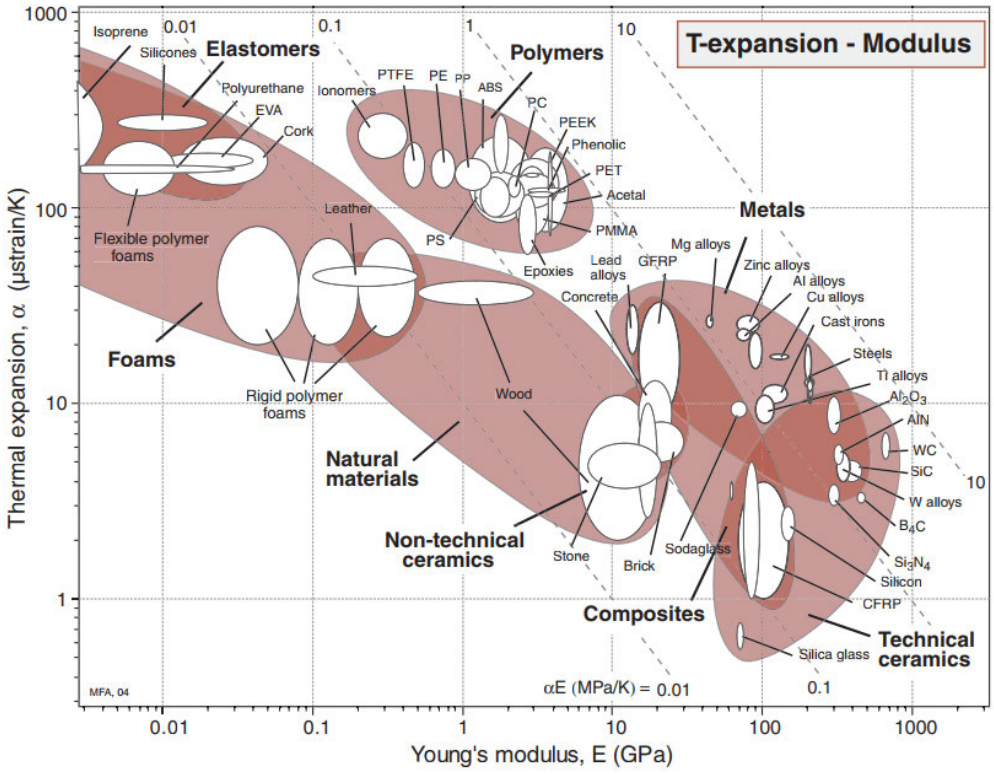

Figure 6-16: A summary of α versus E for different materials [**?**].

during the measurement. A temperature controller (Lakeshore 325) equipped with liquid nitrogen was used to change the temperature of the devices.

Figure 6-18 and Figure 6-19 plot two typical temperature dependence of the ThM bolometer. The first type shows a gradual change in resistance in terms of temperature (Figure 6-18), and the second type shows an abrupt transition at a specific temperature (Figure 6-19). The type 1 behavior may be associated with the average overlap area decrease of adjacent nano-flakes in the case of strongly bonded graphene nanoflake network, whereas abrupt "switch" like response (type 2) are presumably due to the decrease of the number of conduction paths of the percolative film in the case of a weakly bonded graphene nanoflake network.

We can extract the temperature coefficient of resistance (TCR) from the slope of the R-T plots, according to the following relation:

$$R(T) = R_0 \exp\left[TCR \cdot (T - T_0)\right] \tag{6.19}$$

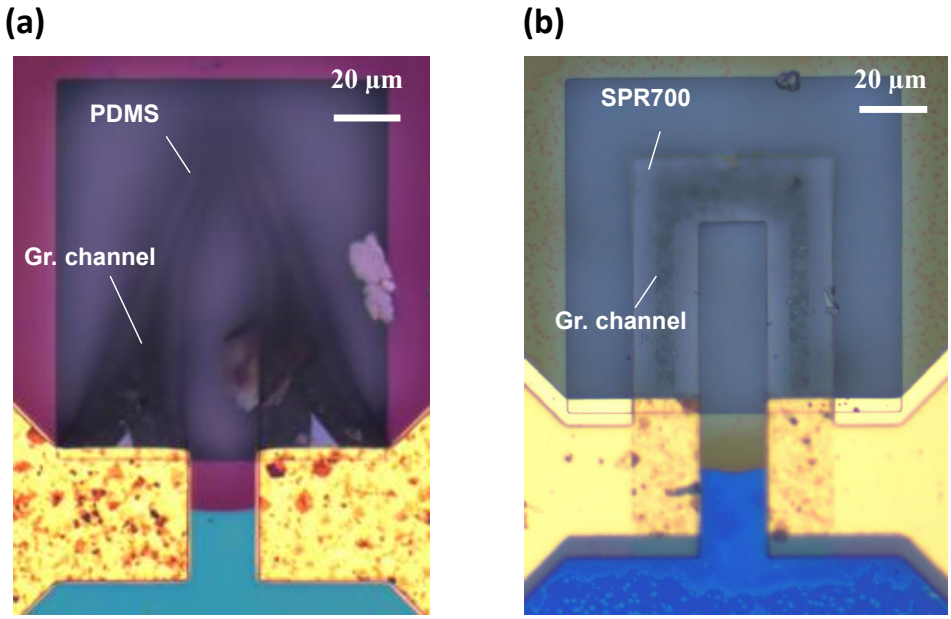

Figure 6-17: Optical microscopic images of (a) PDMS/graphene and (b) photoresist/graphene vertical thermal actuators.

Table 6.3 summarizes the extracted *TCR* and the temperature range of effective operation of the graphene/polymer ThM bolometer. The extracted *TCR* are compared with the state-of-the-art bolometers, which is shown in Figure 6-20. As we can see, our graphene/polymer ThM bolometer is more than one order of magnitude better than other technologies.

Table 6.3: A summary of the extracted *TCR* and operation temperature range T_{op} of graphene/polymer ThM bolometers.

Structure	*TCR*	T_{op}
Vertical Type 1	0.005-0.014 K^{-1}	Wide
Vertical Type 2	4.88 K^{-1}	80-110 °C
Lateral Type 2	20 K^{-1}	5-15 °C

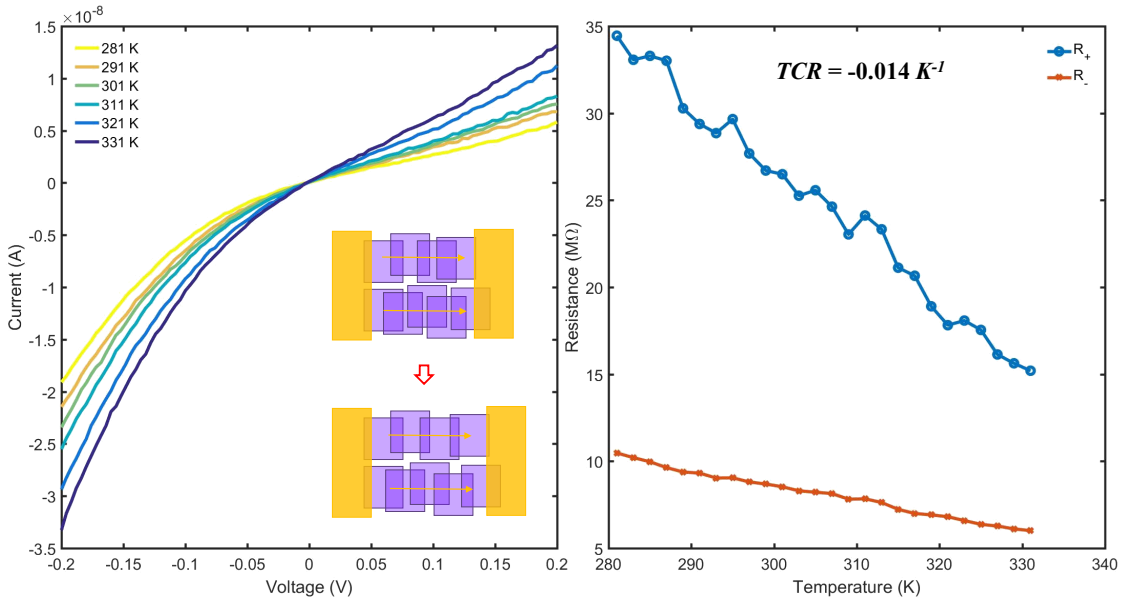

Figure 6-18: Temperature dependent I-V characteristics of a graphene/polymer ThM bolometer. Type 1: gradual change.

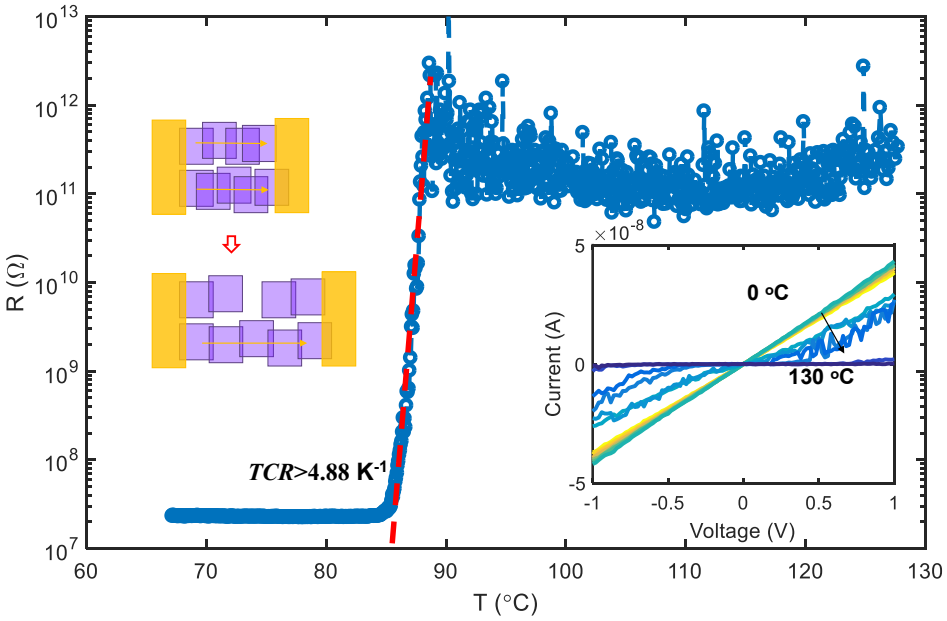

Figure 6-19: Temperature dependent I-V characteristics of a graphene/polymer ThM bolometer. Type 2: abrupt transition.

There are still some issues that need to be addressed. First, the device-to-device variation and the yield still need to be improved. Because of the random distribution

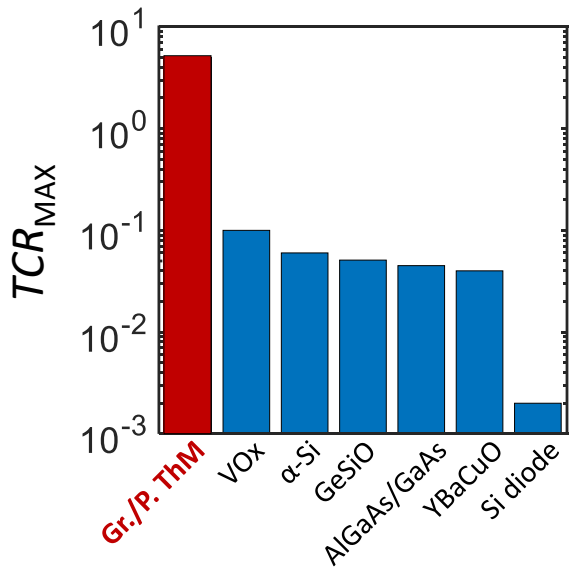

Figure 6-20: *TCR* values for different bolometric technologies [25].

of the graphene nanoflake network, only a small portion of the devices after fabrication are conductive and can respond strongly to the temperature change. To solve this, the electrochemical exfoliation and the self-assembly process for the graphene nanoflake network need to be optimized. Second, for the same device, we found a hysteretic behavior as we increase and decrease the temperature. In addition, the transition temperature was found to drift randomly as we swept the temperature repeatedly. The plots in Figure 6-21 are representative characteristics with the hysteresis and the transition temperature drifting effects. Possible causes of these non-ideal effects may be the plastic mechanical response of the polymer beams, the change of locations of the graphene flakes, and the mechanical instability due to the abrupt vdW force change with the nanogap distance.

IR Radiation Response

We performed a scanning photocurrent microscopy measurement on the graphene/polymer ThM bolometer. A CO_2 laser with 10.6 μm wavelength was used as the IR light

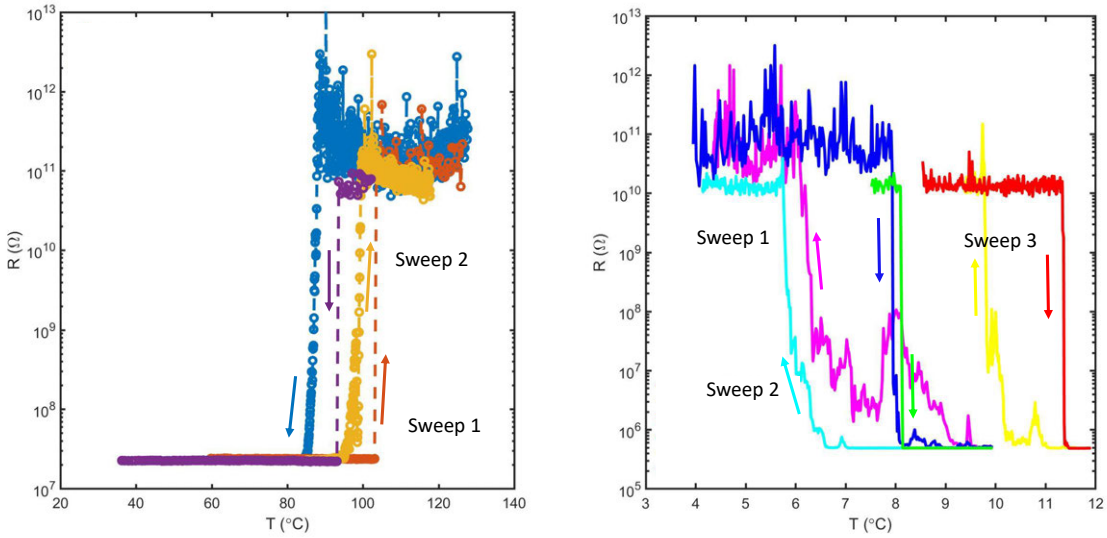

Figure 6-21: Hysteresis and transition temperature drifting.

source. Figure 6-22 displays the microscopic image, the IR reflectance mapping, as well as the photo-resistance mapping of a vertical graphene/polymer ThM bolometer. It corresponds to a 4.58% resistance change per mW input power.

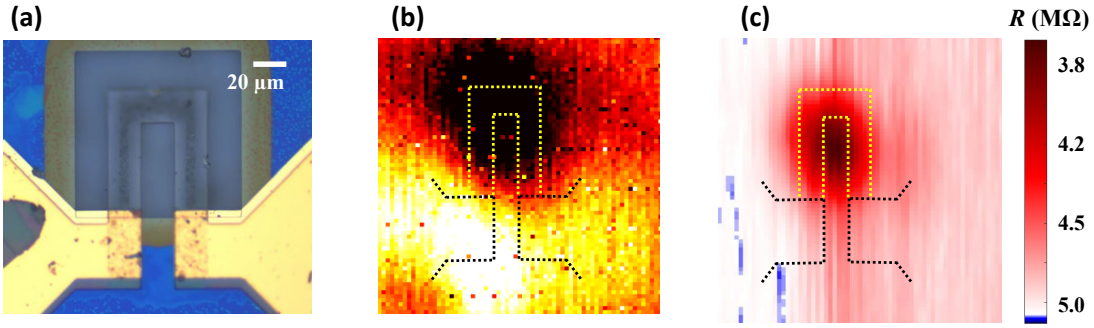

Figure 6-22: IR response of the graphene/polymer ThM bolometer. (a) Optical microscopic image. (b) Reflectance mapping. (c) Resistance mapping. The incident laser is a 10.6 μm CO_2 laser. The incident power density is 335 W/cm^2.

6.4 Metal/Molecule/Metal Thermo-Mechanical Bolometer

6.4.1 Device Structure and Fabrication Process

Figure 6-23 illustrate the structure of the metal/molecule/metal ThM bolometer. It is composed of two thin Pt films placed horizontally and separated by a nanogap filled with a SAM layer. On top of the Pt films are thicker Ni films as the supporting

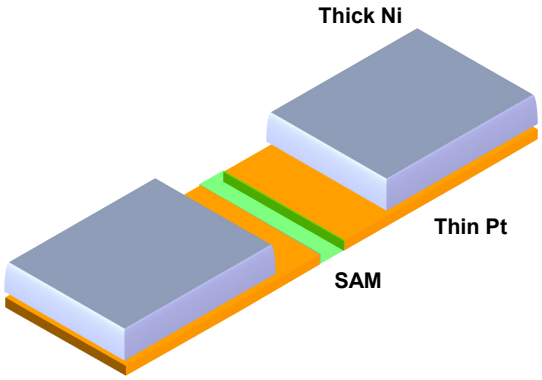

Figure 6-23: Schematic of the metal/molecule/metal ThM bolometer.

The process flow is illustrated in Figure 6-24. First, a poly(methyl methacrylate) (PMMA)/methyl methacrylate (MMA) double layer e-beam resist was spin-coated onto the substrate. After electron-beam lithography to define the narrow lines (100-300 nm width) for the nanogap mask and development, the PMMA masks were suspended on the substrate. Then, two steps of thin metal evaporation (5 nm Pt) with opposite tilted angles ($\pm 15°$) were done to form the nanometer-sized gaps. A third layer of thick metal (100 nm Ni) were evaporated with normal angle as the mechanical support of the suspended structure. After PMMA removel, the underlying SiO_2 was undercut in a diluted HF solution (4%) followed by critical point drying to suspend this metal nanogap structure. Finally, the sample was cleaned in a O_2 plasma cleaner

and the SAM layer was grown in a vapor phase as described in subsection 6.2.2.

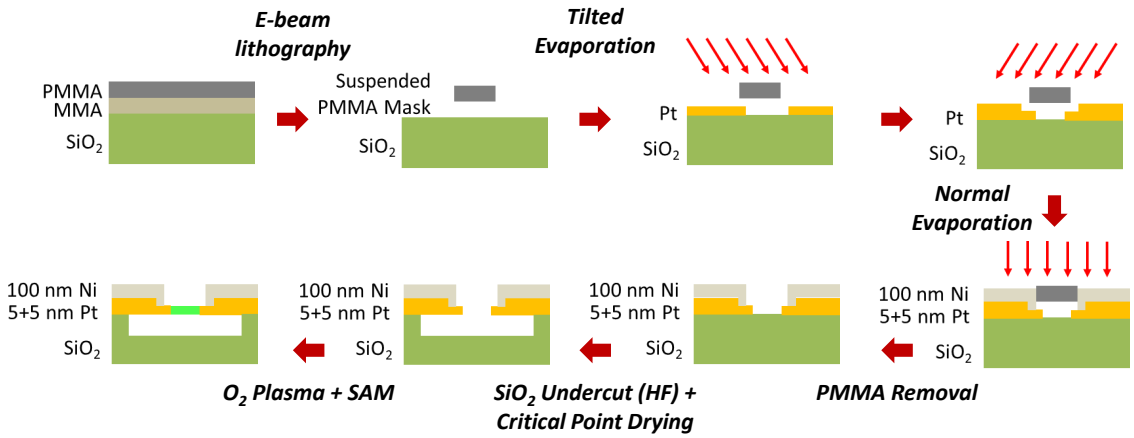

Figure 6-24: Fabrication process flow for the metal/molecule/metal ThM bolometer.

The steps of tilted metal deposition with suspended resist mask can lead to sub-10-nm scale nanogaps with a 100-nm scale resist pattern which can be defined easily by e-beam lithography. Figure 6-25 shows the SEM images of the suspended PMMA masks with different dimensions. Depending on the lengths and widths of the suspended PMMA bridges, the bottom surfaces have different degree of flatness. The masks with 1 and 2 μm lengths are with the desired flatness and smoothness on the bottom. For the masks with 5 μm length, the bottom surface become curvy and rough, probably because of the overdose and the severe back scattering of the electron beams reflected by the substrate surface during the e-beam lithography.

Figure 6-26 (a) is a typical SEM image of the metal nanogap defined by this method. The thickness of the Pt film is 5 nm. The gap distance is measured to be around 15 nm. It corresponds to a 240-nm wide PMMA mask. Wit this method, the gap can be tuned with very good accuracy through changing the width of the PMMA mask, as shown in Figure 6-26 (b).

We also found that the thick metal supporting layer is essential for the suspension to be successful. With only 5 nm Pt, the metal films will break and droop after suspension (Figure 6-27 (a)). With the addition of the thick metal layer, the structure strengthens mechanically, so it will maintain its shape after suspension (Figure 6-27

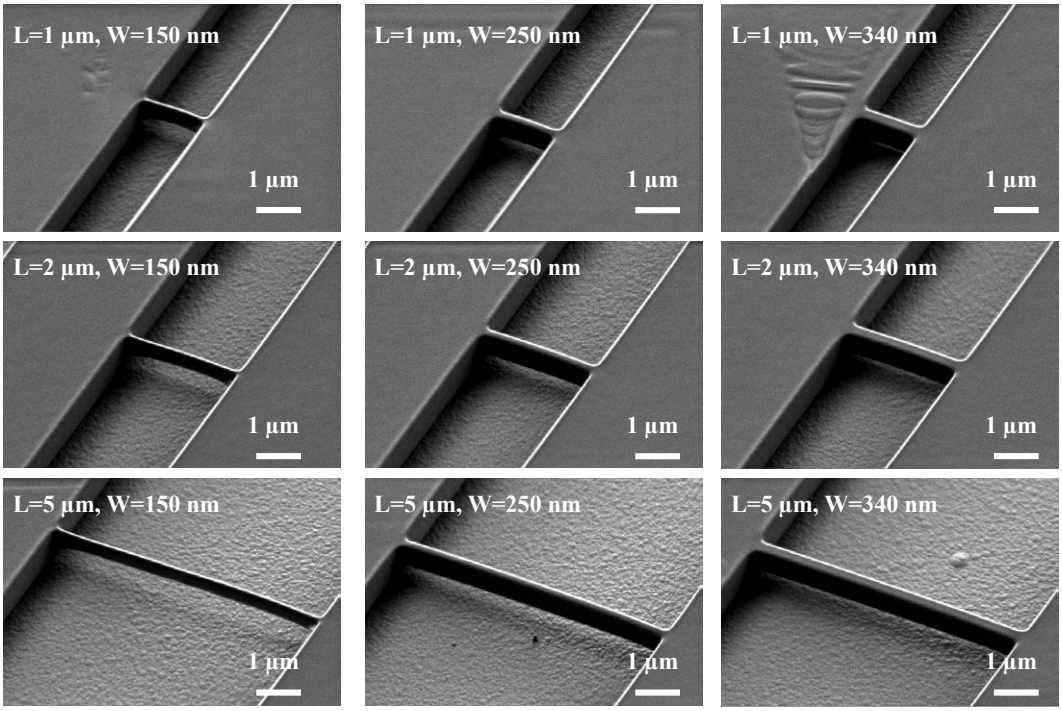

Figure 6-25: SEM images of the suspended PMMA masks with different dimensions.

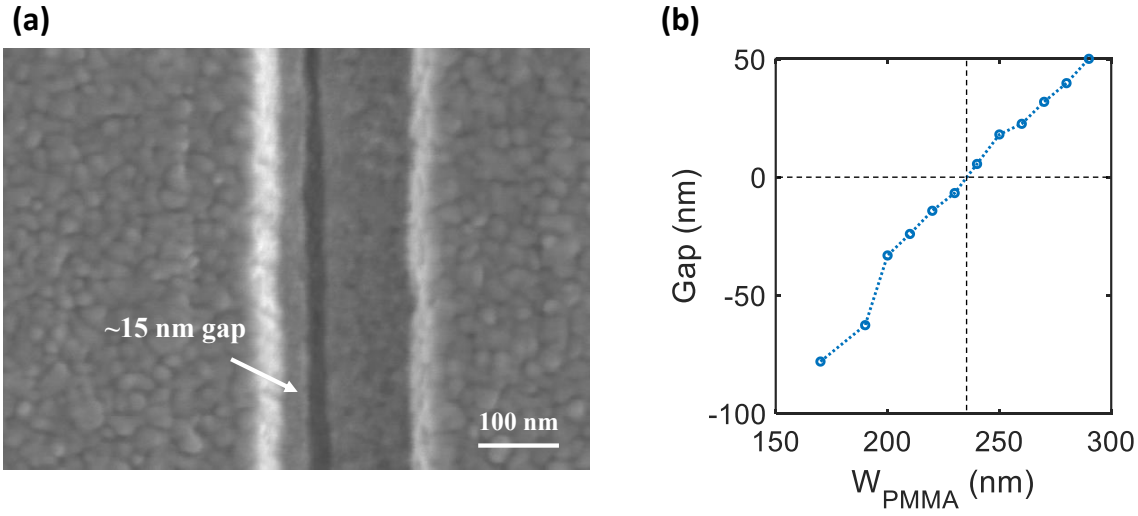

Figure 6-26: (a) a SEM image of the metal nanogap. (b) metal nanogap distance versus PMMA mask width.

(b)).

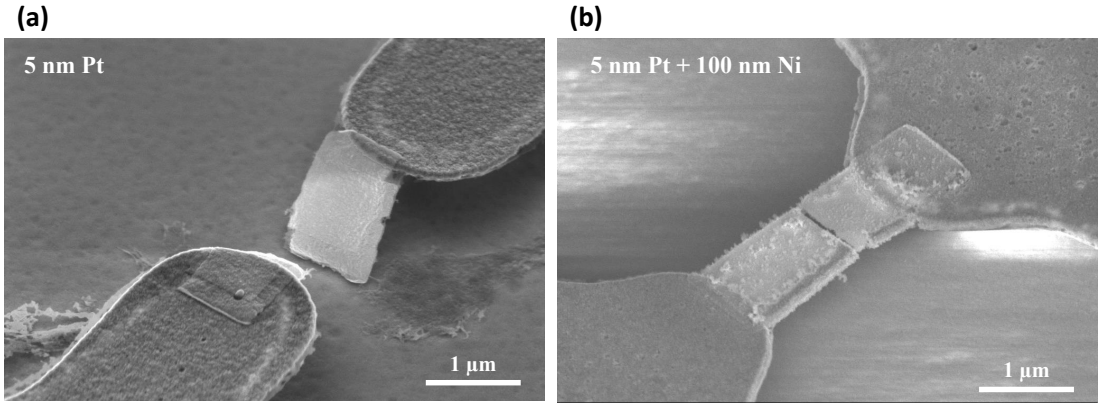

Figure 6-27: SEM images of the suspended metal nanogap (a) without and (b) with the thick Ni supporting layer.

6.4.2 Results and Discussion

We first measured the I-V characteristics of the metal nanogap devices when they are supported, suspended, and functionalized with the SAM layer. Figure 6-28 plots the I-V characteristics of three devices when they are still supported by the SiO_2 substrate. They follow the tunneling behavior as described by the Simmons model Eq. (6.4). Such behaviors can be measured repeatedly as long as we limit the current to below a certain level (100 nA). However, if we apply a higher bias voltage, a permanent current increase will be induced. This can be seen more clearly for a device with wider gap distance (>100 nm) as shown in Figure 6-29. As we sweep the voltage repeatedly on the device, the current increases from pA all the way to 10 nA and starts to stabilize (Figure 6-29 (a)). From the SEM images taken before and after the measurements (Figure 6-29 (b) and (c)), the edges become much rougher after the measurement, which may be caused by the electro-migration.

The devices after suspension also have the tunneling I-V characteristics, as shown in Figure 6-30. Note that for some of the devices, a much lower current was measured for the initial voltage sweep (Figure 6-30 (a)). After the initial sweep, the device is "activated" and a repeatable I-V response with larger current can be measured. This is presumably because of the small deformation of the metal nanogap structure during the suspension process. With the initial voltage sweeping, it is possible that

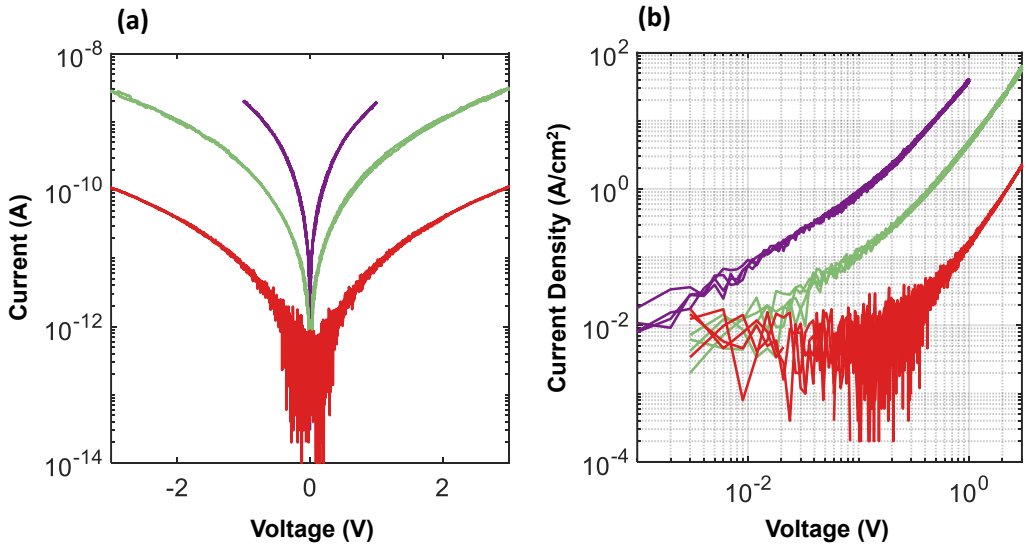

Figure 6-28: I-V characteristics of the metal nanogap devices supported on a SiO_2 substrate.

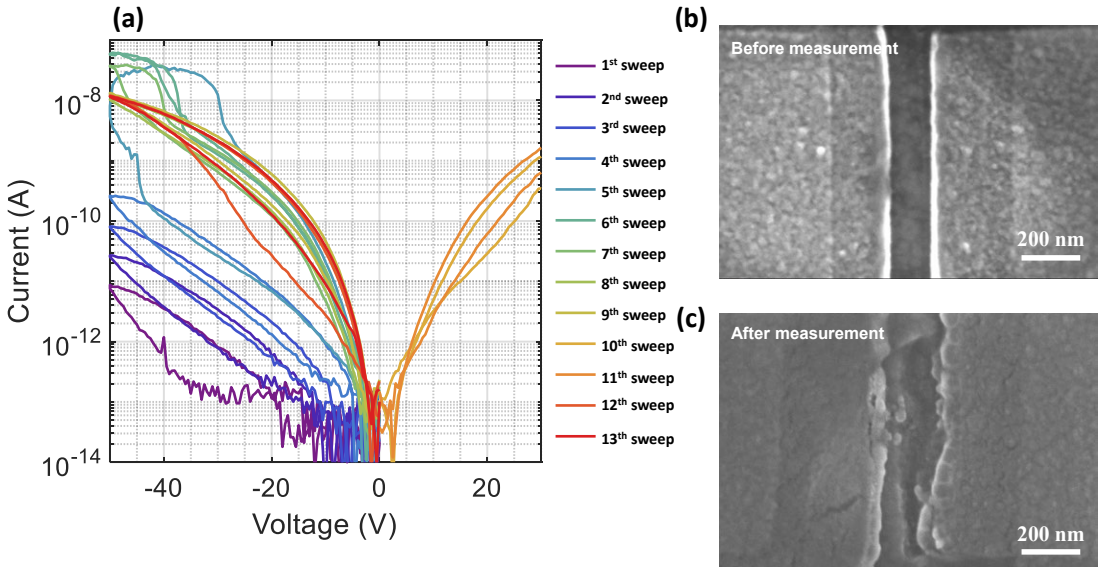

Figure 6-29: The effect of electro-migration. (a) I-V characteristics of a 100 nm metal nanogap devices supported on a SiO_2 substrate. (b) The SEM image of the nanogap before measurement. (c) The SEM image of the nanogap after measurement.

the electrostatic force drags the metal beams back to its original position, which recovers the electrical performance of the device.

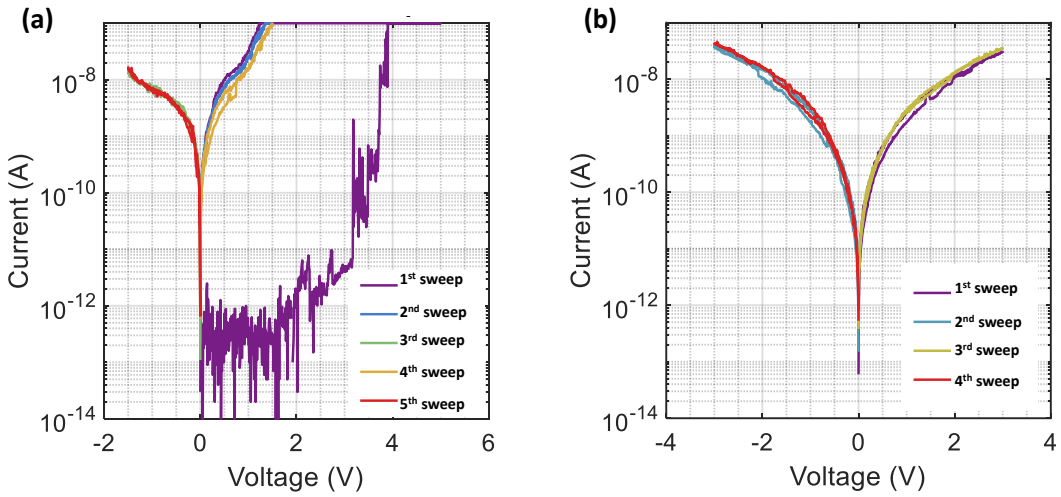

Figure 6-30: Typical I-V characteristics of the nanogap devices after suspension.

We observed a clear change of the I-V characteristics after the SAM layer is grown, although the trend is still inconsistent and need further investigation (Figure 6-31 to Figure 6-33): some of the devices maintain the I-V characteristics (Figure 6-31); a small portion of the devices have improved current (Figure 6-32); but most of the devices are degraded after the SAM process (Figure 6-33).

In the current design, the thick metal supporting beams (100 nm Ni layer) play the role of the IR absorber and the thermal actuator. Because of its low thermal expansion coefficient ($\sim 10^{-5}$ K^{-1}), and high thermal conductivity (~ 90 Wm^{-1}K^{-1}), the temperature response and the IR radiation response is still on its lower end. Figure 6-34 plots the temperature dependent current of a final metal/molecule/metal ThM bolometer with the bias voltage $V = 2$ V. The tunneling resistance degrease with the temperature, because the thermal expansion of the two thick metal beams brings the nanogap closer. The TCR is extracted to be -0.0033 K^{-1}. The IR radiation response (10.6 μm wavelength) of this device is shown in Figure 6-35. The corresponding resistance responsivity is 8.4% per mW incident power.

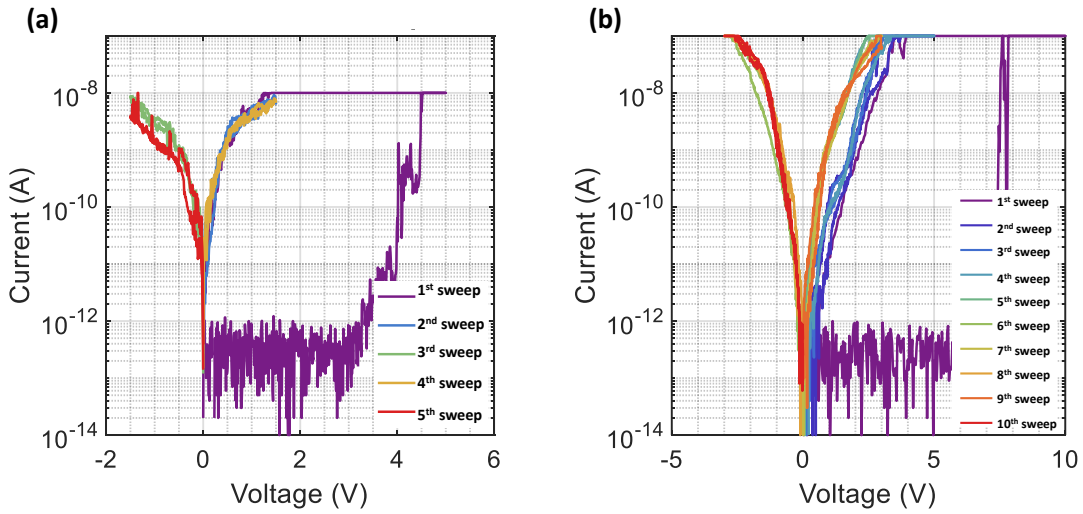

Figure 6-31: I-V characteristics of a nanogap device (a) after suspension and (b) after SAM. This device displays a maintained behavior after SAM.

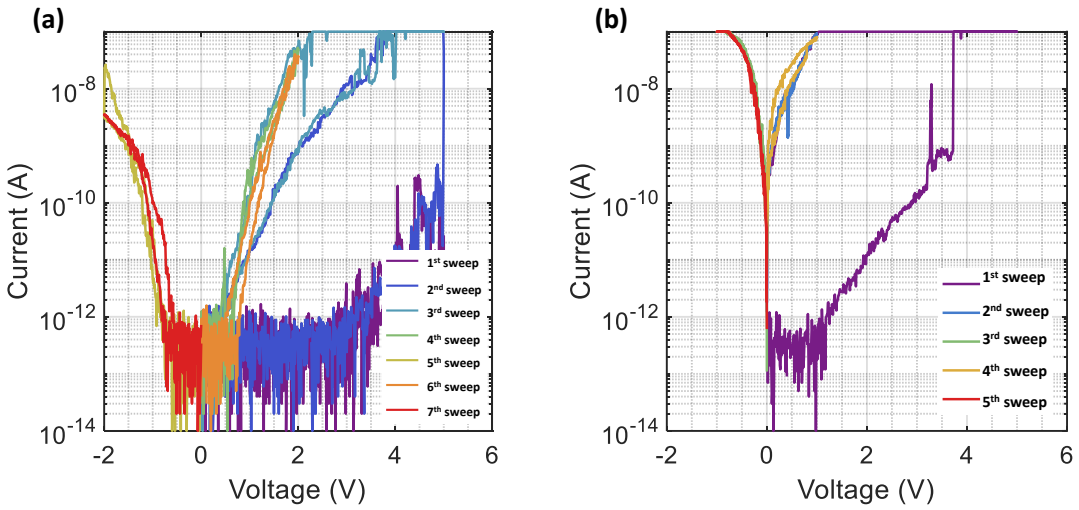

Figure 6-32: I-V characteristics of a nanogap device (a) after suspension and (b) after SAM. This device displays a improved behavior after SAM.

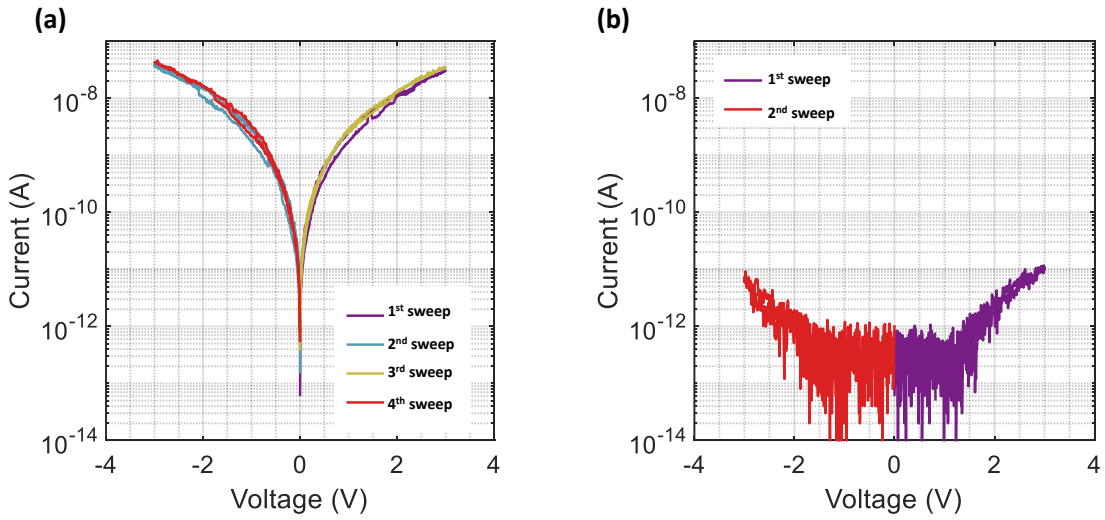

Figure 6-33: I-V characteristics of a nanogap device (a) after suspension and (b) after SAM. This device displays a degraded behavior after SAM.

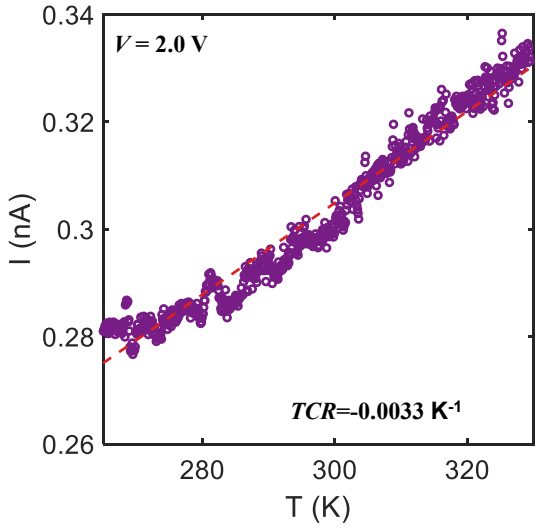

Figure 6-34: Temperature dependent measurement of the metal/molecule/metal ThM bolometer.

6.5 Benchmark of Thermo-Mechanical Bolometers

If we assume the thermal relaxation dominated response time and only consider the shot noise, the $(D^*)^2/\tau$ of the ThM bolometer can be expressed as

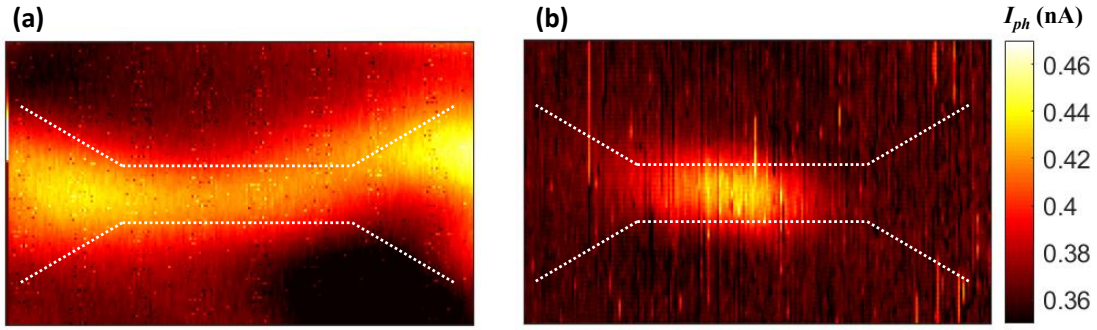

Figure 6-35: IR radiation response of the metal/molecule/metal ThM bolometer. (a) Reflectance mapping. (b) Photocurrent mapping. The excitation wavelength is 10.6 μm. The incident power density is 168 W/cm^2.

$$\frac{(D^*)^2}{\tau} = \left(\frac{ABS}{t}\right)^2 \left(\frac{1}{\kappa_{th} c_V}\right) \left(\frac{I_{bias}\, TCR^2}{2q}\right) \left(\frac{L_{total}}{W_{total}}\right) \tag{6.20}$$

where t is the thickness of the IR absorber/thermal actuator; L_{total} and W_{total} are the overall length and width of the device that dominates the thermal transport. To compare different designs, we assume I_{bias}=1 μA, and $L_{total}/W_{total} \sim 1$. For the sensing component, we assume TCR=0.1-10 K^{-1}. For a polymer based thermal actuator, the thickness is in the range of 0.5-5 μm, the absorbance can be 0.1-1, the thermal conductivity is 0.1-1 W/m/K, and the heat capacity is 10^6-10^7 J/m^3/K. Then $(D^*)^2/\tau \approx 1.25 \times 10^{16}$–$1.25 \times 10^{26}$ cm^{2}Hz/W/s. For a dielectric based thermal actuator, the thickness is in the range of 0.05-0.5 μm, the absorbance can be 0.1-1, the thermal conductivity is 10-100 W/m/K, and the heat capacity is 10^6-10^7 J/m^3/K. Then $(D^*)^2/\tau \approx 1.25 \times 10^{16}$–$1.25 \times 10^{26}$ cm^{2}Hz/W/s. Figure 6-36 plots the D^* versus τ relation for the ThM bolometer with an optimized polymer or dielectric actuator and the sensing component TCR=0.1-10 K^{-1}. We can tune the device geometry to design ThM bolometers and imagers with either much better sensitivity, or much faster frame rate. For example, if we increase the vertical thickness and decrease the lateral sizes, the thermal coupling components between the active region and the heat sink region of the device can be strengthened, and the thermal mass can be

reduced. As a result, we can make a ThM bolometer that can respond to the IR radiation change two to three orders of magnitude faster than the state of the art. With this design strategy, we can implement an uncooled thermal camera with a much faster frame rates. On this other hand, if we push the device geometries to the opposite direction, that is, to decrease the vertical thickness and to increase the lateral sizes, thermal energies can be accumulated more easily in the active regions of the device, which would lead to an enhanced specific detectivity but slower response time. Nonetheless, our ThM bolometer expanded the design space to a great extend, so that it is possible to design the next-generation IR detector technology with much improved performance. Also note that the fundamental limit shown in Figure 6-36 is determined by the thermal fluctuation noise of the 300 K black-body radiation background and a 2π-FOV. If we were to relax this limit by, for example, engineering the spectral response of the detector, or the FOV of the optical systems, we could potentially realize ThM bolometers with orders of magnitude better sensitivity, which were not possible with the conventional bolometric IR detector technologies.

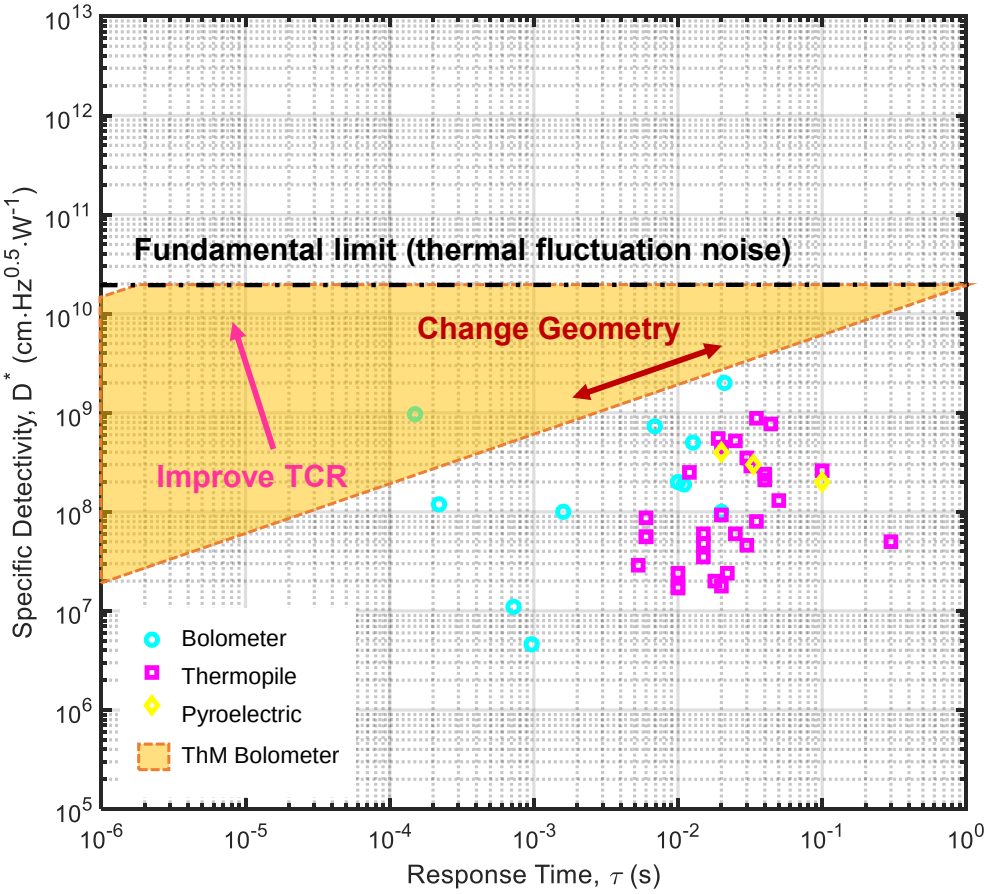

Figure 6-36: Specific detectivity (D^*) versus response time (τ) for ThM bolometers in comparison with mainstream uncooled thermal IR detectors.

Chapter 7

Summary and Outlook

7.1 Contributions of This Thesis

This thesis contributes to three two major areas: (1) synthesis and optical characterization of two-dimensional materials and their heterostructures; and (2) device applications based on two-dimensional materials and other emerging nanomaterials with an emphasis on the development of novel infrared detection technologies. In the following, we summarize the key achievements and the corresponding publications in each of the two areas.

7.1.1 Synthesis and Optical Characterization of Two-Dimensional Materials and Heterostructures

Key Achievements

1. **Synthesis of 2D materials and their heterostructures** (chapter 2). Diverse parallel stitched 2D heterostructures, including metal–semiconductor, semiconductor–semiconductor, and insulator–semiconductor, are synthesized directly through selective "sowing" of aromatic molecules as the seeds in the chemical vapor deposition (CVD) method. The methodology also enables the large-scale fabrication of lateral heterostructures.

2. **Deep-learning-enabled optical characterization of 2D materials** (chapter 3). Characterization of nanomaterial morphologies with advanced microscopy and/or spectroscopy tools plays an indispensable role in nanoscience and nanotechnology research. However, the interpretation of imaging data heavily relies on the "intuition" of experienced researchers. As a result, many of the deep graphical features are often unused because of difficulties in processing the data and finding the correlations. Such difficulties can be well addressed by deep learning. In this work, we use the optical characterization of two-dimensional (2D) materials as a case study, and demonstrate an algorithm based on a neural network for the material and thickness identification of exfoliated 2D materials with high prediction accuracy and real-time processing capability. Further analysis shows that the trained network can be used to predict physical properties of the materials. Finally, a transfer learning technique is applied to adapt the pretrained network to more optical characterization applications such as identifying layer numbers of chemically synthesized graphene domains.

Publication

- B. Han*, **Y. Lin***, Y. Yang, N. Mao, W. Li, H. Wang, V. Fatemi, L. Zhou, J. I-J. Wang, Q. Ma, Y. Cao, D. Rodan-Legrain, Y.-Q. Bie, E. Navarro-Moratalla, D. Klein, D. MacNeill, S. Wu, W. S. Leong, H. Kitadai, X. Ling, P. Jarillo-Herrero, T. Palacios, J. Yin, J. Kong, "Deep learning enabled fast optical characterization of two-dimensional materials", under review. arXiv:1906.11220.

- Y. Guo, P.-C. Shen, C. Su, A.-Y. Lu, M. Hempel, Y. Han, Q. Ji, **Y. Lin**, E. Shi, E. McVay, L. Dou, D. A. Muller, T. Palacios, J. Li, X. Ling, J. Kong, "Additive manufacturing of patterned 2D semiconductor through recyclable masked growth", *PNAS* 116, 3437-3442 (2019). doi:10.1073/pnas.1816197116.

- P.-C. Shen, **Y. Lin**, H. Wang, J.-H. Park, W. S. Leong, A.-Y. Lu, T. Palacios, J. Kong, "CVD technology for 2D materials", *IEEE Trans. Electon Devices*, 65, 4040-4052 (2018). doi:10.1109/TED.2018.2866390.

- X. Ling*, **Y. Lin***, Q. Ma, Z. Wang, Y. Song, L. Yu, S. Huang, W. Fang, X. Zhang, A. L. Hsu, Y. Bie, Y.-H. Lee, Y. Zhu, L. Wu, J. Li, P. Jarillo-Herrero, M. Dresselhaus, T. Palacios, J. Kong, "Parallel stitching of 2D materials", *Adv. Mater.* 28, 2322-2329 (2016). doi:10.1002/adma.201505070; arXiv:1512.04492.

- **Y. Lin**#, X. Ling, L. Yu, S. Huang, A. L. Hsu, Y.-H. Lee, J. Kong, M. S. Dresselhaus, T. Palacios, "Dielectric screening of excitons and trions in single-layer MoS_2", *Nano Lett.* 14, 5569-5576 (2014). doi:10.1021/nl501988y.

- X. Ling, W. Fang, Y.-H. Lee, P. T. Araujo, X. Zhang, J. F. Rodriguez-Nieva, **Y. Lin**, J. Zhang, J. Kong, M. S. Dresselhaus, "Raman enhancement effect on two-dimensional layered materials: graphene, h-BN and MoS_2", *Nano Lett.*, 14, 3033-3040 (2014). doi:10.1021/nl404610c.

- X. Ling, Y.-H. Lee, **Y. Lin**, W. Fang, L. Yu, M. S. Dresselhaus, J. Kong, "Role of the seeding promoter in MoS_2 growth by chemical vapor deposition", *Nano Lett.*, 14, 464-472 (2014). doi:10.1021/nl4033704.

7.1.2 IR Detectors and Other Device Applications Based on Emerging Nanomaterials

Key Achievements

1. **An ultrasensitive thermo-mechanical bolometer** (chapter 6). With nanoengineering, it is possible to fabricate nanometer-sized quantum tunneling barriers that can be tuned mechanically. Such a tremendous mechanical tunability can be harnessed for mechanical sensors and many other types of sensors with extremely high sensitivity. Here we demonstrate two nanostructures that implement such a mechanically tunable tunneling barrier and use them for either a mechanical/strain sensor or a mid-infrared bolometric detector. The first nanostructure is the self-assembled graphene nanoflake network composed of a resistance network of sub-micron graphene flakes that connect with each other with $<$100 nm overlap. The second nanostructure is a metal nano-gap with the

gap defined by self-assembled monolayers (SAMs) . The proposed structures show high gauge factors and/or improved linear dynamic range as a strain sensor. Such mechanical sensors can also be integrated with a thermal actuator to realize a highly sensitive, uncooled bolometer-type mid-infrared detector . The measured temperature coefficient of resistance (TCR) can be as high as 5 K^{-1}, which is more than one order of magnitude better than the state of the art.

2. **Photothermoelectric effect in graphene-2D semiconductor lateral heterostructures** (chapter 5). A variety of unique light-matter interaction phenomena have been discovered in graphene, which promise many novel optoelectronic applications. Most of the effects are only accessible by breaking the spatial symmetry. The recent development of direct synthesis of lateral heterostructures offers new opportunities to achieve the desired asymmetry. As a proof of concept, we study the photothermoelectric effect in an asymmetric lateral heterojunction between the Dirac semimetallic monolayer graphene and the parabolic semiconducting monolayer MoS_2. Very different hot-carrier cooling mechanisms on the graphene and the MoS_2 sides allow us to resolve the asymmetric thermalization pathways of photoinduced hot carriers spatially with electrostatic gate tunability. We also demonstrate the potential of graphene-2D semiconductor lateral heterojunctions as broadband infrared photodetectors. The proposed structure shows an extreme in-plane asymmetry and provides a new platform to study light-matter interactions in low-dimensional systems.

3. **Graphene thermopile and graphene-CMOS integration** (chapter 4). The low dimensionality of 2D materials and the easy and universal transfer process make it possible to decouple the low-temperature fabrication process from the high-temperature growth of high-quality 2D materials and realize the monolithic integration between 2D material based technologies and conventional silicon CMOS technologies. As a proof-of-concept, we developed a back-end-of-line process to fabricate a graphene thermopile mid-infrared detector array directly onto a specifically designed silicon CMOS integrated circuit chip. Such

a monolithically integrated graphene-CMOS system can perform real-time thermal imaging that can potentially be used in next generation night vision goggles, surveillance cameras as well self-driving systems.

4. **Integrated circuits based on graphene-MoS_2-graphene lateral heterostructures** (chapter 2). We developed a large-scale synthetic approach to construct lateral heterostructures between graphene and 2D semiconductors such as MoS_2. Temperature transport measurements have shown that such a lateral structure has a very small Schottky barrier height, which is ideal for the 1D contact to 2D semiconductor field effect transistors. Based on this idea, we implemented a variety of building blocks for logic integrated circuits.

Publication

- **Y. Lin***, Q. Ma*, P.-C. Shen*, B. Ilyas, Y. Bie, A. Liao, E. Ergeçen, B. Han, N. Mao, X. Zhang, X. Ji, Y. Zhang, J. Yin, S. Huang, M. Dresselhaus, N. Gedik, P. Jarillo-Herrero, X. Ling, J. Kong, T. Palacios, "Asymmetric hot-carrier thermalization and broadband photoresponse in graphene-2D semiconductor lateral heterojunctions", *Sci. Adv.* 5, eaav1493 (2019). doi:10.1126/sciadv.aav1493.

- Y. Sun, L. Qian, D. Xie, **Y. Lin**, M. Sun, W. Li, L. Ding, T. Ren, T. Palacios, "Photoelectric synaptic plasticity realized by 2D perovskite", *Adv. Funct. Mater.* 29, 1902538 (2019).doi:10.1002/adfm.201902538.

- X. Zhang, J. Grajal, J. L. Vazquez-Roy, U. Radhakrishna, X. Wang, W. Chern, L. Zhou, **Y. Lin**, P.-C. Shen, X. Ji, X. Ling, A. Zubair, Y. Zhang, H. Wang, M. Dubey, J. Kong, M. Dresselhaus, T. Palacios, "Two-dimensional MoS_2-enabled flexible rectenna for Wi-Fi-band wireless energy harvesting", *Nature* 566, 368-372 (2019). doi:10.1038/s41586-019-0892-1.

- Q. Ma, C. H. Lui, J. C. W. Song, **Y. Lin**, J. F. Kong, Y. Cao, T. H. Dinh, N. L. Nair, W. Fang, K. Watanabe, T. Taniguchi, S.-Y. Xu, J. Kong, T. Palacios, N. Gedik, N. M. Gabor, P. Jarillo-Herrero, "Giant intrinsic photoresponse in

pristine graphene", *Nat. Nanotechn.* 14, 145-150 (2019). doi:10.1038/s41565-018-0323-8; arXiv:1812.07111.

- A. Nourbakhsh, L. Yu, **Y. Lin**, M. Hempel, R.-J. Shiue, D. Englund, T. Palacios, "Heterogeneous integration of 2D materials and devices on a Si platform", in: Topaloglu R., Wong HS. (eds) *Beyond-CMOS Technologies for Next Generation Computer*, Springer, Charm (2019). doi:10.1007/978-3-319-90385-9_3

- Q. Ma, S.-Y. Xu, C.-K. Chan, C.-L. Zhang, G. Chang, **Y. Lin**, T. Palacios, H. Lin, S. Jia, P. A. Lee, P. Jarillo-Herrero, N. Gedik, "Direct optical detection of Weyl fermion chirality in TaAs", *Nat. Phys.* 13, 842-847 (2017). doi:10.1038/nphys4146; arXiv:1705.00590.

- Y. Zhang, M. Sun, D. Piedra, J. Hu, Z. Liu, **Y. Lin**, X. Gao, K. Shepard, T. Palacios, "1200 V GaN vertical fin power field-effect transistors", *2017 IEEE International Electron Device Meeting (IEDM)*, San Francisco, CA, December 2017. doi:10.1109/IEDM.2017.8268357.

- S. Huang, T. Ming, **Y. Lin**, X. Ling, Q. Ruan, T. Palacios, J. Wang, M. Dresselhaus, J. Kong, "Ultrasmall mode volumes in plasmonic cavities of nanoparticle-on-mirror structures", *Small* 12, 5190-5199 (2016). doi:10.1002/smll.201601318.

- L. Yu, D. El-Damak, U. Radhakrishna, X. Ling, A. Zubair, **Y. Lin**, Y. Zhang, M.-H. Chuang, Y.-H. Lee, D. Antoniadis, J. Kong, A. Chandrakasan, T. Palacios, "Design, modeling, and fabrication of chemical vapor deposition grown MoS_2 circuits with E-mode FETs for large-area electronics", *Nano Lett.* 16, 6349-6356 (2016). doi:10.1021/acs.nanolett.6b02739.

- Y. Zhang, M. Sun, Z. Liu, D. Piedra, M. Pan, X. Gao, **Y. Lin**, A. Zubair, L. Yu, T. Palacios, "Novel GaN trench MIS barrier Schottky rectifiers with implanted field rings", *2016 IEEE International Electron Device Meeting (IEDM)*, San Francisco, CA, December 2016. doi:10.1109/IEDM.2016.7838386.

- L. Yu, D. El-Damak, U. Radhakrishna, A. Zubair, D. Peidra, X. Ling, **Y. Lin**, Y. Zhang, Y.-H. Lee, D. Antoniadis, J. Kong, A. Chandrakasan, T. Palacios, "High-yield large-area MoS_2 technology: material, device and circuits co-optimization", *2016 IEEE International Electron Device Meeting (IEDM)*, San Francisco, CA, December 2016. doi:10.1109/IEDM.2016.7838356.

- L. Yu, A. Zubair, E. J. G. Santos, X. Zhang, **Y. Lin**, Y. Zhang, T. Palacios, "High-performance WSe_2 complementary metal oxide semiconductor technology and integrated circuits", *Nano Lett.* 15, 4928-4934 (2015). doi:10.1021/acs.nanolett.5b00668.

- L. Yu, D. El-Damak, S. Ha, X. Ling, **Y. Lin**, A. Zubair, Y. Zhang, Y.-H. Lee, J. Kong, A. Chandrakasan, T. Palacios, "Enhancement-mode single-layer CVD MoS_2 FET technology for digital electronics", *2015 IEEE International Electron Device Meeting (IEDM)*, Washington, DC, December 2015. doi:10.1109/IEDM.2015.7409814.

- G. M. Akselrod, T. Ming, C. Argyropoulos, T. B. Hoang, **Y. Lin**, X. Ling, D. R. Smith, J. Kong, M. H. Mikkelsen, "Leveraging nanocavity harmonics for control of optical processes in 2D semiconductors", *Nano Lett.* 15, 3578-3584 (2015). doi:10.1021/acs.nanolett.5b01062.

- Y. Zhang, M. Sun, H.-Y. Wong, **Y. Lin**, P. Srivastava, C. Hatem, M. Azize, D. Piedra, L. Yu, T. Sumitomo, N. A. de Braga, R. V. Mickevicius, T. Palacios, "Origin and control of OFF-state leakage current in GaN-on-Si vertical diodes", *IEEE Trans. Elect. Dev.* 62, 2155-2161 (2015). doi:10.1109/TED.2015.2426711.

- L. Yu, Y.-H. Lee, X. Ling, E. J. G. Santos, Y. C. Shin, **Y. Lin**, M. Dubey, E. Kaxiras, J. Kong, H. Wang, T. Palacios, "Graphene/MoS_2 hybrid technology for large-scale two-dimensional electronics", *Nano Lett.*, 14, 3055-3063 (2014). doi:10.1021/nl404795z.

7.2 Future Work

In this section, we examine some future work that is worth studying as an extension of this thesis. Four directions will be covered: (1) graphene p-i-n photothermoelectric detector; (2) miniaturized pyroelectric IR detector; (3) multi-/hyperspectral imaging system based on the emerging IR detector technologies; and (4) mechanical/chemical sensors based on engineered nanostructures.

7.2.1 Graphene p-i-n Photothermoelectric Detector

In chapter 5, we have discussed the unique hot electron transport properties in graphene, and the photothermoelectric photocurrent response in a graphene-2D semiconductor lateral heterostructure. Here we propose a graphene p-i-n lateral homojunction that can efficiently decouple the wavelength cutoff determined by the Pauli blocking from the gate-dependent Seebeck coefficient change. With this structure, it is still possible to take advantage of the hot carrier photoresponse in graphene and make highly sensitive and fast response photodetector in longer wavelengths.

The proposed device structure is schematically shown in Figure 7-1. A sheet of graphene encapsulated with hBN will be electrostatically doped into a p-i-n junction device, with the intrinsic region absorbing light and the doped regions providing high Seebeck coefficients. Interestingly, the electronic temperature in intrinsic, very clean graphene can be enhanced by at least one order of magnitude due to the anomalous hydrodynamic behavior of electron transport near the Dirac point [221, 222]; this can be used to eliminate the need to concentrate light in such a small intrinsic region. The intrinsic time response of such a device structure is determined by the electron-lattice cooling rate. The detectivity, after geometric optimization, is mainly limited by the IR absorbance, the cooling length, and the Seebeck coefficient difference in the device. The predicted D^*–τ relation, plotted in Figure 7-2, shows improved detectivity and faster operating frequency compared to other state-of-the-art technologies.

Our preliminary measurements (Figure 7-3) have indicated that the hBN encapsulated graphene p-i-n junction leads to much better graphene quality and improved

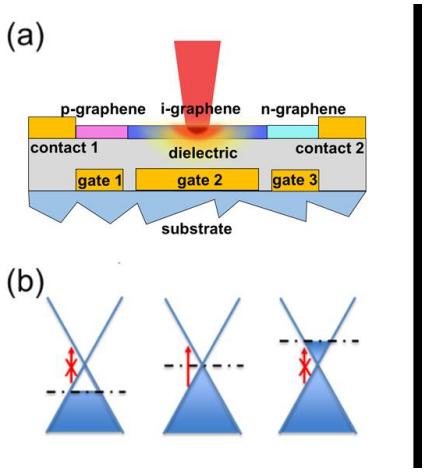

Figure 7-1: (a) Schematic of the proposed graphene p-i-n homojunction PTE detector. (b) Band diagrams of graphene in the k-space, with dashed lines indicating the Fermi energy of p-, i-, and n-doped graphene regions. The red arrows represent the permission or forbiddance of the light absorption.

PTE photoresponse. A much sharper peak was observed from the the transfer characteristics Figure 7-3 (b), which corresponds to the field effect mobility, μ_{FET}, of 50,000 $\mathrm{cm^2V^{-1}s^{-1}}$ at room temperature, and 130,000 $\mathrm{cm^2V^{-1}s^{-1}}$ at 15 K. The photocurrent response as a function of the split gate voltages at different temperatures show the six-lobe distribution, which indicate a PTE effect dominated photoresponse (Figure 7-3 (d) to (f)). The current responsivity at 830 nm wavelength was extracted to be around 10 mA/W at low temperature, and 1 mA/W at room temperature, which is at least one order of magnitude better than previously reported values measure in a graphene p-n junction on a SiO_2 substrate [122].

7.2.2 Miniaturized Pyroelectric IR Detector

Pyroelectric IR detector is another type of mainstream thermal detector technologies (subsection 1.1.1). The basic structure of traditional pyroelectric technology is a metal/dielectric/metal capacitor, where the dielectric is a pyroelectric material. The pyroelectric material is a non-centrosymmetric crystal with a spontaneous polarization along the vertical direction. Such a polarization is usually as a function of temperature. If a periodically amplitude-modulated IR radiation is present, the

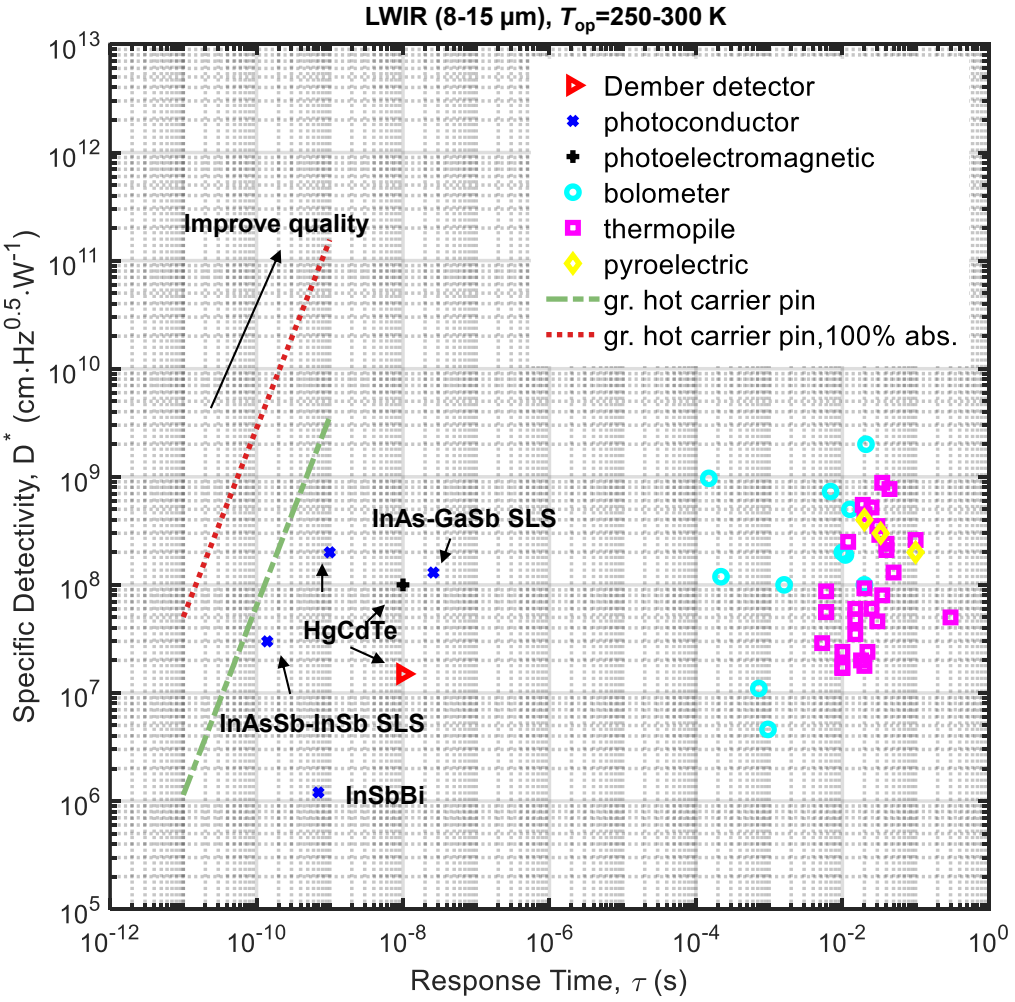

Figure 7-2: D^*–τ plot for graphene p-i-n junction PTE detectors in comparison with state-of-the-art uncooled thermal detector technologies in the LWIR range.

temperature change induced polarization would give rise to a temporal current that can be measured by the capacitor. This technology is sensitive, but usually need builk pyroelectric crystals and optical modulation, which make this technology difficult for miniaturization.

Two recent studies [130, 131] combined a graphene field effect transistor and a $LiNbO_3$ pyroelectric capacitor and realize a pyroelectric IR detector without the optical chopping and with the resistance readout. In their devices, the polarization change in the pyroelectric crystal can be coupled, either directly or indirectly, to the

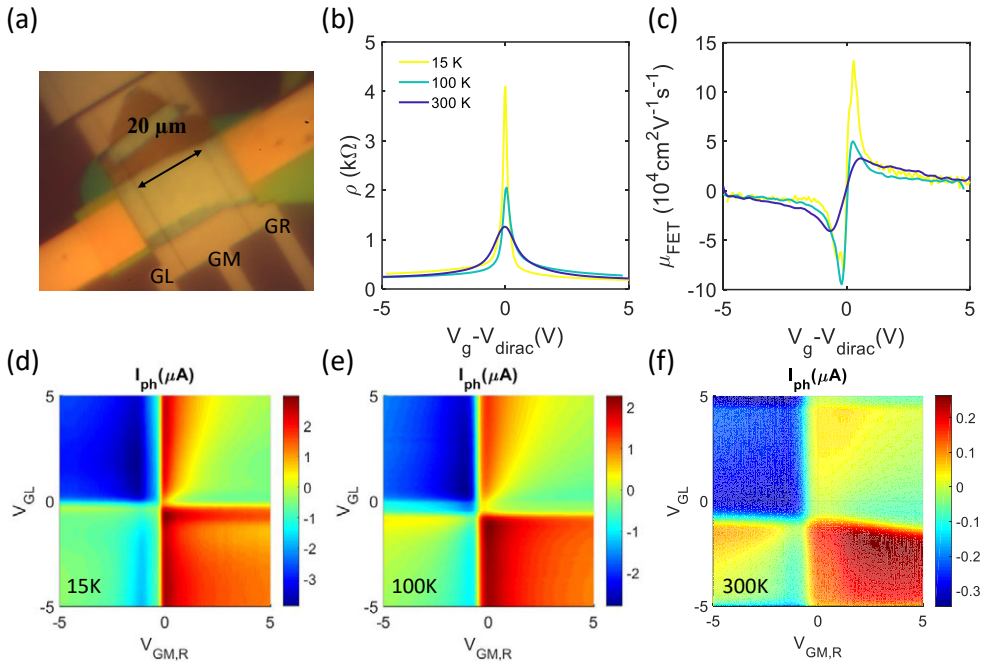

Figure 7-3: Preliminary results of the graphene p-i-n PTE detector. (a) Optical microscopic image. (b) Transfer characteristics at different temperature. (c) field effect mobility extracted from (b). (c)-(e) Photocurrent response as a function of the split gate voltages at different temperature, when a 830 nm laser is shined at the junction.

graphene which leads to a electrostatic doping and a resulting resistance change of the graphene channel. There is still much room for improving the performance of these device structures. Here we propose three new designs.

1. *2D semiconductor/ALD pyroelectric dielectric transistor.* We can adapt the recently developed ferroelectric/pyroelectric ALD dielectric materials (doped AlOx and HfOx), and use them as the gate dielectric of a 2D semiconductor transistor to implement a pyroelectric transistor with much smaller form factors. This makes it possible to reduce the thermal mas substantially and improve the sensitivity and/or response time of the detector. Another benefit of miniaturization is that we can fabricate focal plane arrays instead of single macroscopic detectors. Furthermore, if we tune the gate voltage so that the 2D semiconductor is in the subthreshold regime, the pyroelectric response might induce an exponential resistance change of the 2D semiconductor channel, which could

lead to even better sensitivity.

2. *2D pyroelectric transistor.* There are several non-centrosymmetric 2D materials that we can use potentially as a good thermal detector. Many of them are semiconductor (for example, Janus monolayer transition metal dichalcogenides, and α-In_2Se_3). The polarization change may lead to a self-gating effect of these semiconductors, which would give rise to a simple, but sensitive resistor-type pyroelectric response.

3. *2D lateral pyroelectric heterojunction.* Some 2D materials also have lateral spontaneous polarization, including Group IV metal monochalcogenides, α-In_2Se_3, *etc.* We can construct a lateral heterojunction between a lateral pyroelectric material and a normal 2D semiconductor, and use the temperature dependent polarization and the barrier height modulation for IR detection.

7.2.3 Multi-/Hyperspectral Imaging System

As discussed in chapter 4 to chapter 6, we have developed several IR detector technologies based on 2D materials, their heterostructures and other artificial nanostructures that can give rise to better sensitivity, faster speed, or wider spectral range. Scaling up these technologies into focal plane arrays is the essential next step that would enable IR/thermal imaging applications such as night vision, surveillance, automated driving, *etc.* Besides the spatial domain, wavelength is another physical dimension that contains even more information, such as chemical compositions, temperature and surface emissivity of the target objects. Therefore, implementing an imaging system that is able to measure the spectrum of each pixel is of great practical interest. This new era of imaging technology is called multispectral or hyperspectral imaging Figure 7-4. This is the key technology for many advanced sensing applications, including remote sensing, chemical composition analysis, air/water body monitoring, medical tomography, and IR communication. We can take advantage of some of the special spectral response of nanophotonic structures and integrate them to the IR detector technologies that we have developed in this thesis to realize a compact, low-power

hyperspectral imager. Integrating the imager and spectrometer into a single chip is beneficial because it does not need the moving parts, scanning components, and complex optical components that are to some extend unreliable, bulky, and extremely power hungry. In the following, we propose two strategies to implement this idea.

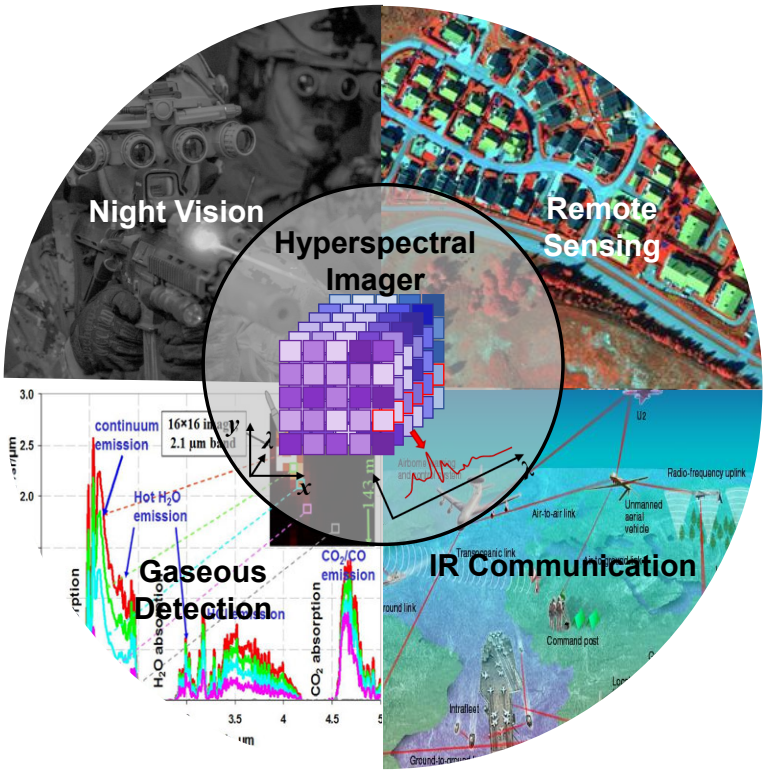

Figure 7-4: Hyperspectral imaging cube (center) with potential applications in night vision, remote sensing, gaseous detection and IR communication.

The first strategy is to harness the unique electrical tunability of the optical responses of graphene (subsection 1.2.1). Two effects can be used. First, when graphene is lightly doped, it can act as a spectral short-pass filter with a cutoff frequency that is tuned by the graphene gate-dependent Fermi level (Pauli blocking). Second, when graphene is heavily doped, the surface plasmon polariton resonances in graphene is very strong, which could also be tuned widely by electrostatic gating. Owing to the gate tunability of graphene's Fermi level E_F and hence the plasmon dispersion, the spectrally selective absorption can be tuned across a wide spectral range by applying a voltage to the graphene sheet to alter its Fermi level. This voltage-tunable en-

hanced absorption is illustrated in Figure 7-5 (a). Compared to the universal 2.3% absorption of a non-structured graphene sheet, Figure 7-5 (b) shows strongly enhanced absorption in different spectral regions when a variable voltage is applied. When such plasmonic nanostructures are used as filters or absorbers, spectrally selective optical detection with high contrast is possible. Figure 7-6 illustrate two possible ways of integrating this graphene plasmonic absorber/filter to single detectors.

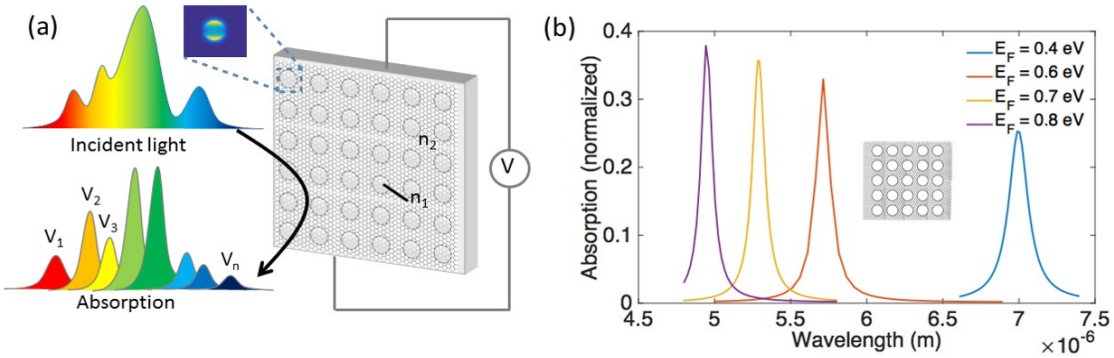

Figure 7-5: (a) Schematics of gate tunable graphene plasmonic nanostructures. Inset: simulated E-field profile of the fundamental plasmonic mode for a unit cell of the periodic nanostructures; (b) simulated absorption spectra of the graphene plasmonic nanostructures with different graphene Fermi level.

In the first implementation, the plasmonic absorber will consist of a hBN-graphene-hBN-graphene-hBN stack as shown in Figure 7-6(a). The lower layer will be patterned into a hole array, used to gate an arrayed Fermi level pattern in the upper layer, which is the plasmonic absorber. In the second implementation, we can use graphene thermopiles to measure the temperature of the plasmonic absorber itself over an array of pixels as the resonant wavelength is shifted. We will implement this idea by stacking patterned graphene and BN isolation/ dielectric layers as shown in Figure 7-6 (b). As before, the topmost two graphene layers will function as a tunable absorber. The bottom two layers will be the thermocouples and pads to gate the thermocouples. The stacked heterostructure pixels will be suspended by under-etching the substrate to decrease thermal leakage from the stack. Plasmon-resonant incident light is absorbed in the stack, leading to an enhanced thermovoltage corresponding to the cavity resonance only (i.e., we obtain a bandpass response).

The second strategy is the integrate metal or graphene plasmonic absorber to the

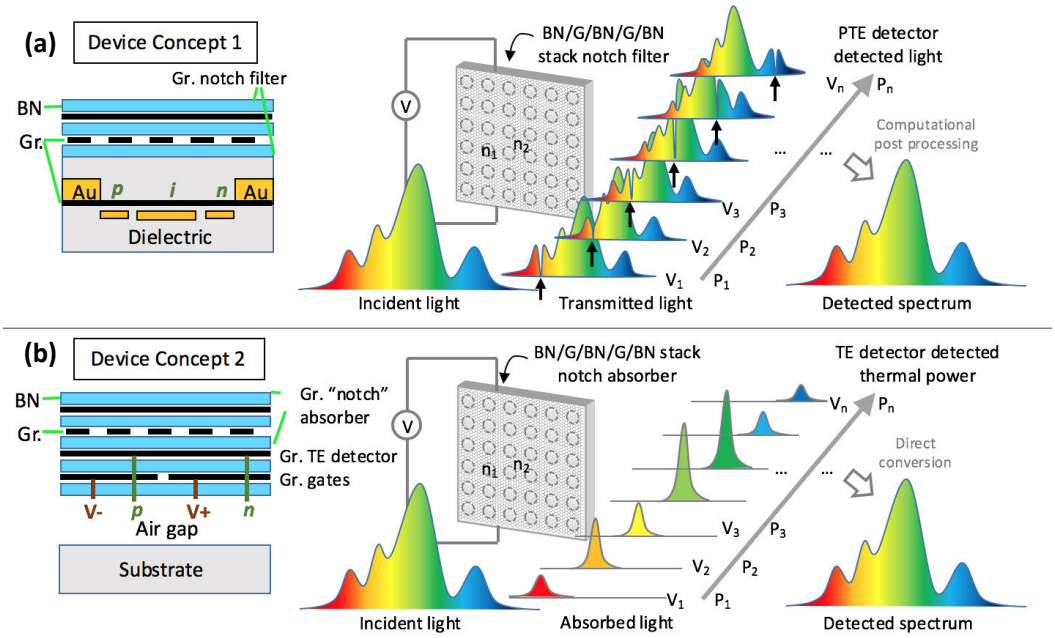

Figure 7-6: Illustration of hyperspectral detection with two proposed device concepts: (a) graphene plasmonic notch filters + graphene PTE detector; (b) graphene plasmonic notch absorbers + graphene TE detector.

thermo-mechanical bolometer as discussed in chapter 6. A straightforward way to introduce spectral selectivity into the device structure is shown in Figure 7-7. In (a), two different designs with positive and negative TCRs are proposed. The plasmonic metasurfaces are fabricated on top of the polymer base to enhance and tailor the absorption of IR radiation. The plasmonic metasurfaces can be made either by a periodically patterned metal (aluminum or gold), or a periodically patterned heavily doped graphene sheet. Although these designs allow designable spectral response and high broadband absorption, they do not serve as efficient hyperspectral imaging because they do not perform spectral binning of incoming light into different photoresponse signals. A more advanced device (called multispectral superpixel) is shown in Figure 7-7 (b), in which the light is binned into different sub-wavelength-width ThM structures with differently tuned metal or heavily-doped graphene antennas. Each ThM bolometer in the superpixel will only respond to a relatively narrow band, but with different center wavelength. The spectrum of the thermal object can be then obtained by combining the measurements from all the ThM bolometers in the

superpixel (Figure 7-7 (c)).

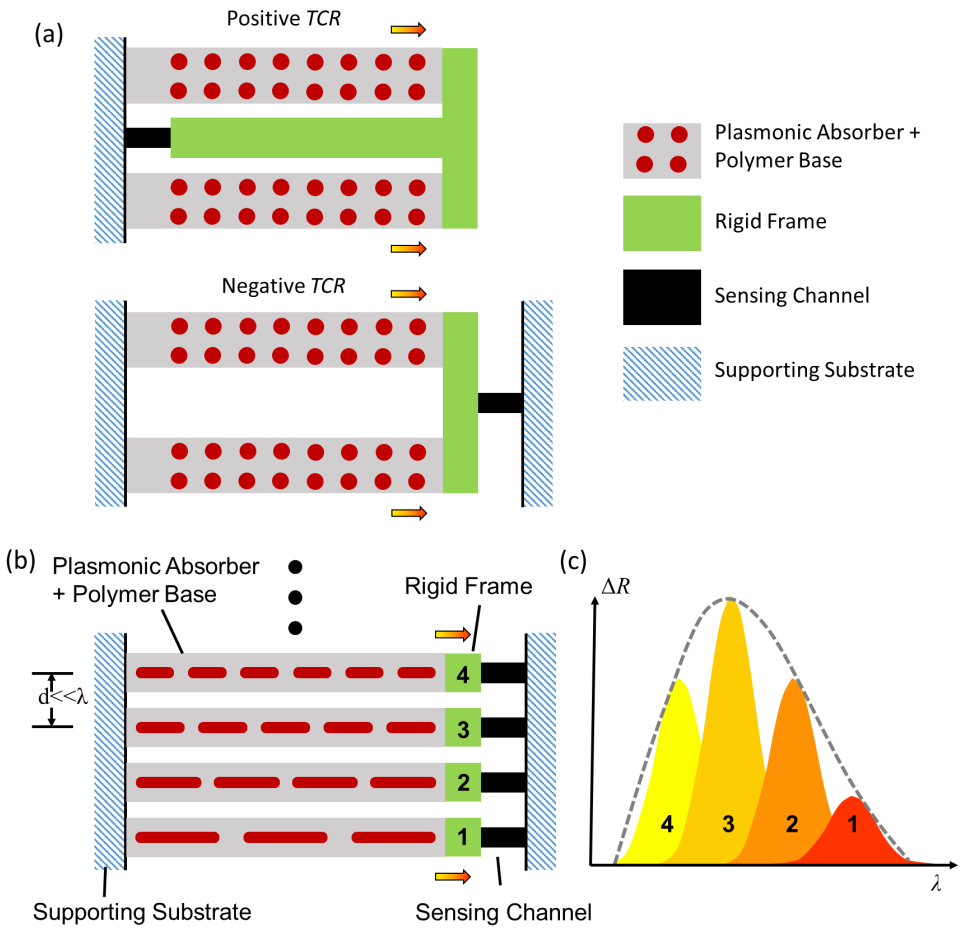

Figure 7-7: ThM bolometer based multispectral superpixel. (a) Schematics of the ThM bolometers integrated with metal metamaterial spectral absorbers. Two designs are proposed: one with positive TCR, and the other one with negative TCR (b) A schematic of a multispectral superpixel. (c) Spectral responses of the multiple ThM bolometers in the multispectral superpixel.

7.2.4 Mechanical/Chemical Sensors Based on Engineered Nanostructures

Finally, we can generalize the sensing mechanism discussed in chapter 6 for sensors in other physical domains. As illustrated in Figure 7-8, we can simply replace the IR absorber/thermal actuator component with another transducer that can convert the physical parameter of interest into a mechanical deformation, and apply this defor-

mation to the two sensitive strain sensor mechanisms discussed in this thesis. We can design the geometry carefully and take advantage of the strain amplification concept to make mechanical or chemical sensors with unprecedented sensitivity. Figure 7-9 illustrate two example designs for chemical sensors.

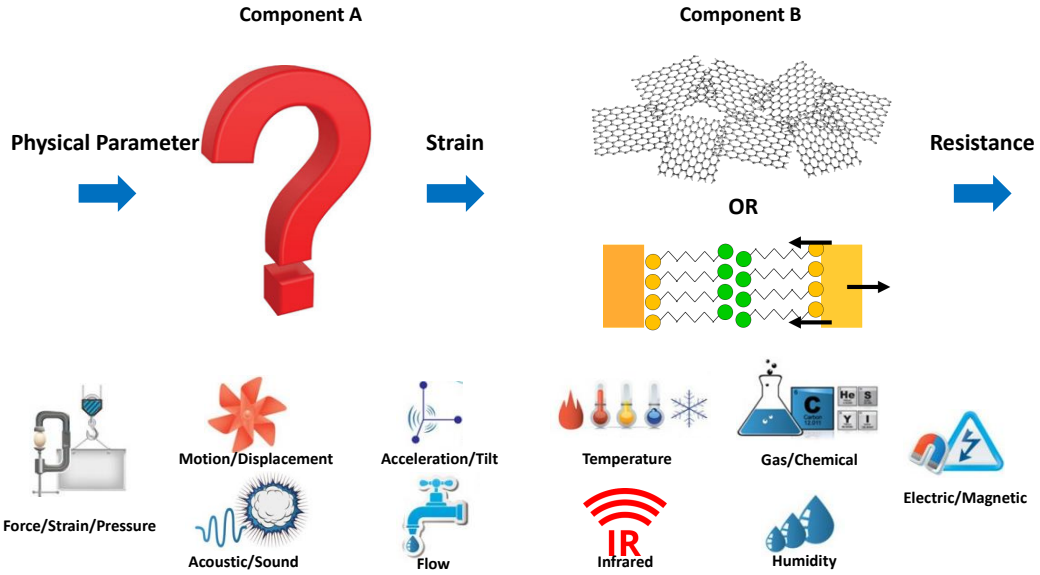

Figure 7-8: A generic sensing scheme based on the mechanically tunable nanostructure.

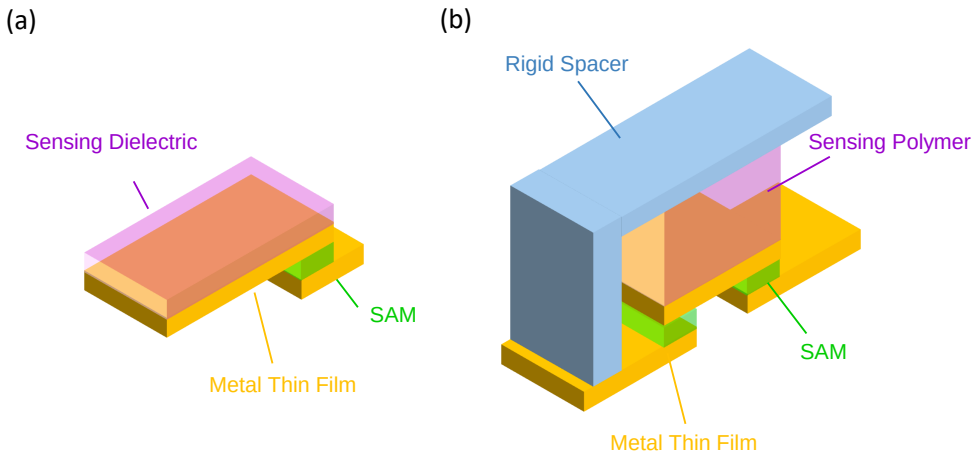

Figure 7-9: Two example designs for chemical sensors.

Appendix A

Process Flow

A.1 Graphene-MoS_2 Lateral Heterojunction Photodetector

A.1.1 Material Synthesis

- Start with 4" Si wafer with 285 nm thermal oxide (Nova Electronic Materials)
- Clean with Nanostrip for 10 mins
- Scotch-tape mechanical exfoliation of graphene
- Inspection under an optical microscope
- Seeding promoter assisted MoS_2 growth
- Searching for monolayer graphene-monolayer MoS_2 heterojunctions under an optical microscope

A.1.2 Wet Transfer

- Spin-coating: PMMA 950A4, 4krpm, 1 min; two layers. baking at 80 °C for 5 mins after each layer
- Detach: immerse in diluted HF (4%) for 20 seconds; dip in DI water; the PMMA/2D material film will float on the water surface
- Clean: Scoop the PMMA/2D mateiral stack with a glass slide and transfer it

to a new DI water bath. Repeat for at least 3 times. Clean the top surface with DI water using a squeeze bottle.

- Transfer: immerse the targeted substrate (285 nm SiO_2/Si wafer with alignment marker grids) into the DI water bath; align the targeted substrate with the PMMA/2D material stack roughly; lift up the targeted substrate up until the PMMA/2D material stack is attached to the substrate.
- Baking: bake the transfered substrate in 80 °C for at least 10 minutes or until the water is fully evaporated; then in 130 °C oven for at least 30 minutes.
- PMMA removal: soak in acetone for at least one hour; rinse with IPA; blow dry with nitrogen gun.

A.1.3 Contact Electrodes

- Spin-coating: TRL coater, PMMA 950A6, 4krpm, 1 min; baking at 180 °C for 7 mins.
- E-beam lithography: Elionix, 30 nA, pitch size 10 nm, dose per area 1600 $\mu C/cm^2$.
- Develop: MIBK:IPA=1:3, 90 seconds; IPA 60 seconds; blow dry with nitrogen gun
- E-beam evaporation: EbeamFP, 30 nm Ni/30 nm Au
- Lift-off: soak in acetone for at least 3 hours; use a pipet to agitate; rinse with IPA and blow dry.

A.1.4 Dry Etching of 2D Materials

- Spin-coating: TRL coater, PMMA 950A6, 4krpm, 1 min; baking at 180 °C for 7 mins.
- E-beam lithography: Elionix, 30 nA, pitch size 10 nm, dose per area 1600 $\mu C/cm^2$.
- Develop: MIBK:IPA=1:3, 90 seconds; IPA 60 seconds; blow dry with nitrogen gun.

- RIE: PlasmaTherm at NSL, O_2 + He; recipe name: testprc.prc; time: 20 seconds.
- Inspection under an optical microscope.
- Asher at TRL: 800W, 5 minutes.
- PMMA removal: immerse the sample in acetone with a tweezer and agitate aggressively for at least 1 minute (This step will help to remove the hardened PMMA surface because of the RIE); soak in acetone for at least 1 hour; rinse with IPA and blow dry.
- Inspection under an optical microscope.

A.2 Top-Gated Transistor Based on Graphene-MoS_2 Lateral Heterojunction

A.2.1 Graphene Patterning

- Start with 4" Si wafer with 285 nm thermal oxide (Nova Electronic Materials)
- Clean with Nanostrip for 10 mins
- Wet transfer of CVD graphene
- Inspection under an optical microscope
- Spin-coating: TRL coater, PMMA 950A6, 4krpm, 1 min; baking at 180 °C for 7 mins.
- E-beam lithography: Elionix, 30 nA, pitch size 10 nm, dose per area 1600 $\mu C/cm^2$.
- Develop: MIBK:IPA=1:3, 90 seconds; IPA 60 seconds; blow dry with nitrogen gun.
- RIE: PlasmaTherm at NSL, O_2 + He; recipe name: testprc.prc; time: 20 seconds.
- Inspection under an optical microscope.
- Asher at TRL: 800W, 5 minutes.
- PMMA removal: immerse the sample in acetone with a tweezer and agitate

aggressively for at least 1 minute (This step will help to remove the hardened PMMA surface because of the RIE); soak in acetone for at least 1 hour; rinse with IPA and blow dry.

- Inspection under an optical microscope.

A.2.2 Formation of Graphene-MoS_2 Lateral Heterostructure

- Seeding promoter assisted MoS_2 growth

A.2.3 Wet Transfer

- Spin-coating: PMMA 950A4, 4krpm, 1 min; two layers. baking at 80 °C for 5 mins after each layer
- Detach: immerse in diluted HF (4%) for 20 seconds; dip in DI water; the PMMA/2D material film will float on the water surface
- Clean: Scoop the PMMA/2D mateiral stack with a glass slide and transfer it to a new DI water bath. Repeat for at least 3 times. Clean the top surface with DI water using a squeeze bottle.
- Transfer: immerse the targeted substrate (285 nm SiO_2/Si wafer with alignment marker grids) into the DI water bath; align the targeted substrate with the PMMA/2D material stack roughly; lift up the targeted substrate up until the PMMA/2D material stack is attached to the substrate.
- Baking: bake the transfered substrate in 80 °C for at least 10 minutes or until the water is fully evaporated; then in 130 °C oven for at least 30 minutes.
- PMMA removal: soak in acetone for at least one hour; rinse with IPA; blow dry with nitrogen gun.

A.2.4 Contact Electrodes

- Spin-coating: TRL coater, PMMA 950A6, 4krpm, 1 min; baking at 180 °C for 7 mins.

- E-beam lithography: Elionix, 30 nA, pitch size 10 nm, dose per area 1600 $\mu C/cm^2$.
- Develop: MIBK:IPA=1:3, 90 seconds; IPA 60 seconds; blow dry with nitrogen gun
- E-beam evaporation: EbeamFP, 30 nm Ni/30 nm Au
- Lift-off: soak in acetone for at least 3 hours; use a pipet to agitate; rinse with IPA and blow dry.

A.2.5 Dry Etching of 2D Materials

- Spin-coating: TRL coater, PMMA 950A6, 4krpm, 1 min; baking at 180 °C for 7 mins.
- E-beam lithography: Elionix, 30 nA, pitch size 10 nm, dose per area 1600 $\mu C/cm^2$.
- Develop: MIBK:IPA=1:3, 90 seconds; IPA 60 seconds; blow dry with nitrogen gun.
- RIE: PlasmaTherm at NSL, O_2 + He; recipe name: testprc.prc; time: 20 seconds.
- Inspection under an optical microscope.
- Asher at TRL: 800W, 5 minutes.
- PMMA removal: immerse the sample in acetone with a tweezer and agitate aggressively for at least 1 minute (This step will help to remove the hardened PMMA surface because of the RIE); soak in acetone for at least 1 hour; rinse with IPA and blow dry.
- Inspection under an optical microscope.

A.2.6 ALD Dielectric

- Seeding layer: Ebeam-FP, 3 nm Al, slow deposition rate (0.1-0.2 Å/s).
- ALD at ICL: H_2O+TMAH, 200 °C, 300 cycles (0.1 nm/cycle).
- Inspection with AFM.

A.2.7 VIA Etching

- Spin-coating: TRL coater, PMMA 950A6, 4krpm, 1 min; baking at 180 °C for 7 mins.
- E-beam lithography: Elionix, 30 nA, pitch size 10 nm, dose per area 1600 $\mu C/cm^2$.
- Develop: MIBK:IPA=1:3, 90 seconds; IPA 60 seconds; blow dry with nitrogen gun.
- RIE: Plasmaquest at TRL, Cl_2 + BCl_3; recipe name: GaNEtch.rcp. Need to calibrate the etching rate.
- Inspection under an optical microscope.
- Asher at TRL: 800W, 5 minutes.
- PMMA removal: immerse the sample in acetone with a tweezer and agitate aggressively for at least 1 minute (This step will help to remove the hardened PMMA surface because of the RIE); soak in acetone for at least 1 hour; rinse with IPA and blow dry.
- Inspection under an optical microscope.

A.2.8 Top-Gate Electrodes

- Spin-coating: TRL coater, PMMA 950A6, 4krpm, 1 min; baking at 180 °C for 7 mins.
- E-beam lithography: Elionix, 30 nA, pitch size 10 nm, dose per area 1600 $\mu C/cm^2$.
- Develop: MIBK:IPA=1:3, 90 seconds; IPA 60 seconds; blow dry with nitrogen gun
- E-beam evaporation: EbeamAu, 50 nm Pd
- Lift-off: soak in acetone for at least 3 hours; use a pipet to agitate; rinse with IPA and blow dry.

A.3 Millimeter-Sized Strain Sensor

A.3.1 Preparation of PDMS Film

- PDMS precursors: Silgard 184, monomer:linker=10:1, mix well.
- Curing: pour the PDMS gel onto a petri dish; poke any air bubbles with a toothpick after 10 minutes; leave on a horizontal surface for 48 hours to fully cure the film.
- Cut the PDMS film into rectangular pieces with a razer blade.

A.3.2 Preparation of Glass Bars

- Cut glass slides into 5 mm bars with the Diesaw at ICL-package.
- Rinse with acetone, IPA and blow dry.

A.3.3 PDMS-Glass Bonding

- O_2 plasma: treat both PDMS film and the glass bars with the Asher at EML, 100 W for 10 seconds
- Attach the exposed surfaces immediately.
- Wait for 20-30 minutes to stablize the bonding.

A.3.4 Contact Metal

- Using Polyimide or PET film as the hard mask for the metal contacts.
- E-beam evaporation: EbeamAJA at EML, 5 nm Ti/80 nm Au, use fast deposition rate to reduce the heating of the PDMS film (2-5 Å/s).

A.3.5 Formation of the Sensing Channel

Graphene Nanoflake Network

- Electrochemical exfoliation in Jing Kong's lab (electrolyte: H_2SO_4 in water).
- Sonicate for 3 hours.

- Replace the solvent to mixed alcohol (methanol:butanol=8:1).
- Marangoni self-assembly on a water surface.
- Pretreat the PDMS surface with a O_2 plasma (Asher-EML, 100W, 1 minute). This step will make PDMS hydrophilic.
- Fish the graphene film with the PDMS substrate.

Cracked Pt film

- Pretreat the PDMS surface with a O_2 plasma (Asher-EML, 100W, 5 minute).
- E-beam evaporation: EbeamAJA at EML, 2-10 nm Pt, deposition rate <0.2 A/s.
- Prestretching: mount the sample onto the strain sensor measurement bench, increase the strain slowly until the device is open.

A.3.6 SAM of Thiol Molecules

Liquid Phase SAM

- Dissolve thiol molecules (1H,1H,2H,2H-Perfluoro-1-hexanethiol, 1H,1H,2H,2H-Perfluorooctyl-1-thiol, or 1H,1H,2H,2H-Perfluorodecyl-1-thiol) in anhydrouds ethanol with a molar concentration of 5 mmol/L in a glove box.
- Immerse the pre-stretched cracked Pt device in to the thiol solution for at least 10 hours. Operate in a fume hood.
- Take the device out and blow dry.

Gas Phase SAM

- Take a trace amount of thiol molecules (1H,1H,2H,2H-Perfluoro-1-hexanethiol, 1H,1H,2H,2H-Perfluorooctyl-1-thiol, or 1H,1H,2H,2H-Perfluorodecyl-1-thiol) in a small vial.
- Immediately put the device and the opened vial into a vacuum chamber. Keep them in vacuum (<0.1 Torr) for at least 10 hours. Operate in a fume hood.

A.4 Graphene-Polymer Thermo-Mechanical Bolometer

A.4.1 Starting Substrate

- Start with a 4-inch Si wafer (purchased from MTL).
- Cleaning: TRL-acidhood, nanostrip for 10 minutes.
- For PDMS device: evaporate 200 nm AlO_x with EbeamAu in TRL.
- For Photoresist device: grow 300 nm SiO_2 with PECVD in TRL.

A.4.2 Etching of Oxides

- HMDS
- Spin-coating: SPR700, 2krpm, 60 s, bake with a hot plate at 95 °C for 5 mins.
- Photolithography: MLA-150, dose 200 mJ/cm^2. Postbake with a hot plate at 115 °C for 1 min.
- Develop: CD26, 90 s; rinse with DI water, 10 s; blow dry.
- Asher-TRL: 800 W, 5 mins.
- Etching: Plasmaquest in TRL.

  For AlO_x: recipe: Al2O3_OS.rcp. BCl_3 20 sccm, Cl_2 5 sccm, ECR 150 W, RF 180 V, chiller 25 °C. Etching rate: around 167 nm/min

  For SiO_2: recipe: CF4H_BL1.rcp. chiller 25 °C. Etching rate: around 38 nm/min.
- Asher-TRL, 800 W, 5 mins.
- Photoresist removal: nanostrip, 10 mins. Agitate to accelerate the process.

A.4.3 Metal Electrode

- HMDS
- AZ5214, 2krpm, 60 sec. Bake with a hot plate at 85 °C for 5 mins.
- Photolithography: MLA150, 27 mJ/cm^2. Post bake at 110 °C for 2 mins.
- Flood exposure: OAI-flood, 35 s.

- Develop: AZ422, 90 s; rinse with DI water, 30 s; blow dry.
- Asher-TRL, 800 W, 5 mins.
- Ebeam evaporation: EbeamAu-TRL, 5 nm Cr/50 nm Au.
- Lift-off: soak in acetone for at least 3 hours; use a pipet to agitate; rinse with IPA and blow dry.

A.4.4 Graphene Sensing Channel

- Nanostrip for 10 mins to make the surface hydrophilic.
- Marangoni self-assembly and transfer onto the chip.
- Spin-coating: TRL coater, PMMA 950A6, 4krpm, 1 min; baking at 180 °C for 7 mins.
- E-beam lithography: Elionix, 30 nA, pitch size 10 nm, dose per area 1600 μC/cm^2.
- Develop: MIBK:IPA=1:3, 90 seconds; IPA 60 seconds; blow dry with nitrogen gun.
- RIE: PlasmaTherm at NSL, O_2 + He; recipe name: testprc.prc; time: 20 seconds.
- Inspection under an optical microscope.
- Asher at TRL: 800W, 5 minutes.
- PMMA removal: immerse the sample in acetone with a tweezer and agitate aggressively for at least 1 minute (This step will help to remove the hardened PMMA surface because of the RIE); soak in acetone for at least 1 hour; rinse with IPA and blow dry.
- Inspection under an optical microscope.

A.4.5 Polymer Base

PDMS

- PDMS solution: PDMS precursors 0.13g+1.3g, dissolved in 10 mL hexane. Use a magnetic spinner.

- Spin-coating: 3krpm, 3 mins, bake at 130 °C oven for 1 hour.
- PR spin-coating: SPR700, 1.5krpm, 60 s. Leave at RT for at least 5 hours. No baking, because the thermal expansion will crumple the PDMS.
- Photolithography: MLA150, dose 200 mJ/cm^2.
- Develop: CD26, 90 s; rinse with DI water, 10 s; blow dry.
- RIE etch: recipe: PDMSETCH_O2.rcp. O_2 13 sccm, CF_4 39 sccm, Pressure 25 mTorr, ECR 150 W, RF 20W, Temp 15 C on chiller, 90 sec per cycle to prevent overheat. Repeat many times until fully etched.
- Asher at TRL: 800W, 5 minutes.
- PR removal in acetone.

Photoresist

- HMDS
- Spin-coating: SPR700, 2krpm, 60 s, bake with a hot plate at 95 °C for 5 mins.
- Photolithography: MLA150, dose 200 mJ/cm^2. Postbake with a hot plate at 115 °C for 1 min.
- Develop: CD26, 90 s; rinse with DI water, 10 s; blow dry.

A.5 Metal/Molecule/Metal Thermo-Mechanical Bolometer

A.5.1 Starting Substrate

- Start with a 4-inch Si wafer (purchased from MTL).
- Cleaning: TRL-acidhood, nanostrip for 10 minutes.
- Grow 1000 nm SiO_2 with PECVD in TRL.

A.5.2 Metal Pads

- HMDS

- AZ5214, 2krpm, 60 sec. Bake with a hot plate at 85 °C for 5 mins.
- Photolithography: MLA150, 27 mJ/cm^2. Post bake at 110 °C for 2 mins.
- Flood exposure: OAI-flood, 35 s.
- Develop: AZ422, 90 s; rinse with DI water, 30 s; blow dry.
- Asher-TRL, 800 W, 5 mins.
- Ebeam evaporation: EbeamAu-TRL, 5 nm Cr/50 nm Au.
- Lift-off: soak in acetone for at least 3 hours; use a pipet to agitate; rinse with IPA and blow dry.

A.5.3 Metal Nanogap

- Spin-coating: TRL coater, MMA 4krpm, 1min; baking at 180 °C for 7 mins; PMMA 495A8, 4krpm, 1 min; baking at 180 °C for 7 mins.
- E-beam lithography: Elionix, 1 nA, pitch size 2.5 nm, dose per area 2000 μC/cm^2.
- Develop: MIBK:IPA=1:3, 90 seconds; methonal:IPA=1:1, 30 seconds; IPA 30 seconds; blow dry with nitrogen gun.
- Inspection under optical microscope and SEM.
- Ebeam evaporation: EbeamAu-TRL, 5 nm Pt with $+15°$ slope, dep. rate 0.1 Å/s; 5 nm Pt with $-15°$ slope, dep. rate 0.1 Å/s; 100 nm Ni with normal angle.
- Lift-off: soak in acetone for at least 3 hours; use a pipet to agitate; rinse with IPA and blow dry.
- Inspection under optical microscope and SEM.

A.5.4 Si Undercut

- Si wet etch: immerse sample in diluted HF (4%) for 3 mins; transfer immediately to DI water bath; transfer again to a new DI water bath; transfer immediately to IPA.
- Critical point drying (NSL).

A.5.5 Gas Phase SAM

- Cleaning: Asher-EML, 100 W, 5 mins.
- Take a trace amount of thiol molecules (1H,1H,2H,2H-Perfluoro-1-hexanethiol, 1H,1H,2H,2H-Perfluorooctyl-1-thiol, or 1H,1H,2H,2H-Perfluorodecyl-1-thiol) in a small vial.
- Immediately put the device and the opened vial into a vacuum chamber. Keep them in vacuum ($<$0.1 Torr) for at least 10 hours. Operate in a fume hood.

Bibliography

[1] Xi Ling, Yi-Hsien Lee, Yuxuan Lin, Wenjing Fang, Lili Yu, Mildred S Dresselhaus, and Jing Kong. Role of the seeding promoter in mos2 growth by chemical vapor deposition. *Nano letters*, 14(2):464–472, 2014.

[2] Xi Ling, Yuxuan Lin, Qiong Ma, Ziqiang Wang, Yi Song, Lili Yu, Shengxi Huang, Wenjing Fang, Xu Zhang, Allen L Hsu, et al. Parallel stitching of 2d materials. *Advanced Materials*, 28(12):2322–2329, 2016.

[3] Bahaa EA Saleh and Malvin Carl Teich. *Fundamentals of photonics*, chapter 5. John Wiley & Sons, 2019.

[4] Antonio Rogalski. *Infrared detectors*, chapter 1. CRC press, 2010.

[5] Antonio Rogalski. *Infrared detectors*, chapter 3. CRC press, 2010.

[6] Antoni Rogalski. Progress in focal plane array technologies. *Progress in Quantum Electronics*, 36(2-3):342–473, 2012.

[7] A Rogalski, P Martyniuk, and M Kopytko. Challenges of small-pixel infrared detectors: a review. *Reports on Progress in Physics*, 79(4):046501, 2016.

[8] Pin-Chun Shen, Yuxuan Lin, Haozhe Wang, Ji-Hoon Park, Wei Sun Leong, Ang-Yu Lu, Tomas Palacios, and Jing Kong. Cvd technology for 2-d materials. *IEEE Transactions on Electron Devices*, 65(10):4040–4052, 2018.

[9] AH Castro Neto, Francisco Guinea, Nuno MR Peres, Kostya S Novoselov, and Andre K Geim. The electronic properties of graphene. *Reviews of modern physics*, 81(1):109, 2009.

[10] Heejun Yang, Sung Wng Kim, Manish Chhowalla, and Young Hee Lee. Structural and quantum-state phase transitions in van der waals layered materials. *Nature Physics*, 13(10):931, 2017.

[11] Kin Fai Mak and Jie Shan. Photonics and optoelectronics of 2d semiconductor transition metal dichalcogenides. *Nature Photonics*, 10(4):216, 2016.

[12] Likai Li, Jonghwan Kim, Chenhao Jin, Guo Jun Ye, Diana Y Qiu, H Felipe, Zhiwen Shi, Long Chen, Zuocheng Zhang, Fangyuan Yang, et al. Direct observation of the layer-dependent electronic structure in phosphorene. *Nature nanotechnology*, 12(1):21, 2017.

[13] Fengnian Xia, Han Wang, James CM Hwang, AH Castro Neto, and Li Yang. Black phosphorus and its isoelectronic materials. *Nature Reviews Physics*, page 1, 2019.

[14] Min Yi and Zhigang Shen. A review on mechanical exfoliation for the scalable production of graphene. *Journal of Materials Chemistry A*, 3(22):11700–11715, 2015.

[15] Deep Jariwala, Artur R Davoyan, Joeson Wong, and Harry A Atwater. Van der waals materials for atomically-thin photovoltaics: promise and outlook. *Acs Photonics*, 4(12):2962–2970, 2017.

[16] Lili Yu, Yi-Hsien Lee, Xi Ling, Elton JG Santos, Yong Cheol Shin, Yuxuan Lin, Madan Dubey, Efthimios Kaxiras, Jing Kong, Han Wang, et al. Graphene/mos2 hybrid technology for large-scale two-dimensional electronics. *Nano letters*, 14(6):3055–3063, 2014.

[17] Amirhasan Nourbakhsh, Lili Yu, Yuxuan Lin, Marek Hempel, Ren-Jye Shiue, Dirk Englund, and Tomás Palacios. *Heterogeneous Integration of 2D Materials and Devices on a Si Platform*, pages 43–84. Springer International Publishing, Cham, 2019.

[18] Søren Ulstrup, Jens Christian Johannsen, Alberto Crepaldi, Federico Cilento, Michele Zacchigna, Cephise Cacho, Richard T Chapman, Emma Springate, Felix Fromm, Christian Raidel, et al. Ultrafast electron dynamics in epitaxial graphene investigated with time-and angle-resolved photoemission spectroscopy. *Journal of Physics: Condensed Matter*, 27(16):164206, 2015.

[19] Justin CW Song, Mark S Rudner, Charles M Marcus, and Leonid S Levitov. Hot carrier transport and photocurrent response in graphene. *Nano letters*, 11(11):4688–4692, 2011.

[20] Yuxuan Lin, Qiong Ma, Pin-Chun Shen, Batyr Ilyas, Yaqing Bie, Albert Liao, Emre Ergeçen, Bingnan Han, Nannan Mao, Xu Zhang, et al. Asymmetric hot-carrier thermalization and broadband photoresponse in graphene-2d semiconductor lateral heterojunctions. *Science Advances*, 5(6):eaav1493, 2019.

[21] Kin Fai Mak, Matthew Y Sfeir, Yang Wu, Chun Hung Lui, James A Misewich, and Tony F Heinz. Measurement of the optical conductivity of graphene. *Physical review letters*, 101(19):196405, 2008.

[22] Yilei Li, Alexey Chernikov, Xian Zhang, Albert Rigosi, Heather M Hill, Arend M van der Zande, Daniel A Chenet, En-Min Shih, James Hone, and Tony F Heinz. Measurement of the optical dielectric function of monolayer transition-metal dichalcogenides: Mos2, mose2, ws2, and wse2. *Physical Review B*, 90(20):205422, 2014.

[23] Morteza Amjadi, Ki-Uk Kyung, Inkyu Park, and Metin Sitti. Stretchable, skin-mountable, and wearable strain sensors and their potential applications: a review. *Advanced Functional Materials*, 26(11):1678–1698, 2016.

[24] AS Fiorillo, CD Critello, and SA Pullano. Theory, technology and applications of piezoresistive sensors: A review. *Sensors and Actuators A: Physical*, 281:156–175, 2018.

[25] Antonio Rogalski. *Infrared detectors*, chapter 6. CRC press, 2010.

[26] Saptarshi Das, Hong-Yan Chen, Ashish Verma Penumatcha, and Joerg Appenzeller. High performance multilayer mos2 transistors with scandium contacts. *Nano letters*, 13(1):100–105, 2012.

[27] Naveen Kaushik, Ankur Nipane, Firdous Basheer, Sudipta Dubey, Sameer Grover, Mandar M Deshmukh, and Saurabh Lodha. Schottky barrier heights for au and pd contacts to mos2. *Applied Physics Letters*, 105(11):113505, 2014.

[28] James Clerk Maxwell. Viii. a dynamical theory of the electromagnetic field. *Philosophical transactions of the Royal Society of London*, 155:459–512, 1865.

[29] Janice L Thomson and John W Salisbury. The mid-infrared reflectance of mineral mixtures (7–14 μm). *Remote Sensing of Environment*, 45(1):1–13, 1993.

[30] Qihao Weng. Thermal infrared remote sensing for urban climate and environmental studies: Methods, applications, and trends. *ISPRS Journal of Photogrammetry and Remote Sensing*, 64(4):335–344, 2009.

[31] Karen E Joyce, Stella E Belliss, Sergey V Samsonov, Stephen J McNeill, and Phil J Glassey. A review of the status of satellite remote sensing and image processing techniques for mapping natural hazards and disasters. *Progress in Physical Geography*, 33(2):183–207, 2009.

[32] Valeria Nicolosi, Manish Chhowalla, Mercouri G Kanatzidis, Michael S Strano, and Jonathan N Coleman. Liquid exfoliation of layered materials. *Science*, 340(6139):1226419, 2013.

[33] Andre K Geim and Konstantin S Novoselov. The rise of graphene. In *Nanoscience and Technology: A Collection of Reviews from Nature Journals*, pages 11–19. World Scientific, 2010.

[34] Kirill I Bolotin, K J Sikes, Zd Jiang, M Klima, G Fudenberg, J Hone, Ph Kim, and HL Stormer. Ultrahigh electron mobility in suspended graphene. *Solid State Communications*, 146(9-10):351–355, 2008.

[35] Cory R Dean, Andrea F Young, Inanc Meric, Chris Lee, Lei Wang, Sebastian Sorgenfrei, Kenji Watanabe, Takashi Taniguchi, Phillip Kim, Kenneth L Shepard, et al. Boron nitride substrates for high-quality graphene electronics. *Nature nanotechnology*, 5(10):722, 2010.

[36] Luca Banszerus, Michael Schmitz, Stephan Engels, Jan Dauber, Martin Oellers, Federica Haupt, Kenji Watanabe, Takashi Taniguchi, Bernd Beschoten, and Christoph Stampfer. Ultrahigh-mobility graphene devices from chemical vapor deposition on reusable copper. *Science advances*, 1(6):e1500222, 2015.

[37] Yuanbo Zhang, Tsung-Ta Tang, Caglar Girit, Zhao Hao, Michael C Martin, Alex Zettl, Michael F Crommie, Y Ron Shen, and Feng Wang. Direct observation of a widely tunable bandgap in bilayer graphene. *Nature*, 459(7248):820, 2009.

[38] Long Ju, Lei Wang, Ting Cao, Takashi Taniguchi, Kenji Watanabe, Steven G Louie, Farhan Rana, Jiwoong Park, James Hone, Feng Wang, et al. Tunable excitons in bilayer graphene. *Science*, 358(6365):907–910, 2017.

[39] Daniel C Elias, Rahul Raveendran Nair, TMG Mohiuddin, SV Morozov, P Blake, MP Halsall, Andrea Carlo Ferrari, DW Boukhvalov, MI Katsnelson, AK Geim, et al. Control of graphene's properties by reversible hydrogenation: evidence for graphane. *Science*, 323(5914):610–613, 2009.

[40] Rahul R Nair, Wencai Ren, Rashid Jalil, Ibtsam Riaz, Vasyl G Kravets, Liam Britnell, Peter Blake, Fredrik Schedin, Alexander S Mayorov, Shengjun Yuan, et al. Fluorographene: a two-dimensional counterpart of teflon. *small*, 6(24):2877–2884, 2010.

[41] Jeremy T Robinson, James S Burgess, Chad E Junkermeier, Stefan C Badescu, Thomas L Reinecke, F Keith Perkins, Maxim K Zalalutdniov, Jeffrey W Baldwin, James C Culbertson, Paul E Sheehan, et al. Properties of fluorinated graphene films. *Nano letters*, 10(8):3001–3005, 2010.

[42] Verónica Barone, Oded Hod, and Gustavo E Scuseria. Electronic structure and stability of semiconducting graphene nanoribbons. *Nano letters*, 6(12):2748–2754, 2006.

[43] C Stampfer, J Güttinger, S Hellmüller, F Molitor, K Ensslin, and T Ihn. Energy gaps in etched graphene nanoribbons. *Physical review letters*, 102(5):056403, 2009.

[44] Daniel J Rizzo, Gregory Veber, Ting Cao, Christopher Bronner, Ting Chen, Fangzhou Zhao, Henry Rodriguez, Steven G Louie, Michael F Crommie, and Felix R Fischer. Topological band engineering of graphene nanoribbons. *Nature*, 560(7717):204, 2018.

[45] Frank HL Koppens, Darrick E Chang, and F Javier Garcia de Abajo. Graphene plasmonics: a platform for strong light–matter interactions. *Nano letters*, 11(8):3370–3377, 2011.

[46] AN Grigorenko, Marco Polini, and KS Novoselov. Graphene plasmonics. *Nature photonics*, 6(11):749, 2012.

[47] Long Ju, Baisong Geng, Jason Horng, Caglar Girit, Michael Martin, Zhao Hao, Hans A Bechtel, Xiaogan Liang, Alex Zettl, Y Ron Shen, et al. Graphene plasmonics for tunable terahertz metamaterials. *Nature nanotechnology*, 6(10):630, 2011.

[48] Zhe Fei, AS Rodin, Gregory O Andreev, W Bao, AS McLeod, M Wagner, LM Zhang, Z Zhao, M Thiemens, G Dominguez, et al. Gate-tuning of graphene plasmons revealed by infrared nano-imaging. *Nature*, 487(7405):82, 2012.

[49] Jianing Chen, Michela Badioli, Pablo Alonso-González, Sukosin Thongrattanasiri, Florian Huth, Johann Osmond, Marko Spasenović, Alba Centeno, Amaia Pesquera, Philippe Godignon, et al. Optical nano-imaging of gate-tunable graphene plasmons. *Nature*, 487(7405):77, 2012.

[50] Manish Chhowalla, Hyeon Suk Shin, Goki Eda, Lain-Jong Li, Kian Ping Loh, and Hua Zhang. The chemistry of two-dimensional layered transition metal dichalcogenide nanosheets. *Nature chemistry*, 5(4):263, 2013.

[51] Andrea Splendiani, Liang Sun, Yuanbo Zhang, Tianshu Li, Jonghwan Kim, Chi-Yung Chim, Giulia Galli, and Feng Wang. Emerging photoluminescence in monolayer mos2. *Nano letters*, 10(4):1271–1275, 2010.

[52] Kin Fai Mak, Changgu Lee, James Hone, Jie Shan, and Tony F Heinz. Atomically thin mos2: a new direct-gap semiconductor. *Physical review letters*, 105(13):136805, 2010.

[53] Yuxuan Lin, Xi Ling, Lili Yu, Shengxi Huang, Allen L Hsu, Yi-Hsien Lee, Jing Kong, Mildred S Dresselhaus, and Tomás Palacios. Dielectric screening of excitons and trions in single-layer mos2. *Nano letters*, 14(10):5569–5576, 2014.

[54] Timothy C Berkelbach, Mark S Hybertsen, and David R Reichman. Theory of neutral and charged excitons in monolayer transition metal dichalcogenides. *Physical Review B*, 88(4):045318, 2013.

[55] Ting Cao, Gang Wang, Wenpeng Han, Huiqi Ye, Chuanrui Zhu, Junren Shi, Qian Niu, Pingheng Tan, Enge Wang, Baoli Liu, et al. Valley-selective circular dichroism of monolayer molybdenum disulphide. *Nature communications*, 3:887, 2012.

[56] Kin Fai Mak, Keliang He, Changgu Lee, Gwan Hyoung Lee, James Hone, Tony F Heinz, and Jie Shan. Tightly bound trions in monolayer mos 2. *Nature materials*, 12(3):207, 2013.

[57] Xiaodong Xu, Wang Yao, Di Xiao, and Tony F Heinz. Spin and pseudospins in layered transition metal dichalcogenides. *Nature Physics*, 10(5):343, 2014.

[58] Kin Fai Mak, Kathryn L McGill, Jiwoong Park, and Paul L McEuen. The valley hall effect in mos2 transistors. *Science*, 344(6191):1489–1492, 2014.

[59] Shun Lien Chuang. *Physics of photonic devices*, volume 80, chapter 8. John Wiley & Sons, 2012.

[60] Ashwin Ramasubramaniam. Large excitonic effects in monolayers of molybdenum and tungsten dichalcogenides. *Physical Review B*, 86(11):115409, 2012.

[61] Hannu-Pekka Komsa and Arkady V Krasheninnikov. Effects of confinement and environment on the electronic structure and exciton binding energy of mos 2 from first principles. *Physical Review B*, 86(24):241201, 2012.

[62] Diana Y Qiu, H Felipe, and Steven G Louie. Optical spectrum of mos 2: many-body effects and diversity of exciton states. *Physical review letters*, 111(21):216805, 2013.

[63] Alexey Chernikov, Timothy C Berkelbach, Heather M Hill, Albert Rigosi, Yilei Li, Ozgur Burak Aslan, David R Reichman, Mark S Hybertsen, and Tony F Heinz. Exciton binding energy and nonhydrogenic rydberg series in monolayer ws 2. *Physical review letters*, 113(7):076802, 2014.

[64] Miguel M Ugeda, Aaron J Bradley, Su-Fei Shi, H Felipe, Yi Zhang, Diana Y Qiu, Wei Ruan, Sung-Kwan Mo, Zahid Hussain, Zhi-Xun Shen, et al. Giant bandgap renormalization and excitonic effects in a monolayer transition metal dichalcogenide semiconductor. *Nature materials*, 13(12):1091, 2014.

[65] Chendong Zhang, Amber Johnson, Chang-Lung Hsu, Lain-Jong Li, and Chih-Kang Shih. Direct imaging of band profile in single layer mos2 on graphite: quasiparticle energy gap, metallic edge states, and edge band bending. *Nano letters*, 14(5):2443–2447, 2014.

[66] Yu-Ming He, Genevieve Clark, John R Schaibley, Yu He, Ming-Cheng Chen, Yu-Jia Wei, Xing Ding, Qiang Zhang, Wang Yao, Xiaodong Xu, et al. Single quantum emitters in monolayer semiconductors. *Nature nanotechnology*, 10(6):497, 2015.

[67] John R Schaibley, Hongyi Yu, Genevieve Clark, Pasqual Rivera, Jason S Ross, Kyle L Seyler, Wang Yao, and Xiaodong Xu. Valleytronics in 2d materials. *Nature Reviews Materials*, 1(11):16055, 2016.

[68] Qing Hua Wang, Kourosh Kalantar-Zadeh, Andras Kis, Jonathan N Coleman, and Michael S Strano. Electronics and optoelectronics of two-dimensional transition metal dichalcogenides. *Nature nanotechnology*, 7(11):699, 2012.

[69] Balazs Sipos, Anna F Kusmartseva, Ana Akrap, Helmut Berger, Laszlo Forró, and Eduard Tutiš. From mott state to superconductivity in 1t-tas 2. *Nature materials*, 7(12):960, 2008.

[70] Igor Vaskivskyi, Jan Gospodaric, Serguei Brazovskii, Damjan Svetin, Petra Sutar, Evgeny Goreshnik, Ian A Mihailovic, Tomaz Mertelj, and Dragan Mihailovic. Controlling the metal-to-insulator relaxation of the metastable hidden quantum state in 1t-tas2. *Science advances*, 1(6):e1500168, 2015.

[71] Yijun Yu, Fangyuan Yang, Xiu Fang Lu, Ya Jun Yan, Yong-Heum Cho, Liguo Ma, Xiaohai Niu, Sejoong Kim, Young-Woo Son, Donglai Feng, et al. Gate-tunable phase transitions in thin flakes of 1t-tas 2. *Nature nanotechnology*, 10(3):270, 2015.

[72] U Chatterjee, J Zhao, M Iavarone, R Di Capua, JP Castellan, G Karapetrov, CD Malliakas, Mercouri G Kanatzidis, H Claus, JPC Ruff, et al. Emergence of coherence in the charge-density wave state of 2h-nbse 2. *Nature communications*, 6:6313, 2015.

[73] Xiaoxiang Xi, Liang Zhao, Zefang Wang, Helmuth Berger, László Forró, Jie Shan, and Kin Fai Mak. Strongly enhanced charge-density-wave order in monolayer nbse 2. *Nature nanotechnology*, 10(9):765, 2015.

[74] G Li, WZ Hu, D Qian, D Hsieh, MZ Hasan, E Morosan, Robert Joseph Cava, and NL Wang. Semimetal-to-semimetal charge density wave transition in 1 t-tise 2. *Physical review letters*, 99(2):027404, 2007.

[75] Fengnian Xia, Han Wang, and Yichen Jia. Rediscovering black phosphorus as an anisotropic layered material for optoelectronics and electronics. *Nature communications*, 5:4458, 2014.

[76] Likai Li, Yijun Yu, Guo Jun Ye, Qingqin Ge, Xuedong Ou, Hua Wu, Donglai Feng, Xian Hui Chen, and Yuanbo Zhang. Black phosphorus field-effect transistors. *Nature nanotechnology*, 9(5):372, 2014.

[77] Xi Ling, Han Wang, Shengxi Huang, Fengnian Xia, and Mildred S Dresselhaus. The renaissance of black phosphorus. *Proceedings of the National Academy of Sciences*, 112(15):4523–4530, 2015.

[78] Xiaomu Wang, Aaron M Jones, Kyle L Seyler, Vy Tran, Yichen Jia, Huan Zhao, Han Wang, Li Yang, Xiaodong Xu, and Fengnian Xia. Highly anisotropic and robust excitons in monolayer black phosphorus. *Nature nanotechnology*, 10(6):517, 2015.

[79] Shenyang Huang, Guowei Zhang, Fengren Fan, Chaoyu Song, Fanjie Wang, Qiaoxia Xing, Chong Wang, Hua Wu, and Hugen Yan. Strain-tunable van der waals interactions in few-layer black phosphorus. *Nature communications*, 10(1):2447, 2019.

[80] Chaoliang Tan, Xiehong Cao, Xue-Jun Wu, Qiyuan He, Jian Yang, Xiao Zhang, Junze Chen, Wei Zhao, Shikui Han, Gwang-Hyeon Nam, et al. Recent advances in ultrathin two-dimensional nanomaterials. *Chemical reviews*, 117(9):6225–6331, 2017.

[81] Sivacarendran Balendhran, Sumeet Walia, Hussein Nili, Sharath Sriram, and Madhu Bhaskaran. Elemental analogues of graphene: silicene, germanene, stanene, and phosphorene. *small*, 11(6):640–652, 2015.

[82] Michael McGuire. Crystal and magnetic structures in layered, transition metal dihalides and trihalides. *Crystals*, 7(5):121, 2017.

[83] Nicolas Mounet, Marco Gibertini, Philippe Schwaller, Davide Campi, Andrius Merkys, Antimo Marrazzo, Thibault Sohier, Ivano Eligio Castelli, Andrea Cepellotti, Giovanni Pizzi, et al. Two-dimensional materials from high-throughput computational exfoliation of experimentally known compounds. *Nature nanotechnology*, 13(3):246, 2018.

[84] Sten Haastrup, Mikkel Strange, Mohnish Pandey, Thorsten Deilmann, Per S Schmidt, Nicki F Hinsche, Morten N Gjerding, Daniele Torelli, Peter M Larsen, Anders C Riis-Jensen, et al. The computational 2d materials database: high-throughput modeling and discovery of atomically thin crystals. *2D Materials*, 5(4):042002, 2018.

[85] SV Morozov, KS Novoselov, AK Geim, D Jiang, Y Zhang, SV Dubonos, IV Grigorieva, AA Firsov, and James Mussell. Electric field effect in atomically thin carbon films. *Science*, 2004.

[86] Kostya S Novoselov, D Jiang, F Schedin, TJ Booth, VV Khotkevich, SV Morozov, and Andre K Geim. Two-dimensional atomic crystals. *Proceedings of the National Academy of Sciences*, 102(30):10451–10453, 2005.

[87] Kostya S Novoselov, Andre K Geim, SVb Morozov, Da Jiang, Michail I Katsnelson, IVa Grigorieva, SVb Dubonos, and AA Firsov. Two-dimensional gas of massless dirac fermions in graphene. *nature*, 438(7065):197, 2005.

[88] Sujay B Desai, Surabhi R Madhvapathy, Matin Amani, Daisuke Kiriya, Mark Hettick, Mahmut Tosun, Yuzhi Zhou, Madan Dubey, Joel W Ager III, Daryl Chrzan, et al. Gold-mediated exfoliation of ultralarge optoelectronically-perfect monolayers. *Advanced Materials*, 28(21):4053–4058, 2016.

[89] Marek Hempel, A-Y Lu, Fei Hui, Tewa Kpulun, Mario Lanza, Gary Harris, Tomas Palacios, and Jing Kong. Repeated roll-to-roll transfer of two-dimensional materials by electrochemical delamination. *Nanoscale*, 10(12):5522–5531, 2018.

[90] Yung-Chang Lin, Chun-Chieh Lu, Chao-Huei Yeh, Chuanhong Jin, Kazu Suenaga, and Po-Wen Chiu. Graphene annealing: how clean can it be? *Nano letters*, 12(1):414–419, 2011.

[91] Chris D English, Gautam Shine, Vincent E Dorgan, Krishna C Saraswat, and Eric Pop. Improved contacts to mos2 transistors by ultra-high vacuum metal deposition. *Nano letters*, 16(6):3824–3830, 2016.

[92] Grzegorz Lupina, Julia Kitzmann, Ioan Costina, Mindaugas Lukosius, Christian Wenger, Andre Wolff, Sam Vaziri, Mikael Ostling, Iwona Pasternak, Aleksandra Krajewska, et al. Residual metallic contamination of transferred chemical vapor deposited graphene. *ACS nano*, 9(5):4776–4785, 2015.

[93] Allen Hsu, Han Wang, Ki Kang Kim, Jing Kong, and Tomas Palacios. Impact of graphene interface quality on contact resistance and rf device performance. *IEEE Electron Device Letters*, 32(8):1008–1010, 2011.

[94] L Wang, I Meric, PY Huang, Q Gao, Y Gao, H Tran, T Taniguchi, Kenji Watanabe, LM Campos, DA Muller, et al. One-dimensional electrical contact to a two-dimensional material. *Science*, 342(6158):614–617, 2013.

[95] Wei Sun Leong, Hao Gong, and John TL Thong. Low-contact-resistance graphene devices with nickel-etched-graphene contacts. *ACS nano*, 8(1):994–1001, 2013.

[96] Rajesh Kappera, Damien Voiry, Sibel Ebru Yalcin, Brittany Branch, Gautam Gupta, Aditya D Mohite, and Manish Chhowalla. Phase-engineered low-resistance contacts for ultrathin mos 2 transistors. *Nature materials*, 13(12):1128, 2014.

[97] Steven Chuang, Corsin Battaglia, Angelica Azcatl, Stephen McDonnell, Jeong Seuk Kang, Xingtian Yin, Mahmut Tosun, Rehan Kapadia, Hui Fang, Robert M Wallace, et al. Mos2 p-type transistors and diodes enabled by high work function moo x contacts. *Nano letters*, 14(3):1337–1342, 2014.

[98] Yuan Liu, Jian Guo, Enbo Zhu, Lei Liao, Sung-Joon Lee, Mengning Ding, Imran Shakir, Vincent Gambin, Yu Huang, and Xiangfeng Duan. Approaching the schottky–mott limit in van der waals metal–semiconductor junctions. *Nature*, 557(7707):696, 2018.

[99] Amal Kasry, Marcelo A Kuroda, Glenn J Martyna, George S Tulevski, and Ageeth A Bol. Chemical doping of large-area stacked graphene films for use as transparent, conducting electrodes. *ACS nano*, 4(7):3839–3844, 2010.

[100] Yumeng Shi, Ki Kang Kim, Alfonso Reina, Mario Hofmann, Lain-Jong Li, and Jing Kong. Work function engineering of graphene electrode via chemical doping. *ACS nano*, 4(5):2689–2694, 2010.

[101] Peida Zhao, Daisuke Kiriya, Angelica Azcatl, Chenxi Zhang, Mahmut Tosun, Yi-Sheng Liu, Mark Hettick, Jeong Seuk Kang, Stephen McDonnell, Santosh KC, et al. Air stable p-doping of wse2 by covalent functionalization. *ACS nano*, 8(10):10808–10814, 2014.

[102] Lili Yu, Ahmad Zubair, Elton JG Santos, Xu Zhang, Yuxuan Lin, Yuhao Zhang, and Tomás Palacios. High-performance wse2 complementary metal oxide semiconductor technology and integrated circuits. *Nano letters*, 15(8):4928–4934, 2015.

[103] Shinichiro Mouri, Yuhei Miyauchi, and Kazunari Matsuda. Tunable photoluminescence of monolayer mos2 via chemical doping. *Nano letters*, 13(12):5944–5948, 2013.

[104] Tingting Feng, Dan Xie, Yuxuan Lin, He Tian, Haiming Zhao, Tianling Ren, and Hongwei Zhu. Unipolar to ambipolar conversion in graphene field-effect transistors. *Applied Physics Letters*, 101(25):253505, 2012.

[105] Hong Li, Qing Zhang, Chao Liu, Shouheng Xu, and Pingqi Gao. Ambipolar to unipolar conversion in graphene field-effect transistors. *ACS nano*, 5(4):3198–3203, 2011.

[106] Xu Zhang, Allen Hsu, Han Wang, Yi Song, Jing Kong, Mildred S Dresselhaus, and Tomás Palacios. Impact of chlorine functionalization on high-mobility chemical vapor deposition grown graphene. *ACS nano*, 7(8):7262–7270, 2013.

[107] Roshni Yadav and CK Dixit. Synthesis, characterization and prospective applications of nitrogen-doped graphene: A short review. *Journal of Science: Advanced Materials and Devices*, 2(2):141–149, 2017.

[108] Huabing Shu, Yunhai Li, Xianghong Niu, and Jinlan Wang. Greatly enhanced optical absorption of a defective mos2 monolayer through oxygen passivation. *ACS applied materials & interfaces*, 8(20):13150–13156, 2016.

[109] Haiyan Nan, Zilu Wang, Wenhui Wang, Zheng Liang, Yan Lu, Qian Chen, Daowei He, Pingheng Tan, Feng Miao, Xinran Wang, et al. Strong photoluminescence enhancement of mos2 through defect engineering and oxygen bonding. *ACS nano*, 8(6):5738–5745, 2014.

[110] Masihhur R Laskar, Digbijoy N Nath, Lu Ma, Edwin W Lee, Choong Hee Lee, Thomas Kent, Zihao Yang, Rohan Mishra, Manuel A Roldan, Juan-Carlos Idrobo, et al. p-type doping of mos2 thin films using nb. *Applied Physics Letters*, 104(9):092104, 2014.

[111] Ankur Nipane, Debjani Karmakar, Naveen Kaushik, Shruti Karande, and Saurabh Lodha. Few-layer mos2 p-type devices enabled by selective doping using low energy phosphorus implantation. *ACS nano*, 10(2):2128–2137, 2016.

[112] Mingsheng Long, Peng Wang, Hehai Fang, and Weida Hu. Progress, challenges, and opportunities for 2d material based photodetectors. *Advanced Functional Materials*, 29(19):1803807, 2019.

[113] Fakun Wang, Yue Zhang, Yu Gao, Peng Luo, Jianwei Su, Wei Han, Kailang Liu, Huiqiao Li, and Tianyou Zhai. 2d metal chalcogenides for ir photodetection. *Small*, page 1901347, 2019.

[114] Chao Xie, Chunhin Mak, Xiaoming Tao, and Feng Yan. Photodetectors based on two-dimensional layered materials beyond graphene. *Advanced Functional Materials*, 27(19):1603886, 2017.

[115] Britton WH Baugher, Hugh OH Churchill, Yafang Yang, and Pablo Jarillo-Herrero. Optoelectronic devices based on electrically tunable p–n diodes in a monolayer dichalcogenide. *Nature nanotechnology*, 9(4):262, 2014.

[116] Ya-Qing Bie, Gabriele Grosso, Mikkel Heuck, Marco M Furchi, Yuan Cao, Jiabao Zheng, Darius Bunandar, Efren Navarro-Moratalla, Lin Zhou, Dmitri K Efetov, et al. A mote 2-based light-emitting diode and photodetector for silicon photonic integrated circuits. *Nature nanotechnology*, 12(12):1124, 2017.

[117] Nengjie Huo and Gerasimos Konstantatos. Ultrasensitive all-2d mos2 phototransistors enabled by an out-of-plane mos2 pn homojunction. *Nature communications*, 8(1):572, 2017.

[118] Anyuan Gao, Jiawei Lai, Yaojia Wang, Zhen Zhu, Junwen Zeng, Geliang Yu, Naizhou Wang, Wenchao Chen, Tianjun Cao, Weida Hu, et al. Observation of ballistic avalanche phenomena in nanoscale vertical inse/bp heterostructures. *Nature nanotechnology*, 14(3):217, 2019.

[119] James Bullock, Matin Amani, Joy Cho, Yu-Ze Chen, Geun Ho Ahn, Valerio Adinolfi, Vivek Raj Shrestha, Yang Gao, Kenneth B Crozier, Yu-Lun Chueh, et al. Polarization-resolved black phosphorus/molybdenum disulfide mid-wave infrared photodiodes with high detectivity at room temperature. *Nature Photonics*, 12(10):601, 2018.

[120] YJ Zhang, T Ideue, M Onga, F Qin, R Suzuki, A Zak, R Tenne, JH Smet, and Y Iwasa. Enhanced intrinsic photovoltaic effect in tungsten disulfide nanotubes. *Nature*, 570(7761):349, 2019.

[121] Gavin B Osterhoudt, Laura K Diebel, Mason J Gray, Xu Yang, John Stanco, Xiangwei Huang, Bing Shen, Ni Ni, Philip JW Moll, Ying Ran, et al. Colossal mid-infrared bulk photovoltaic effect in a type-i weyl semimetal. *Nature materials*, 18(5):471, 2019.

[122] FHL Koppens, T Mueller, Ph Avouris, AC Ferrari, MS Vitiello, and M Polini. Photodetectors based on graphene, other two-dimensional materials and hybrid systems. *Nature nanotechnology*, 9(10):780, 2014.

[123] Hehai Fang and Weida Hu. Photogating in low dimensional photodetectors. *Advanced Science*, 4(12):1700323, 2017.

[124] Gerasimos Konstantatos, Michela Badioli, Louis Gaudreau, Johann Osmond, Maria Bernechea, F Pelayo Garcia De Arquer, Fabio Gatti, and Frank HL Koppens. Hybrid graphene–quantum dot phototransistors with ultrahigh gain. *Nature nanotechnology*, 7(6):363, 2012.

[125] Marcus Freitag, Tony Low, Fengnian Xia, and Phaedon Avouris. Photoconductivity of biased graphene. *Nature Photonics*, 7(1):53, 2013.

[126] Qiushi Guo, Renwen Yu, Cheng Li, Shaofan Yuan, Bingchen Deng, F Javier García de Abajo, and Fengnian Xia. Efficient electrical detection of mid-infrared graphene plasmons at room temperature. *Nature materials*, page 1, 2018.

[127] Jun Yan, Mann Ho Kim, Jennifer A Elle, Andrei B Sushkov, Greg S Jenkins, Ho-ward M Milchberg, Michael S Fuhrer, and HD Drew. Dual-gated bilayer graphene hot-electron bolometer. *Nature nanotechnology*, 7(7):472, 2012.

[128] Dong Wu, Yongchang Ma, Yingying Niu, Qiaomei Liu, Tao Dong, Sijie Zhang, Jiasen Niu, Huibin Zhou, Jian Wei, Yingxin Wang, et al. Ultrabroadband photosensitivity from visible to terahertz at room temperature. *Science advances*, 4(8):eaao3057, 2018.

[129] Xinsheng Wang, Haining Liu, Juanxia Wu, Junhao Lin, Wen He, Hui Wang, Xinghua Shi, Kazutomo Suenaga, and Liming Xie. Chemical growth of 1t-tas2 monolayer and thin films: Robust charge density wave transitions and high bolometric responsivity. *Advanced Materials*, 30(38):1800074, 2018.

[130] Kavitha K Gopalan, Davide Janner, Sebastien Nanot, Romain Parret, Mark B Lundeberg, Frank HL Koppens, and Valerio Pruneri. Mid-infrared pyroresistive graphene detector on linbo3. *Advanced Optical Materials*, 5(4):1600723, 2017.

[131] U Sassi, Romain Parret, S Nanot, M Bruna, S Borini, Domenico De Fazio, Z Zhao, E Lidorikis, FHL Koppens, Andrea Carlo Ferrari, et al. Graphene-based mid-infrared room-temperature pyroelectric bolometers with ultrahigh temperature coefficient of resistance. *Nature communications*, 8:14311, 2017.

[132] Lili Yu. *Two-dimensional materials for ubiquitous electronics*. PhD thesis, Massachusetts Institute of Technology, 2013.

[133] Arokia Nathan, Arman Ahnood, Matthew T Cole, Sungsik Lee, Yuji Suzuki, Pritesh Hiralal, Francesco Bonaccorso, Tawfique Hasan, Luis Garcia-Gancedo, Andriy Dyadyusha, et al. Flexible electronics: the next ubiquitous platform. *Proceedings of the IEEE*, 100(Special Centennial Issue):1486–1517, 2012.

[134] Kallol Roy, Medini Padmanabhan, Srijit Goswami, T Phanindra Sai, Gopalakrishnan Ramalingam, Srinivasan Raghavan, and Arindam Ghosh. Graphene–mos 2 hybrid structures for multifunctional photoresponsive memory devices. *Nature nanotechnology*, 8(11):826, 2013.

[135] Woo Jong Yu, Zheng Li, Hailong Zhou, Yu Chen, Yang Wang, Yu Huang, and Xiangfeng Duan. Vertically stacked multi-heterostructures of layered materials for logic transistors and complementary inverters. *Nature materials*, 12(3):246, 2013.

[136] Zheng Liu, Lulu Ma, Gang Shi, Wu Zhou, Yongji Gong, Sidong Lei, Xuebei Yang, Jiangnan Zhang, Jingjiang Yu, Ken P Hackenberg, et al. In-plane heterostructures of graphene and hexagonal boron nitride with controlled domain sizes. *Nature nanotechnology*, 8(2):119, 2013.

[137] Woo Jong Yu, Yuan Liu, Hailong Zhou, Anxiang Yin, Zheng Li, Yu Huang, and Xiangfeng Duan. Highly efficient gate-tunable photocurrent generation in vertical heterostructures of layered materials. *Nature nanotechnology*, 8(12):952, 2013.

[138] Liam Britnell, RM Ribeiro, A Eckmann, R Jalil, BD Belle, A Mishchenko, Y-J Kim, RV Gorbachev, T Georgiou, SV Morozov, et al. Strong light-matter interactions in heterostructures of atomically thin films. *Science*, 340(6138):1311–1314, 2013.

[139] Ming-Yang Li, Yumeng Shi, Chia-Chin Cheng, Li-Syuan Lu, Yung-Chang Lin, Hao-Lin Tang, Meng-Lin Tsai, Chih-Wei Chu, Kung-Hwa Wei, Jr-Hau He, et al. Epitaxial growth of a monolayer wse2-mos2 lateral pn junction with an atomically sharp interface. *Science*, 349(6247):524–528, 2015.

[140] M Iqbal Bakti Utama, Xin Lu, Yanwen Yuan, and Qihua Xiong. Detrimental influence of catalyst seeding on the device properties of cvd-grown 2d layered materials: A case study on mose2. *Applied Physics Letters*, 105(25):253102, 2014.

[141] Yi-Hsien Lee, Lili Yu, Han Wang, Wenjing Fang, Xi Ling, Yumeng Shi, Cheng-Te Lin, Jing-Kai Huang, Mu-Tung Chang, Chia-Seng Chang, et al. Synthesis and transfer of single-layer transition metal disulfides on diverse surfaces. *Nano letters*, 13(4):1852–1857, 2013.

[142] Kathleen M McCreary, Aubrey T Hanbicki, Glenn G Jernigan, James C Culbertson, and Berend T Jonker. Synthesis of large-area ws 2 monolayers with exceptional photoluminescence. *Scientific reports*, 6:19159, 2016.

[143] Yunfan Guo, Pin-Chun Shen, Cong Su, Ang-Yu Lu, Marek Hempel, Yimo Han, Qingqing Ji, Yuxuan Lin, Enzheng Shi, Elaine McVay, et al. Additive manufacturing of patterned 2d semiconductor through recyclable masked growth. *Proceedings of the National Academy of Sciences*, 116(9):3437–3442, 2019.

[144] Simon M Sze and Kwok K Ng. *Physics of semiconductor devices*. John wiley & sons, 2006.

[145] Joon Young Kwak, Jeonghyun Hwang, Brian Calderon, Hussain Alsalman, Nini Munoz, Brian Schutter, and Michael G Spencer. Electrical characteristics of multilayer mos2 fet's with mos2/graphene heterojunction contacts. *Nano letters*, 14(8):4511–4516, 2014.

[146] Nan Yao and Zhong Lin Wang. *Handbook of microscopy for nanotechnology*. Springer, 2005.

[147] Karel Hendrik Wouter van den Bos, Thomas Altantzis, Annick De Backer, Sandra Van Aert, and Sara Bals. Recent breakthroughs in scanning transmission electron microscopy of small species. *Advances in Physics: X*, 3(1):1480420, 2018.

[148] Prabhat Verma. Tip-enhanced raman spectroscopy: technique and recent advances. *Chemical reviews*, 117(9):6447–6466, 2017.

[149] N Rotenberg and L Kuipers. Mapping nanoscale light fields. *Nature Photonics*, 8(12):919, 2014.

[150] Leo Gross. Recent advances in submolecular resolution with scanning probe microscopy. *Nature chemistry*, 3(4):273, 2011.

[151] Jonathan Long, Evan Shelhamer, and Trevor Darrell. Fully convolutional networks for semantic segmentation. In *Proceedings of the IEEE conference on computer vision and pattern recognition*, pages 3431–3440, 2015.

[152] Liang-Chieh Chen, George Papandreou, Iasonas Kokkinos, Kevin Murphy, and Alan L Yuille. Deeplab: Semantic image segmentation with deep convolutional nets, atrous convolution, and fully connected crfs. *IEEE transactions on pattern analysis and machine intelligence*, 40(4):834–848, 2017.

[153] Olaf Ronneberger, Philipp Fischer, and Thomas Brox. U-net: Convolutional networks for biomedical image segmentation. In *International Conference on Medical image computing and computer-assisted intervention*, pages 234–241. Springer, 2015.

[154] Vijay Badrinarayanan, Alex Kendall, and Roberto Cipolla. Segnet: A deep convolutional encoder-decoder architecture for image segmentation. *IEEE transactions on pattern analysis and machine intelligence*, 39(12):2481–2495, 2017.

[155] Satoru Masubuchi, Masataka Morimoto, Sei Morikawa, Momoko Onodera, Yuta Asakawa, Kenji Watanabe, Takashi Taniguchi, and Tomoki Machida. Autonomous robotic searching and assembly of two-dimensional crystals to build van der waals superlattices. *Nature communications*, 9(1):1413, 2018.

[156] Hai Li, Jumiati Wu, Xiao Huang, Gang Lu, Jian Yang, Xin Lu, Qihua Xiong, and Hua Zhang. Rapid and reliable thickness identification of two-dimensional nanosheets using optical microscopy. *ACS nano*, 7(11):10344–10353, 2013.

[157] Xiaoyang Lin, Zhizhong Si, Wenzhi Fu, Jianlei Yang, Side Guo, Yuan Cao, Jin Zhang, Xinhe Wang, Peng Liu, Kaili Jiang, et al. Intelligent identification of two-dimensional nanostructures by machine-learning optical microscopy. *Nano Research*, 11(12):6316–6324, 2018.

[158] Satoru Masubuchi and Tomoki Machida. Classifying optical microscope images of exfoliated graphene flakes by data-driven machine learning. *npj 2D Materials and Applications*, 3(1):4, 2019.

[159] ZH Ni, HM Wang, J Kasim, HM Fan, T Yu, YH Wu, YP Feng, and ZX Shen. Graphene thickness determination using reflection and contrast spectroscopy. *Nano letters*, 7(9):2758–2763, 2007.

[160] Craig M Nolen, Giovanni Denina, Desalegne Teweldebrhan, Bir Bhanu, and Alexander A Balandin. High-throughput large-area automated identification and quality control of graphene and few-layer graphene films. *Acs Nano*, 5(2):914–922, 2011.

[161] P Blake, EW Hill, AH Castro Neto, KS Novoselov, D Jiang, R Yang, TJ Booth, and AK Geim. Making graphene visible. *Applied physics letters*, 91(6):063124, 2007.

[162] Karen Simonyan and Andrew Zisserman. Very deep convolutional networks for large-scale image recognition. *arXiv preprint arXiv:1409.1556*, 2014.

[163] Yuri Y Boykov and M-P Jolly. Interactive graph cuts for optimal boundary & region segmentation of objects in nd images. In *Proceedings eighth IEEE international conference on computer vision. ICCV 2001*, volume 1, pages 105–112. IEEE, 2001.

[164] Ilya Sutskever, James Martens, George Dahl, and Geoffrey Hinton. On the importance of initialization and momentum in deep learning. In *International conference on machine learning*, pages 1139–1147, 2013.

[165] Jl A Wilson and AD Yoffe. The transition metal dichalcogenides discussion and interpretation of the observed optical, electrical and structural properties. *Advances in Physics*, 18(73):193–335, 1969.

[166] AR Beal, HP Hughes, and WY Liang. The reflectivity spectra of some group va transition metal dichalcogenides. *Journal of physics C: solid state physics*, 8(24):4236, 1975.

[167] Michael A McGuire, Genevieve Clark, KC Santosh, W Michael Chance, Gerald E Jellison Jr, Valentino R Cooper, Xiaodong Xu, and Brian C Sales. Magnetic behavior and spin-lattice coupling in cleavable van der waals layered crcl 3 crystals. *Physical Review Materials*, 1(1):014001, 2017.

[168] Jose L Lado and Joaquín Fernández-Rossier. On the origin of magnetic anisotropy in two dimensional cri3. *2D Materials*, 4(3):035002, 2017.

[169] Soobin Sinn, Choong Hyun Kim, Beom Hyun Kim, Kyung Dong Lee, Choong Jae Won, Ji Seop Oh, Moonsup Han, Young Jun Chang, Namjung Hur, Hitoshi Sato, et al. Electronic structure of the kitaev material α-rucl 3

probed by photoemission and inverse photoemission spectroscopies. *Scientific reports*, 6:39544, 2016.

[170] H Xiong, JA Sobota, S-L Yang, H Soifer, A Gauthier, M-H Lu, Y-Y Lv, S-H Yao, D Lu, M Hashimoto, et al. Three-dimensional nature of the band structure of zrte 5 measured by high-momentum-resolution photoemission spectroscopy. *Physical Review B*, 95(19):195119, 2017.

[171] G Guizzetti, L Nosenzo, I Pollini, E Reguzzoni, G Samoggia, and G Spinolo. Reflectance and thermoreflectance studies of crcl 3, crbr 3, nicl 2, and nibr 2 crystals. *Physical Review B*, 14(10):4622, 1976.

[172] Kenan Zhang, Ke Deng, Jiaheng Li, Haoxiong Zhang, Wei Yao, Jonathan Denlinger, Yang Wu, Wenhui Duan, and Shuyun Zhou. Widely tunable band gap in a multivalley semiconductor snse by potassium doping. *Physical Review Materials*, 2(5):054603, 2018.

[173] Lee A Burton, Thomas J Whittles, David Hesp, Wojciech M Linhart, Jonathan M Skelton, Bo Hou, Richard F Webster, Graeme O'Dowd, Christian Reece, David Cherns, et al. Electronic and optical properties of single crystal sns 2: an earth-abundant disulfide photocatalyst. *Journal of Materials Chemistry A*, 4(4):1312–1318, 2016.

[174] BL Evans and RA Hazelwood. Optical and electrical properties of snse2. *Journal of Physics D: Applied Physics*, 2(11):1507, 1969.

[175] Aday J Molina-Mendoza, Mariam Barawi, Robert Biele, Eduardo Flores, José R Ares, Carlos Sánchez, Gabino Rubio-Bollinger, Nicolás Agraït, Roberto D'Agosta, Isabel J Ferrer, et al. Electronic bandgap and exciton binding energy of layered semiconductor tis3. *Advanced Electronic Materials*, 1(9):1500126, 2015.

[176] S Kurita, JL Staehli, M Guzzi, and F Lévy. Optical properties of zrs3 and zrse3. *Physica B+ C*, 105(1-3):169–173, 1981.

[177] Ke-zhao Du, Xing-zhi Wang, Yang Liu, Peng Hu, M Iqbal Bakti Utama, Chee Kwan Gan, Qihua Xiong, and Christian Kloc. Weak van der waals stacking, wide-range band gap, and raman study on ultrathin layers of metal phosphorus trichalcogenides. *ACS nano*, 10(2):1738–1743, 2015.

[178] V Grasso, F Neri, P Perillo, L Silipigni, and M Piacentini. Optical-absorption spectra of crystal-field transitions in mnps 3 at low temperatures. *Physical Review B*, 44(20):11060, 1991.

[179] Gabriel Autès, Anna Isaeva, Luca Moreschini, Jens C Johannsen, Andrea Pisoni, Ryo Mori, Wentao Zhang, Taisia G Filatova, Alexey N Kuznetsov, László Forró, et al. A novel quasi-one-dimensional topological insulator in bismuth iodide β-bi 4 i 4. *Nature materials*, 15(2):154, 2016.

[180] Kamal Choudhary, Gowoon Cheon, Evan Reed, and Francesca Tavazza. Elastic properties of bulk and low-dimensional materials using van der waals density functional. *Physical Review B*, 98(1):014107, 2018.

[181] Jun Zhou, Lei Shen, Miguel Dias Costa, Kristin A Persson, Shyue Ping Ong, Patrick Huck, Yunhao Lu, Xiaoyang Ma, Yiming Chen, Hanmei Tang, et al. 2dmatpedia, an open computational database of two-dimensional materials from top-down and bottom-up approaches. *Scientific data*, 6(1):86, 2019.

[182] Patrick K Herring, Allen L Hsu, Nathaniel M Gabor, Yong Cheol Shin, Jing Kong, Tomas Palacios, and Pablo Jarillo-Herrero. Photoresponse of an electrically tunable ambipolar graphene infrared thermocouple. *Nano letters*, 14(2):901–907, 2014.

[183] Michela Badioli, Achim Woessner, Klaas-Jan Tielrooij, Sebastien Nanot, Gabriele Navickaite, Tobias Stauber, FJ García de Abajo, and Frank HL Koppens. Phonon-mediated mid-infrared photoresponse of graphene. *Nano letters*, 14(11):6374–6381, 2014.

[184] Allen L Hsu, Patrick K Herring, Nathaniel M Gabor, Sungjae Ha, Yong Cheol Shin, Yi Song, Matthew Chin, Madan Dubey, Anantha P Chandrakasan, Jing Kong, et al. Graphene-based thermopile for thermal imaging applications. *Nano letters*, 15(11):7211–7216, 2015.

[185] Yu Yao, Raji Shankar, Mikhail A Kats, Yi Song, Jing Kong, Marko Loncar, and Federico Capasso. Electrically tunable metasurface perfect absorbers for ultrathin mid-infrared optical modulators. *Nano letters*, 14(11):6526–6532, 2014.

[186] Isaac J Luxmoore, Peter Q Liu, Penglei Li, Jérôme Faist, and Geoffrey R Nash. Graphene–metamaterial photodetectors for integrated infrared sensing. *ACS photonics*, 3(6):936–941, 2016.

[187] Shichao Song, Qin Chen, Lin Jin, and Fuhe Sun. Great light absorption enhancement in a graphene photodetector integrated with a metamaterial perfect absorber. *Nanoscale*, 5(20):9615–9619, 2013.

[188] Peining Li, Martin Lewin, Andrey V Kretinin, Joshua D Caldwell, Kostya S Novoselov, Takashi Taniguchi, Kenji Watanabe, Fabian Gaussmann, and Thomas Taubner. Hyperbolic phonon-polaritons in boron nitride for near-field optical imaging and focusing. *Nature communications*, 6:7507, 2015.

[189] S Dai, Z Fei, Q Ma, AS Rodin, M Wagner, AS McLeod, MK Liu, W Gannett, W Regan, K Watanabe, et al. Tunable phonon polaritons in atomically thin van der waals crystals of boron nitride. *Science*, 343(6175):1125–1129, 2014.

[190] Antonio Rogalski. *Infrared detectors*, chapter 2. CRC press, 2010.

[191] Nguyen Chi-Anh, Hyun-Joon Shin, KunTae Kim, Yong-Hee Han, and Sung Moon. Characterization of uncooled bolometer with vanadium tungsten oxide infrared active layer. *Sensors and Actuators A: Physical*, 123:87–91, 2005.

[192] Hongchen Wang, Xinjian Yi, Guang Huang, Jing Xiao, Xiongwei Li, and Sihai Chen. Ir microbolometer with self-supporting structure operating at room temperature. *Infrared Physics & Technology*, 45(1):53–57, 2004.

[193] Ali Yildiz, Zeynep Celik-Butler, and Donald P Butler. Microbolometers on a flexible substrate for infrared detection. *IEEE Sensors Journal*, 4(1):112–117, 2004.

[194] Hyung-Kew Lee, Jun-Bo Yoon, Euisik Yoon, Sang-Baek Ju, Yoon-Joong Yong, Wook Lee, and Sang-Gook Kim. A high fill-factor infrared bolometer using micromachined multilevel electrothermal structures. *IEEE Transactions on Electron Devices*, 46(7):1489–1491, 1999.

[195] D Sabuncuoglu Tezcan, Selim Eminoglu, and Tayfun Akin. A low-cost uncooled infrared microbolometer detector in standard cmos technology. *IEEE Transactions on electron devices*, 50(2):494–502, 2003.

[196] S Yoneoka, M Liger, G Yama, R Schuster, F Purkl, J Provine, FB Prinz, RT Howe, and TW Kenny. Ald-metal uncooled bolometer. In *2011 IEEE 24th International Conference on Micro Electro Mechanical Systems*, pages 676–679. IEEE, 2011.

[197] Changhong Chen, Xinjian Yi, Jing Zhang, and Xingrong Zhao. Linear uncooled microbolometer array based on vox thin films. *Infrared physics & technology*, 42(2):87–90, 2001.

[198] Mahmoud Almasri, Donald P Butler, and Zeynep Celik-Butler. Self-supporting uncooled infrared microbolometers with low-thermal mass. *Journal of microelectromechanical systems*, 10(3):469–476, 2001.

[199] Sherif Sedky, Paolo Fiorini, Matty Caymax, C Baert, Lou Hermans, and Robert Mertens. Characterization of bolometers based on polycrystalline silicon germanium alloys. *IEEE Electron Device Letters*, 19(10):376–378, 1998.

[200] Hubert Jerominek, Martin Renaud, Nicholas R Swart, Francis Picard, Timothy D Pope, Marc Levesque, Mario Lehoux, Ghislain Bilodeau, Martin Pelletier, Danick Audet, et al. Micromachined vo2-based uncooled ir bolometric detector arrays with integrated cmos readout electronics. In *Micromachined Devices and Components II*, volume 2882, pages 111–121. International Society for Optics and Photonics, 1996.

[201] A Graf, M Arndt, M Sauer, and G Gerlach. Review of micromachined thermopiles for infrared detection. *Measurement Science and Technology*, 18(7):R59, 2007.

[202] Dehui Xu, Bin Xiong, Yuelin Wang, and Tie Li. Robust array-composite micromachined thermopile ir detector by cmos technology. *IEEE Electron Device Letters*, 32(12):1761–1763, 2011.

[203] Paul Muralt. Micromachined infrared detectors based on pyroelectric thin films. *Reports on Progress in Physics*, 64(10):1339, 2001.

[204] Nathaniel M Gabor, Justin CW Song, Qiong Ma, Nityan L Nair, Thiti Taychatanapat, Kenji Watanabe, Takashi Taniguchi, Leonid S Levitov, and Pablo Jarillo-Herrero. Hot carrier–assisted intrinsic photoresponse in graphene. *Science*, 334(6056):648–652, 2011.

[205] Qiong Ma, Nathaniel M Gabor, Trond I Andersen, Nityan L Nair, Kenji Watanabe, Takashi Taniguchi, and Pablo Jarillo-Herrero. Competing channels for hot-electron cooling in graphene. *Physical review letters*, 112(24):247401, 2014.

[206] Mervin Zhao, Yu Ye, Yimo Han, Yang Xia, Hanyu Zhu, Siqi Wang, Yuan Wang, David A Muller, and Xiang Zhang. Large-scale chemical assembly of atomically thin transistors and circuits. *Nature nanotechnology*, 11(11):954, 2016.

[207] Marcos HD Guimaraes, Hui Gao, Yimo Han, Kibum Kang, Saien Xie, Cheol-Joo Kim, David A Muller, Daniel C Ralph, and Jiwoong Park. Atomically thin ohmic edge contacts between two-dimensional materials. *Acs Nano*, 10(6):6392–6399, 2016.

[208] R Bistritzer and Allan H MacDonald. Electronic cooling in graphene. *Physical Review Letters*, 102(20):206410, 2009.

[209] Justin CW Song, Michael Y Reizer, and Leonid S Levitov. Disorder-assisted electron-phonon scattering and cooling pathways in graphene. *Physical review letters*, 109(10):106602, 2012.

[210] Matt W Graham, Su-Fei Shi, Daniel C Ralph, Jiwoong Park, and Paul L McEuen. Photocurrent measurements of supercollision cooling in graphene. *Nature Physics*, 9(2):103, 2013.

[211] Justin CW Song and Leonid S Levitov. Energy flows in graphene: hot carrier dynamics and cooling. *Journal of Physics: Condensed Matter*, 27(16):164201, 2015.

[212] Eric Pop, David A Mann, Kenneth E Goodson, and Hongjie Dai. Electrical and thermal transport in metallic single-wall carbon nanotubes on insulating substrates. *Journal of Applied Physics*, 101(9):093710, 2007.

[213] Rusen Yan, Jeffrey R Simpson, Simone Bertolazzi, Jacopo Brivio, Michael Watson, Xufei Wu, Andras Kis, Tengfei Luo, Angela R Hight Walker, and Huili Grace Xing. Thermal conductivity of monolayer molybdenum disulfide obtained from temperature-dependent raman spectroscopy. *ACS nano*, 8(1):986–993, 2014.

[214] Ching-Yuan Su, Ang-Yu Lu, Yanping Xu, Fu-Rong Chen, Andrei N Khlobystov, and Lain-Jong Li. High-quality thin graphene films from fast electrochemical exfoliation. *ACS nano*, 5(3):2332–2339, 2011.

[215] Xinming Li, Tingting Yang, Yao Yang, Jia Zhu, Li Li, Fakhr E Alam, Xiao Li, Kunlin Wang, Huanyu Cheng, Cheng-Te Lin, et al. Large-area ultrathin graphene films by single-step marangoni self-assembly for highly sensitive strain sensing application. *Advanced Functional Materials*, 26(9):1322–1329, 2016.

[216] Marek Hempel, Daniel Nezich, Jing Kong, and Mario Hofmann. A novel class of strain gauges based on layered percolative films of 2d materials. *Nano letters*, 12(11):5714–5718, 2012.

[217] John G Simmons. Electric tunnel effect between dissimilar electrodes separated by a thin insulating film. *Journal of applied physics*, 34(9):2581–2590, 1963.

[218] John G Simmons. Generalized formula for the electric tunnel effect between similar electrodes separated by a thin insulating film. *Journal of applied physics*, 34(6):1793–1803, 1963.

[219] Hylke B Akkerman, Ronald CG Naber, Bert Jongbloed, Paul A van Hal, Paul WM Blom, Dago M de Leeuw, and Bert de Boer. Electron tunneling through alkanedithiol self-assembled monolayers in large-area molecular junctions. *Proceedings of the National Academy of Sciences*, 104(27):11161–11166, 2007.

[220] Farnaz Niroui, Annie I Wang, Ellen M Sletten, Yi Song, Jing Kong, Eli Yablonovitch, Timothy M Swager, Jeffrey H Lang, and Vladimir Bulovic. Tunneling nanoelectromechanical switches based on compressible molecular thin films. *ACS nano*, 9(8):7886–7894, 2015.

[221] Jesse Crossno, Jing K Shi, Ke Wang, Xiaomeng Liu, Achim Harzheim, Andrew Lucas, Subir Sachdev, Philip Kim, Takashi Taniguchi, Kenji Watanabe, et al. Observation of the dirac fluid and the breakdown of the wiedemann-franz law in graphene. *Science*, 351(6277):1058–1061, 2016.

[222] Leonid Levitov and Gregory Falkovich. Electron viscosity, current vortices and negative nonlocal resistance in graphene. *Nature Physics*, 12(7):672, 2016.